LA-UR 95- 157

Los Alamos National Laboratory is operated by the University of California for the United States Department of Energy under contract W-7405-ENG-36.

TITLE: SILICON SUBSYSTEM MECHANICAL ENGINEERING WORK FOR THE SOLENOIDAL DETECTOR COLLABORATION

AUTHOR(S): W. O. Miller, M. Barney, D. Byrd, R. W. Christensen, G. Dransfield, M. Elder, M. Gamble, C. Crastataro, J. Hanlon, D. C. Jones, G. Jordan, B. Michaud, A.P.T. Palounek, D. Pierce, R. Ricketts, R. Reid, H. Salazar, L. Salzer, S. Schramm, T. Thompson, W. Wilds, J. Williams, K. Woloshun, H.-J. Ziock

SUBMITTED TO: This is a report detailing work contracted to do for the Superconducting Super Collider Laboratory.

DISCLAIMER

Los Alamos National Laboratory
Los Alamos, New Mexico 87545

FORM NO 836 R4
ST NO 2629 5/81

SILICON SUBSYSTEM MECHANICAL ENGINEERING WORK FOR THE SOLENOIDAL DETECTOR COLLABORATION

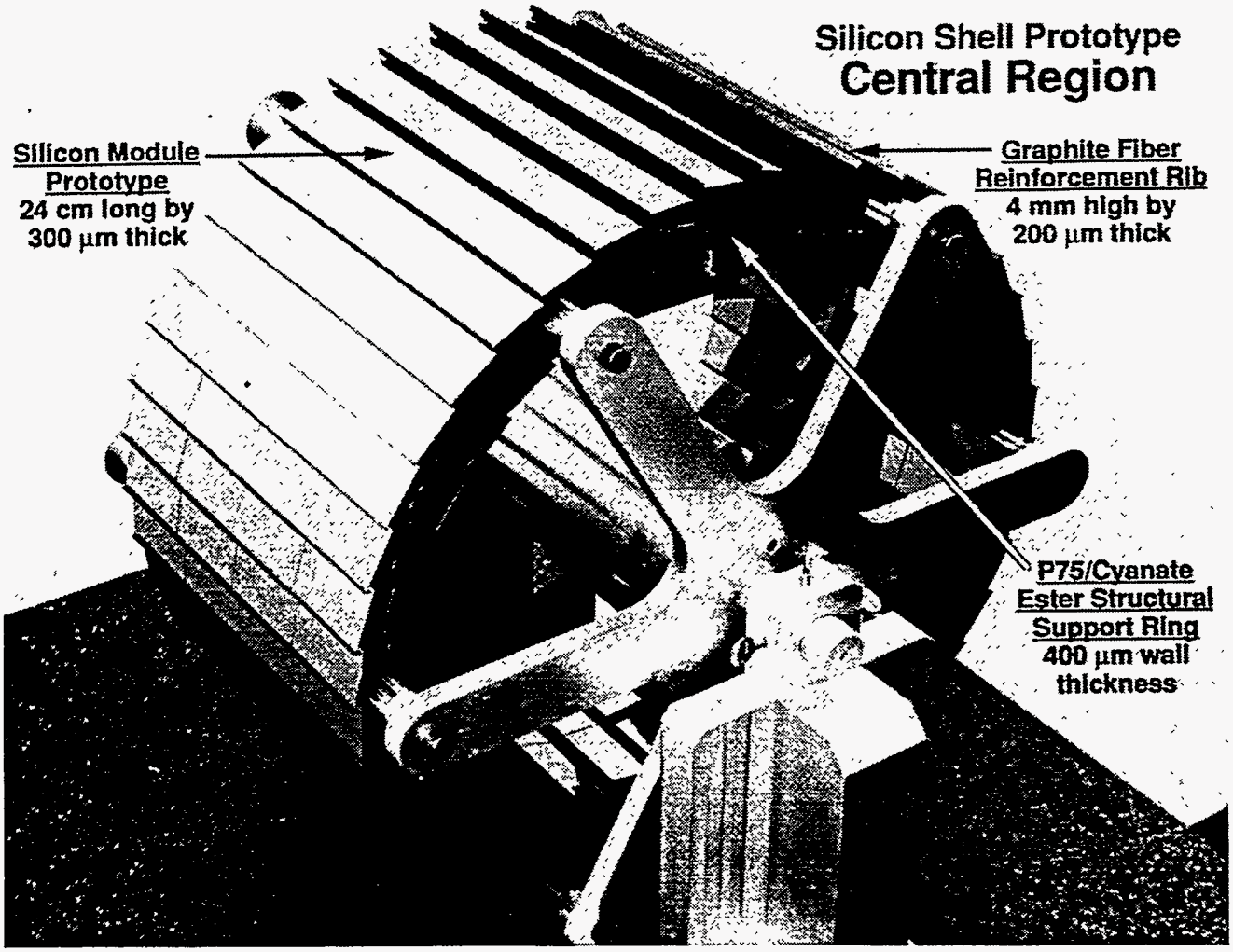

W.O. Miller, M. Barney, D. Byrd, R.W. Christensen, G Dransfield, M. Elder, M. Gamble, C. Grastataro, J. Hanlon, D.C. Jones, G. Jordan, B. Michaud, A.P.T. Palounek, D. Pierce, R. Ricketts, R. Reid, H. Salazar, L. Salzer, S. Schramm, T. Thompson, W. Wilds, J. Williams, K. Woloshun, H.-J. Ziock

Los Alamos National Laboratory

Table of Contents

Figures

Tables

1.0 INTRODUCTION

The silicon tracking system (STS) for the Solenoidal Detector Collaboration (SDC) represented an order of magnitude increase in size over any silicon system that had been previously built or even planned. In order to meet its performance requirements, it could not simply be a linear scaling of earlier systems, but instead required completely new concepts. The small size of the early systems made it possible to simply move the support hardware and services largely outside the active volume of the system. For a system five meters long, that simply is not an option. The design of the STS for the SDC experiment was the result of numerous compromises between the capabilities required to do the physics and the limitations imposed by cost, material properties, and silicon strip detector characteristics.

From the point of view of the physics, the silicon system should start as close to the interaction point as possible. In addition, the detectors should measure the position of particles passing through them with no errors, and should not deflect or interact with the particles in any way. However, cost, radiation damage, and other factors limiting detector performance dictated, other, more realistic values. Radiation damage limited the inner radius of the silicon detectors to about 9 cm, whereas cost limited the outer radius of the detectors to about 50 cm. Cost also limits the half length of the system to about 250 cm. To control the effects of radiation damage on the detectors required operating the system at a temperature of 0°C or below, and maintaining that temperature throughout life of the system. The position resolution of the detectors is given by the pitch of their readout strips (50 μm). That value reflected a compromise between desires (small pitch), and cost (small pitch corresponds to large cost), a realistic assessment of detector performance as limited by their thickness, magnetic field effects, charge diffusion, *etc.*, and the matching of the STS performance with that of other parts of the overall SDC detector system. The 50 μm pitch implied a position resolution of 50 $\mu m/\sqrt{12}$ for a hit/no-hit readout scheme. Information from the stereo strips and charge sharing between neighboring strips (using only a hit/no-hit readout) improved the resolution to ~ 10 μm. In order that the capabilities of the strip detectors determined the overall STS performance, the detector support structure had to be stable to about 5 μm. The desire to use the raw silicon data directly in the trigger, coupled with the tolerance build up during system assembly, required positioning parts to approximately 5 μm accuracy, at least in certain directions.

Due to effects such as electron bremsstrahlung and pair production, accurate reconstruction of the physics events required that the various services (support, supply of electrical power, cooling, *etc.*) be achieved using the minimal number of radiation lengths of material possible. In order to achieve that, one had to use materials which possessed as large a radiation length value as possible (*e.g.* Be: 1 X_o = 35.4 cm; or graphite/epoxy: 1 X_o = 25 cm), so that one would have the maximal material thickness, and therefore strength, for a given number of radiation lengths.

To summarize, the physics and properties of the silicon strip detectors requires that the detectors be operated at or below 0°C, be positioned very accurately during assembly and remain positionally stable throughout their operation, and that all materials used be radiation hard and have a large thickness for one radiation length.

2.0 EXECUTIVE SUMMARY

Clearly fiscal year 1993 proved to be very tumultuous and fraught with uncertainties regarding the future of the SSC program. In spite of these distractions, LANL pressed on and advanced many of the key engineering concepts embodied in SDC's precision silicon tracking subsystem. Many detector prototypes were constructed during the course of the year to investigate fundamental issues inherent in large, extremely lightweight detector systems. This report should serve to highlight these many accomplishments, and where appropriate identify work remaining.

The innermost part of the SDC tracking system was a silicon-based detector system composed of 14,000 optimally placed, double-sided, silicon strip detectors, providing a resolution of 10 μm. Stringent limitations placed on materials essential for detector stability, cooling, electronics, data readout, and cabling resulted in unique engineering challenges. An individual interested in some of the key decisions leading to our engineering approach in these areas would be advised to review SDC's Technical Design Report (TDR). The TDR outlines detector performance, and concomitant engineering choices that formed the basis of our initial approach to the overall detector. Topical information on composite material construction techniques, evaporative cooling, stable structures, along with other points of interest, can be found in this document.

The following list summarizes the activities that were the focus of last year's effort:

- verification of the silicon module structural robustness and materials compatibility;
- composite material property testing, and thermal conductivity enhancements;
- material compatibility tests in a butane and high radiation environment;
- development of both compression molded and carbon foam core sandwich fabrication techniques for ultra-thin, ring-like structures;
- evaluation of resin transfer molding technique for a complex space frame joint;
- demonstration of the operation of an evaporative cooling system for removing heat from the highly dispersed array of electronic chips;
- development of a large aperture viewing TV Holographic system for quantifying thermal and dynamic strains, at the sub-micron level;
- completion of the design and construction of a semi-automated work station capable of silicon module placements to within 5 μm; and
- investigation of water-based cooling as an alternate to evaporative cooling.

Confirmation of the structural robustness of the adhesively bonded 24 cm long silicon detector module was provided through a series of module tensile tests, and 10 Mrad radiation and butane exposure tests. These combined butane and radiation tests strengthened our confidence in adhesive selections for module construction. An earlier evaluation had confirmed the adhesive compatibility with an active silicon strip detector.

Our primary tracker program objective was to conduct a dimensional stability test on a typical silicon sub-structure. To this end, as shown in Figure 2.0-1, we chose to construct a 42 cm diameter prototype silicon shell, with 78, 24 cm long modules. Individual detector modules were bonded to a pair of composite support rings with a demountable adhesive, thus forming a silicon shell-like structure. To complete the structural simulation, beryllium ground planes were added to each silicon detector module prototype along with resistive heaters and cooling system wicks. This assembly was used to quantify the stability behavior of this first generation silicon structure under a simulated electronic heat load condition of 1.56 m/W per strip. The TV Holographic system, developed for this program, made it possible to demonstrate the

thermal/mechanical stability goal. The butane evaporative cooling system was used to remove the simulated electronic heat load, imposed by individual electrical heaters. This first prototype was cooled to 0°C, where it remained dimensionally stable to better than 1 μm throughout the test period.

A prototype space frame joint was constructed using a resin transfer molding (RTM) process that greatly simplifies the fabrication of complex intersecting tubular shapes. We chose this construction technique over more costly cast metal matrix, discontinuous graphite fiber combinations. The woven graphite fiber joint obtained by RTM provides a comparatively low coefficient of thermal expansion, which is advantageous. Again, through a novel adaptation of the TV Holographic system, we were able to show that the adhesively bonded space frame joints did not creep under constant axial load.

Major accomplishments were made in design and construction of a semi-automated work station for assembling the delicate silicon sub-structures. The work station has been assembled and demonstrated to repeat positions to better than 2 μm. The unit was configured to place modules onto composite support structures to the order of 5 μm, without accumulative errors being introduced. An optical reference system essential to the repetitive placement of modules remains to be constructed and demonstrated.

Considerable work was accomplished in the areas of composite material testing, ultra-thin composite material fabrication techniques, and achievement of thermal property enhancements in composite materials. Our goal was to produce composite ring structures with a wall thickness less than 450 μm, and this objective was achieved. We also investigated both a carbon foam and honey-comb core sandwich structure for the support rings. At year's end we had focused in on carbon foam as the most practical and least expensive core material for ring and plate structures. The composite sandwich plate structure had originally been intended to be only used for the flat planar arrays planned for the forward detector regions.

Studies were initiated with a water-based forced convective cooling system, as an alternative concept to the evaporative system. Small individual rectangular heat exchangers were tested. The high aspect ratio channel, 1.5 mm by 1 cm, developed very high convective film coefficients, in spite of the low through-put velocities.

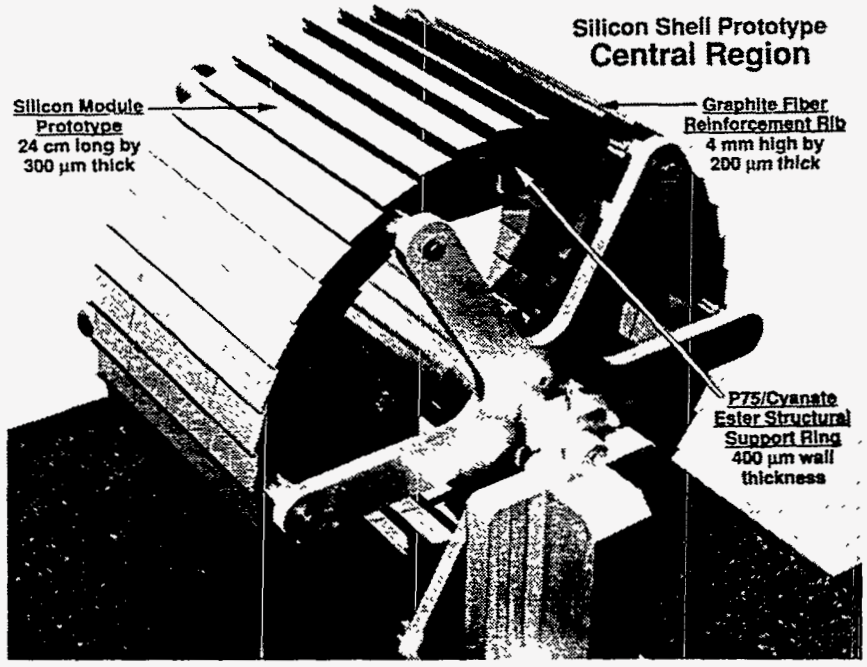

Figure 2.0-1 A 42-cm diameter prototype silicon shell prior to bonding "electronic" and cooling components.

3.0 TECHNICAL DISCUSSION

3.1 Baseline Design Description

The silicon tracking system (STS) is composed of silicon wafers arranged in an array of concentric cylinders and in two arrays of circular flat panels, one at each end of the detector. All arrays are centered on the beam pipe. The cylindrical array is referred to as the central or barrel region and the flat panel arrays, which are normal to the beam axis, are referred to as the forward regions. The overall system length is 5.2 m, and the outer diameter, including the shell enclosure, is approximately 1.2 m. Figure 3.1-1 depicts a cutaway of the silicon detector array and space frame support.

The current STS differs considerably from the version described in an earlier Los Alamos report[1]. Much of the design work and analysis performed on that system, however, are germane to the current system under study, hence that report may be consulted if the evolution of the current design is sought.

The STS baseline design arrangement is shown in Figure 3.1-2, while the baseline design requirements are listed in Tables 3.1-1 and 3.1-2. The stability requirements are quite stringent, especially considering the overall detector size, thermal heat load, and the potential effects of the radiation environment on material properties. The requirement to use the absolute minimal amount of material for the support and service structures is also a rigorous design constraint.

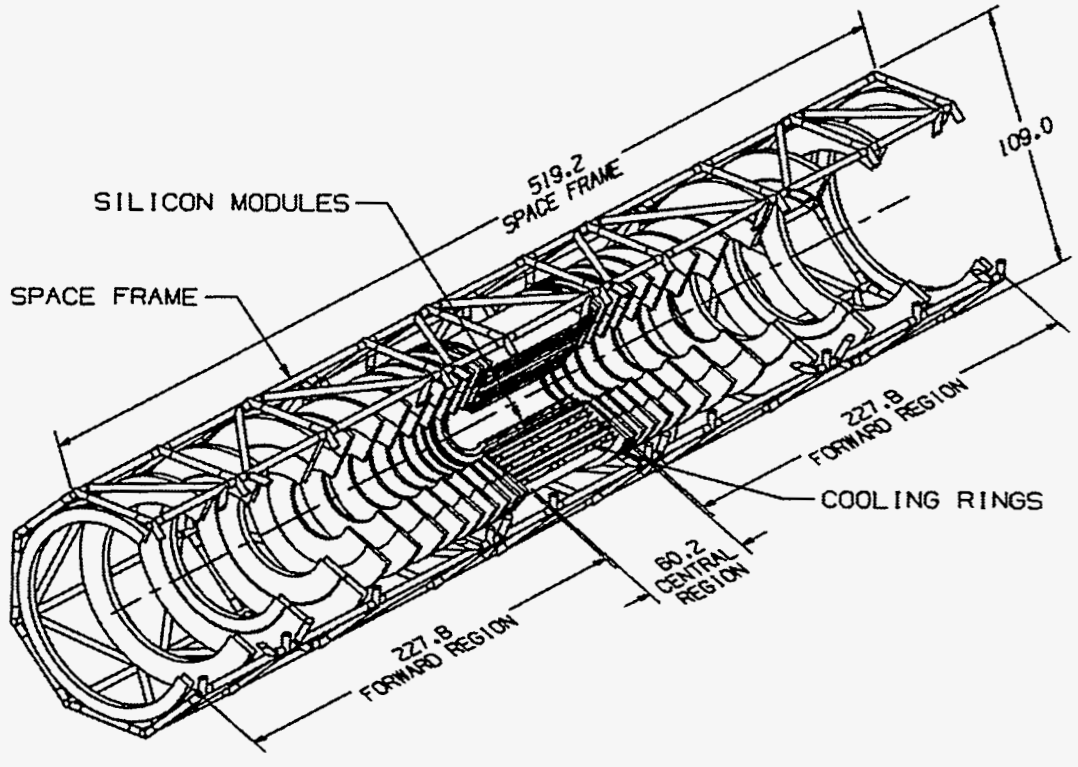

Figure 3.1-1 A cutaway of the silicon detector array and space frame support.

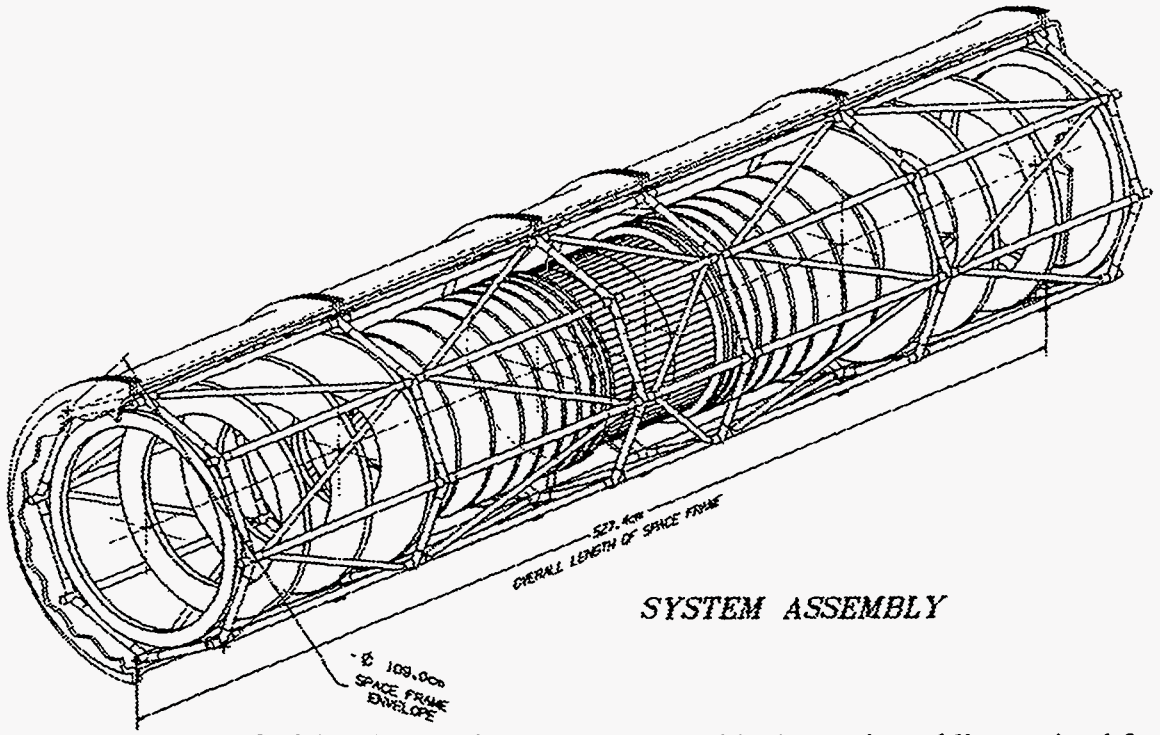

Figure 3.1-2 The STS baseline design arrangement with electronics cabling omitted for clarity.

A three dimensional shaded image of the conceptual silicon shell structure is shown in Figure 3.1-3. This structure is typical of the 12 individual silicon shells that comprise the STS central region. Each silicon structure is composed of two graphite fiber/cyanate ester (G/C-E) resin composite rings onto which individual silicon detector modules are precisely bonded in place. Detector modules are attached on the inside as well as the outside of the rings, thus forming two silicon layers into one structure. Two such silicon layers are generally referred to as a "super-layer". The composite ring structures are herein referred to as cooling rings, since they potentially serve a dual function of supporting the polystyrene wick structure. We considered two different cooling methods: one based on a chilled "water" system, and the other based on an evaporative technique. As will be discussed in more detail in the evaporative cooling section, the wick structure distributes liquid butane to each detector module for cooling the electronics. The radiation length penalty associated with this composite ring should be considered part of the STS structure budget, since the ring is required regardless of the cooling system approach. Hereafter, we refer to the ring as a "cooling ring" solely to remain consistent with earlier publications.

Each detector module's normal is tilted at a 7.4° angle with respect to a radial line emanating from the shell's centerline to mitigate the effect of the Lorentz forces, which potentially compromise the detector's measurement resolution. This construction feature also permits azimuthal detector hermeticity by allowing the modules to be placed in a shingle-like pattern with module overlap. This important feature is obtained at some expense to composite cooling ring fabrication complexity.

The maximum silicon detector module length in the central region is 24 cm; correspondingly, the maximum shell length is 24 cm. Three silicon shell assemblies, two 24 cm long and one 12 cm long, comprise a 60 cm long central region super-layer, which is supported from a 60 cm long G/C-E cylindrical shell. Four such super-layers of differing radii comprise the central region. The ordering of the three shell combinations in the super-layers is reversed in Z as a function of R to disperse the structural support mass.

Table 3.1-1 Silicon detector module specifications.

	Central Region	Forward Region
Shape:	Rectangular	Trapezoidal
Active detector width:	3.2 cm	~6.4 cm
Number of channels:	1280	2560
Heat dissipation:	2 mW/channel	2 mW/channel
Module heat load:	2.56 W	5.12 W
Thermal conductive area: (@ cooling ring surface)	2.6 cm^2	~5.1 cm^2
Module heat flux: (@ cooling ring surface)	1.0 W/cm^2	1.0 W/cm^2
Cant angle:	7.4°	0°

Table 3.1-2 STS performance specifications.

Positional stability: r, rø, z = 80. 5, 250μm
Mounting precision: r, rø, z = 80. 25. 250 μm
Radiation exposure: 10 Mrad over 10 year service life. No measurable stability effects: 5μm
Material radiation length budget: Structure and related service connections 3% @ normal incidence (excepting transition from central to forward regions and very high rapidity regions)

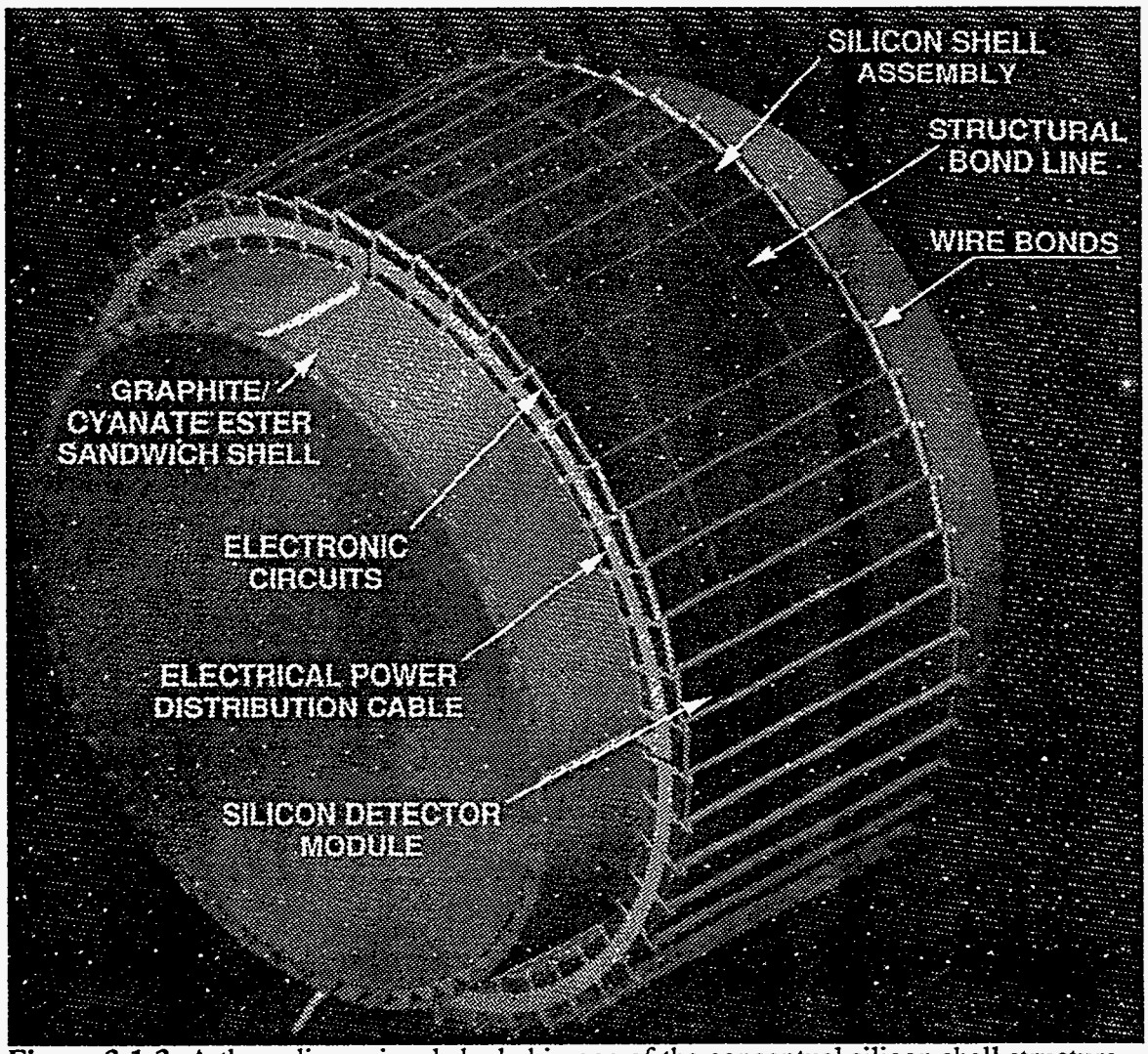

Figure 3.1-3 A three dimensional shaded image of the conceptual silicon shell structure

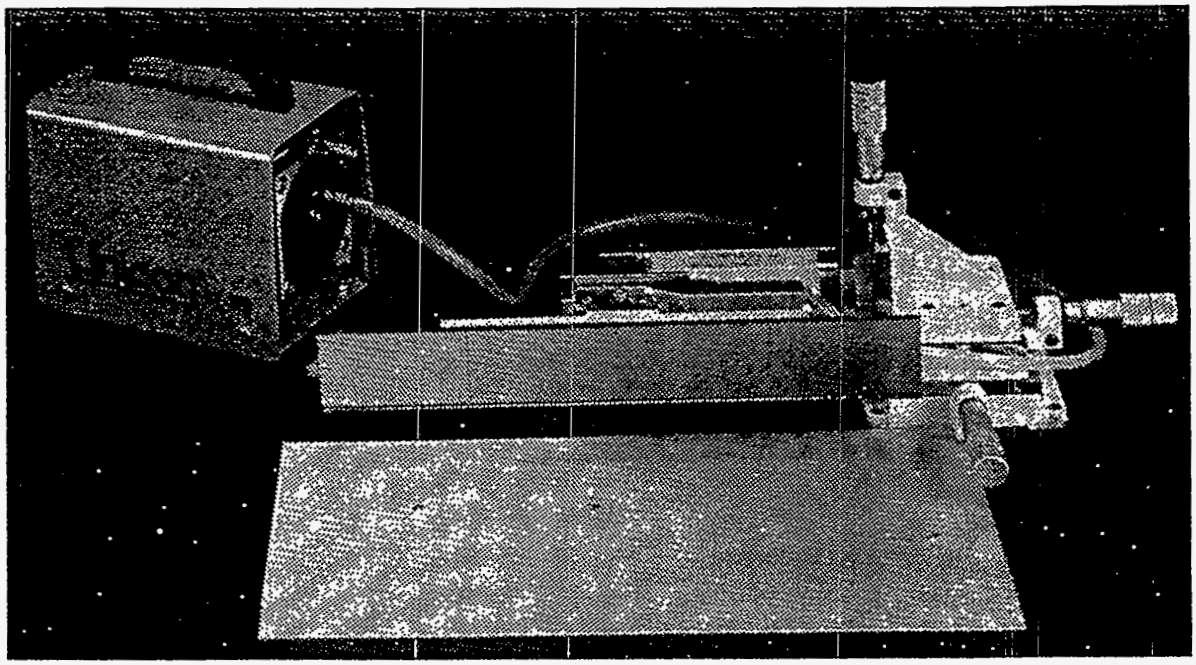

Figure 3.1-4 A photograph of a structural model of a silicon detector module mounted on a vacuum chuck fixture.

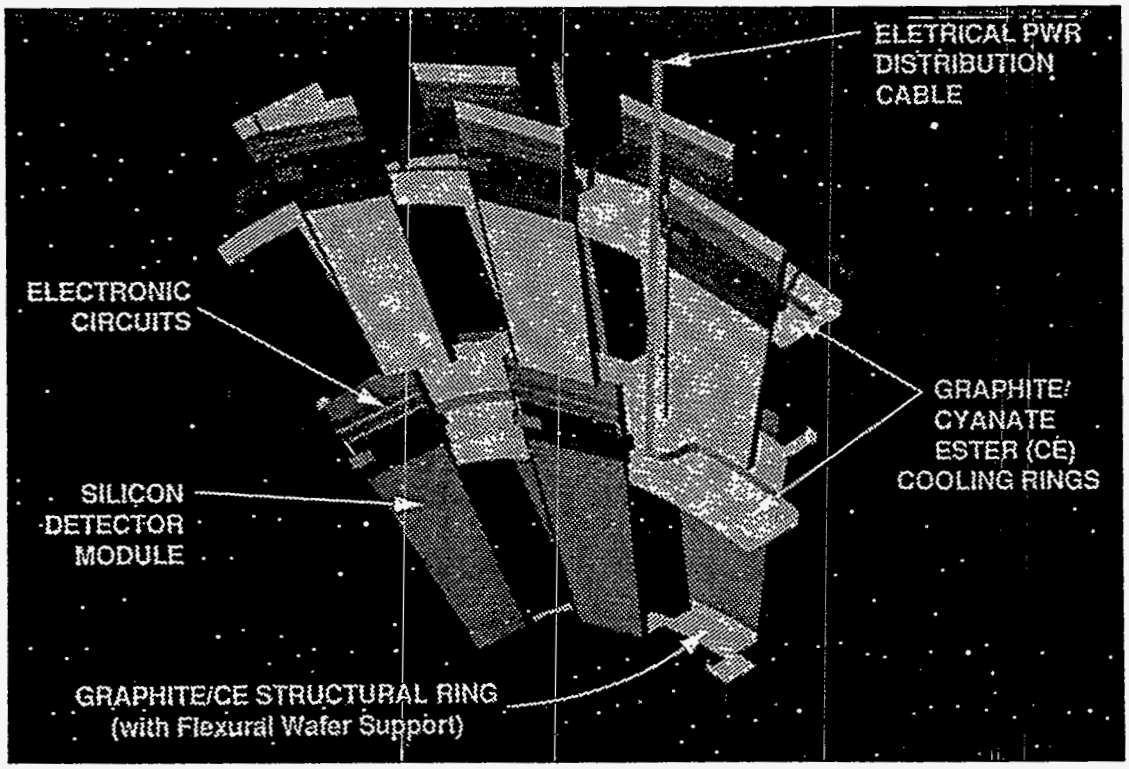

Figure 3.1-5 Conceptual layout of a forward region ring structure.

Electronics for the strips and the communication links are mounted at the end of each module. The 24 cm modules have electronics at both ends; the 12 cm modules at only one end. Ten electronic read-out chip pairs (128 channels each), five per side of the double-sided strip detector, are required for each 12 cm detector module section. The silicon module is stiffened by edge bonding two ultra-thin graphite/cyanate-ester composite strips along the length of the detector edges to form a symmetric I-beam structure. A photograph of a structural model is shown in Figure 3.1-4. It is intended for these individual detector module assemblies be structurally robust so that they can be assembled and pretested without danger of damage.

Each of the two forward regions is composed of thirteen silicon annular disks. The detector modules in the forward region are not canted, which significantly simplifies the cooling ring design. Large separations between individual silicon layers make the prospect of combining adjacent layers into super-layers unattractive. The trapezoidal shaped modules in this region are arranged azimuthally around the beam axis, and they are approximately twice as wide as those in the central region. The maximum active strip detector length is 12 cm long, the same length used in the central region. The forward modules are trapezoidal in shape to fit as individual arc sectors. Circumferential hermeticity is preserved by overlapping the adjacent trapezoidal modules. Further simplification of the cooling and structural support ring construction is achieved by having adjacent modules in one disk on alternating sides of the ring structures; reference Figure 3.1-5.

A space frame provides structural support for the central region cylindrical arrays and the forward region flat, planar arrays. The design of this structure is intended to satisfy the performance specifications set forth in Table 3.1-2. Dimensional stability requirements motivated the use of metal matrix composites (MMC) construction materials. Their ultrahigh elastic modulus is supplemented by their immunity to moisture-induced distortions. With these materials, it is also possible to tailor their longitudinal coefficient of thermal expansion (CTE) to approach zero. The two materials under study are Al-MMC and Mg-MMC, which are constructed of 60% by volume P120 fibers with a predicted CTE of -0.25 ppm/°C and -0.6 ppm/°C respectively. Figure 3.1-6 illustrates the predicted mechanical properties as a function of fiber volume fraction. A long radiation length parameter is consistent with the need to minimize deleterious effects on high energy particle tracking and momentum measurements. The selection of these materials also facilitates the use of adhesives for demountable joints as a design option. Finally, the MMC space frame readily satisfies the requirement for butane compatibility in a high-radiation environment if required.

The entire assembly is contained within a G/C-E structure, which in addition to containing the evaporated butane coolant and acting as a thermal shield, also provides the primary conduit for transferring the mechanical loads on the silicon tracker space frame to the primary central tracker support structure. The outer structure and the kinematic mounts prevent extraneous loads from being directly imposed on the delicately aligned silicon structures. Hence, the outer shell structure is a key member in maintaining STS stability. An ultra-lightweight G/C-E sandwich construction has been chosen for the outer shell and two end cover plates. A 0.5-mm thin beryllium shell will be used for the inner liner.

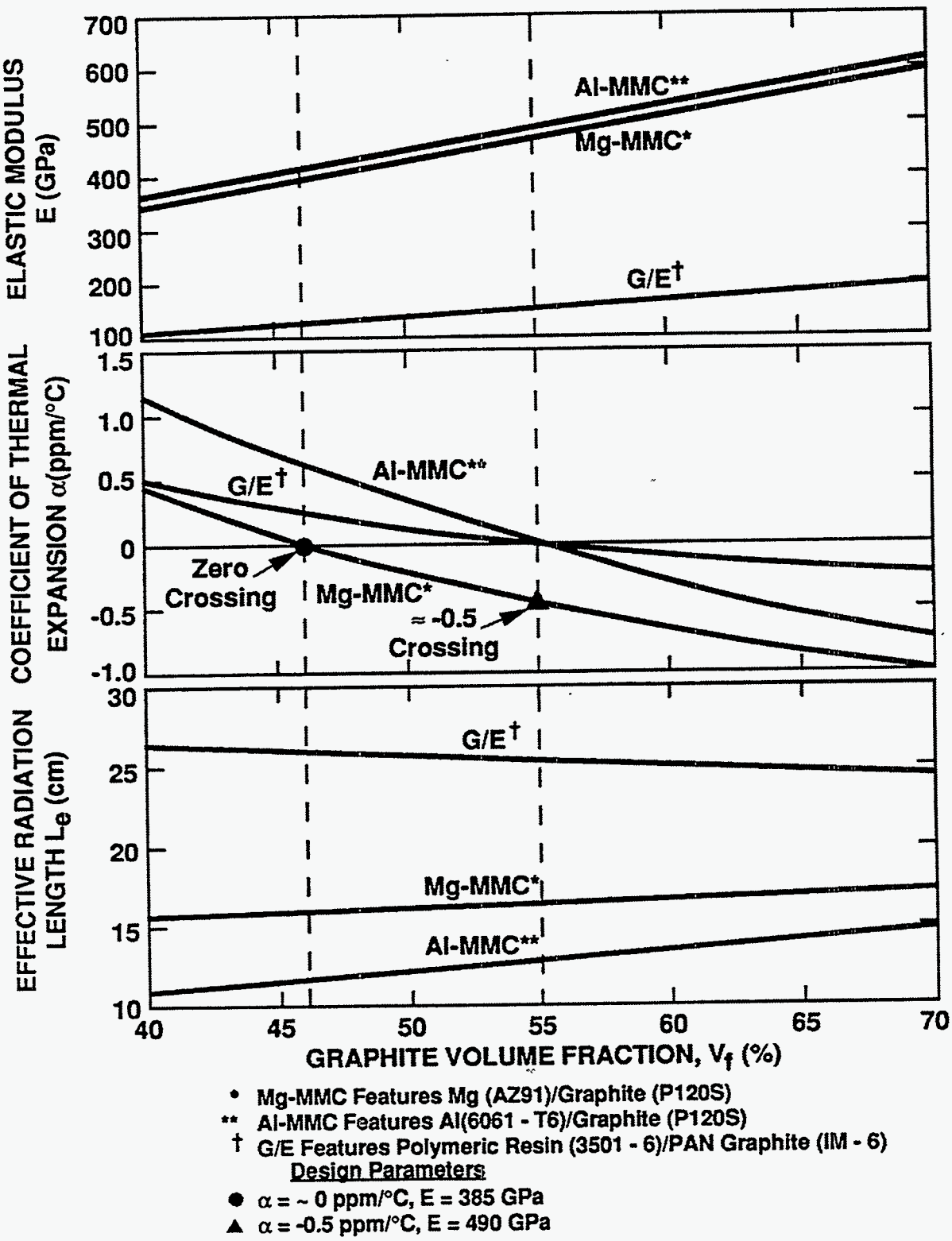

Figure 3.1-6 The predicted mechanical properties of composite materials as a function of fiber volume fraction.

3.2 Component Design and Development Activities

This section of the report details the work done in developing the concepts used and the design work done to come up with the final design we had for the silicon tracking system. The subsections herein describe the work done for the different components that were to make up the overall STS, starting from outside of the tracker and working inwards. To meet the design requirements materials with special properties were needed. Materials were needed that had a high radiation length parameter, low coefficients of thermal and moisture expansion, high thermal conductivities, high strength to mass ratios, and that could be formed to complex shapes. Since the material properties were so important and directly influenced the design of the STS, an effort to develop new materials, measure their properties, and find suitable manufacturing techniques for them was undertaken. That work is described in detail in Appendix A.

3.2.1 Enclosure/Supports

The enclosure/support system for the silicon tracker performs two important functions. First, the shell assembly provides containment of the evaporated butane coolant (vapor space) and acts as a themal shield. Secondly, the outer shell structure serves as the primary conduit for transferring the mechanical loads on the silicon tracker space frame to the outer tracker space frame. The outer structure, and the kinematic mounts prevent extraneous loads from being directly imposed on the delicate silicon structures, while maintaining precision alignment. Hence, the outer shell structure is a *key* member in maintaining the stability of the STS.

An ultra-lightweight G/C-E sandwich wall construction was chosen for the outer shell and two end cover plates. The shell is a truss core sandwich structure with an areal density of 1.2 kg/m^2. Experimental quasi-isotropic panels (an 8-ply layup of 1-mil thick sheets; nominally 200 μm total thickness, actually ~250 μm thick) have been constructed from graphite/epoxy (P75/1939-3) and tested in a proton beam with a fluence of 10^{15} particles/cm^2, in excess of what was expected in 10 SSC operational years. Out-of-plane mechanical distortions were measured to be less than 5 μm. This preliminary test instilled confidence in our general material selections and construction approach. This combination will provide a stiff low-mass structure. A very thin beryllium (0.5 mm) shell will be used for the inner liner. This combination will provide a stiff low-mass structure of minimal radiation length. A description of the individual wall structures is given in Table 3.2-1.

Under normal operation, the shell structures will not be exposed to a pressure differential, since the butane cooling system works at one atmosphere. Also, filling and emptying the butane system will be accomplished without imposing any significant pressure differential. Consequently, the gravitational loads associated with the various structural mass components largely dictate the stiffness requirements for the outer shell. In contrast, the end cover structural design is dictated by the 0.2 atm. maximum design pressure differential chosen.

Table 3.2-1 Enclosure Description

Component	Material	Size	Remarks
Outer shell	P75/954-3	5.6 m long x 1.2 m diam.	Truss core sandwich wall: three ~250-μm-thick G/C-E lamina
Inner shell	Beryllium	5.6 m long x 10 cm diam.	0.5 mm wall w/reinforcing ribs
End covers	P75/954-3	1.2 m diam. x 2.54 cm wall	Double truss core composite: five ~250-μm-thick G/C-E lamina

Access to the internal cable connections at each detector end is provided by the removable end covers. Provisions for access *in situ* will be required. Consequently, the outermost shell/flange combinations must be sufficiently stiff to carry the entire support reactions with the covers removed. With this prospect in mind, we have chosen a sandwich shell wall construction with a truss core possessing a 45° included angle that provides considerable longitudinal stiffness and minimizes gravity sag along the shell axis. The shell prototype, depicted in Figure 3.2.1-1, consists of a truss core sandwich composite with a 70° included angle. In addition, in the vicinity of the shell flange, the truss core will be circumferentially reinforced to minimize radial deflection when the covers are removed. The flange, a G/C-E honeycomb structure, provides most of the circumferential rigidity necessary for the silicon tracking system mounting interface.

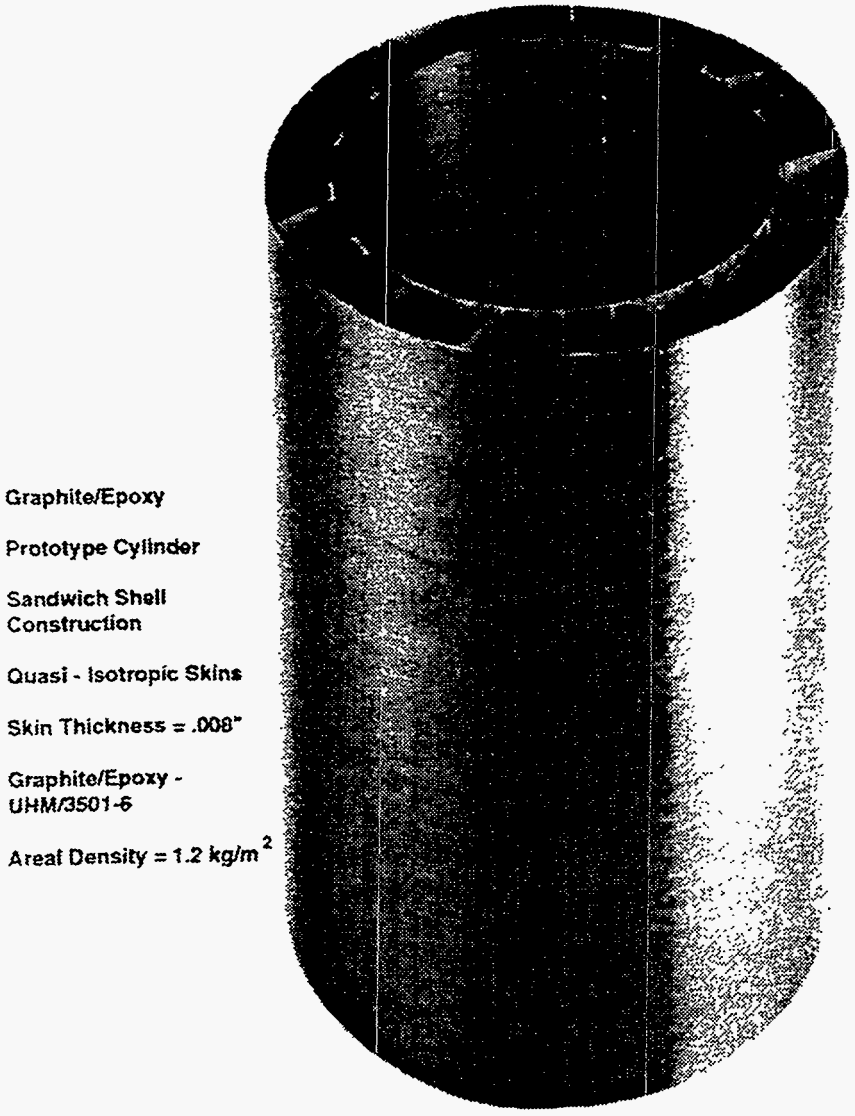

Figure 3.2.1-1 The shell prototype consisting of a truss core sandwich composite with a 70° included angle.

To facilitate STS assembly and detector maintenance, the outer enclosure will be composed of multiple sections. Flanges, spaced at nearly equal intervals, significantly enhance radial stiffness, as previously described. It is desirable that the internal space frame mechanical loads be transmitted to the outer shell at these reinforcement points. These flanged interfaces also provide intermediate points to construct pass-throughs for cables and services. Figure 3.2.1-2 illustrates the cabling and fiber optics exiting at the ends of the tracker. Because the outer enclosure is an integral part of the STS support system, the structural design of this particular element is quite critical. Before proceeding with the construction of a shell prototype planned for FY94, an analysis of the various shell design parameters was undertaken and is described in the following sections.

STS Enclosure FEA Model The loading conditions for the nominal, or baseline, solution were held constant for the static and dynamic analyses. These conditions were:

- 0.2 atm. of external pressure on the enclosure's cylindrical sections and end cover plates
- 100 kg of space frame mass (includes all mass carried by the space frame) concentrated at the two in-board flanges, nominally the shell quarter points. The mass was concentrated below the horizontal shell centerline.
- Weight of the enclosure.

A buckling analysis was performed in which only the midsection of the enclosure shell was considered because of that region's susceptibility to buckling.

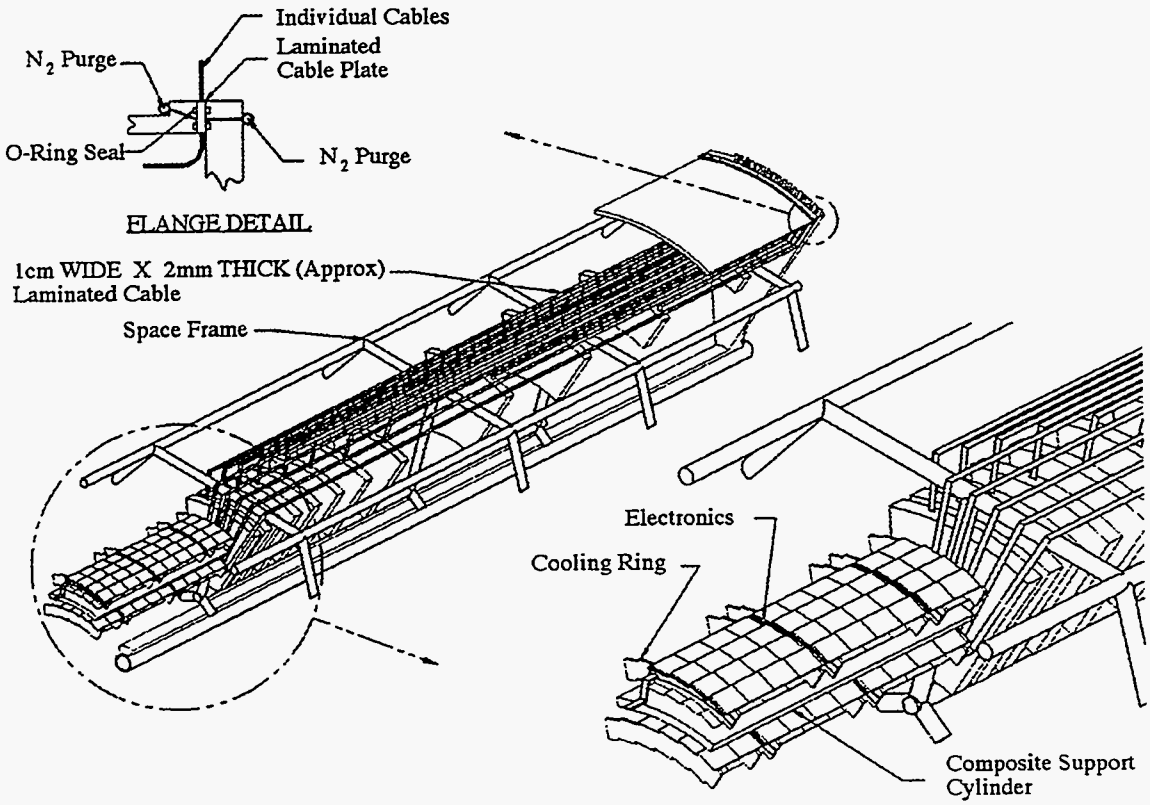

Figure 3.2.1-2 Cut-away view of the outer enclosure with cabling routes illustrated.

The boundary conditions for the model were designed to simulate a kinematic mounting scheme composed of three bars that are tangent to the enclosure's surface. (See Section 3.2.4.1 for more details on the tangent bar kinematic mounting scheme.) These bars which are tangent to the enclosure's perimeter, with 120° of circumferential separation, provide an idealized self-centering STS enclosure mount. In practice, the three bars would terminate at the outer straw tracker space frame to which they would transfer the STS' and its enclosure's loads.

The material properties of the enclosure's sandwich facings and core as well as the physical dimensions of these elements were varied parametrically using the FEA. The results of these investigation will now be discussed.

STS Enclosure Static FEA Results A shell sandwich composed of 200 μm thick facings, separated a distance of 1.27 cm with a 200 μm thick ribbon truss core, comprised the study baseline configuration. Similarly, an elastic modulus corresponding to quasi-isotropic P75 laminate material was fixed initially, and the flange heights were set at 3.81 cm. The composite flange sandwich was modeled using core properties typical of aluminum honeycomb material. In the final shell analysis, the aluminum honeycomb core properties would be replaced with graphite fiber composite material properties to reflect the intended construction plans. In this initial study phase, a sensitivity type study was performed and each of the above parameters were varied, including the number of flanges which produce enhancements to radial stiffness.

For the initial *combined* loading conditions, the shell deformed radially 220 μm; 176 μm was due solely to the 0.2 atm. external pressure, whereas the space frame gravity load, when individually applied, was observed to locally distort the flange only 78 μm. For the combined loading, the maximum stress concentration occurred around the cylinder and end flanges, where the end covers attach. Not surprisingly, the most effective means, excluding increasing the number of flanges, found for reducing these deflections was to increase the sandwich facing thickness and elastic modulus. Increasing the core thickness produces only half the benefit achieved by an increase in facing thickness. This effect was expected; our previous studies on this aspect are presented in reference 1. Specifically, the maximum deflection associated with doubling the 200 μm facing thickness was a reduction from 220 μm to 150 μm, and a reduction of Von Mises stresses from 31.9 MPa to 16.6 MPa. Similarly, when doubling the 103 GPa, nominal-case, elastic modulus, the maximum deflection was reduced from the nominal-case value to 127 μm. No reduction in stresses occurred from the elastic modulus change, as one would expect.

STS Enclosure Dynamic FEA Results The fundamental and second natural frequencies of vibration of the enclosure are ovalization modes, possessing two circumferential lobes, about orthogonal basis axes. This was expected because of the shell's small length to diameter ratio. Furthermore, the third and fourth modes were characterized by three circumferential lobes about basis axes 120° apart. The frequencies of these vibrations were approximately 84 Hz for modes one and two, and approximately 166 Hz for modes three and four, of the nominal case. Parametric studies of the sandwich core thickness and elastic modulus demonstrated that to achieve a fundamental vibrational frequency of 100 Hz, using the nominal-case core modulus elastic modulus, a core thickness of 1.9 cm would be required. This 100 Hz fundamental frequency will provide ample margin for materials performance uncertainties.

STS Enclosure Buckling Analysis The enclosure's central region was analyzed as an unreinforced, nominal-case, vacuum shell, and as a flange stiffen and facing-thicken vessel. For 0.2 atm. of external pressure and nominal-case materials properties, 0.7 atm. critical buckling pressure was determined. Theoretically the shell would become unstable at pressure above this level. By increasing the number and/or the dimensions of

intermediate stiffening flanges we are able to increase the critical pressure substantially. To obtain a safety factor of 5 for buckling, over the nominal-case of 0.2 atm., would require one additional flange over the four used in the initial study. This same increase could be achieved by increasing the facing thickness to 300 μm . Unlike adding the flange, the increased facing thickness would appreciably improve the deflections and stresses experienced by the shell as well as distribute the added material more uniformly over the volume. However, this contemplated change would be at greater expense to radiation length considerations.

STS Enclosure and FEA Conclusions These preliminary FEA results clearly indicate several areas for optimization. Generally the most sensitive parameters for the static, dynamic, and buckling performance of the enclosure shell are the sandwich facing thickness and elastic modulus. The mechanical strength of the design constituents was shown not to be an issue. The decision to increase the thickness and/or the elastic modulus of the nominal case must be considered in the presence of other ramifications on the overall system. An increase in radiation length would result from increasing facing thickness. The fabrication difficulty, availability, and cost of ultra-high elastic modulus laminates also have a negative influence on this issue. However, recent product developments in high moduli fibers, with reasonable strain to failure characteristics, suggest that continued interest in this possibility is warranted.

The unconventional nature of a truss-core sandwich construction mandates prototyping exercises. These will illuminate the enclosure design considerably and can be used to normalize the FEA results obtained thus far. After careful deliberation on the analytical and test results, a new outer enclosure design may necessarily follow.

In closing, should an alternative cooling system replace the baseline evaporative butane concept, the outer enclosure must still provide the thermal isolation barrier function. The interior butane vapor space would become a cold gas space, (*e.g.*, nitrogen) which would be circulated at a very low velocity. Insulation would be placed around the outer silicon tracker surface in either case to preclude temperature gradients being established in adjacent subsystems.

3.2.2 Space Frame

Stable support of the large array of silicon detectors is achieved by attaching the silicon substructures to a stiff, low mass, space frame like structure. The tubular frame network, like other critical tracker structural supports, is constructed of materials specifically chosen to resist dimensional changes from either thermal expansion, moisture expansion, radiation damage, and/or a combination thereof. The large spatial dimensions of the tracker volume, an approximately 5-meter long by 1-meter diameter cylinder, necessitated this consideration.

Choosing ultra-stable frame materials was not the only factor in the design, there were other added complications that drove this process. For example, cost had a strong influence on our choice of a joint material and construction technique. Of equal importance, the joint had to be demountable and of minimum cross section (low mass and low Z). The space frame is assembled in stages, thus forming natural subsections for ease of handling and subsequent maintenance. To achieve this versatility, it was necessary to introduce six transverse frame members, and associated joints. Figures 3.2.2-1 and 3.2.2-2 depict several stages of the frame assembly. One may note that an assembly frame is required which serves two purposes: (1) it provides a robust assembly staging arrangement; and (2) it eliminates the need for redundant transverse members at final assembly. By adopting a single transverse frame section for each sub-assembly we were able to significantly reduce mass installed within the tracker volume.

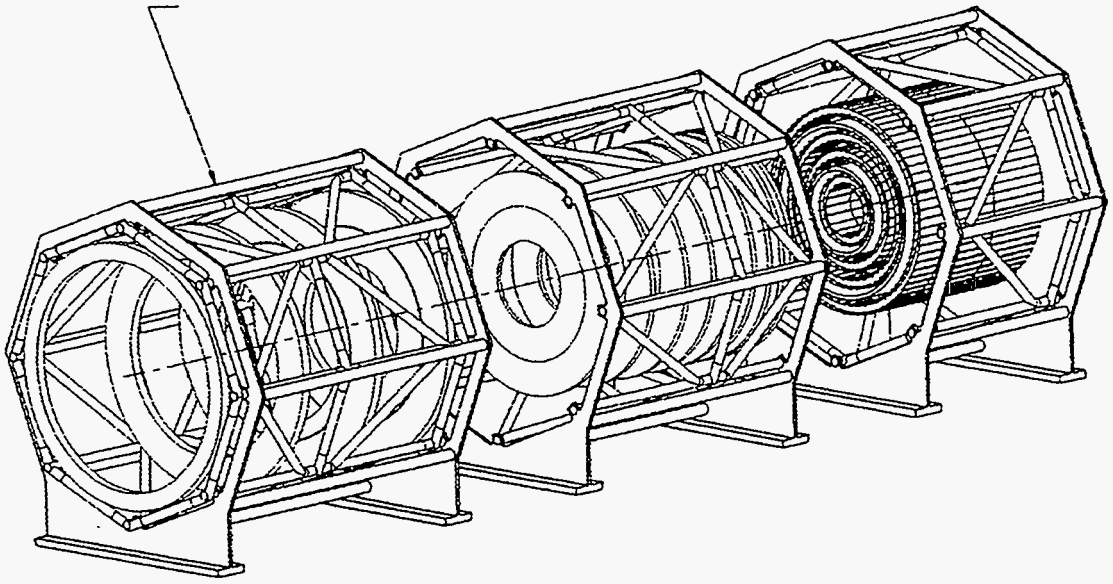

Figure 3.2.2-1 One of several stages in the space frame assembly.

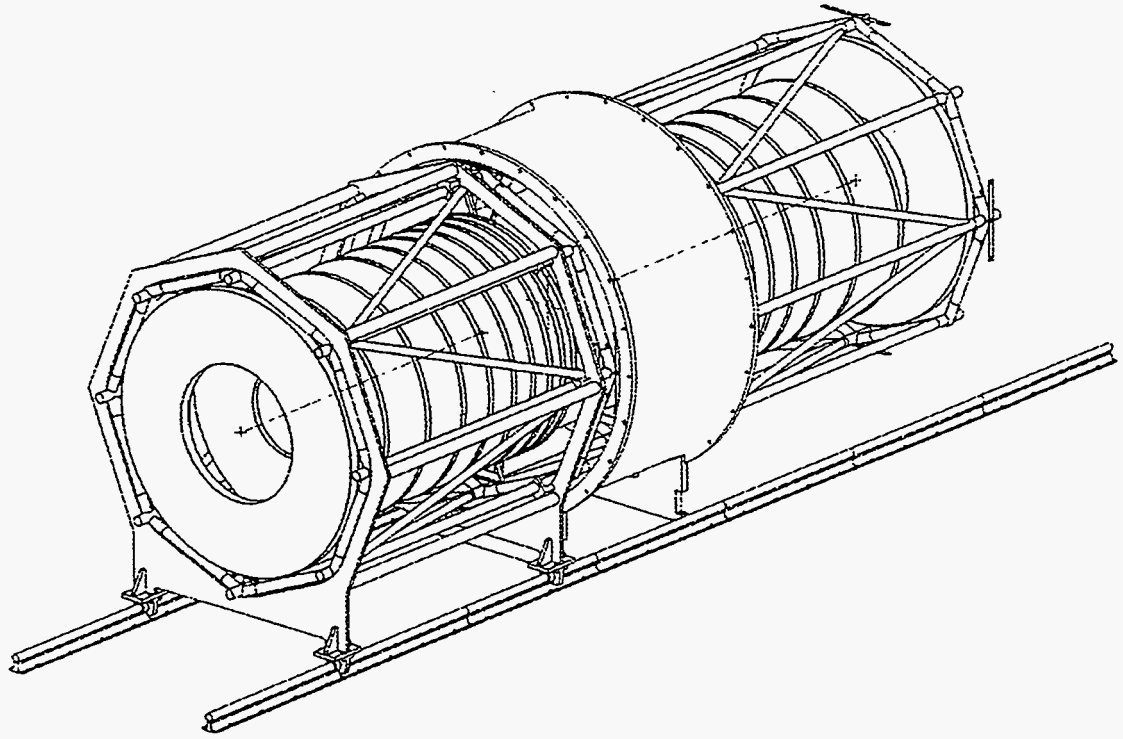

Figure 3.2.2-2 Another stage in the space frame assembly.

The final frame design configuration embodied two composite materials, an aluminum metal matrix composite (AL-MMC) for the long tubes and, polymeric/graphite fiber composite for the joints. Both metal matrix and polymeric resin matrix systems,

with high modulus graphite fibers will satisfy the basic thermal expansion criterion of zero expansion over the 20°C cool-down from room temperature. The metal matrix composite is immune to either moisture, or in our situation butane ingress. Consequently, it was chosen to achieve ultra-stability in the long tubes. Manufacturing processes for these tubes is well established. We chose to fabricate the joints with a comparatively inexpensive resin transfer molding process. Tooling for molding a joint that accepts the four intersecting tubes is not expensive. The joint and the connecting tubes were designed to minimize material over-lap, in an effort to control the material radiation length. Only at the intersection of the transverse frame members was the material thickness allowed to increase above the nominal wall value of 1 mm. Figure **3.2.2-3** is a photograph of the molded joint. A very low moisture sensitive cyanate resin system was used with AMOCO T300 graphite fibers to produce our first joint prototypes.

Since rather high angle weave patterns are used in the joint to achieve a near quasi-isotropic composite, the thermal expansivity of the joint is not zero, rather it is a near uniform 2.8 ppm/°C. Since the joint is very short, the zero expansion property can be relaxed without impacting the design. Our design evaluation made allowance for the lower joint modulus of elasticity typified by the resin transfer molding process. The first development joint had a modulus of elasticity of 48.3 GPa, about half of our stiff flat panel quasi-isotropic composites that were constructed with very high modulus graphite fibers; reference appendix Section A.2.1. Reduction in the joint modulus stems from using low modulus flexible graphite fibers which permit weaving of the tubular joint without fiber fracture. As a point of reference, the joint modulus is about 70% of that of an aluminum alloy; by most standards this modulus is still fairly high.

Figure 3.2.2-3 A photograph of the molded joint.

The AL-MMC frame tube is constructed with highly uni-directional longitudinal properties, thus maximizing modulus, and minimizing thermal expansion in this preferred direction. If one uses 60% by volume P120 graphite fibers in an aluminum matrix the resulting Young's Modulus is 515 GPa and the CTE is -0.25 ppm/°C. A cross-section of a sample tube using P100 fibers is shown in Figure 3.2.2-4. The slightly negative CTE causes the frame to expand when the unit is cooled from room temperature to 0°C.

We have made an initial evaluation of two frame geometries constructed from the tube and joint properties just presented. Frame geometries are distinguished by the arrangement of the transverse frame members, in one case hexagonal, and in the other an octagonal pattern. Longitudinal tube members, denoted longerons, are 3.175 cm in diameter, while each transverse tube diameter is 2.54 cm. The stiffness comparison between the two frames was assessed by determining the fundamental mode of vibration. This calculation was performed for various joint moduli, reference Figure 3.2.2-5. The frequency (frame stiffness) is influenced in part by the compliance associated with the joint and the method of frame support. In the finite element model representation, the frame was supported at three points around the frame perimeter, at two locations. The circumferential supports were placed longitudinally at what is intended to be nominally 'quarter-points' of the overall frame, the first transverse support, inward from each end. These supports are idealized to allow radial motion of the frame while providing vertical and longitudinal restraint. This feature of the model was factored in to simulate a condition whereby radial pressure loads on the outer shell and corresponding deflections are not imposed on the frame. This simulation technique models the kinematic mount concept that also allows for small CTE mismatch between the frame and the outer shell.

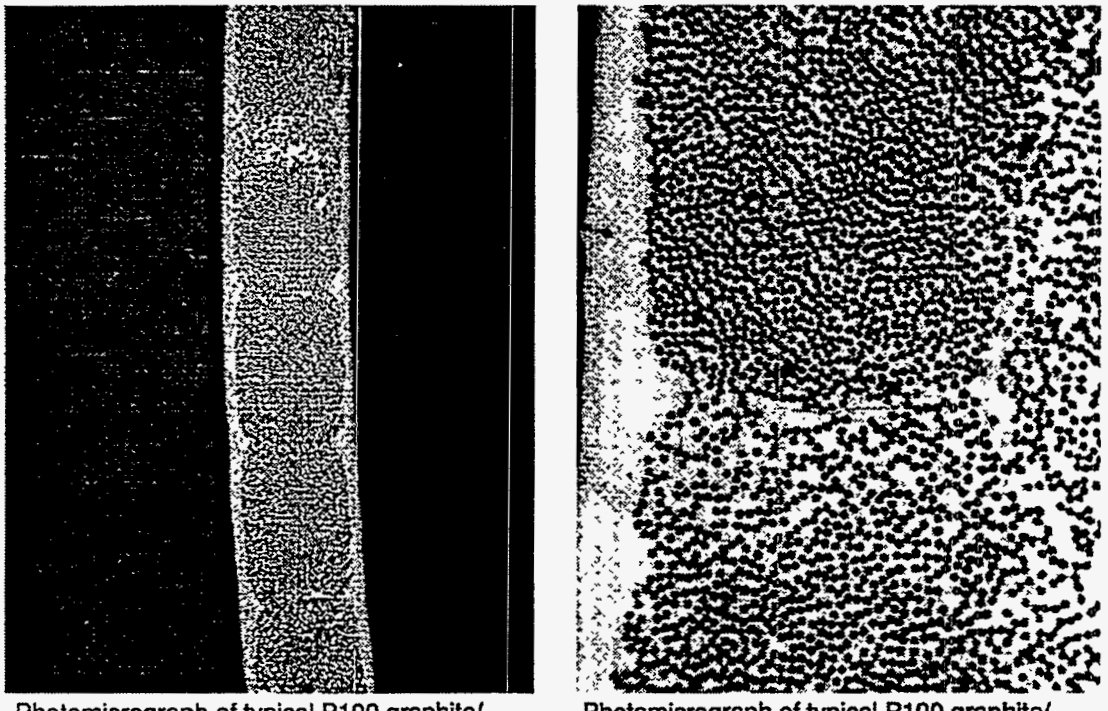

Photomicrograph of typical P100 graphite/ aluminum 1-ply tube with 40% fiber by volume

Photomicrograph of typical P100 graphite/ aluminum 2-ply tube with 45% fiber by volume

(photo courtesy of DWA Composite Specialties,Inc)

Figure 3.2.2-4 A cross-section of a sample metal matrix composite tube using P100 fibers.

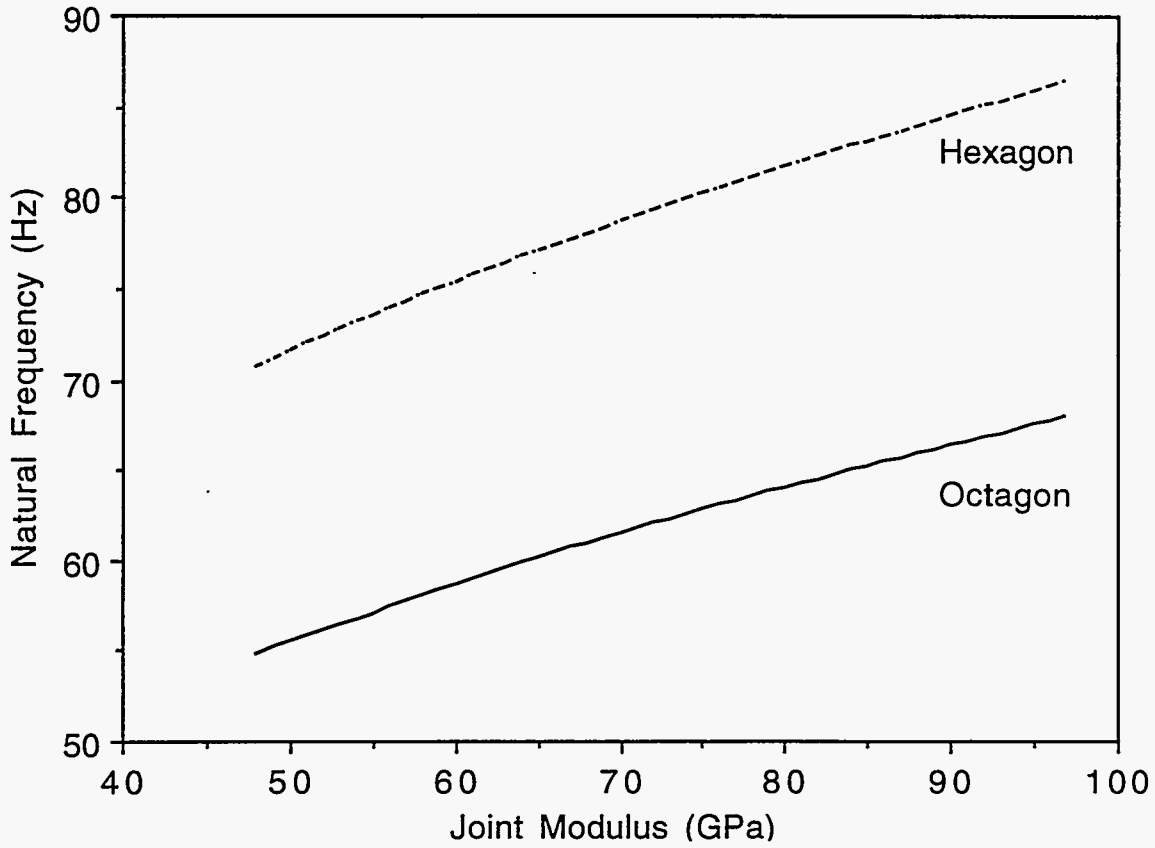

Figure 3.2.2-5 The stiffness comparison between the two frames was assessed by determining the fundamental mode of vibration The calculation was performed for various joint moduli.

Since the hexagonal frame, by the nature of its geometry, uses fewer joints, it has a higher natural frequency. This fact emphasizes the importance of achieving the highest practical joint modulus consistent with other objectives cited earlier. It is worth mentioning that cast aluminum with a discontinuous ceramic fiber matrix joint construction technique is an available option to the joint proposed. However, this method entails significant increases in cost, weight, and much higher CTE's. The primary virtue of this concept would be to produce a joint which completely offsets the longitudinal expansion of the high modulus tubes during cool down. This effect with the polymeric resin joints is shown in Figure 3.2.2-6. Notice that the expansion of the tube is slightly diminished by the positive CTE of the joint. Also, one might realize that a slight reduction in the fiber volume concentration in the tube would produce a less negative tube CTE, and in conjunction with this prototype joint provide a net zero dimensional change in the frame. In other words, there still exists some opportunity for design adjustments through the tailorability of the material properties.

A test was performed on the bonded joint concept to assess whether creep would be a problem, and if it were possible to debond the joint interface without damage. The adhesive used in these tests was DYMAX 991. It is a room temperature, activator cured adhesive with a bond strength of 31 MPa. The joint was debonded successfully with a application of heat, and no visible damage was noted on any surfaces. The creep test was performed using TV Holographic techniques discussed in Section 3.3.1. Figure 3.2.2-7 illustrates that no slip was observed in the joint after 66 hours of constant applied load. It was intended that subsequent tests be performed to establish the load corresponding to creep. Curtailment of the program precluded investigation of this aspect.

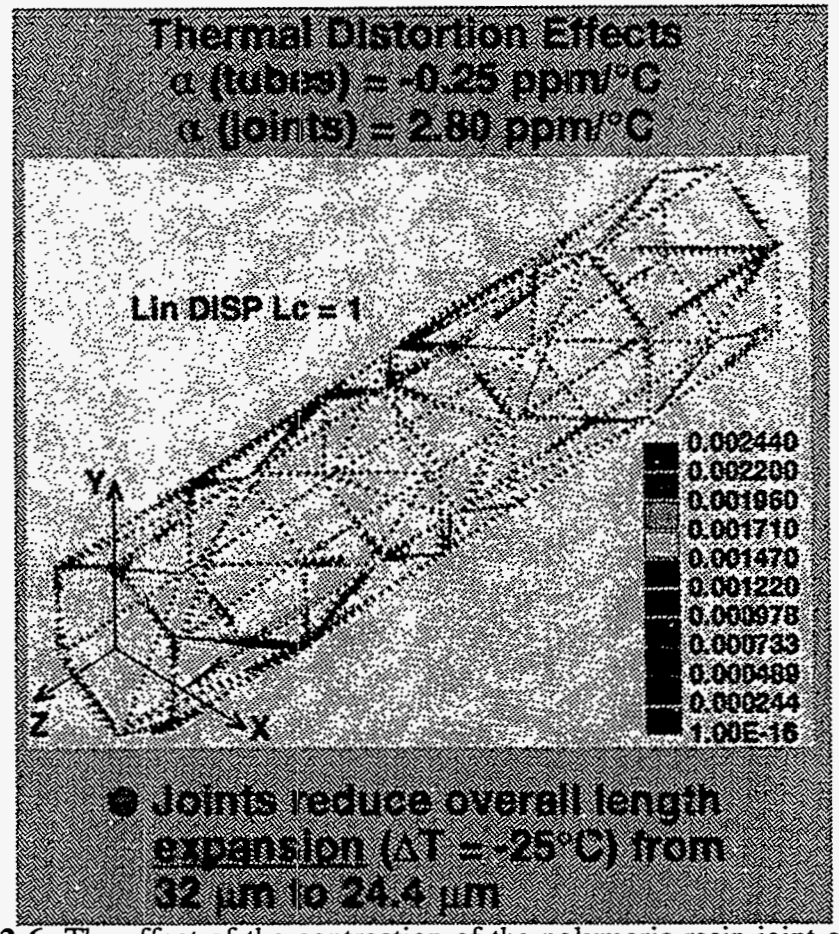

Figure 3.2.2-6 The effect of the contraction of the polymeric resin joint offsetting the longitudinal expansion of the high modulus tubes during cool down.

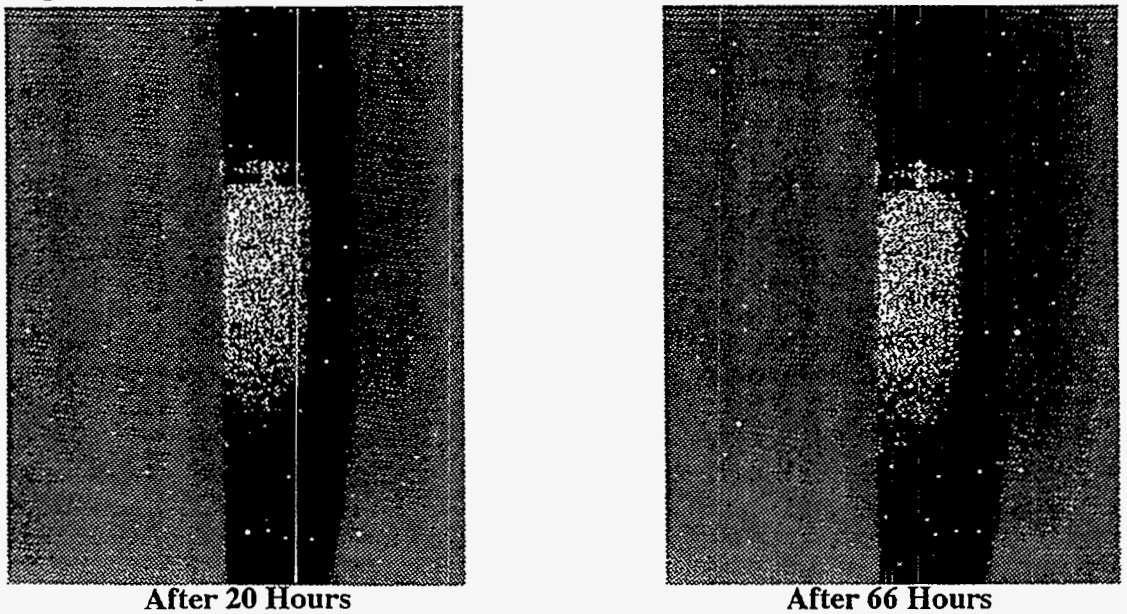

After 20 Hours **After 66 Hours**

Figure 3.2.2-7 A TV Holographic picture illustrating that no slip was observed in the joint after 66 hours of constant applied load.

Additional FEA studies were planned to finalize selection of the tube sizes, and desired joint properties. Assessment of the structural dynamic behavior of the space frame fully loaded with all the masses representing silicon structures, cabling and cooling lines has not been made. These tasks are essential to completing the space frame design.

3.2.3 Central Region

Silicon shell like structures comprise the central region tracking volume, as cited earlier. One of our primary objectives for the past year was to evaluate the design ramifications embodied in our technical approach. Of the technical issues involved, we identified the stability demonstration of the central region to be a major milestone for the LANL portion of the FY 93 tracking effort. Moreover, salient features of the central region design approach which address silicon detector cooling, mounting, alignment, and stability are used to a large extent throughout the forward region. We aspired for success in this effort in order that we might make significant strides forward in our quest for strengthening the overall technical foundation of the entire silicon tracking detector.

Development activities undertaken for the central region focused largely on characterizing the structural behavior of a typical silicon shell structure using FEA techniques, exploring silicon shell construction methods, including associated material developments, and the stable cooling of the simulated detectors using an evaporative process. Other technical areas of concern, that were addressed with equal interest, but at a lower level, were related to kinematic mounting and aligning of a silicon shell assembly. The overall detector design approach was advanced and, as time permitted, integration issues associated with the large array of cables for the multi-chip electronic modules were addressed. The following sections discuss the progress made in these specific areas.

3.2.3.1 Silicon Shell Design Considerations

A significant part of the STS development program concentrated on the development of a cooling ring for the detector central region. Our investigation into the fabrication and material development issues was initiated on a 42 cm outer diameter ring. We constructed an engineering prototype of a 42 cm silicon shell assembly, and conducted stability tests by monitoring shell distortions with TV Holography (Section 3.3.1). The subsequent sections deal with the ring fabrication and material developments, shell and ring thermal/mechanical performance predictions, and kinematic mount developments for supporting the completed silicon shell. A semi-automated work station assembly unit was designed and built for the precision construction of a typical central region silicon shell assembly. The work station was also intended to be used to assemble the flat planar arrays characteristic of the forward regions. Work accomplished to date in these areas is detailed in subsequent sections.

3.2.3.2 Composite Cooling Ring Thermal Analysis

A primary objective of the evaporative cooling system is to hold the silicon strip detector near 0°C during operation. Leakage current in irradiated detectors, markedly increases with temperature[2], as does the amount of anti-annealing, which raises the required operating voltage for the detectors[3]. The benefit of maintaining the detector at this baseline temperature is clearly established. Other requirements one must impose on the cooling ring design, which relate to detector stability and precision, are less clear. Specific requirements for structure isothermality and thermal stability are intuitively stringent, but must be quantified in light of our understanding of material properties and

structural characteristics. Continuing design studies were intended to address these issues.

A three dimensional section view (Figure 3.2.3-1) of a central region silicon shell assembly depicts several of the silicon detector modules mounted onto the Graphite Fiber/(C-E) cooling ring. The arrangement depicted formed the baseline design approach described in the SDC Technical Design Report (TDR).

This view illustrates the close proximity of the polystyrene wick structure to the electronics heat load. One may notice that we have interposed the cooling between this heat source and the body of the 24 cm long detector module. This arrangement was chosen to provide thermal isolation for most of the silicon wafer surface. The detector hybrid, noted in the figure, is constructed as a Multi-Chip-Module (MCM). The individual modules are composed of analog and digital electronic chips bonded onto a 300 μm thick beryllium ground plane with a thin kapton film/adhesive layer interposed between the two elements. Thin film etched aluminum or copper circuits traces run on the kapton film and were to provide the power, control, and communication lines to the electronic chips. Various different means to provide the channel to channel interconnections from the detector to the analog chips to the digital chips were being explored. The beryllium ground plane is in turn bonded to the silicon strip detector only in the region where the assembled module attaches to the cooling ring. A thin void exists between the beryllium ground plane and the silicon strip detector, over most of the ground plane span, which provides some degree of thermal isolation. The void is achieved by locally increasing the beryllium ground plane thickness to 400 μm in the region where the ground plane is bonded to the cooling ring. A cross section through the individual components is shown in Figure 3.2.3-2. Heat dissipated by the electronic chips is conducted through the beryllium ground plane and cooling ring wall to evaporate the liquid butane that is continuously supplied by the wick capillary action. It is this particular arrangement that forms the basis for the thermal/structural performance predictions discussed herein.

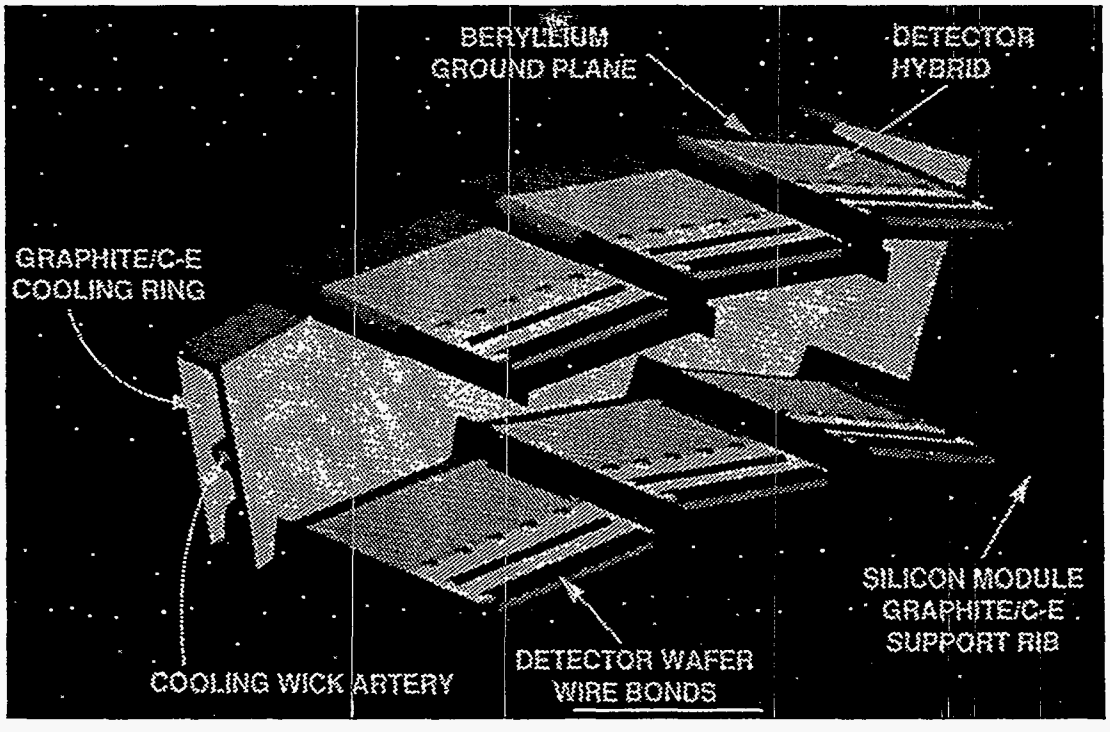

Figure 3.2.3-1 Cooling ring/silicon module cut-away with butane evaporative cooling elements.

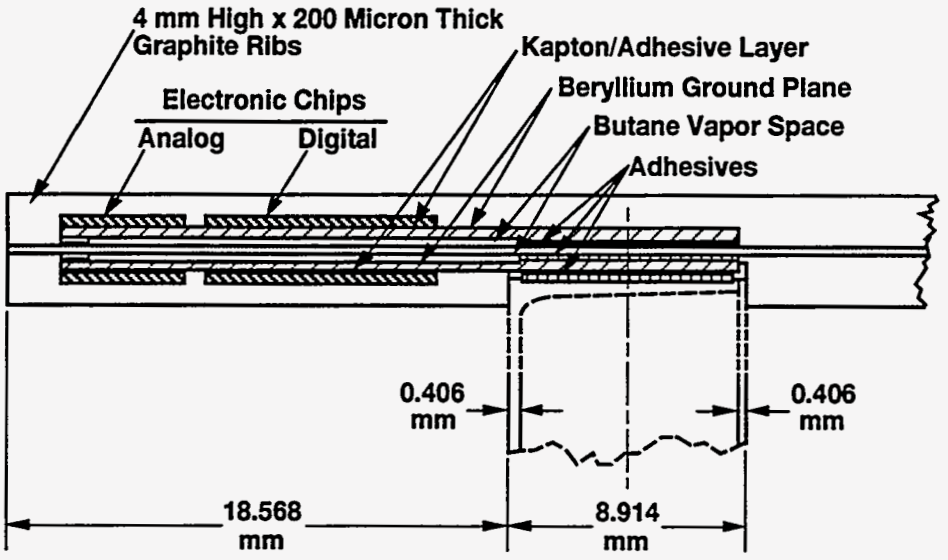

Figure 3.2.3-2 Cooling ring/silicon module cross-section.

As is evident from Figure 3.2.3-2, the overall heat conductive path is composed of numerous thermal resistances. One major thermal resistance is the cooling ring graphite composite wall. In spite of its thin section, the wall can contribute a noticeable thermal resistance. Much of our work to date has centered not only on demonstrating composite ring fabricability, but also on lowering this particular thermal resistance by enhancing the transverse thermal conductivity of the composite cooling ring.

Significant progress has been achieved in molding composite rings. Quality ring segments were produced and bonded into a full ring; Figure 3.2.3-3. Material properties enhancements of the ring are discussed in Appendix A. Thermal/structural predictions discussed here are intended to quantify material requirements in light of the overall detector performance goals, as dictated by the present arrangement.

There are many issues which we must address. Excessive thermal distortion of the composite ring structures, resultant silicon strip detector operational temperature, long term stability as influenced by thermal changes, and tolerance buildup in manufacturing are priority concerns. Thermal distortion effects will be estimated analytically, but until material properties are fully quantified significant uncertainty will remain.

Thermal Studies In our original baseline design, the silicon module was bonded directly to the composite ring, with no beryllium ground plane. The coefficient of thermal expansion (CTE) of the ring was to be matched to that of silicon, within reasonable limits. We had configured such a system, which minimized dissimilar CTE's, to avoid a "bi-metallic" effect. The additional elements, which now comprise a MCM, potentially lead to larger and more complex thermally induced distortions and contribute to an increased tolerance build-up. That in turn hence dictates an even more accurate placement of the silicon strip detector in three dimensional space. Also, the more complex array of thermal resistances introduces a question regarding detector isothermality within a silicon substructure. The importance of structure isothermality must be investigated thoroughly as the design progresses and more material information becomes available.

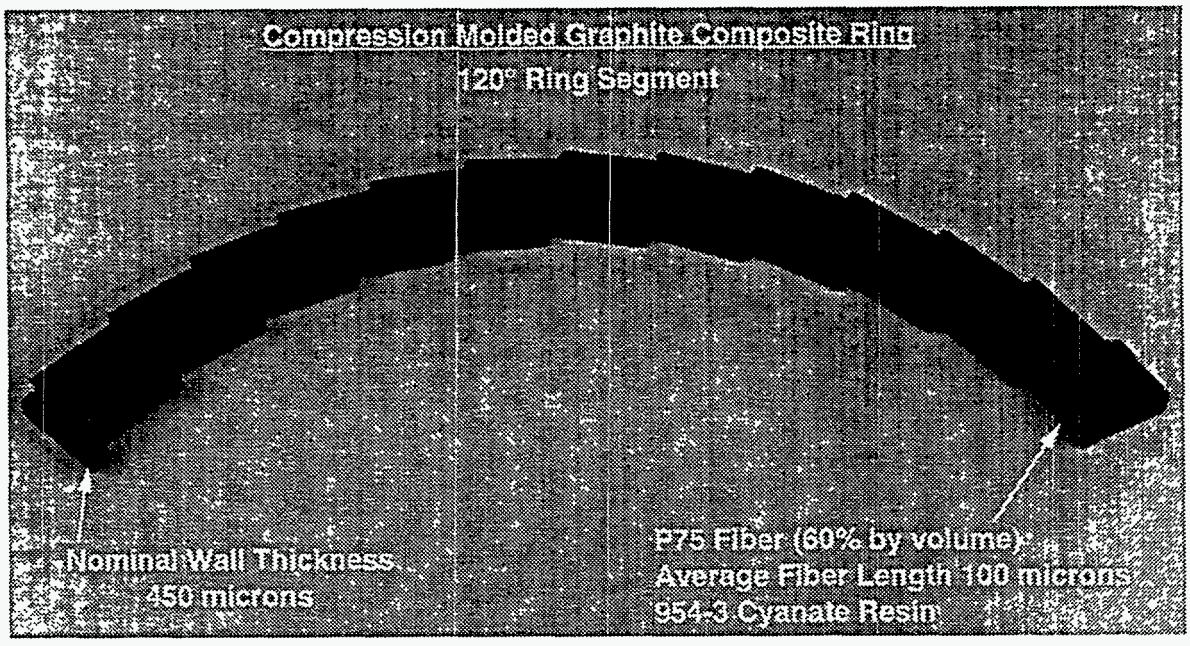

Figure 3.2.3-3 Compression molded cooling ring segment.

Table 3.2.3-1 Material Properties

Material	Elastic Modulus E (GPa)	CTE (ppm/K)	Thermal Conductivity (W/m-°K)	Thickness (μm)
Beryllium	290	11.6	146	400
Silicon	131	2.6	129	300
Kapton/Adhesive Layer @ chips	2.1	50	0.39	50
Cooling Ring (G/C-E)	14.7	3	4-Transverse 15-In plane	500 (avg.)
Adhesive(*)	2.1	50	0.87	100
Adhesive @ Cooling Ring Cover	4.2	55.6	0.33	50

(*) For bonding, Be, Silicon, Graphite Ring Layers

Table 3.2.3-1 lists the material properties used in constructing a thermal/structural model of the silicon detector module and cooling ring. The thermal conductivity chosen for the cooling ring represents our Phase I design goal, a value obtained to date with a 30 degree arc segment (P-75S fiber/C-E, 400 μm wall thickness). Also, the evaporative wick effective film coefficient used in this evaluation is 3000 W/m^2-°K. This value is optimistic for the present stage of wick development, but it is taken as representative of what can be attained through continued development. The values chosen for thermal

resistances and material thicknesses are representative nominal values. Departure from these values will most likely result in an increase in temperature predicted for the silicon strip detector, (*i.e.*, we do not expect material thicknesses to become thinner, rather thicker, and we can expect the thermal conductivities to be lower than specified in vendor literature). The cooling ring and wick properties may not be realized within the present budget constraints. These caveats should be kept in mind during an examination of the predicted results.

Figure 3.2.3-4 depicts the temperature profiles through the silicon detector mid-plane, upper and lower beryllium ground planes, and cooling ring internal and exterior surfaces. This solution includes free convective cooling from the butane vapor on one side of the strip detector surface and from the interior cooling ring wall (opposite the polystyrene wick side). The solution, however, does not take into account any resistive heat load generated by leakage current within the detector itself. That effect is discussed in a later section. A nominal convective film coefficient of 5 W/m^2-°K was used for both surfaces, which would be consistent for very low driving temperature differences. The free convective cooling of the silicon strip detector over its entire surface is responsible for lowering the silicon temperature somewhat. The silicon temperature at the cooling ring interface is approximately 5.6°C, whereas this value diminishes to 3.6°C at mid-span. It may be difficult to realize even this small degree of free convective cooling in the innermost central region layers. A thermal barrier is created by the outer layers which tends to destroy the vapor circulation necessary to transport heat away. A proper assessment of the magnitude of free convective cooling and expected variance throughout the detector volume is a subject of a separate analysis. As explained shortly, free convective cooling may be of some importance with regards to dissipating some leakage current induced internal detector heating.

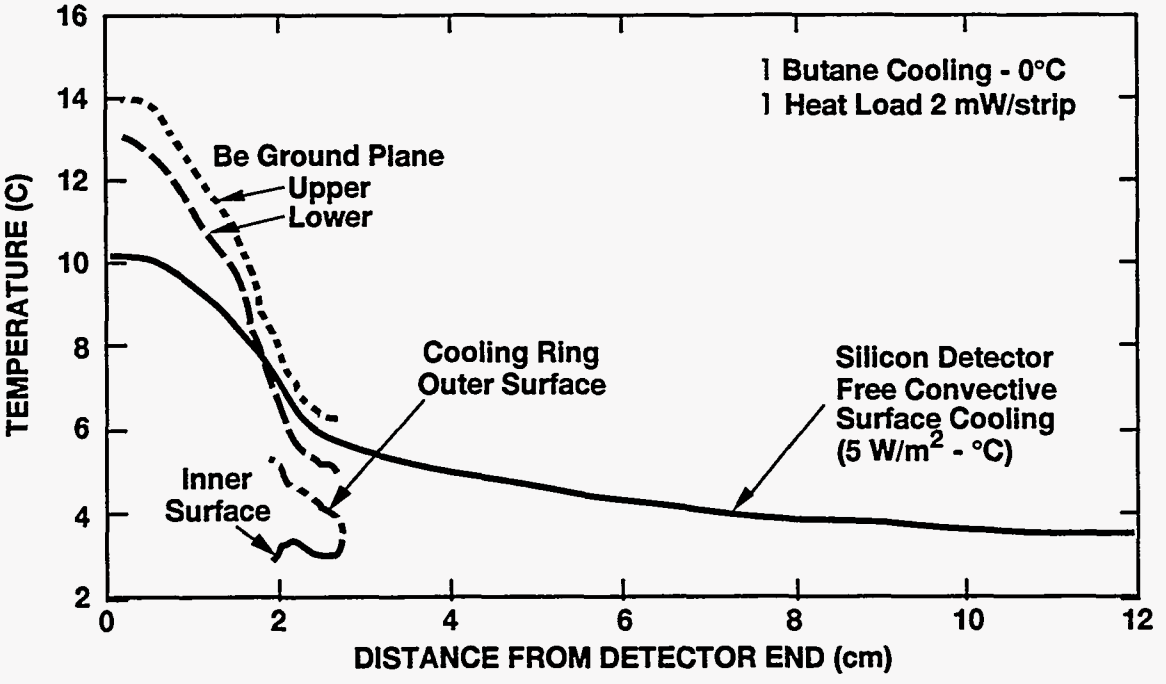

Figure 3.2.3-4 Detector module mid-plane temperature distribution for combined 2 mW/strip electronic chip thermal heat load vs. longitudinal distance from detector end (butane cooling, 0°C).

Notice that the free end of the silicon detector is at a nominal temperature of 10°C, whereas at the cooling ring base it is approximately 7.5°C. Thermal isolation of the silicon detector by the 100 μm thick butane vapor film, between the beryllium ground plane and wafer surface, is realized to some extent, but is far from perfect. Some heat is transferred across the butane vapor barrier film, and is transported down the silicon wafer to the cooling ring. Conduction down the silicon wafer to the cooling ring is the only means for removing this small heat load. The gradient is not large (Ref. Figure 3.2.3-4). and a larger vapor barrier would further reduce this temperature gradient. However, further refinements to the thermal model would include the dense array of wire bonds. Thus, any initial benefit from increasing the vapor film would be partially offset by this additional heat transport term. In any case, the silicon temperature in this area would not diminish over the temperature at the cooling ring base. Additional cooling of the electronic chips from their present temperature of 14.5°C may be derived through inclusion of a free convective coefficient, as was done for the strip detector, but the resulting small reduction in chip temperature would most likely be offset by the existing underestimates of the thermal conductive path resistance. In a sense, the unknowns in the material thermal conductivities overshadow this small additional cooling contribution.

There are a myriad of possible solutions to this thermal problem, where for example, various material thicknesses and thermal conductivities are varied. Because of our limited understanding of key material properties at that time we chose not to conduct an extensive sensitivity analysis. When the cooling properties are more firmly established it was our intent to study this subject in more detail.

Since the thermal model of the ring is a two dimensional approximation to a portion of the silicon shell assembly, one must be rather careful to explore the distortions which result from predicted temperature distributions in the ring, MCMs, and silicon detector. It is possible with this model to initialize the problem with a reference temperature corresponding to the assembly temperature (20°C), and with the predicted operational temperature profile, solve for the deformed structural shape. This solution will give a measure of distortions from CTE mismatch. It is important that material CTE's and elastic moduli be properly represented since the solution is very sensitive to these values. At this juncture the material properties of the cooling ring are not fully established, and consequently some uncertainty exists until these parameters are firmly established. We can, however, bracket the expected values and develop some cogent observations.

The elastic modulus listed in Table 3.2.3-1 for the cooling ring is quite a bit below our expectations for the final composite ring. The value used is representative of our first attempts with rings molded from P-75S /C-E prepreg material, where the prepreg material did not meet our fiber volume fraction specification. The value is only 14% of what has been demonstrated in continuous fiber (P-75S) quasi-isotropic (QI) cyanate-ester laminate. The CTE for the QI laminate is very low and slightly negative. For discontinuous fiber molded ring composites, the CTE will increase with decreasing modulus; thus, we chose 3 ppm/°K for our initial value. The higher ring CTE reduces the CTE mismatch with beryllium, and the lower modulus reduces the thermal strain effect. This solution would tend to underestimate the thermal distortions if we had used the material properties which we had hoped to achieve for other reasons (*e.g.* gravitational effects).

Figure 3.2.3-5 depicts the individual module element mid-plane deflections. The distorted shape accounts for both the cool-down from room temperature, and the module thermal distributions calculated earlier. The figure clearly shows the detector bowing upward as a result of the combined strains induced in the cooling ring from the various CTE mismatches and gradient effects. If the cool down from room temperature was removed, the detector would bow downward, not upward. Also, there is a reduction in cooling ring diameter that must be superimposed on these results, should the absolute deformation be desired. It is also noted that the beryllium ground planes bend from their mismatch in CTE's with the silicon electronic chips. Replacement of the beryllium ground plane with a different material, like aluminum nitride would reduce this effect.

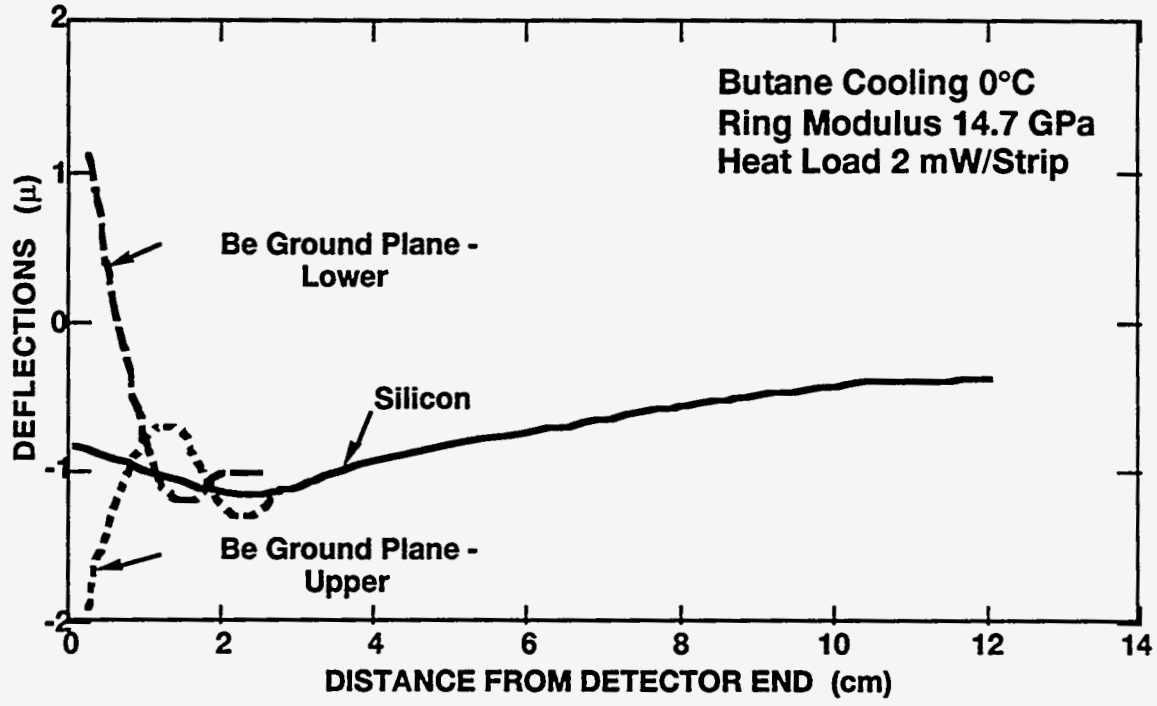

Figure 3.2.3-5 Detector module mid-plane deflections for a combined 2 mW/strip electronic chip heat load vs. longitudinal distance from detector end (butane cooling, 0°C, ring modulus: 14.7 GPa). The results shown in this figure reflect only the local relative contractions in the vicinity of the detector being studied. They do not include the overall contraction of the entire cooling ring.

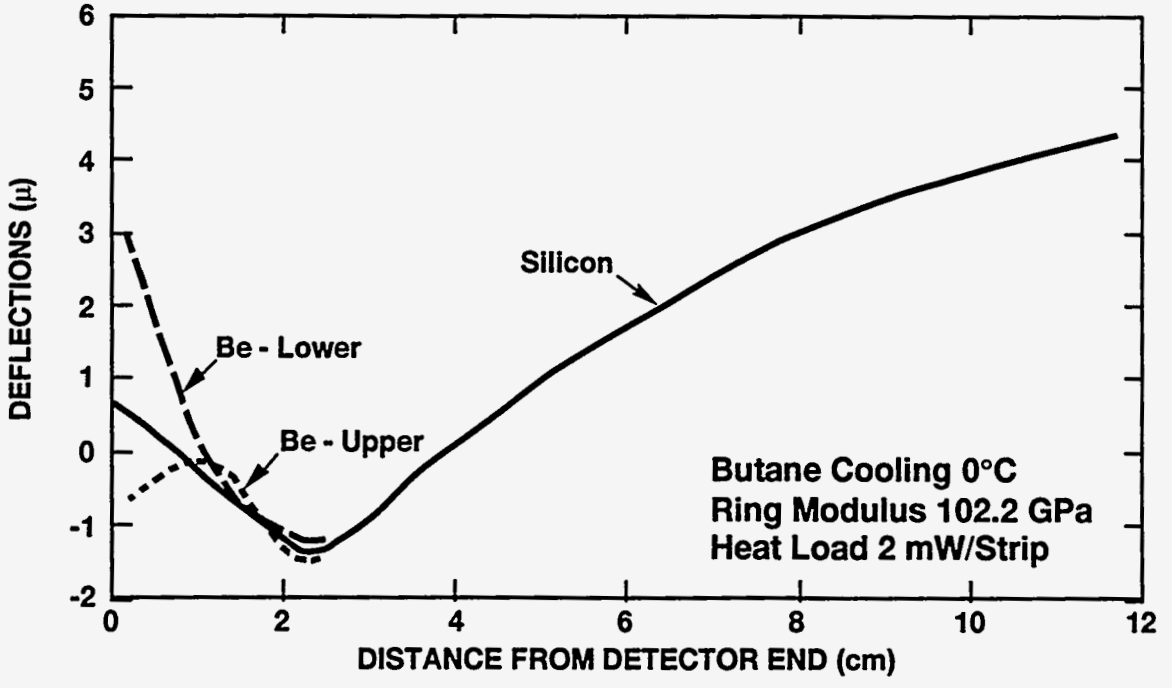

Figure 3.2.3-6 Detector module deflections for 2 mW/strip electronic chip heat load as a function of longitudinal distance from detector end (butane cooling, 0°C, ring modulus: 102.2 GPa).

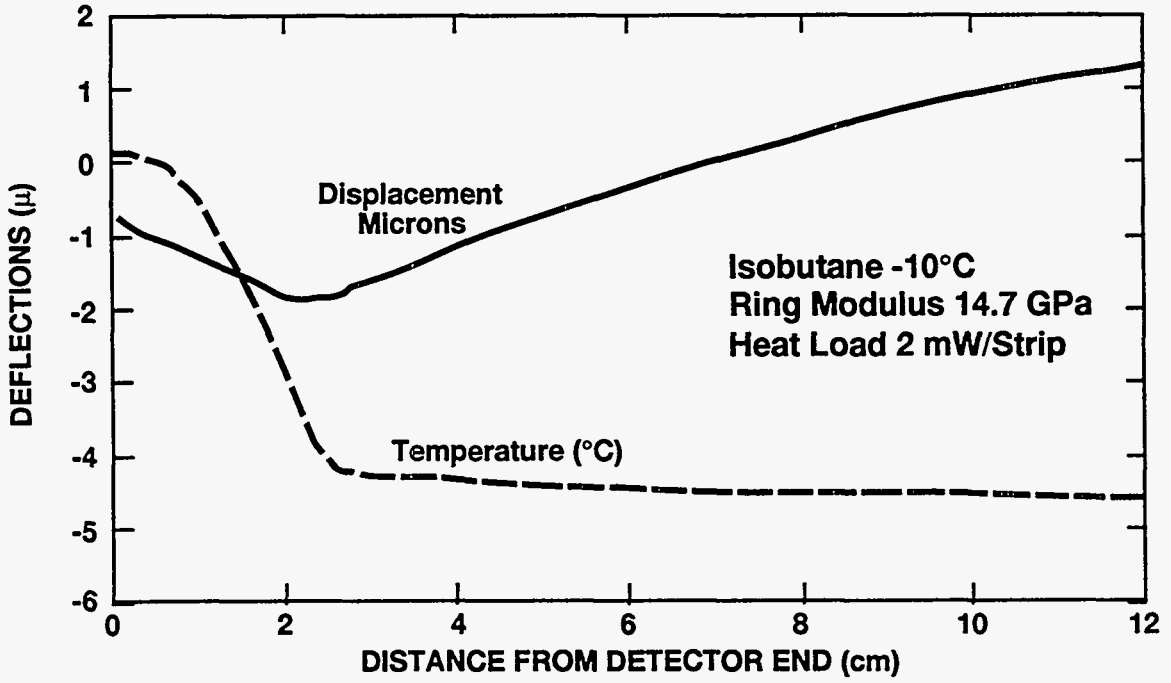

Figure 3.2.3-7 Silicon strip detector temperature and mid-plane deflections for 2 mW/strip electronic chip heat load vs. longitudinal distance from detector end (isobutane cooling, -10°C, ring modulus: 14.7 GPa).

A second solution was made using the modulus for a P-75S/C-E QI laminate. This value is roughly twice what we can hope to achieve. High stiffness is needed to offset gravitational and other extraneous loads not considered in this model. To observe only the results of the higher modulus, the CTE of the cooling ring was not changed from the value used in the preceding calculation. Figure 3.2.3-6 shows a marked increase in wafer distortion, up to 4 μm. Increased distortion in the beryllium/MCM combination is induced from shape changes at the cooling ring. In this case, from purely an engineering consideration, the distortions are still not alarming, although when combined with the various positional errors in the construction we may have a problem. The induced stresses need to be studied with a more refined model, although a cursory review has not uncovered a serious problem.

As a point of future reference, the temperature drop through the wick and cooling ring are nominally 3° and 2°C respectively. If the ring transverse thermal conductivity remained at 1 W/m-°K , representative of the present prototype, instead of the value of 4 W/m-°K which we are trying to achieve and which was used in the calculations, the silicon strip temperature would rise by roughly an additional 6°C. This effect would aggravate the strains somewhat but of greater concern would be increases in leakage current and anti-annealing for the detectors.

An important option to consider is the use of isobutane in place of butane for the coolant. At atmospheric pressure, isobutane evaporates at -10°C versus -0.5°C for butane. Figure 3.2.3-7 depicts the temperature distribution and silicon strip detector deflection which results from the use of isobutane. The solution includes free convective cooling over the strip detector exposed directly to the vapor surroundings. Until a careful study is made of the vapor space temperature, a -5°C reference temperature was assumed. The slightly elevated temperature was used to provide some measure of conservatism for detectors located in the innermost regions of the barrel arrangement. The results show rather graphically that the detector will operate well within the desired 0°C range, without any appreciable increase in distortion. Also, as before, this case is representative of the

current stiffness in the cooling ring. Any significant increase in stiffness would warrant a revised calculation. It is important to note that if no further improvements were realized in the cooling ring transverse thermal conductivity, we would still have an adequate margin in detector operational temperature if isobutane were used. This margin is most important to leakage current induced thermal heating, which will be discussed next.

Leakage Current Induced Heating The silicon detector modules are subject to radiation damage from the large particle fluences expected in the innermost regions of the SDC detector. Radiation damage will result in a substantial increase in silicon strip detector leakage current. This leakage current imposes an additional thermal load which must be factored into the prediction of detector operational temperature. Because of the strong dependence of leakage current on temperature[2], a concern exists that thermal equilibrium will not be attained, (*i.e.*, an increase in leakage current causes an increased temperature that cannot be controlled with the heat sink afforded by the cooling system).

Our recent thermal studies of the preliminary design of the silicon detector module/cooling ring structure interaction have included a first order determination of the temperature dependent leakage current effect. Our first objective was to investigate whether a thermal runaway condition could exist. A FEM thermal solution was made for two idealized boundary conditions. First, no cooling of the detector module was accounted for except for that provided by the evaporation of fluid within the cooling ring structure. No free convective cooling directly from the silicon surface was included here, which would have ameliorated the increase in temperature. In the second solution, a convective film coefficient of 5 W/m^2-°K was added over the surface of the silicon exposed to the butane vapor. Only the area of the silicon detector surface between the two cooling rings was modeled. The model predicts the temperature rise in the strip detector, with the maximum occurring at the midpoint of the detector module.

For the purpose of our calculations, the leakage current temperature dependence has been converted into an equivalent temperature dependent heat flux Q, which is imposed on the detector silicon surface. For a detector with a bias voltage of 150 VDC operating at 0°C the heat flux is 0.0036 W/cm^2 (~1.4 μA/strip). This value corresponds to an inner detector exposed to approximately 10 SSC operational years. The following expression provides the temperature dependence:

$$Q(T_2) = Q(T_1)\left\{\frac{T_2}{T_1}\right\}^2 \exp\left\{\frac{-E}{2k}\left(\frac{T_1-T_2}{T_1T_2}\right)\right\}$$

Experiments in a proton beam at the Clinton P. Anderson Meson Physics Facility (LAMPF) at Los Alamos National Laboratory, as reported in reference 2, provided:

$E = 1.2$ eV (k = Boltzmann constant = $8.617 \cdot 10^{-5}$ eV/°K)

Figure 3.2.3-8 depicts the strong dependence of leakage current induced heat flux used in establishing the final detector temperature. The heat flux corresponds to 0.0036 W/cm^2 at 0°C, and increases significantly with temperature thereafter. The strong temperature dependence exhibited in this figure also emphasizes the importance of maintaining the detector operational temperature below the 0°C threshold.

The analysis method used a series of steady state solutions to arrive at a final estimate of the temperature profile in the silicon. Between successive solutions, the heat flux along the detector surface was updated, based on the previous temperate estimate. With no convective cooling on the detector surface, a stable temperature was not attained. If the only mechanism for rejecting heat from the silicon is by conduction, through the 300 μm thick wafers, to the cooling ring, then it is very unlikely a stable temperature will be achieved. This model ignored the small contribution of heat transfer by the graphite support ribs. Also, the thermal resistance of the silicon wafer adhesive butt joints were not included; these effects together tend to be offsetting.

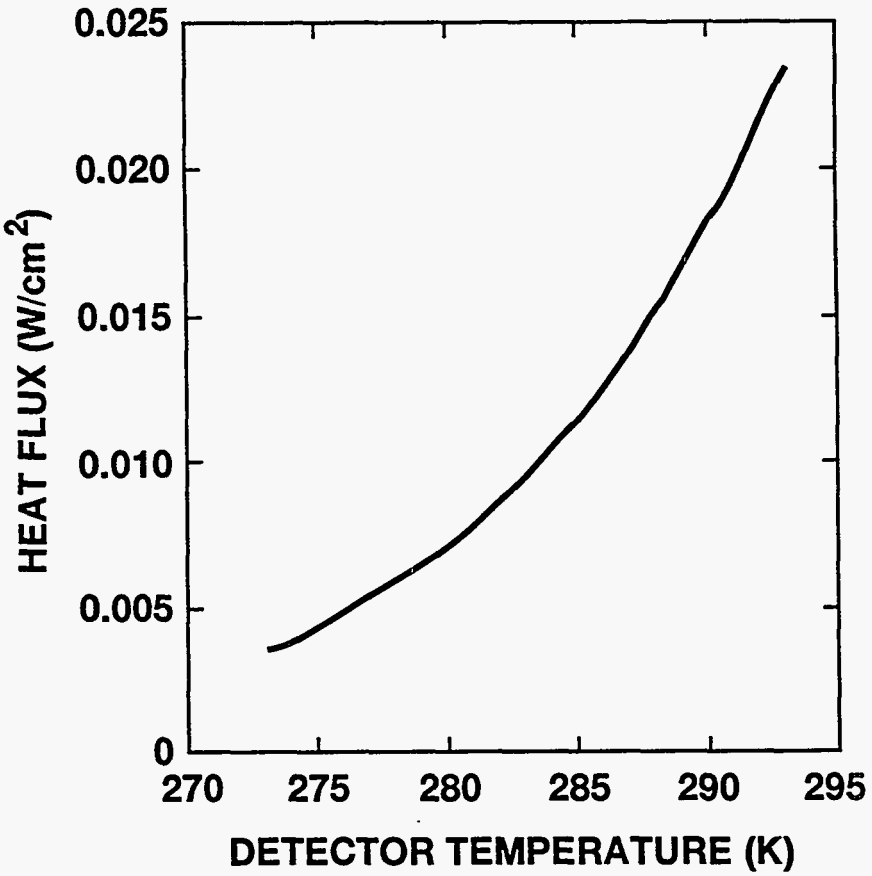

Figure 3.2.3-8 Silicon detector leakage current induced heat flux vs. detector temperature.

Convective cooling of the detector surface stabilized the solution. A maximum temperature rise in the detector of 9.6°C for a base temperature of 5.6°C (at cooling ring) was obtained. Figure 3.2.3-9 illustrates this distribution. For this to be representative of the detector temperature, one must be assured that nothing impedes the creation of free convective currents to transport the heat away from the detector surface. In the central region a certain amount of compartmentalization exists that may impede this transfer mechanism, particularly at the innermost layers. In the forward region flat planar array geometry this problem would not exist. If the cooling ring base temperature were lowered below the 5.6°C value (*e.g.*, slightly negative), the leakage current induced heating would become a non-issue, as would the need for additional free convective film cooling on the strip detector surface. We chose this design consideration as the most conservative direction to take in finalizing our cooling study. It is further recommended that isobutane be used in place of butane to insure a detector operational temperature of 0°C, with some adequate margin.

Summary Our preliminary thermal/mechanical studies of the cooling ring/MCM combination were quite useful and provided insight into key design considerations. First, we concluded that to maintain the detector operating temperature near 0°C we needed to place the wick structure for the evaporative system between the heat source (MCM's) and the bulk of the silicon strip detector. Even in this arrangement, cooling with an evaporative cooling media with a saturation temperature of -0.5°C (1 atm) would not preclude thermal run-away in radiation damaged detectors. A significant temperature

gradient was required to transport the heat from the electronic chips to the wick structure inside the cooling ring under our best performance predictions. To solve this aspect of the problem we would recommend using isobutane with a saturation temperature of -10°C. Thermal runaway would no longer be a problem with this implementation.

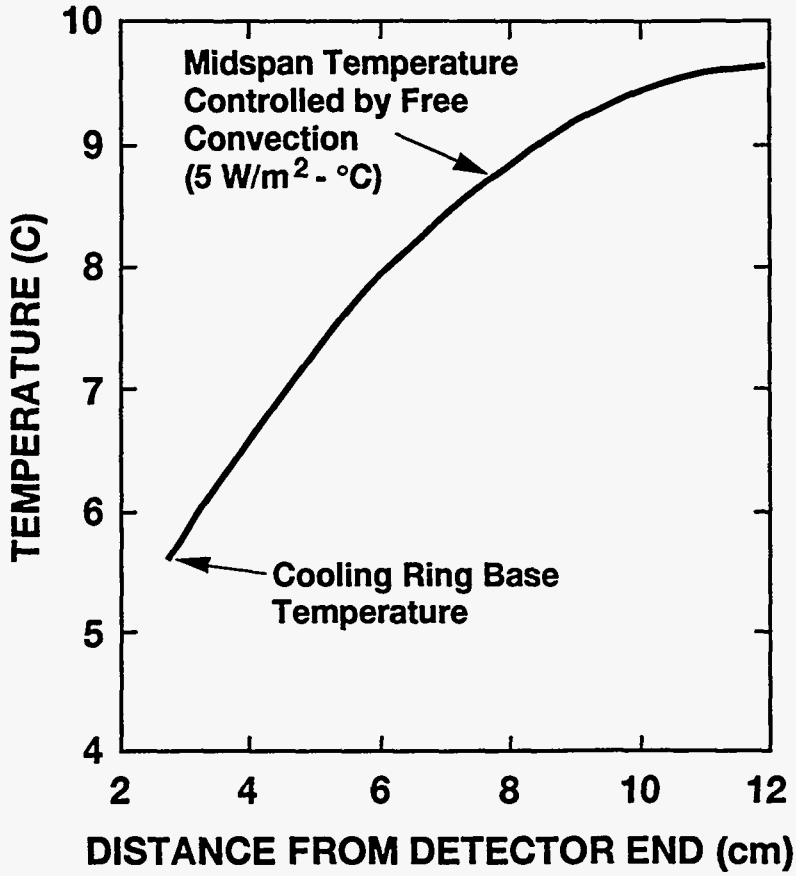

Figure 3.2.3-9 Silicon detector temperature vs. distance from detector end (cooling ring face @ 2.7 cm).

Recent changes in the design of the evaporative cooling approach lead to placement of the evaporative wick (or water channel) right on the MCM surface. This change, coupled with the improved wick performance, significantly reduced the silicon strip detector temperature. The composite ring thermal resistance was eliminated, removing an estimated 3°C from the overall temperature gradient. However, we can not say at this time that the need for depressing cooling system temperature further (*e.g.*, isobutane) has been eliminated.

Our studies showed that different CTE values among the detector module components, however slight, can produced some bowing of the strip detector. This effect came largely from the thermal gradient through the beryllium/silicon/beryllium dissimilar material sandwich effect, combined with the composite ring material properties. The more recent cooling system design change we believe will serve to reduce this effect, although analysis would be required to explore this change.

Thermal run-away in the innermost silicon strip detectors is quite possible from leakage current induced heating. Our results showed that the strip detector must be maintained at zero degrees to avoid this possibility. Free convective cooling does not appear to be a reasonable means of controlling this effect. Conduction down the 300 μm

thick wafer offers too much thermal resistance, so this heat path does not offer much promise. Forced gas (low velocities) circulation to enhance convective cooling certainly offers promise to alleviate this problem, but this option opens the prospect to detector induced vibration. More analysis is justified in this area.

3.2.3.3 Silicon Shell Structural Analysis

A model of a central region shell was constructed to calculate the behavior of the individual silicon modules to thermal loads, and gravity sag with different support conditions. With this preliminary model of the shell stiffness and mass distribution it was possible to extract the fundamental vibration mode. The model does not include the detector hybrid area. The objective of this analysis was to investigate module deflections between the cooling (support) rings.

Model Description The finite element model represents the second shell in the central region assembly. This shell has an inner diameter of 360 mm, an outer diameter of 420 mm, and a length of 240 mm. Each composite cooling ring is modeled as a hollow shell with a cross section 8 mm wide by 30 mm high, and a wall thickness of 0.40 mm. P75/C-E quasi-isotropic material properties (reference Section A.2.1) were used in the model for the ring. This material is quite stiff and its coefficient of thermal expansion is quite close to that of silicon, as discussed in the preceding section.

The silicon module, composed of 300 μm, thick wafers with edge bonded graphite ribs, were simplified in the shell model. Mass per unit length and section moment of inertia properties for the actual silicon module, are used to calculate the equivalent quad element material density and thickness. This greatly reduces the number of nodes and quadrilateral elements, and number of equations in the problem solution, and still produces very reliable results.

Boundary conditions applied to the model simulate the degrees of restraint provided by the 2-2-2 kinematic mount described in Section 3.2.4 of this report. In practice, three of these mounts are located at points equally spaced around both ends of the silicon shell structure. At one end, each mount prevents movement in the azimuthal and axial directions, but allows radial movement. Mounts at the opposite end prevent only the azimuthal movement of the shell. Therefore, the silicon structure can expand and contract both axially and radially as needed. Cantilever mounting of the silicon shell is simulated by simply removing the latter restraints. Results of the calculations are given in the following sections.

Gravity Effects Maximum displacements due to self weight of the shell were calculated for two kinematic constraint conditions. In the first case, the shell is assumed to be supported at both ends with the boundary conditions simulating the restraints described above. Under these conditions the maximum sag due to gravity occurs at mid-span of the top-most and lower-most sets of modules, as expected. The magnitude of these displacements is about 12.2 μm. If this displacement is superposed on the worst case radial displacement due to thermal distortion discussed below (Case 3, Table 3.2.3-2), the total maximum radial displacement of some of the lower-most modules could exceed 20 μm. It should be noted that in this model the unsupported length of silicon is 224 mm. In a recent design revision the unsupported length was reduced to only 170 mm by moving the cooling rings closer together. Since the lateral stiffness of the silicon is a function of the cube of its length the maximum sag due to gravity may be only 5-6 μm. The shorter unsupported length will also reduce the radial displacement due to thermal loading. Thus, some improvement in overall stiffness of the structure can be expected if the latest design revision is implemented in the FEM. This aspect had not been implemented due to program curtailment.

Gravity sag distortion of a shell supported in a cantilever manner was also considered. In this case boundary conditions simulating a modified 2-2-2 mount capable of reacting certain moments were applied. As in the first case, the maximum displacements occur at mid-span of the upper and lower sets of modules, but with an additional out-of-plane bowing of both cooling rings. Modules at 90° to the upper and lower modules, with optimal orientation of their moments of inertia to resist gravity sag (*i.e.*, stiff side up) are responsible for supporting the cantilevered shell. The upper and lower modules sag at mid-span from gravity since their orientation places the low moment of inertia normal to the gravity vector. While the bowing for this diameter shell is only a few microns, it is expected that it would be much more pronounced for the larger diameter shells because of the increased span between support points. This, in turn, would contribute to increased mid-span sag from the increased ring compliance. The sag for this diameter shell is still only 14.5 μm. Even so, cantilever mounting is probably not a viable alternative because the geometry is extremely sensitive to external forces applied to the free end of the shell. Such forces could be caused by the large number of electrical jumpers connecting the shell to a distribution bus.

Table 3.2.3-2 Central region Thermal Distortion

Case	Description	Max. Radial Displ. (μm)	Max. Axial Displ. (μm)
1A	Outer silicon layer at uniform temperature of 2°C	1.56	1.23
1B	Outer silicon layer at uniform temperature of 4°C	3.20	2.45
1C	Outer silicon layer at uniform temperature of 6°C	4.80	3.68
1D	Outer silicon layer at uniform temperature of 8°C	6.40	4.91
2	Outer silicon layer symmetric temperature distribution over 120° sector; temp. distribution: 1-2-3-4-5-6-6-5-4-3-2-1 °C	5.41	1.99
3	Same distribution as Case 2 over both inner and outer silicon layers	10.00	1.92
4	Outer silicon layer symmetric temperature distribution over center three modules of 120° sector; temp. distribution 4-8-4 °C	4.90	2.21
5	Same distribution as Case 4 over both inner and outer silicon modules	9.03	2.19
6	Outer silicon module symmetric temperature distribution over length; temperature distribution 2-4-6-8-6-4-2 °C	2.49	0.94

Thermal Effects To evaluate the effects of symmetric and asymmetric temperature distributions on the shape of the silicon shell a number of cases were considered. Results of these cases are summarized in Table 3.2.3-2. Cases 1A through 1D show that, as the temperature of the entire outer layer of silicon is varied from 2 to 8°C above the temperature of the rest of the structure, which is held at 0°C, the resulting radial and axial expansions are fairly modest, even in the worst case. It should be noted also that these displacements are linear functions of temperature. Figure 3.2.3-10 shows the distorted shape of the shell when this kind of temperature distribution exists.

In Case 2, a uniformly increasing temperature distribution is applied to one 120° arc segment of the outer layer of modules between kinematic mounting points. The temperature difference ranges from 1°C, for the modules at each end of the arc segment, to 7°C for the two modules at the center of the segment. In this case it is noted that the maximum radial displacements do not differ significantly from those in Case 1C and 1D. However, when the same temperature distribution is applied to the inner layer of modules as well (Case 3), the maximum radial displacement nearly doubles, while the maximum axial displacement is about the same. Similar results are produced when only the three

center modules in the same arc segment have temperatures of 4, 8, 4°C applied as in Cases 4 and 5. In Case 6, a uniformly increasing temperature distribution is applied over the length of the center module in the outer layer of the same arc segment. Temperature differences range from 2°C at each end of the module to 8°C at the module center. Displacements in this case are still relatively small.

While the results of the nine cases are not conclusive, extrapolation suggests that temperature differentials ranging to 15°C, due to poor heat transfer from modules in a *single layer*, may not cause displacements that exceed the design tolerances. Reduced heat transfer of such a magnitude may be caused by local separation of the wick from the cooling ring, partial separation of, or discontinuities in a silicon module bond joint, non-uniform convection at the module surface, or any combination of these. On the other hand, any of these conditions that cause poor heat removal from *both layers* of silicon in the same region may result in unacceptable radial displacements.

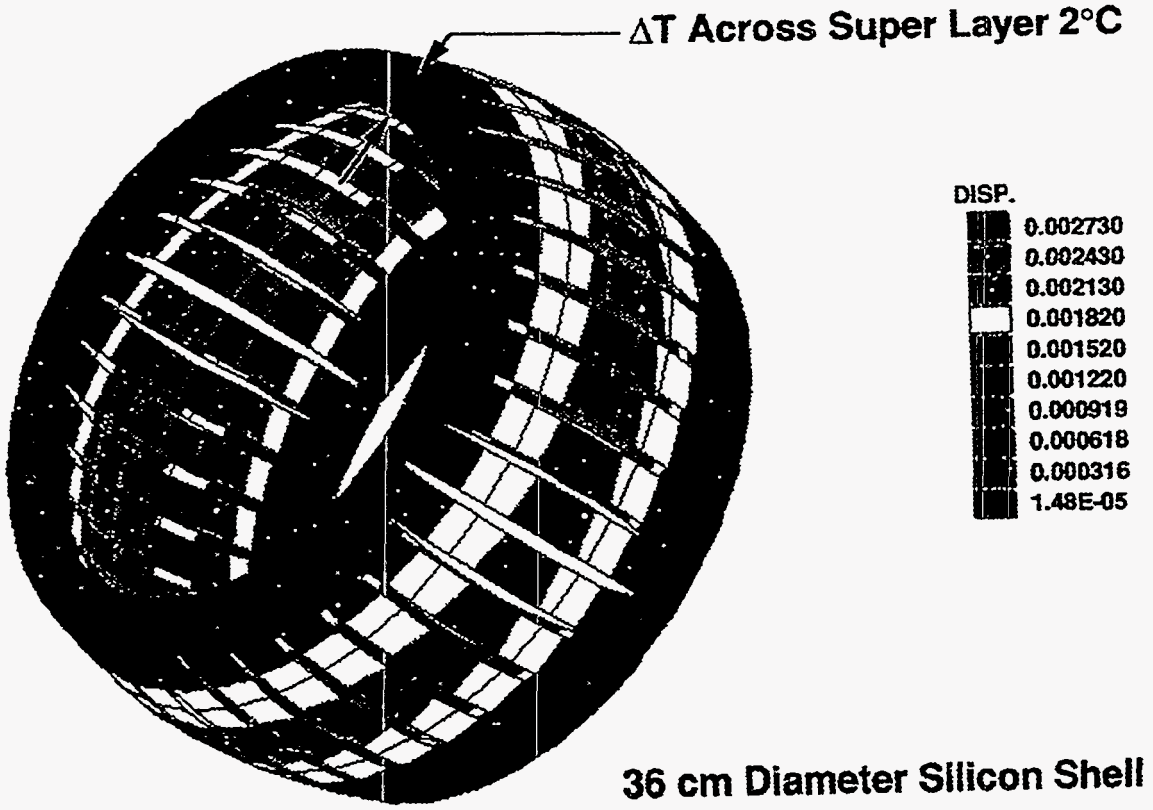

Figure 3.2.3-10 Predicted shape for a silicon shell when the outer layer of silicon is heated by 2°C over that of the remainder of the shell. The support points are indicated.

Natural Frequency The fundamental frequency was calculated for a silicon structure supported by mounts on both ends as described in model description subsection above. Under these conditions the first frequency is about 165 Hz. It is important to have a high natural frequency (>60 Hz) in order to avoid resonance with devices driven at the 60 Hz AC line frequency and because more energy is required to induce vibrations in systems that have a high natural frequency. The relatively high frequency found for the support shell can probably be attributed to the high stiffness of the mounting. The next generation shell model was to have included boundary conditions that simulate the tangent bar mount described in Section 3.2.4 of this report. It is possible that, because such a mount may have greater compliance than the 2-2-2 mount, the shell structure could experience a rigid body motion with a somewhat lower natural frequency.

Summary The foregoing analysis quantified the *bowing* of individual detector modules for an assumed temperature gradient in the radial direction. For the high ring modulus of elasticity used in this prediction the result was 0.78 μm per °C. This predicted value is directly proportional to material modulus. Lower moduli rings will increase our sensitivity to temperature, although under this extreme situation the sensitivity is tolerable. For example, a ring constructed with a material whose modulus is only 14% of the quasi-isotropic value, see Section 3.2.3.4, the coefficient would be 5.6 μm per °C. Initially, Reference 1, we had set a design goal of ±0.1°C temperature stability for the evaporative system, and the foregoing analysis suggests we may be able to relax this stringent tolerance. Even though most of the 80 μm radial positional accuracy specified for the SDC tracker is used in construction and alignment, thermal bowing of the detectors should not be a problem based on these initial calculations. A comprehensive FEA of the shell structure, which includes the hybrid module extension, must be conducted to completely define these distortions.

Realizing this shell is only one component in a complex array of detector elements, we are still encouraged by these preliminary observations. To achieve a relative insensitivity to temperature change in the shell, one must realize the high composite material modulus. We still feel that this a worthwhile objective for our ring design.

3.2.3.4 Molded Composite Cooling Ring Construction

The cooling ring development for the SSC application was a very difficult and challenging task. Our objective, albeit ambitious, was to produce a highly stable, dimensionally accurate compression molded ring, with tailored material properties, and with a wall thickness on the order of 400 to 450 μm. Largely, it was the extremely thin wall that made this project task so difficult. The final ring geometry was composed of two individually molded elements that were bonded together after installation of the polystyrene molded wick. This section deals with the development of molding techniques for producing ultra-stable thin composite ring structures and the advanced inspection techniques used in their inspection.

Graphite Fiber Material Preparation A critical manufacturing operation for producing thin compression molded parts is the sizing of fiber. In typical commercial operations, large quantities (500 kg) of continuous fiber are shortened to approximately 100 μm length fibers. The commercial ball milled fibers are typically the low modulus variety and not the high modulus variety that we required. Also, since much smaller quantities of material and non-standard length fibers are required for the SSC program, ball milling operations were established at Sandia National Laboratories and Programmed Composites. Programmed Composites worked on milling lengths of 400 μm and Sandia worked on both producing 100 μm lengths in still small, but somewhat larger quantities than at Programmed Composites. The objective was to establish a fiber length that was the best compromise between what was required for ease of manufacture (short fiber) and for optimal thermo-physical properties (long fiber).

The ball milling at Programmed Composites used a small one quart capacity mill. A well defined process was worked out, with the resulting fiber length distribution for a 15-minute milling time shown in Figure 3.2.3-11.

A matrix of ball milling parameters was evaluated at Sandia to try and establish consistent sizing of the fiber. The ball mill used at Sandia consisted of a two gallon container and ZrO_2 balls and a suspension fluid. After many trials of different weight loading of fiber and media, we consistently got our best results with 230 g of fiber, milling with 30 kg of ZrO_2 and the container filled to 90% of capacity with Freon.

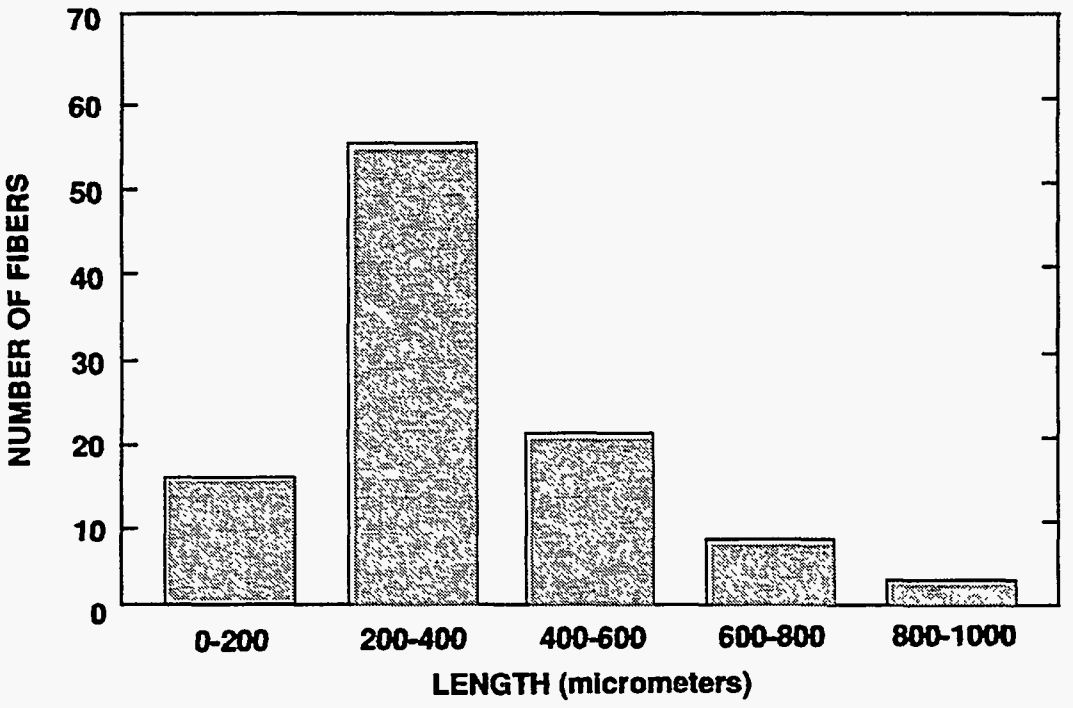

Figure 3.2.3-11 Fiber length distribution for Programmed Composites ball milling operation.

The dispersion of fiber within the media is usually critical to achieving repeatable results. Our best results were obtained by distributing the fiber between layers of ZrO_2, with each layer being nominally 1/7 of the total. Photos of typical ball milling results from SNL are shown in Figure 3.2.3-12. It is interesting to note that although the mean fiber length is function of milling time, the spread in fiber length is always quite large using this process.

Due to the very wide dispersion of fiber lengths that we consistently got, the ball milling operation was not deemed as adequate for achieving the uniform fiber length we sought. It is currently believed that to produce high quality uniform fibers, a new chopping process will need to be developed.

Matched Metal Mold The manufacturing of the composite rings has taken several evolutionary steps. The first step was to start with commercially available materials and then evolve into the materials that we had baselined for the STS. The original 30-degree ring arc segment was molded using MX4925 molding compound material, which uses intermediate-modulus, ~1 mm long fibers, along with a phenolic resin system. Because of the extremely thin wall section, the charge had to be distributed carefully within the mold to enable the compound to move small distances prior to curing. A procedure was developed that produced high-quality 30° arc segments.

The MX4925 material did not suit our long-term objectives for several reasons. For example, we required an extremely thin wall, which required going to shorter, high modulus fibers which were not commercially available. Furthermore, the resin system was not hydrophobic and, therefore, was not considered to be stable.

In the second phase of the manufacturing development, the 30° arc segment was extended to 120° and we used the materials we had baselined for the other structural components. The geometry was also modified to reflect the latest physics design requirements, and the wall thickness was reduced to 400 μm. The compression mold was

equipped with several new features to improve moldability. These features included the use of air ejection to release the part from the mandrel, and grips, which could easily be attached to automate the opening and closing of the mold while in the press.

Figure 3.2.3-12 Typical graphite fiber appearance after ball milling for one hour.

The mold was manufactured from A2 tool steel, which is typical for this type of mold. The quality was quite good, and the tight tolerances were held. Figures 3.2.3-13 and 3.3.2.3-14 show the tooling which was used. The only deviation from the specification was in the wall thickness. The mold had a slight offset that could not be taken out easily. It was therefore decided to use the mold as received from the manufacturer. The wall thickness was nominally 380 μm for the inner radius wall of the ring, and 420 μm for the outer radius wall of the ring.

The second molding compound used a Fiberite product, ICI CF90 for the fibers. This higher modulus fiber came in 90-μm mean fiber lengths. The resin system was TEM9000, a toughened epoxy system from Fiberite, made for production of high-quality graphite components. The resin was loaded with filler material in an attempt to enhance its thermal conductivity. Three different resin batches were evaluated: 40%, 50%, and 60% matrix filler by volume.

The resin's viscosity was high and we found that the cooling ring could not be satisfactorily molded if the resin content fell below 50%. This was in direct conflict with the extreme importance of maintaining a resin content around 40% needed to achieve the required thermo-physical properties.

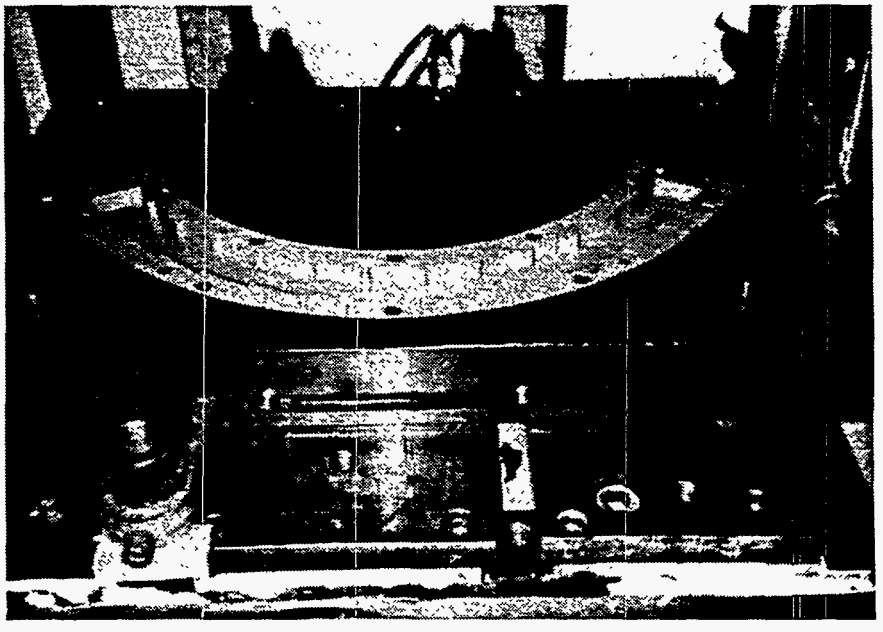

Figure 3.2.3-13 Female Portion of the Matched Mold Tooling.

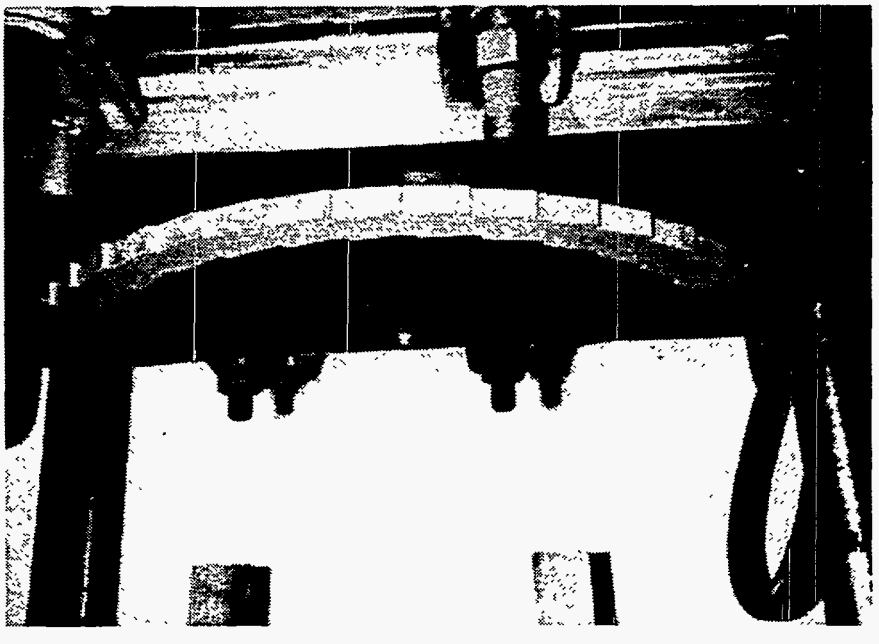

Figure 3.2.3-14 Male Portion of the Matched Mold Tooling.

The next iteration of material was to incorporate the high- modulus P-75S fiber with pure TEM9000 resin. This combination produced good quality components as long as the resin volume content remained above 50%. A substantial amount of work was put into developing the moldability of the 40% resin combination, but with little success. Figure 3.2.3-15 shows a typical micrograph of a cross-section of a cooling ring in a defective area. The time, temperature, and preheat cycles were all varied with little improvement. We found that the viscosity could not be lowered enough to move the material around in the extremely thin wall mold. We also found that in tight corners, the

resin tended to separate from the fibers, leaving fiber poor regions. It may be possible, with further development, to get this system to work, but the accelerator that is used for commercial components in the epoxy system would need to be removed.

The next iteration of material was the incorporation of the toughened cyanate ester based resin system, Fiberite 954-3. This system's viscosity is approximately 100 times lower than that of the TEM9000 epoxy. Two systems were tried, 40% and 50% resin. Both systems had a low enough viscosity to flow easily within the mold.

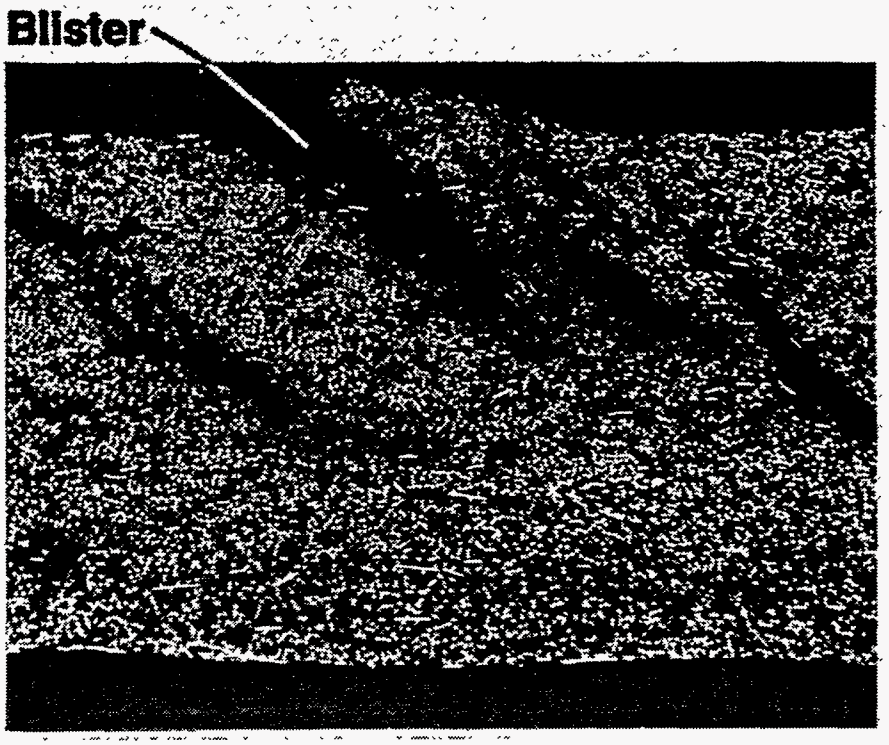

Figure 3.2.3-15 Cooling Ring Cross-Section, 40% Epoxy, 60% Graphite by weight, showing imperfections resulting from its high viscosity.

Cyanate ester is an excellent adhesive, and no commercial mold releases that we tried were successful in releasing the arc segment from the mold without breakage. A TEFLON® base coat, Dupont 850-314 with a thermoplastic Dupont PFA Powder Coat 532-5010 was finally found to work. The mold was coated with this system, and we successfully released the molded part from our mold.

The last issue to be resolved was the fragility of the P-75S/954-3 system. The molding compound was not as robust as the TEM9000, and it was very susceptible to breakage if the standard mold cycle was followed. However, if the component was removed from the mold after 30 minutes instead of 2 hours, the part was compliant enough to survive the separation of the two mold halves. It was now necessary to use a post curing mandrel to finish the cure cycle.

Hard Rubber Molding A second parallel path to make cooling rings was being developed at Sandia National Laboratories (SNL) and Programmed Composites. Because of the difficulty and cost associated with matched metal molds, a spray process was being worked out to spray the graphite/resin system directly onto the mandrel. If such a system could be developed, it would eliminate the high program costs of matched metal molds and solve another problem found for the matched metal mold system. During the

compression process, as the molding compound flows to distribute itself in the mold, the fibers tend to align themselves in the plane of the mold. Since fibers have relatively poor thermal conductivity across their diameter, the resultant cooling ring has poor conductivity through its wall Unfortunately, this is exactly the direction that heat must flow in order to be removed by the evaporative system in the center of the cooling ring. A solution to this problem was to develop a technique in which the fibers were deposited in a random orientation and uniformly over the entire surface of the mold, so that little molding compound flow was required.

Different diluents were evaluated to see which carried the compound with minimal interaction with the epoxy. Our earliest success came by using acetone as the diluent The resulting product had a shelf life of a couple of days and provided even distribution and excellent adhesion to the mold surfaces in any orientation.

Test articles were prepared on a flat plate to demonstrate if the graphite/resin system could be sprayed effectively and then consolidated under pressure and temperature. The results are shown in Figure 3.2.3-16 for both standard material dispensing and the sprayed concept. It can be readily seen that the fibers from the sprayed process does exhibit a more random particle distribution that a standard charge dispensing technique.

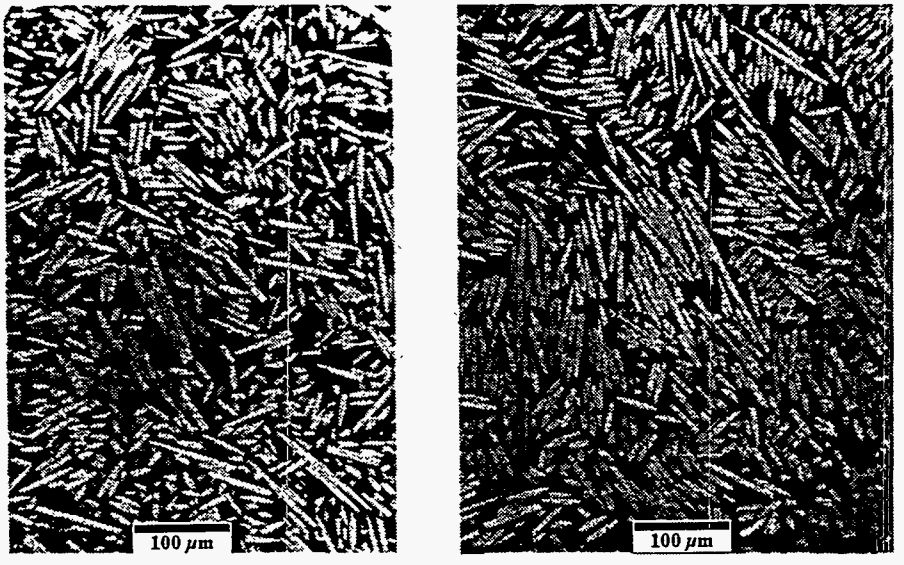

Sprayed Standard Charge

Figure 3.2.3-16 Photomicrographs comparing the fiber orientation of Sprayed versus Standard Charge dispensing.

We were encouraged by the improvement in material orientation enough to continue the development process. The next step was to try and spray over the actual male mandrel and then consolidate the constituents under pressure.

The first attempt of using the hard rubber mold resulted in non-uniform part thickness. The mold consisted of a male mandrel with a hard rubber over press approximately 2.5 cm in thickness and two sturdy outer aluminum shells, as shown in Figure 3.2.3-17. This configuration did not develop enough pressure at 175°C to uniformly consolidate the Graphite and produce a high quality part. Work continued at Programmed Composites in an attempt to increase the pressure by using TEFLON® inserts in place of the hard rubber. A fully satisfactory solution was not found.

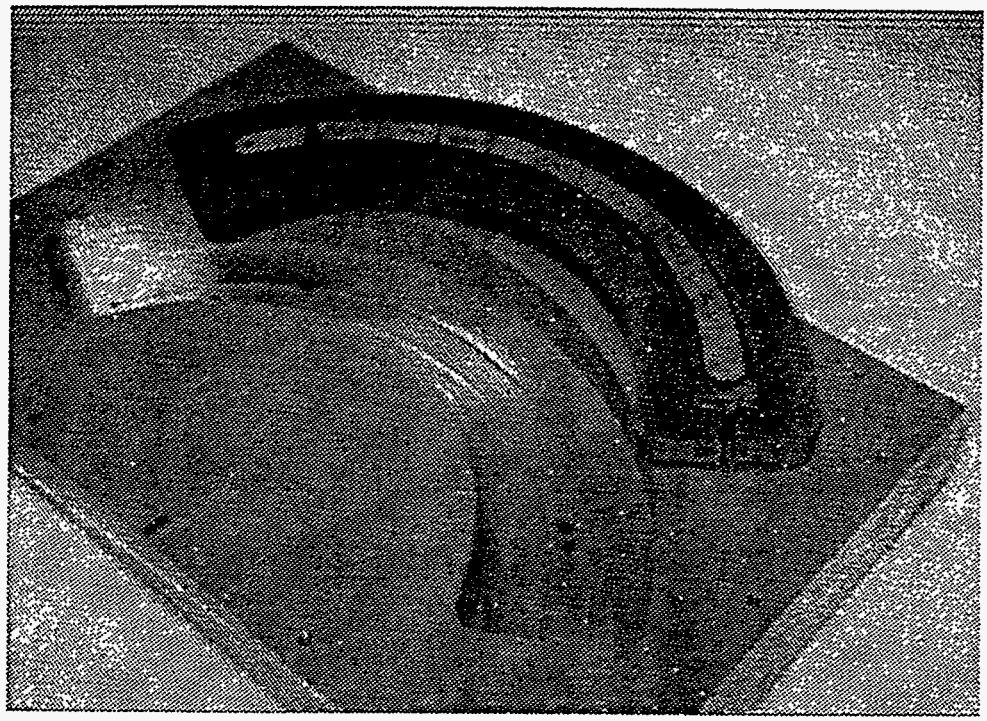

Figure 3.2.3-17 Mold used in the spray deposition process.

Molded / Machined Rings A variant of the hard rubber molding technique was attempted next. The process again involved a precision male mandrel, but this time with a considerably oversized female rubber piece. The part produced had walls a few mm thick. As such, the molding compound could be easily applied, and since the wall thickness was now considerably greater than the fiber length, a truly random fiber orientation could be obtained. Also only small amounts of flow were required to fill any voids, and such flow was no longer restricted by passages of thin cross section as in all the earlier processes. Once the part had cured, the oversized walls were machined to produce the final desired shape and wall thicknesses. This process allowed us for the first time to reach 60% fiber volume fraction and highly random fiber orientation. Nevertheless, some problems remained. The very high fiber volume content in thin cross section pieces turned out to be extremely brittle and tended to break during the machining process, especially as one approached the 400 μm desired wall thickness.

Molding Summary A large variety of different molding techniques were tried in order to produce cooling rings that possessed the combined properties of high transverse thermal conductivities, very thin wall thicknesses, high strength, and low CTE and CME values. Although the different individual goals were met using different techniques, no single technique found was able to meet all the requirements simultaneously. That was borne out through a wide variety of non-destructive evaluation techniques discussed next.

As a result of the problems encountered in the molding processes for the rings, and also in the attempt to produce molded polystyrene wicks (Section 3.4), we began to investigate alternative means of producing the support rings as discussed in Section 3.2.3.5.

Non-Destructive Evaluation Ultrasonic techniques were used to evaluate the material variation and mechanical properties of the cooling ring. This evaluation was used to assess the manufacturing development of the cooling ring. The techniques used included pulse-echo scanning techniques and time-of-flight measurements.

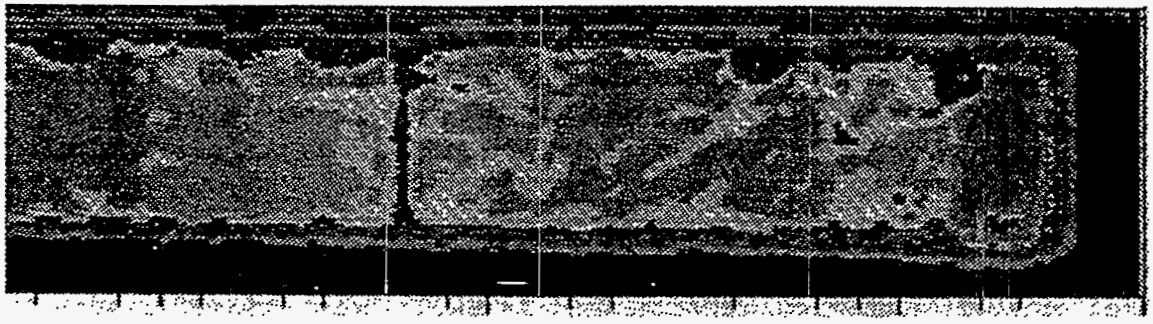

Figure 3.2.3-18 Image of pulse-echo amplitude variations indicating where compositional changes occur within the composite.

The intensity of an ultrasonic wave following reflection and transmission at a material interface is governed by the acoustic impedances of the materials. The acoustic impedance of a material is given by the product of its density and the acoustic velocity in the material. For a composite composed of many material interfaces, a measure of the transmitted and reflected intensities by well known pulse-echo techniques is an efficient measure of the qualitative uniformity of the composite. These techniques are quick and make for efficient evaluation of the manufacturing parameters. Volume fraction variations of the fiber/matrix, as well as voids or resin poor areas, are easily detected. The images that result from spatial variations in the acoustic impedance is well documented in the published literature[4].

Macroscopic and microscopic material composite variations were imaged for the composites of this study. A typical pulse-echo amplitude plot of the full thickness echo is shown in Figure 3.2.3-18, using a 30-MHz focused transducer. The image of Figure 3.2.3-18 indicates a uniform composite except for the resin rich area indicated in black on the right side of the image. The vertical line was due to an imperfection in the mold surface. The images of Figure 3.2.3-19 show the pulse-echo amplitude variations for four test pieces representing different manufacturing options. The light areas in Figure 3.2.3-19 show where high amplitude pulse-echo signals were obtained. The dark areas show where high attenuation of the signals occurred, indicating poor material interfaces between fibers and matrix or an increase in thickness. A uniform color would indicate a homogeneous composite composition. The variations shown in Figure 3.2.3-19 indicate a less desirable fiber composite uniformity.

A scanning acoustic microscope (SAM) was used to image the reflection intensities due to variations of the surface constituents of the fiber composite on a micron scale. The SAM used in this study was an Olympus UH3 acoustic microscope. Figure 3.2.3-20 shows a side view of the cooling ring in the area of one of the serration steps. The non-uniform distribution of the fibers is clearly observed. These images were obtained with a 400 MHz focused transducer.

The distribution of the fiber and particulate composition for two test pieces of different manufacturing options are shown in the SAM images of Figure 3.2.3-21. Those images show that only a few 400-μm fibers are present in the composite. Many much shorter fibers are present than is desired. This is also reflected in the low in-plane moduli values measured for the composites shown below.

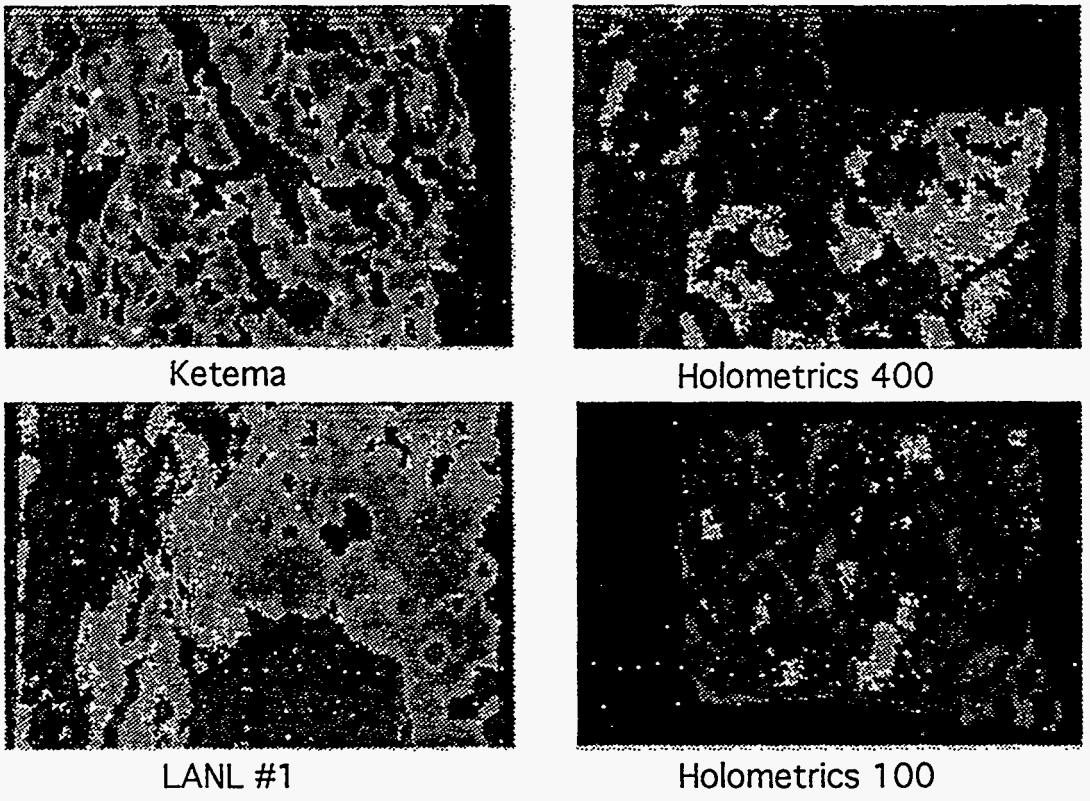

Figure 3.2.3-19 Images of the pulse-echo amplitude variations for four test pieces representing several different manufacturing options.

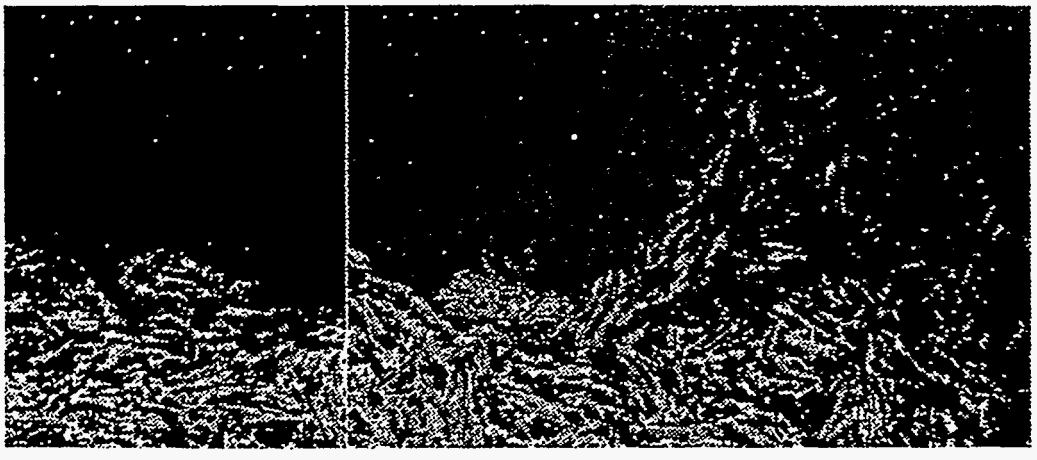

Figure 3.2.3-20 A side view of the cooling ring in the area of one of the serration steps;. The non-uniform distribution of the fibers is clearly observed.

Time-of-flight measurements were obtained by contact through-transmission buffer rod techniques and liquid immersion through-transmission techniques[1,2]. Acoustic velocities were calculated from the time-of-flight measurements in the principal axes of the composite, and with a density determination, the elastic constants and engineering moduli were computed. The results of the moduli calculations are shown in Table 3.2.3-3.

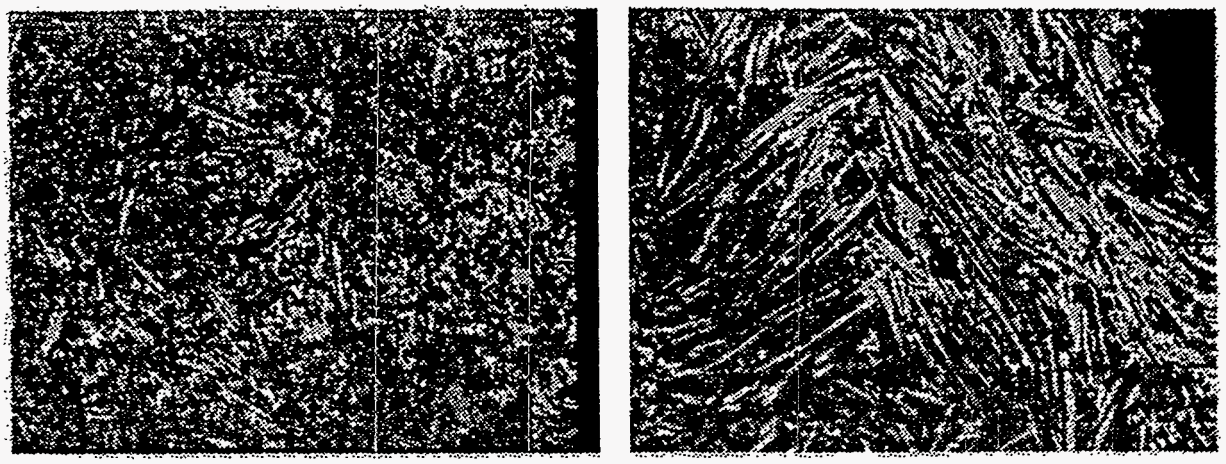

Figure 3.2.3-21 SAM images of (a) Holometrics 400-μm test piece and (b) PCI 400-μm test piece.

Table 3.2.3-3 Results of the moduli calculations: (1) In-plane, (3) Out-of-Plane

Sample	C11[a] (GPa)	C33[a] (GPa)	E1[b] (GPa)	E3[b] (GPa)
LANL 1	25.1	20.8	22.3	20.5
Ketema 2	17.8	16.7	15.3	14.0
Holometric 400 3	19.4	13.9	14.0	11.4
Holometric 100 4	22.3	13.4	15.7	9.7
Holometric 400 5	19.1	12.3	14.8	8.3
50/50	25.1	15.4	17.7	9.3
Quasi Isotropic	266.5	11.2	97.6	3.5

[a]Longitudinal Moduli C11 and C33 were obtained by multiplying the density by the velocity squared where 1 is the in-plane velocity direction and 3 is the thickness direction.

[b]E1 and E3 are obtained by making longitudinal and shear velocity measurements in the principle directions and at a 45° direction to the thickness direction.

Table 3.2.3-3 also lists the moduli measured for a 50/50 volume fraction sample of 400 μm fibers and a long fiber quasi isotropic tensile sample. The 50/50 sample showed the proper mixture of 400-μm fibers. The quasi-isotropic sample was manufactured with many alternating plies of long fibers resulting in a thick layered sample of 62.2% fiber volume. These two samples are listed as examples of the high moduli obtainable with an ideal manufacturing process.

3.2.3.5 Composite Ring Sandwich Construction

Due to the difficulties encountered in the development of the molded composite cooling ring a different ring construction technique was undertaken. The prospect of using a new construction technique was made possible by changes that were simultaneously taking place in the cooling system design. The successful move toward a cooling system configuration with the heat sinks located directly on the module hybrid (MCM) meant that it was very unlikely we would return to placing wicks or cooling

elements on the inside of the cooling ring, in spite of the desirable features of this arrangement. A requirement that the ring be hollow, with a wall material exhibiting a high transverse thermal conductivity no longer existed. The ring function became solely one of support. Our first approach was to construct rings composed of a composite sandwich construction.

Prototype ring segments were initially constructed as a sandwich of two, 8-ply quasi-isotropic lay-ups of P-75/C-E prepreg material using both low density graphite honeycomb and carbon foam cores. In each case the sandwich was nominally 1 cm thick. The 8-ply lay-ups were constructed using 1-mil thick B-staged prepregs yielding a nominal wall thickness of 200 μm for each face. Following these sample constructions we made a decision to construct full size rings using a carbon core, possessing a 97% void fraction. This decision was largely based on the availability of the carbon foam and the ease of construction associated with this approach. Small cell size graphite fiber honeycomb material was just not available.

Figure 3.2.3-22 depicts the 42 cm diameter carbon foam sandwich ring constructed as a replacement prototype for the compression molded ring. The carbon foam open edge can be seen from this view. We did not have an opportunity to perform tests to characterize the structural stiffness, nor to finish bonding edge pieces that serve to close out the open foam edge. An enhanced photograph of this open foam edge is shown in Figure 3.2.3-23. The adhesive bond lines are discernible in this view, as white areas separating the core and laminate facings. These bond lines are not equal, and somewhat thicker than desired, ranging from 250 to 670 μm. In future ring constructions we would plan to control these bond lines in the range of 125-250 μm, solely in the interest of minimizing radiation length penalties. In comparison, the carbon foam sandwich ring, with thin bond lines and constructed on the same 8 mm width as before, would have a radiation length roughly 78% of that exhibited by the molded ring technique.

Another important aspect of this new ring construction technique is the near zero CTE achievable with the quasi-isotropic laminate. The superior control and uniformity that we are likely to achieve in the value of the CTE, also meant that we should be able to simplify the design of kinematic mounts. We would design for a zero CTE, which would mean that the shell could be treated as stationary in the radial-circumferential plane, and that one would only have to accommodate an axial expansion caused by the non-zero value of the silicon ladder CTE.

Figure 3.2.3-22 Picture of the 42 cm diameter carbon foam sandwich ring constructed as a replacement prototype for the compression molded ring.

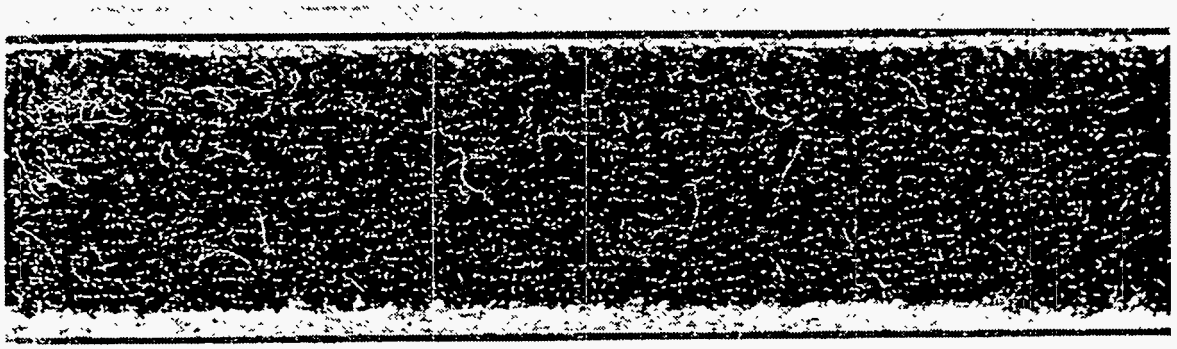

Figure 3.2.3-23 An enhanced photograph of the open foam edge. The adhesive bond lines are discernible in this view, as white areas separating the core and laminate facings.

3.2.3.6 Silicon Detector Prototype

Structural tests that were performed on two prototype silicon detector modules. These tests are similar to much earlier tests, but reflected the changes in the manufacturing methods and the preferred adhesives that had since been adopted.

The test pieces approximated the silicon modules that were to be used in final fabrication of the silicon detector. Four silicon wafers were bonded edge to edge to create a 24 cm long wafer. Graphite/epoxy side rails were bonded along the length and perpendicular to the face of the wafer subassembly, using Norland 61 UV curing adhesive (section 3.2.3.7). The rails serve to stiffen the silicon structure. The epoxy used for bonding the wafers was EPO-TEK H70S, and the bond line thicknesses were approximately 25 μm. These components comprise a detector module. Two module prototypes were glued to a pair of graphite/epoxy separator blocks, one block near the each end of the ladders as shown in Figure 3.2.3-24. The adhesive used was Loctite Output 384, a repairable and thermally conductive glue. The glue line thickness for this test ranged from 125 to 250 μm. The separator block simulates the approximate cross sectional dimensions of the cooling ring. The assembly was cantilevered on one end with an imposed symmetric, or centered load, on the opposite end for load case 1, and with an imposed asymmetric, or off centered load, for load case 2. Theoretical calculations and actual test results were compared.

A finite element analysis was made using COSMOSM to compare with the experimental results. In the model, several simplifying assumptions were made, based on past experience. For instance, the bond lines were not taken into account as past tests had shown that to be a reasonable approximation.

A mechanical deflection test was executed for both load case 1 and 2 using a simple test fixture. The test fixture for the procedure cantilevered the test piece on one end in a horizontal position. The opposite end of the fixture supported a micrometer head and a 250 gram capacity load cell. An arm with a slide allowed the desired load, symmetric or asymmetric, to be positioned.

Comparison between the experimental data and the FEA predictions is shown in Figure 3.2.3-25. The FEA yielded a maximum deflection of 280 μm for the cantilevered orientation as a result of gravitational sag. Actual measurements indicated a 400 μm value. For the load case tests, the results closely paralleled those of the FEA up to the 50 gram load in both load cases, aside from the offset already seen in the gravitational sag case. After the 50 gram load, a deviation occurred from the predicted data. A possible explanation for this could be a buckling in the graphite ribs. The results indicated that the structure was very stiff and behaved as a wide flanged beam. An interesting point of note is the symmetric load and the asymmetric load produced nearly identical maximum

deflections and maximum stresses. This assembly proved to be very stiff structure both in bending and as well as in torsion.

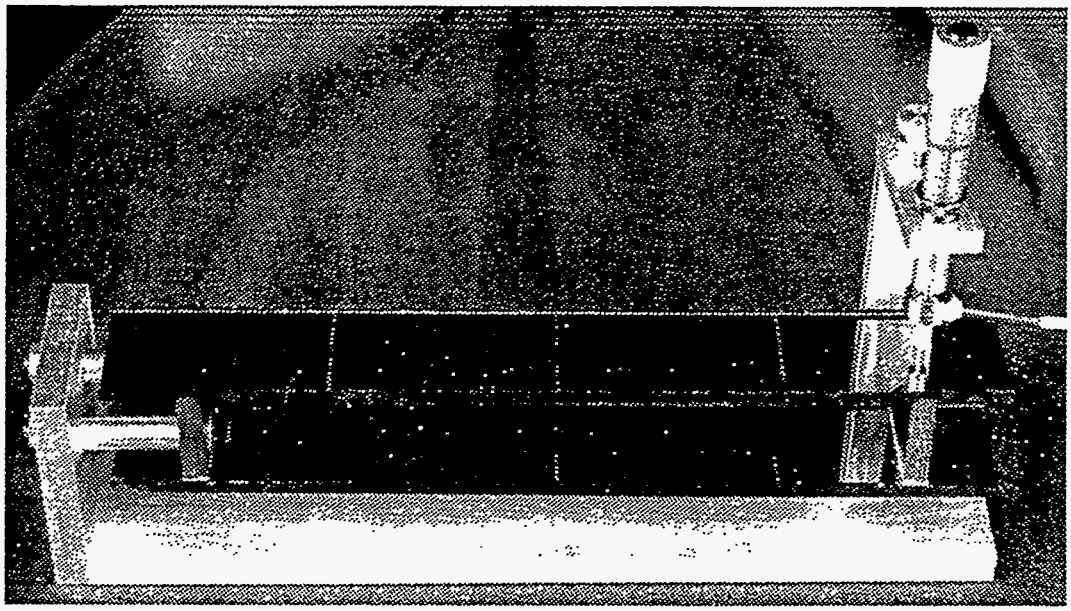

Figure 3.2.3-24 Picture of the module assembly tested. Loads were applied at the cantilevered end as indicated: either at the center (Case 1); or at the corner (Case 2).

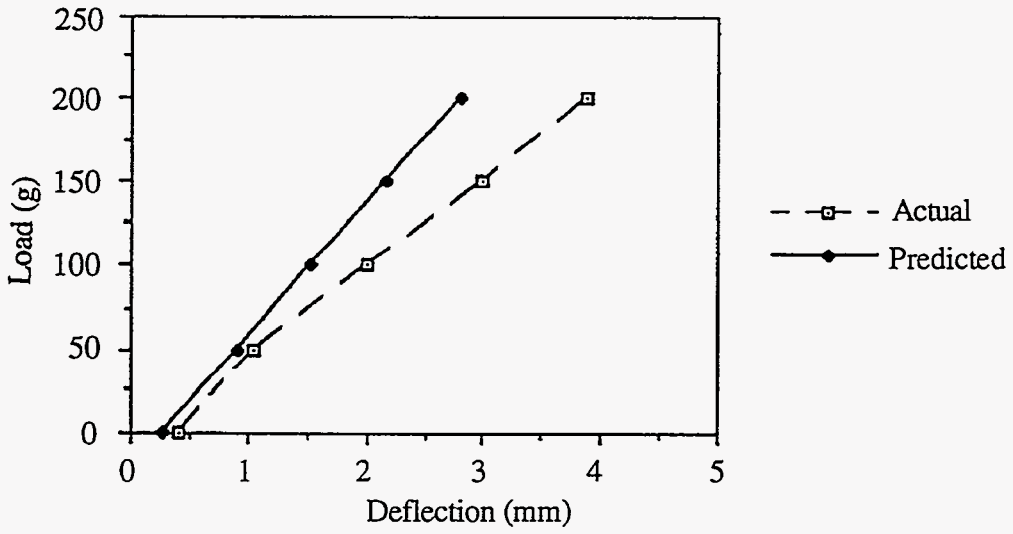

Figure 3.2.3-25 A comparison between the experimental data and the FEA predictions.

The test pieces were cycled through the loads approximately 5 times to verify the repeatability of the results. The results were reproducible. On the basis of these limited tests we observed no apparent problems with the epoxy used. We were exceptionally pleased with the robust behavior exhibited throughout the tests. The module was subjected to an enormous amount of strain for such a delicate device, and withstood these loading conditions exceeding well.

Butane / ^{60}Co Irradiation Test Results After the above test, the module/graphite block assembly was placed in a butane filled canister and subjected to irradiation tests at the University of California at Santa Cruz. The canister was maintained under pressure at room temperature. The specimens were irradiated with ^{60}Co gamma rays for roughly two weeks to create the 10 MRad exposure characteristic of the maximum dose expected after 30 years of SSC operation, at design luminosity. The modules were placed in the test apparatus discussed in the preceding section, and the strain tests were repeated. We did not observe any property changes or deleterious effects on the adhesives from either the butane exposure or radiation, nor the combination of the two environmental effects.

3.2.3.7 Adhesive Selections and Testing

For all practical purposes mechanical joints from the most fundamental silicon wafer joining process to the final assembly of the space frame are achieved through adhesive bonding. We purposely eliminated, with the exception of the outer enclosure flange connections, all mechanical fasteners to realize a significant savings in structural mass. In this process, it was not clear at the onset what would be the best adhesive for a specific joint connection. However, since our design was committed to successful application of adhesives we endeavored, within the available time and resources, to conduct a systematic selection process. Initially, the following adhesive material property goals were set:

- withstand 10 Mrad's without appreciable change in structural properties
- high purity, nearly devoid of chlorine and sodium ions, typical of materials chosen for the semiconductor and electronic chip applications
- rigid adhesive, zero creep under design load
- fast curing
- thermally conductive, electrically non-conductive

We had the added complication of material compatibility in a combined radiation and hydrocarbon environment because of the butane evaporative cooling system. Fortunately, the butane does not act like an electrolyte that would accelerate any potential electrochemical processes (corrosion, or leakage current effects) traceable to impurities in adhesives. In anticipation of this potential problem we evaluated the leakage current on a miniature strip detector before and after exposure to a butane/radiation environment and found no incompatibilities. Although, the test series was quite limited in extent, the results were encouraging and added confidence to our selection.

Our initial construction of the 24 cm long module with 4 adhesively edge-bonded wafers was done entirely with EPO-TEK H72, which cures at 150°C. The adhesive would cure roughly within 10 minutes. Since the joints were made serially, previously cured joints had to be held below their heat distortion temperature (glass transition). Otherwise, the joints would soften and dimensional control of the overall assembly was affected. We later switched to EPO-TEK H70S, which had a slightly faster cure time to improve on this situation. The most difficult step involved adding the 4 mm high graphite fiber laminated rib to the sides of the detector. Using the EPO-TEK product here, on a finished bonded wafer assembly, only aggravated the glass transition problem. For this final assembly step, the adhesive chosen was an ultra-violet light cured product by Norland (61). With the proper UV lamp, this adhesive sets in less than a minute. As a matter of interest, we also butt bonded wafers with this adhesive. A pull test specimen cured with Norland 61 agreed quite well with the tensile strength given for this product.

Bonding the finished module onto a composite ring structure introduced several new requirements. First, we wanted a repairable structure, one where the module could be demounted. Secondly, a fast curing room temperature adhesive was needed to be compatible with the semi-automated work station being developed to place modules in a repetitive manner. Temperature curing adhesives would present serious problems to the thin composite structures as well as the optical alignment system. An adhesive was found that could be cured within minutes with either an accelerator or UV light. Applying the accelerator proved to be the best arrangement, since access for the UV light was essentially non-existent.

Table 3.2.3- 4 lists the adhesives that were being pursued and tested for the specific components listed.

The Loctite and DYMAX products are quite similar in the respect that both can be either activator cured or with a UV lamp. DYMAX was ultimately chosen for bonding modules to the composite structures because of its lower viscosity, making the application more controllable. Our goal was to minimize the adhesive joint thickness, and the higher viscosity material impeded this process. The above candidates are not electrically conductive, but do possess a reasonable thermal conductivity, a trait desired for situations involving heat removal from the electronic chips or wafers. The first four candidates fulfilled this requirement.

The adhesive curing time for joining our composite structures, Hysol EA 9394, can be accelerated through an oven curing process. Curing at 66°C requires 1 hour. We have not tested this material in a radiation environment, although we have reason to expect no problems will be experienced since it is quite close to an epoxy candidate that we did irradiate. Epoxies as a general class are highly radiation resistant. Our first composite truss core panels that were tested in a high radiation environment were bonded with Hysol EA 9335, and no deterioration was evident in the adhesive joints joining the truss core surfaces.

Table 3.2.3-4 Adhesive Candidates

Name	Type	Cure Temp °C/min.	Shear Strength (MPa)	Tensile (MPa)	CTE (ppm/°C)	K (W/m-°C)	Use
EPO-TEK H70S	Epoxy	150/5	8.27	68.25	50	1.15	Wafers
EPO-TEK H72	Epoxy	150/10	17.24	39.30	42	0.86	Wafers
Loctite 384	Acrylic (mod)	Activator/ 5 secs	4.14	12.41	110	0.82	Modules
DYMAX 991	Urethane (mod)	Activator/ 30 secs	17.24			0.86	Modules, Space Frame
Hysol EA 9394	Epoxy, Structural	Room Temp. 24 hours	28.96	46.02	55	0.33	Composite Laminates
Norland 61	Proprietary	UV/30 secs		20.68			Modules

We did verify the bond line joint tensile strength of the silicon wafers for the first two EPO-TEK candidates. The values shown in the table are from LANL butt-joint tests. The wafer bond line joint thickness was controlled to a thickness of 25 μm in the bonding operation with precision assembly stages. The bonded edges are prepared by applying a small coating of adhesive to one wafer edge, thereafter the precision mechanical stage brings the two butt joints into contact. After contact, the mechanical adjuster is repositioned to create a precise 25 μm gap. The adhesive surface tension maintains

complete filling of the small gap, thus removing any edge defects in the bond line. Controlling the bond line thickness in this manner eliminated imperceptible edge defects that larger gaps cause as the adhesive retreats away from the detector edge. These edge defects act effectively as incipient cracks and serve to greatly reduce the joint tensile strength. This was observed by using scanning electron microscope (SEM) techniques. Through extreme magnification we were able to discern bond line defects. Figure 3.2.3-26 is an SEM of a bonded 100 μm joint that illustrates the aforementioned defect. The retreated area would normally be completely filled in a 25 μm bond line joint. Uniformity in structural behavior of each module was desired to ensure that the elastic behavior of the assembled silicon shell would be predictable and symmetric. Although we proved our module design to be quite robust and the strengths of individual joints high, the support method under development was intended to ensure that these joints would be exposed to at most a very small fraction of their ultimate strengths.

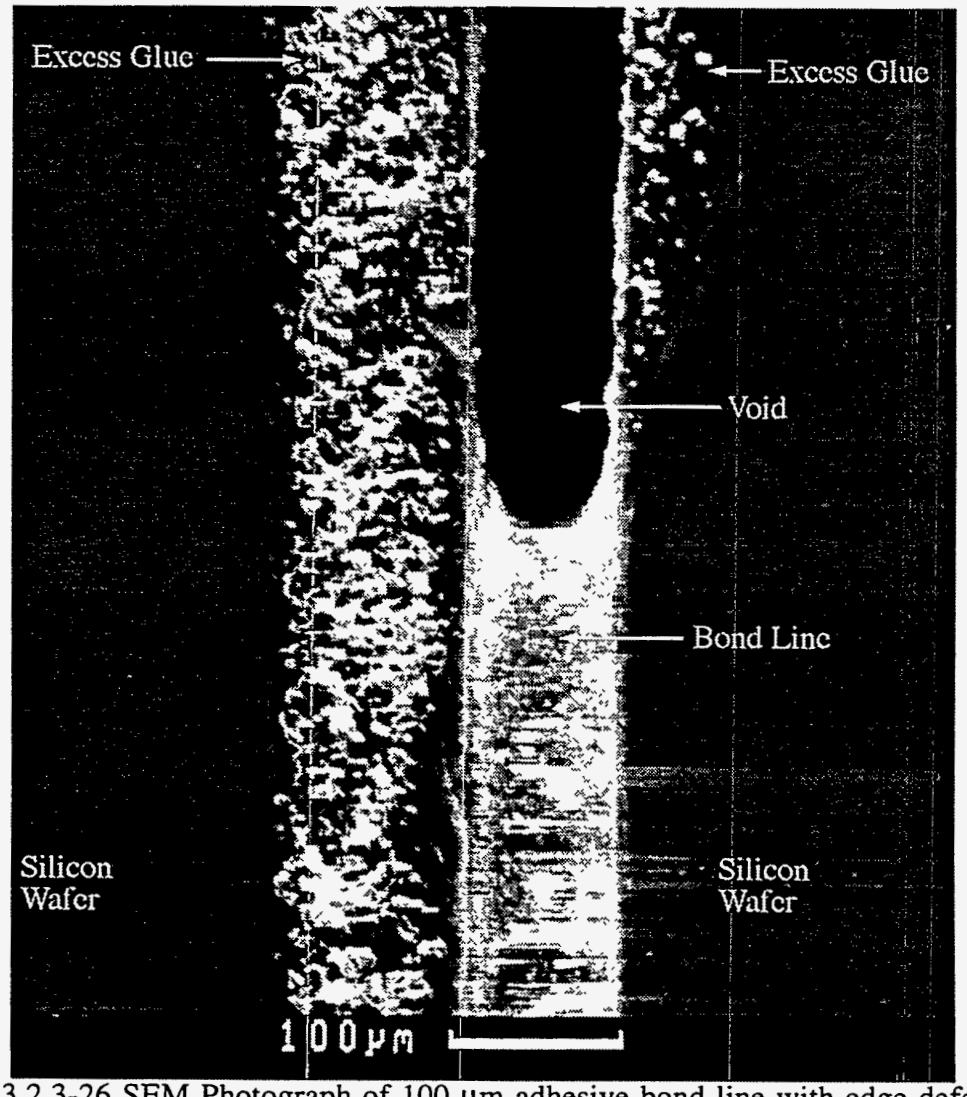

Figure 3.2.3-26 SEM Photograph of 100 μm adhesive bond line with edge defect (top portion of view).

3.2.3.8 Central Region Component Test Summary and Conclusions

For SDC's central region, we chose to combine the cylindrical array of silicon wafers into edge-bonded, 24 cm and 12 cm long modules; using these self-supporting modules, silicon shell like structures were formed by bonding the modules to cooling rings. Two module lengths were chosen to accommodate the 60 cm central region length. In the final design the cooling rings became ultralightweight support rings. It is important to understand that the silicon shell assemblies *are not part of the basic tracker support structure*, but rather individual kinematically supported shells that are not subjected to unpredictable external loads. The silicon modules are intended to support only their weight, and not to bear the weight of any other tracker components. A discussion of the kinematic mounts that support the shell in a strain-free manner is discussed in the next section.

A major objective that was accomplished in this year's development effort was to concentrate on the individual technical areas required to build a stable silicon shell for the central region. The preceding sections present the fundamental issues that we addressed before attempting the construction of a full shell assembly. A major portion of this effort centered on constructing thin-walled composite molded rings suitable for supporting the silicon modules, while providing a receptacle for integration of the wick for the evaporative cooling system. Significant progress was made in this regard, although toward the end of the year it was obvious that mounting the wick inside the ring would not be practical within the time remaining for achieving this goal. A large number of detector modules were constructed and tested to establish their mechanical properties before and after exposure to a combined radiation/butane environment. The module design proved to be extremely robust, and in the course of this investigation we demonstrated the acceptability of several adhesives combinations. FEA studies were made that quantified the structural stiffness of the combined shell/silicon module assembly. The unit proved to be quite stiff when constructed with the molded composite support rings. A silicon shell was being prepared for assembly using a sandwich ring construction with a carbon foam core and graphite fiber laminated facings. The prototypical silicon structure with molded rings was used in a combined cooling/stability test; reference Section 3.3.

3.2.4 Kinematic Mount

As the temperature of the detector is reduced to its operating level, components having near zero, but slightly different coefficients of thermal expansion, will undergo small dimensional changes that could result in undesirable stresses or displacements. In spite of our objective to construct an ultra-stable system we must acknowledge this prospect and factor those effects into our design. This situation was discussed briefly Section in 3.2.3.3; here we intend to present mount design concepts that address this issue specifically. This section presents the results of our first mounting investigation and details thoughts being pursued in area of mounts constructed of composite materials.

It is desirable to support the sensitive silicon components of the detector in a manner that allows nearly strain-free thermal expansion and contraction. There are two basic silicon structures that need to be supported, 26 comparatively thin planar arrays, and 12 cylindrical shell components. Different issues are involved in mounting those two structures. The flat planar arrays are typified by their large diameter, approximately 1 meter, and thin aspect ratio. In contrast, the cylindrical shells vary in diameter from 19 cm radius to 78 cm, and come in two lengths 24 and 12 cm.

It would appear that the most difficult of the two structures to support are the central region silicon shells. The earlier description of the central region pointed out that two super-layers are supported by one concentric composite shell. In a fully assembled state

one can only see silicon surfaces. There is little access for physical support, and even less access to the individual silicon shell mounts. In our original concept, because several silicon shells are mounted in tandem, both inside and outside the composite shell, access to the innermost mounts is severely limited. In order to assemble both sets of silicon shells on a composite shell it was judged prudent to assemble and align either the inner or the outer set first, then remove that set so that mounts for the other set are accessible. Hence, the capability to uncouple the individual mounts from a silicon shell without disturbing their alignment appeared warranted. In our recent visualization of the tracker concept, pairs of composite shells are used for supporting two superlayers. The inner shell of the pair supports a super-layer of silicon detectors on its inside, while the outer shell of the pair supports a super-layer of detectors on its outside. After the detectors shells are mounted and aligned on their composite shells, the pair of composite shells are aligned with respect to each other and secured to each other. With this arrangement the assembly problems are definitely eased, and the prospect for simplifying the mounting concept was introduced. The capability to uncouple the individual mounts from a silicon shell without disturbing their alignment is a desirable feature. This objective must be weighed in terms of increased mount material requirements versus time saved in replacement of silicon modules.

Mounting Concepts With these criteria in mind, several mounting concepts were studied. The first concept is a classical 2-2-2 mount. In its simplest form, this concept consists of three co-planar balls, equally spaced around the periphery at one end of a silicon shell, with each ball resting in a radially-oriented vee groove seat. In this configuration the seats, which are attached to the composite shell, allow growth or contraction of the silicon shell while maintaining its radial centering. A set of balls in a similar configuration, but resting on flat, compliant surfaces oriented tangent to the cylinder, are located at the opposite end of the shell and allow for changes in the length of the shell. With this mount geometry two axial restraint methods are possible; first, by lightly clamping the balls in the vee grooves, and second, by tilting the flat surfaces at the opposite end so an axial component of force exists. The first axial restraint method has the disadvantages of potential overconstraint due to the radial loads imposed by the flat surfaces or, underconstraint which would result in cantilever support. The second axial restraint method has less of a potential for overconstraint, but would impose axial compressive loads on the entire shell. Neither of these conditions is desirable. Theoretically, the major advantage of the 2-2-2 mount is its ability to produce very symmetric expansion and contraction in a cylindrical geometry. In practice, the mount has the potential for stick-slip, or "stiction" problems due to external friction.

The second, and most promising concept being studied is the tangent bar. As its name implies this device is a flat, compliant strip oriented tangent to the silicon shell. A spherical surface, or ball, mounted on the silicon shell rests on the tangent bar, which is attached to the composite shell. The rest feature for the ball on the tangent bar can be a flat, groove or conical detent. With some initial deflection of the strip when mounting a silicon shell, a preload can be effected that will accommodate radial expansion or contraction of the shell without decentering. Several combinations of the flat, groove, and detent features are the subjects for upcoming tests on two tangent bar designs. The first combination consists of three equally spaced tangent bars around each end of the silicon shell. All six bars allow radial movement of the silicon shell by virtue of their flexibility. At one end of the shell, the set of bars includes a flat, a groove, and a conical detent. By orienting the groove parallel to the axis of the shell, the shell is locally unrestrained in the axial direction, but is restrained from rotating about its axis. The bar with the conical detent prevents all but the radial movement, and the third bar, which is flat, merely constrains the shell against the other two. At the opposite end all three bars have flats, thus, free movement in five degrees of freedom and limited movement in the radial direction is allowed. The principal advantage of this arrangement is that none of

the balls on either end have to be coplanar or precisely aligned in the axial direction in order to meet the shell's most stringent position tolerance of 5 μm. The shell's alignment, with respect to skew of its axis with respect to the overall detector axis, is set by adjusting the radial positions of the bars at the end opposite that of the conical detent. These bars must be positioned radially within 5 μm to meet the requirement, regardless of shell diameter. The major disadvantage of this arrangement is that the constraint is asymmetric and, therefore, the structure has the potential for asymmetric distortion as it contracts and expands.

A variation of the above configuration is one in which all three mounts at one end of the shell are conical detents and the ones at the opposite end are flats. Because of its symmetry and complete axial constraint at one end, this geometry ensures symmetric radial movement, and uniform axial contraction and expansion relative to the fixed end. Its major disadvantage is that the shell's alignment with respect to skew is set by the accuracy with which the detents are placed. The tolerance in this instance is directly proportional to the shell radius. For example, for the smallest silicon shell to meet the 5 μm requirement, the axial position of the detents relative to the shell (or balls) must be within 5 μm, but for the larger shells the tolerance is relaxed.

3.2.4.1 Tangent Bar Mount Assembly

Figure 3.2.4-1 shows the tangent bar mount described above with adjustment capability in three orthogonal directions. In the figure, the X, Y, and Z directions correspond to the tangential, radial, and axial directions on a typical central region shell, or on a forward region planar array.

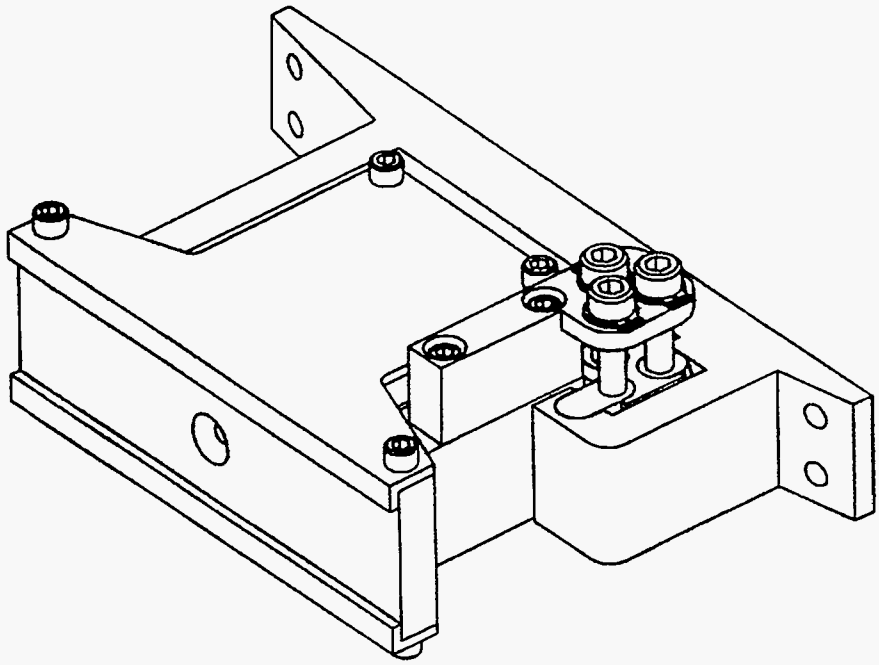

Figure 3.2.4-1 A tangent bar mount with adjustment capability in three orthogonal directions.

Incorporation of these integral adjustment features into the tangent bar mount concept, or any mount for that matter, presents a significant challenge. Adjustment of the individual mounts can produce serious structural loads and strains in the delicate silicon structures through inadvertent overconstraining of the structure. During this critical phase of assembly strain deformations in the structures should be monitored, holo-

graphically as described in the Section 3.3.1. The mechanical adjusters that effect these positional changes are called primer movers, for lack of a better designation. These devices must be capable of positioning the silicon substructures within 5 μm. To ensure stability of the mount after it has been adjusted, it should be possible to lock the prime mover with simple clamping, or the flexures must be constructed with sufficient stiffness to prevent drift. While it is possible to clamp the X and Z stages, the Y stage will most likely have to depend on flexure stiffness for its stability because of the uncoupling requirement. The flexure for this stage must also be stiff enough to ensure a suitable fundamental natural frequency for the shell assembly. Additionally, it should be stiff enough to be insensitive to the tangent bar preload. If clamping is used to lock a stage, the force applied must be orthogonal to the direction of adjustment. Clamping schemes using opposing forces in the direction of the adjustment for micron level of accuracy are not feasible. Threaded devices such as differential screws and screw-driven wedges typically suffer from manufacturing imperfections that result in backlash and roughness of motion. Although some of these problems can be overcome by single-point turning of threads, lapping of mating parts, and vapor deposition of durable dry lubricants such as tungsten disulfide, other problems will remain, requiring the use of an alternate approach.

Since the prime movers are used only to precisely control the position of the mount during assembly, and not necessarily to provide any operational stability, it may be feasible to use a removable setup fixture that carries the prime movers only. In this concept, it is conceivable that commercially available micrometers and piezoelectric devices could be used to achieve accuracies on the order of several microns. The micrometers would be used to coarsely position the piezoelectrics, which would then be used to drive the mount stages. After the adjustments are made, and the stages or flexure motion stops are fixed by clamping, the fixture with the movers would be removed. This concept also has the potential for reducing the amount of unwanted material in the detector. It should be noted here that this concept for positioning the mount stages is quite new and has not been studied in any detail. Problems concerning mount accessibility during assembly, and mount stability during stage locking need to be investigated. It is important to note also that this concept is for positioning the mount on the silicon shell, not for adjusting the position of the latter. It is assumed that the shell itself is supported, positioned, and held stable by a completely independent device during the mount engagement operation, reference Section 3.2.5. Regardless of the assembly procedure it is imperative that distortion of the silicon structure be monitored during the procedure if alignment is to be maintained and deformations controlled.

The adjustment compliance mechanism constructed for our initial prototype mount is a set of three parallelograms that form an enclosed box structure. Two parallel sides of each parallelogram are thin compliant strips, or flat blade flexures. The other two sides are rigid plates. When one rigid plate is fixed and a force is applied to the other in a direction normal to the plane of the flexures, the flexures behave as a pair of elastic beams with the free ends guided. For small displacements, the resulting motion is essentially linear and parallel to the fixed plate. In this design, the three stages are considered to be tandem; that is, the Z stage, which carries the tangent bar, is carried by the X stage, which in turn is carried by the Y stage. The stages are stacked in this manner because the Y, or radial direction is the one in which the mount must move when disengaging from the shell. The number of stages required on any given mount is determined by the tangent bar rest feature. A conical detent bar requires all three stages, whereas the groove needs only the Y and X stages, and the flat needs only the Y stage. It is also possible for a groove bar to have a Z stage instead of the X stage. The tangent bar itself is simply a wide, flat flexure with its ends fixed and a stiff section at its mid-span for the rest feature. When a normal force is applied at the rest point, such as the preload mentioned above, the flexure behaves somewhat like a pair of elastic beams with the free ends guided.

Materials of Construction Compliant members, or flexures, are ideal devices for the mount structures because their mechanical behavior is quite predictable and they perform in a smooth, frictionless manner with no backlash. They are, however, subject to relatively large strains that result in high stresses. In this design, for example, the displacements of the XYZ stages range from 0.50 mm to 1.25 mm with corresponding normal stresses ranging from 190 MPa to 370 MPa. Stresses in the tangent bar itself are also in this range. Although there are a number of excellent high strength materials available for flexure construction, most of the more desirable ones must be used sparingly or avoided altogether because material volume, density, and number of radiation lengths must be minimized in this application. Commonly used materials, such as 17-4 PH stainless steel, beryllium copper, and Ni-Span C all have yield strengths in the range of 1040 - 1380 MPa, but all have high densities and high atomic numbers, with one radiation length corresponding to less than 2 cm of material. Wrought beryllium has the most desirable density (1.85 g/cm^3) and the most desirable value from a radiation length standpoint (35.3 cm), but its yield strength is only about 276 MPa. A material suited for the bulk of the mount construction is aluminum alloy 7075 in the T6 condition. Its yield strength is about 520 MPa and its density is 2.7 g/cm^3. Unfortunately, its radiation length is a factor four lower (8.9 cm) than beryllium. In our initial mount construction we used the aluminum alloy. From a cursory observation, beryllium would appear the best choice in a fully optimized design. We could use up to four times the thickness of beryllium, versus aluminum, for the same radiation length, but the differences in yield strength belie the apparent advantage. We need to assess whether the beryllium is too brittle for the highly stressed parts before making a decision.

Although most of the mount assembly can be made of aluminum or beryllium, it may be necessary to use harder high strength materials for components subjected to concentrated loads. The worst case for this kind of loading in the mount occurs at the interface of the spherical feature on a silicon shell and the flat on a tangent bar. Because the load is concentrated at a point, the Hertzian (contact) stresses, which depend on the radius of the spherical surface and the material properties, can be extremely high. For example, if a 4.45 N force is imposed on the interface, and the spherical radius varies from 2.0 mm to 7.0 mm, the resulting compressive stresses range from 1400 MPa to 600 MPa for steel components. It should be noted that the largest silicon shell will impose a total force of about 14 N on the mount system due to its weight alone, that is, neglecting any flexure preload. Harder, wear resistant materials are needed to prevent wear patterns that may develop with time due to thermal cycling. While these patterns may not upset the 5 μm position requirement because of the preload on the flexure, they would make realignment very difficult if not impossible. Dimpling or peening of the surfaces due to local yielding would cause the same problem. Materials best suited for the mount interface components include 17-4 PH and 440C stainless steels. The latter has a yield strength of about 1900 MPa and a hardness of 57 Rockwell C, whereas 17-4PH has a hardness of 44 Rockwell C. By comparison, 7075-T6 aluminum has a Brinell hardness of 150, which is roughly zero on the Rockwell C scale. Oxides such as alumina or beryllia are harder than 440C stainless, but have relatively low tensile strengths (193 MPa and 138 MPa, respectively). Under the conditions described above for the steel example, the maximum radial tensile stresses range from 277 MPa to 120 MPa. Clearly, the oxides have the greatest potential for failure in tension.

Prototype Testing At the time of the termination of the SSC, we had just begun the what was expected to be a series of prototype tests to determine certain characteristics of the adjustable tangent bar mount. Of particular interest were the mount's adjustment precision and manageability, its long term stability, and its behavior during thermal cycling. For the initial tests the mounts, which were made primarily of 7075-T6 aluminum, included various combinations of X, Y, and Z adjustments with the flat, cone

and groove tangent bar features. A cylindrical aluminum shell, similar to one of the smaller central region silicon shells in size and weight, was used to represent the silicon structure in the these tests.

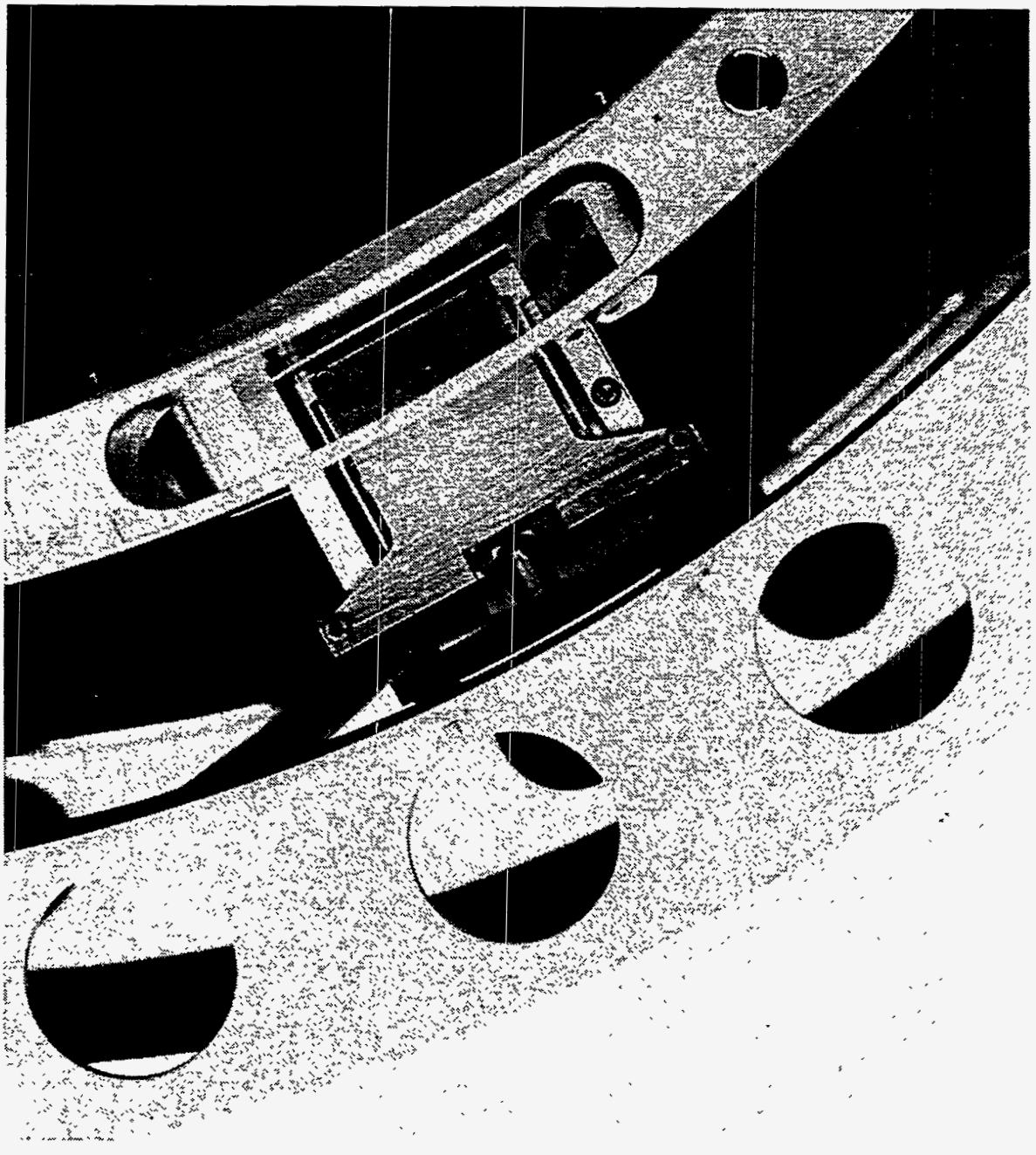

Figure 3.2.4-2 The test assembly used to evaluate the tangent bar mounts.

A photograph of the test assembly is shown in Figure 3.2.4-2. Six flexure mounts are used to support the simulated silicon shell. Targets were mounted on the aluminum shell and monitored with an array of autocollimators to establish precision of adjustment and mount stability. As we expected, very sensitive adjustments could be achieved with the independent motions provided by the mount adjustment screws. However, it was observed that the various combinations of cones, vee grooves, and flats did not provide

the desired rigid body silicon shell restraint stiffness. It didn't take much force to produce a small shift in overall position. Since we are required to maintain our placement after initial alignment to the order of 25 μm, this characteristic was indeed worrisome. Time did not permit an adequate investigation into this problem, as the initial silicon shell stability tests were consuming our personnel resources. We did obtain a measure of the thermal stability of this mount, however. The entire assembly was placed into a thermally controlled box, and monitored during temperature cycling. The autocollimators were arranged to measure drifts in the shell centroidal position. The position was monitored over repeated temperature cycles, with differential changes of 20°C. The maximum drift was 10 μm (*i.e.*, 0.5 μm/°C). Thus, the mount would have achieved our long term stability goal of 5 μm since our temperature drifts during detector operation are less than 1°C.

3.2.4.2 Carbon Fiber Fixed Mount Assembly

A conceptual design was produced for a composite material, non-adjustable mount. This mount was configured to be used in the central region as a support for the individual silicon shells. The basis for eliminating the adjustment features in the flexure mount previously discussed, was our intent to make initial alignment of the shell independent of the mount support. It was judged reasonable to hold the silicon shell in its aligned state with the large massive automated work station (see Section 3.2.5.2) permitting placement of the composite material support shell. This operation became an option when the composite support shell was reconfigured to be constructed of two co-axial assemblies. In this new concept, access for mount placement was greatly facilitated. The mount shown in Figure 3.2.4-3 requires a length correction when the desired aligned state of the silicon shell is achieved. This feature is provided by bonding the co-axial tube members of the mount while in the installed state. The mount can be removed by extracting the mechanical fastener shown; it is not necessary to debond the tubes in a confined space.

This particular mount design offers the potential for greater dimensional stability. Composite materials would be selected on the basis of their near zero CTE property. Thermal drift should not be a problem, however, some compliance in the axial direction may be needed. The silicon shell length changes in cooling down from room temperature; this contraction is controlled by the silicon wafer CTE. If it is established that the composite shell mount interface doesn't have sufficient compliance to accommodate this small motion, we would then introduce a small compliance contribution in the mount. Since this mount configuration does not have any sliding contact interfaces, as discussed above, it should provide a positive silicon shell restraint. This feature would eliminate our concern regarding extraneous loads (*e.g.*, cable loads) causing misalignments to develop.

3.2.5 Tracker Silicon Substructure Assembly

Prototype detector assemblies for the tracker's central and forward regions were to be constructed with a semi-automated, computer controlled assembly and alignment system. The primary objective of our activity in this area wass to demonstrate the feasibility of constructing bonded silicon structures that meet the most stringent placement tolerance requirement of 5 μm. The integrated system includes: a manipulator (pick-and-place machine) for handling individual silicon modules; a feed device for preparing individual modules for the manipulator; a rotary alignment fixture for supporting, indexing, and aligning the cooling rings; an adhesive dispenser; an optical alignment system; and a controller. This section describes the design and operation of the mechanical and control systems. The optical alignment system is discussed in more detail in Section 3.2.5.4 of this report.

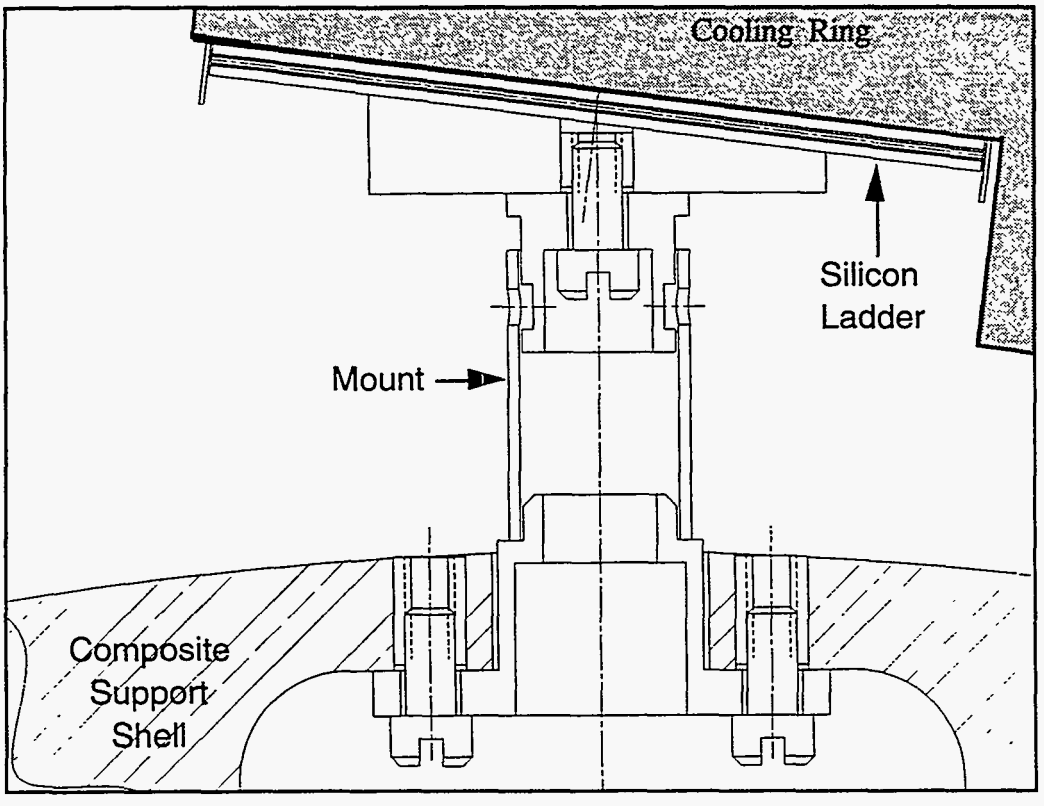

Figure 3.2.4-3 A conceptual design for a composite material, non-adjustable mount.

3.2.5.1 System Requirements

To produce a large number of very precise silicon assemblies, each constructed with numerous bond joints of consistent high quality, the assembly process is automated to the greatest extent practical. The basis for the assembly system design is the silicon shell's most stringent fabrication tolerance. In the central region, for example, the silicon detectors comprising each shell must be placed within 80 μm in the radial (R) direction, within 250 μm in the axial (Z) direction, and within 5 μm in the azimuthal (ϕ) direction. The actual azimuthal alignment requirement for the fully assembled silicon tracker is 25 μm. In order to meet that, one must allow for tolerance build-up in the many steps required to reach the fully assembled state. Therefore, the azimuthal precision in the individual steps must meet the much tighter constraint of 5 μm. While it is possible to satisfy the R and Z requirements using conventional methods, more sophisticated techniques in material handling, inspection, and alignment are needed to meet the third requirement. Commercial equipment incorporated in the assembly system overall design is selected on the basis of stability and precision. Unique or custom designs used throughout the overall design are based on established techniques and principles of precision mechanics and optomechanical design and hence the 5 μm requirement does not have a significant impact on cost.

A primary goal in the development of this system is a design that satisfies the operational requirements for the construction of both central region shells and forward region planar arrays. The design described in this section achieves that goal. In this design, all the equipment is mounted on a large optical table, and the rotary fixture, which is the component most difficult to set up and align, remains fixed for construction of

either type of structure. The other pieces of equipment are modular and can easily be repositioned and realigned when changing from one structure type to another. Figures 3.2.5-1 and 3.2.5-2 show the equipment arrangements needed to construct both types of silicon structures.

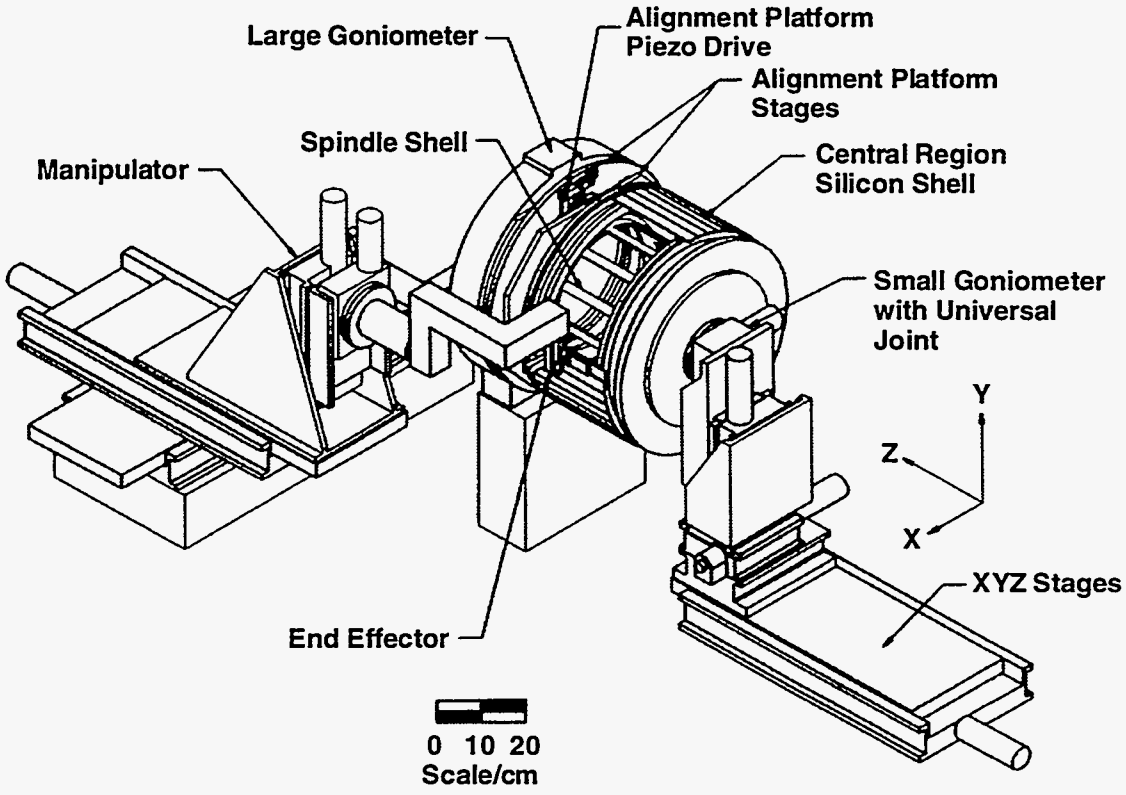

Figure 3.2.5-1 Central region silicon shell assembly arrangement.

In the following discussion, emphasis is placed on the construction of the central region silicon shells because they are the most difficult to fabricate. Although some minor variations in mechanical equipment design are necessary because of the differences in the shapes and sizes of the silicon modules, the basic construction operations are generally the same for both types of structures. The following sequence of operations outlines the construction of a typical silicon assembly:

1. manually mount and align a pair of cooling rings on the rotary fixture;
2. apply adhesive to a silicon module mounting surface on each cooling ring;
3. index, inspect, and realign rotary fixture;
4. manually place silicon module in manipulator feed device;
5. verify silicon module's orientation with respect to the manipulator end effector;
6. retrieve silicon module from the feed device with the manipulator;
7. apply adhesive activator to the silicon module;
8. position silicon module near the mounting surfaces on the cooling rings;
9. inspect and realign the silicon module with manipulator end effector;
10. place the silicon module on cooling rings;
11. repeat steps 2-10 until all modules have been attached
12. place the kinematic mount components; and
13. remove finished silicon structure.

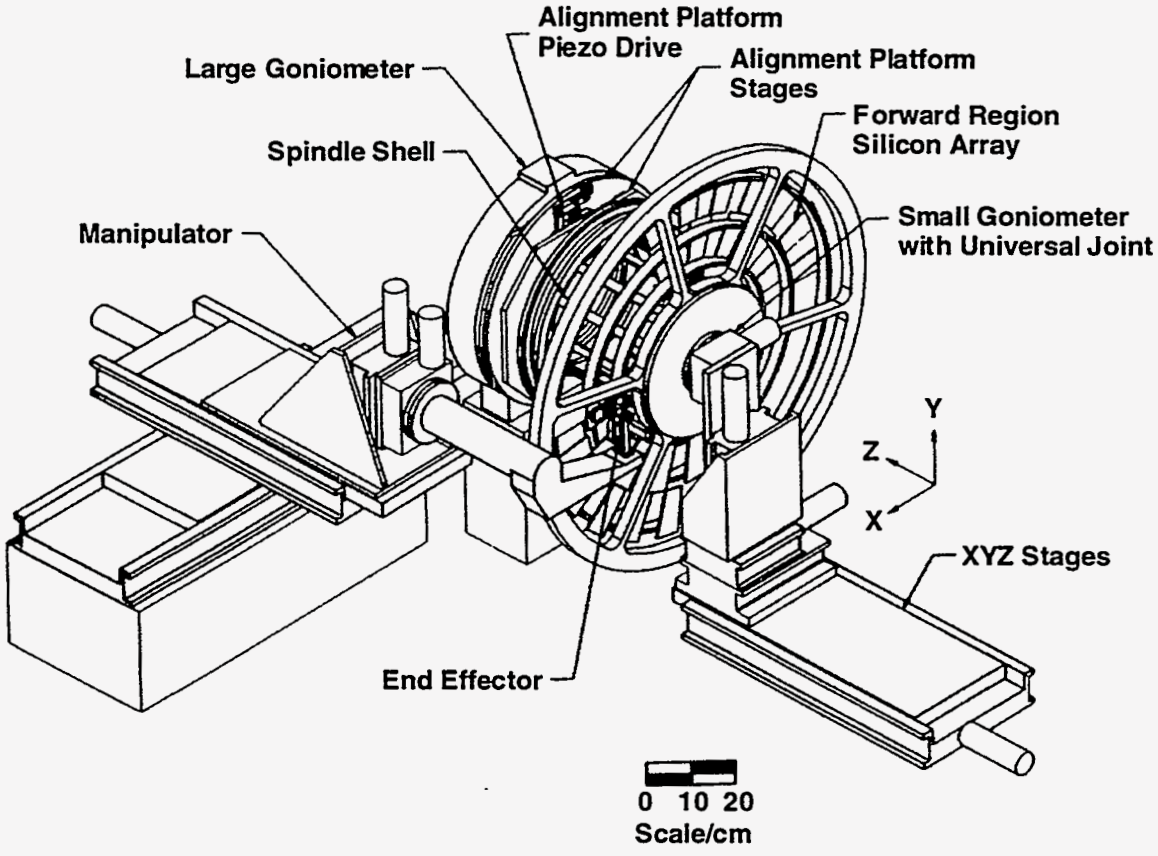

Figure 3.2.5-2 Forward region silicon array assembly arrangement.

3.2.5.2 Automated Work Station Design

The design, operation, and salient features of the major mechanical subassemblies comprising the silicon module assembly system are discussed in this section. Most of these subassemblies are identified in Figures 3.2.5-1 and 3.2.5-2. Components of the optical alignment system have been omitted for clarity. Figures showing the relationship between the optical alignment system and the mechanical assembly system can be found in Section 3.2.5.4 of this report.

Manipulator The manipulator is used primarily for the transfer of individual modules from the feed device to the cooling rings on the rotary fixture. The manipulator base unit has three translation stages and one rotary stage. Two of the translation stages are horizontal and the third is vertical, with all three stages being orthogonal to one another. Each translation stage is ball screw driven with a D.C. servomotor and includes a glass linear incremental encoder for position indication. The encoder has a line grating of 50 lines per millimeter and, when used with 128X logic, provides a resolution of 0.156 μm. Although there is no speed requirement for this application, the linear system is capable of this resolution at speeds ranging to 0.50 m/second. A fail-safe electro-mechanical brake is included on the vertical translation stage to prevent drift when the motor is deenergized. The vertical translation stage carries the rotary stage. The rotary stage in turn carries the actual manipulator arm on which the end effector is mounted. The rotary stage provides for motion in a vertical plane which is parallel to the disk surfaces during forward plane assembly. When used to assemble the central region cells, the rotary stage

provides motion in a vertical plane whose normal is parallel to the axis of the shell being assembled. This stage is a geared, D.C. servo-driven unit with a glass rotary encoder for position indication. The encoder has a resolution of 50,000 counts per revolution, or an accuracy of ±25.9 arc seconds.

Before a silicon module is placed on the cooling rings, its orientation must be verified by viewing its alignment fiducials with a pair of telescopes, which are part of the optical alignment system. If corrections are needed, they are made with the manipulator's end effector. This device, shown in Figure 3.2.5-3, is a vacuum platen mounted on three piezo-driven rotary stages. The rotary stages provide the necessary roll, pitch, and yaw motions for final alignment of the silicon module immediately before it is placed on the cooling rings. Flexures, rather than ordinary radial bearings, are used for the rotary stage pivots because they provide smooth, frictionless motion without backlash. The piezoelectric translator driving each stage can produce a maximum angular displacement of about 8.0 milliradians. This angular displacement results in linear displacements in the range of 200 to 400 μm, at the location of the alignment fiducials near the ends of the silicon module. Because of the space constraints imposed by the different equipment configurations, the end effector can be mounted in any attitude with the vacuum platen in either of two orientations relative to the rotary stage subassembly. For example, when placing silicon modules on the inside of the cooling rings during the construction of a central region shell, both the rotary stage subassembly and the vacuum platen must be in the horizontal attitude to fit inside the rotary fixture that holds the cooling ring. When placing silicon modules on the outside of a shell, or on either side of a forward region array, the rotary stage subassembly must be in the vertical attitude with the vacuum platen in the horizontal orientation. This configuration is necessary because the space between the rotary fixture and the alignment telescope is limited by the telescope's focal length. Other access limitations make it necessary to use several interchangeable manipulator arms for the construction of the different silicon structures.

Silicon Module Feed Individual silicon modules are prepared for transfer to the manipulator by a manually loaded feed device. For the manipulator to receive the module in the proper orientation, that is, within the range of motion of the end effector, the module must first be accurately positioned. After a module is placed on a vacuum platen in the feed mechanism, it is transferred to a location under an inspection device to determine its orientation. If alignment is needed, the vacuum platen is repositioned by a set of piezoelectric translators; then, it is returned to its initial loading position where the silicon module can be picked up by the manipulator. While this module is being placed on the cooling rings by the manipulator, the loading and alignment process can be repeated with a new module. The piezoelectric translators for the vacuum platen are arranged to produce both linear and rotary alignment motions. The vacuum platen and piezoelectric translators are mounted on a translation stage similar to the ones used for the manipulator base unit. Several position inspection devices for determining the orientation of the module in the feed device are being considered for this application.

Rotary Fixture The rotary fixture serves not only as a mount for cooling rings and structural rings for both the central and forward region silicon structures, it also performs the incremental indexing function during construction of these components, and it provides a means of actively compensating for runout errors. Three major subassemblies comprise the rotary fixture; they include a spindle, an alignment platform, and a rotary bearing set. The relationship of these subassemblies is shown in Figure 3.2.5-1.

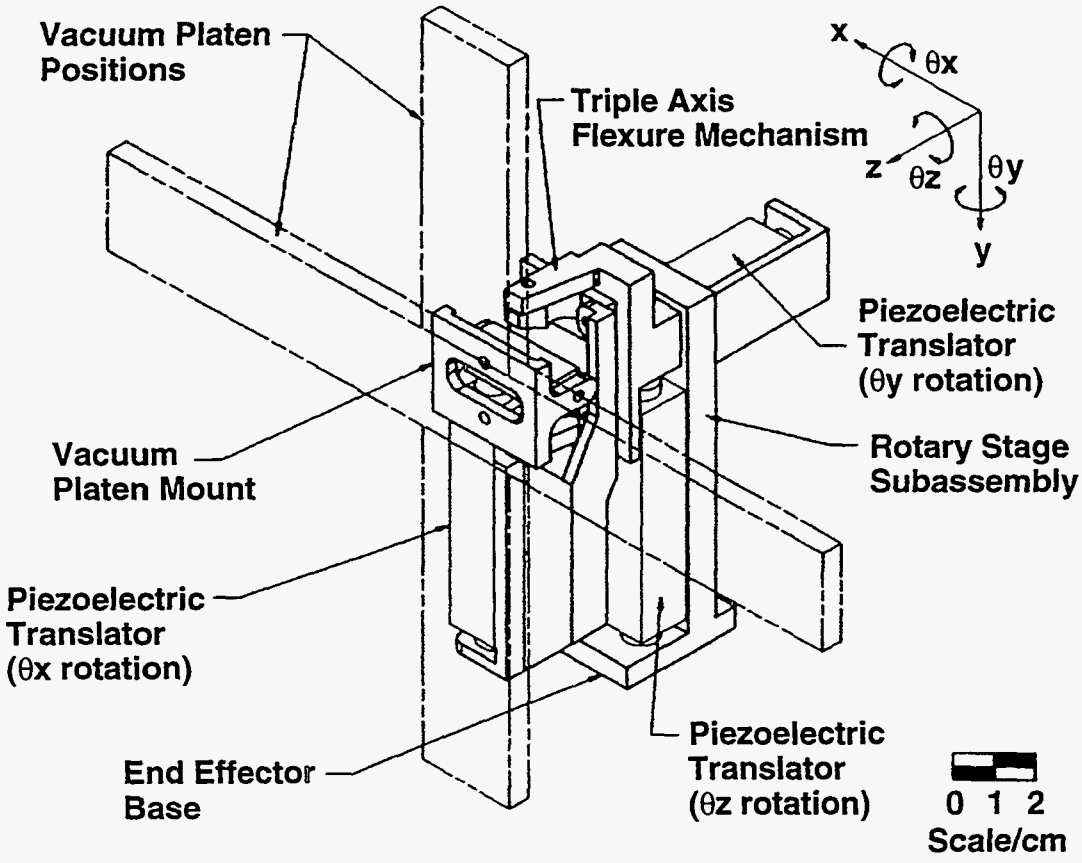

Figure 3.2.5-3 Manipulator end effector.

When configured to assemble the shells for the central region, the rotary bearing set is composed of a pair of precision single-circle goniometers that supports the spindle assembly and the alignment platform. The primary bearing in the set is a large goniometer with a 400 mm diameter bore. This bore is the manipulator access to the inside surfaces of a pair cooling rings for a central region shell mounted on the spindle, with the shell and spindle axes coinciding. One of the two stages of the alignment platform is mounted on the rotating ring of this goniometer, and the second stage is attached to the large open end of the spindle. The other end of the spindle is supported by a much smaller goniometer. A D.C. servo motor drives the rotating ring of the large goniometer, alignment platform, and spindle as a unit. Angular position of the entire assembly is indicated by the output from a glass incremental rotary encoder. The small goniometer is mounted on a set of XYZ translation stages, similar to those used for the manipulator base unit, so that small lateral (X) and vertical (Y) adjustments can be made during the initial alignment of the system. The Z, or axial stage has a much longer stroke, and is used to remove a silicon structure from the spindle when it is finished. This procedure is described below, immediately before Section 3.2.5.3.

The small goniometer has an 80 mm diameter bore for on-axis mounting of a small sphere used for establishing the optical reference axis for the spindle alignment system (Section 3.2.5.4). Another sphere, which is also a part of this alignment system, is mounted on the second stage of the alignment platform at the other end of the spindle. While a silicon module is being placed on the inside of the cooling rings, this sphere, which is mounted on a short lever arm, is stored between the alignment platform stages outside the bore of the spindle. After the module has been placed, and the spindle

indexed, its alignment is checked by pivoting the sphere into position at the center of the spindle bore and observing the resulting fringe pattern from the reference laser beam. Realignment is done with the alignment platform described in the next paragraph. To ensure that the sphere insertion into the bore is repeatable with a high degree of accuracy, the lever arm to which it is mounted, is pulled against a fixed stop by a linear spring motor. The lever arm is pivoted back to its storage position by a small power screw driven by a miniature D.C. servo motor. Since the precise location of the sphere in the bore of the spindle is determined by the fixed stop alone, the rest of the mechanism can be fairly imprecise.

Radial deviation (runout) of the small goniometer is predicted to be less than ± 5 μm, but that of the large one may be as much as 10 μm. To permit active realignment of the spindle's axis, the end of the spindle supported by the small goniometer is coupled to the goniometer's rotating ring with a flexure pivot universal joint. This allows the spindle's axis to be pivoted slightly about the universal joint's two orthogonal axes by moving the opposite end of the spindle. The two-stage alignment platform mounted on the large goniometer's rotating ring serves this purpose. Geometrically, the platform is a short, truncated pyramid structure with its stages mounted in tandem (*i.e.*, one stage carried by the other, and coupled by links with flexure pivots). The stages move orthogonally in much the same way as a set of conventional XY stages. The links connecting one stage to another lie in two planes that form opposite faces of the pyramid, with their virtual line of intersection on one axis of the spindle's universal joint. Thus, when a lateral force is applied to a stage, its motion is very nearly linear for small angular displacements of the links. In this application, the lateral displacements are approximately ± 1.00 millimeters. The motive force is applied to a stage through a mechanism that provides a mechanical advantage of more than 15 to 1. The actuator for this motion is a commercial, long stroke piezoelectric translator. Although this device has a load capacity of only 1.5 kg when used alone, it is capable of moving a 23 kg payload in this instance because of the mechanical advantage. This is important because the actuator must be capable of reacting gravity loads of mechanical components in the platform/spindle assembly. Resolution of the translator, which is expected to be about 4 nanometers, is more than adequate for this application. Overall compliance of the mechanism is estimated to be less than 5 μm for a design payload of 16 kg. Because flexures, rather than conventional radial bearings, are used throughout the spindle and alignment platform assembly, the entire mechanism is frictionless and free of backlash.

Since the spindle must have some structural continuity over its length in order to support a silicon shell, and at the same time provide access for placement of silicon modules on the cooling rings' inner diameters, a cage-like structure is needed. Even though the number of longitudinal webs in this structure is minimized, some of the internal silicon modules cannot be placed because the surfaces to which they are to be attached are obscured by the webs. After modules have been placed on all the accessible inner surfaces on the cooling rings, the partially completed silicon shell must be rotated, relative to the spindle shell, to expose the unused surfaces. This concept is implemented by mounting a narrow rotary table on a set of large bore bearings at each end of the spindle. These tables carry backing rings to which the individual cooling rings are mounted. The rotary tables are initially locked to the spindle shell while all the accessible surfaces are covered with silicon modules, then unlocked so the partially completed shell can be indexed to expose the remaining surfaces. Two spindle shell sizes are needed to construct all four central region shells because the smallest shell's inside diameter is not large enough to accept the manipulator arm needed for constructing the larger silicon shells.

Before construction of a central region shell can begin, the individual cooling rings must be mounted on rigid backing rings to facilitate handling and alignment on the spindle shell. A set of studs, bonded to a cooling ring wall, are clamped by small fixtures attached to the backing ring. After the cooling rings are clamped in place, the backing

rings are mounted on the spindle shell's rotary tables. The cooling ring is centered on the spindle by manipulating the backing ring with three micrometer heads attached to the rotary table which are removed after this alignment is finished. Azimuthal, or "clocking" alignment of the cooling rings is done with the rotary tables.

Adhesive Dispenser To date, only limited design work has been done on the adhesive dispensing problem. It is apparent, however, that a method of applying a high viscosity adhesive to the cooling ring surfaces, or to the silicon modules, in precisely controlled amounts, is required. Either a single, or a two component adhesive system, with adhesive and activator, could be used. A single part system has the advantage that the adhesive would have to be applied only to the silicon module immediately before it is placed on the cooling rings. In contrast, a two part system also requires that the activator be applied to the cooling ring surfaces (or vice versa), a process that further complicates the assembly procedure because additional application equipment with more complex software is needed. If a two part system is necessary, it would be advantageous to use a manipulator which incorporates both an adhesive dispensing head and a vacuum platen end effector. The two part adhesive system does have the advantage that one has essentially an infinite amount of time for manipulation of the parts before the bond is made.

Placement of Kinematic Mount Parts Only preconceptual work has been done on the placement of kinematic mount parts. If the kinematic mounts on the graphite composite shell are adjustable tangent bars on which the silicon shells are supported, as described in Section 3.2.4, the support points on the silicon shell structure can be a simple hemispheres bonded to the beryllium layer on the appropriate silicon modules. Since the tangent bar is adjustable, the placement tolerances can be relatively liberal, and the six hemispheres can be placed manually with simple fixtures and micrometer heads temporarily mounted on the spindle shell's rotary tables.

Silicon Structure Removal Before a completed silicon structure can be removed from the rotary fixture, it must first be stabilized to prevent rotation about its axis. A spider ring, rigidly fixed to the small goniometer base, is coupled to the backing ring to which the nearest cooling ring is mounted. The cooling ring at the opposite end of the silicon structure is then released from its backing ring by releasing the stud clamping fixtures. Next several fasteners, which join the small goniometer and the nearest backing ring to the spindle shell, are removed. At this point in the removal process, the silicon structure, still attached to one backing ring, is supported by the spider ring in a cantilever manner. The entire assembly can then be transferred in the axial direction, by the small goniometer's Z translation stage, until it clears the spindle shell. In the fully retracted position the silicon structure can be manually removed from the backing ring.

3.2.5.3 Control System Description

The control system for the silicon module detector assembly system is a PC based controller with capabilities to control 16 axes of motion driven by servo motors, two axes of long stroke piezoelectric translators, and three axes of short stroke piezoelectric translators. Several axes are under closed-loop control with closed-circuit TV cameras, position sensitive devices (PSD), fiber optic probes, and laser interferometers acting as the position sensors. The system also controls the vacuum service for the platens on the manipulator end effector and silicon module feed device, as well as the pneumatic service for the adhesive dispenser. Diagnostic data is transmitted to a microcomputer that serves as a data logging, graphing, archiving, and trending device using commercial software. Figure 3.2.5-4 is a block diagram of the control system.

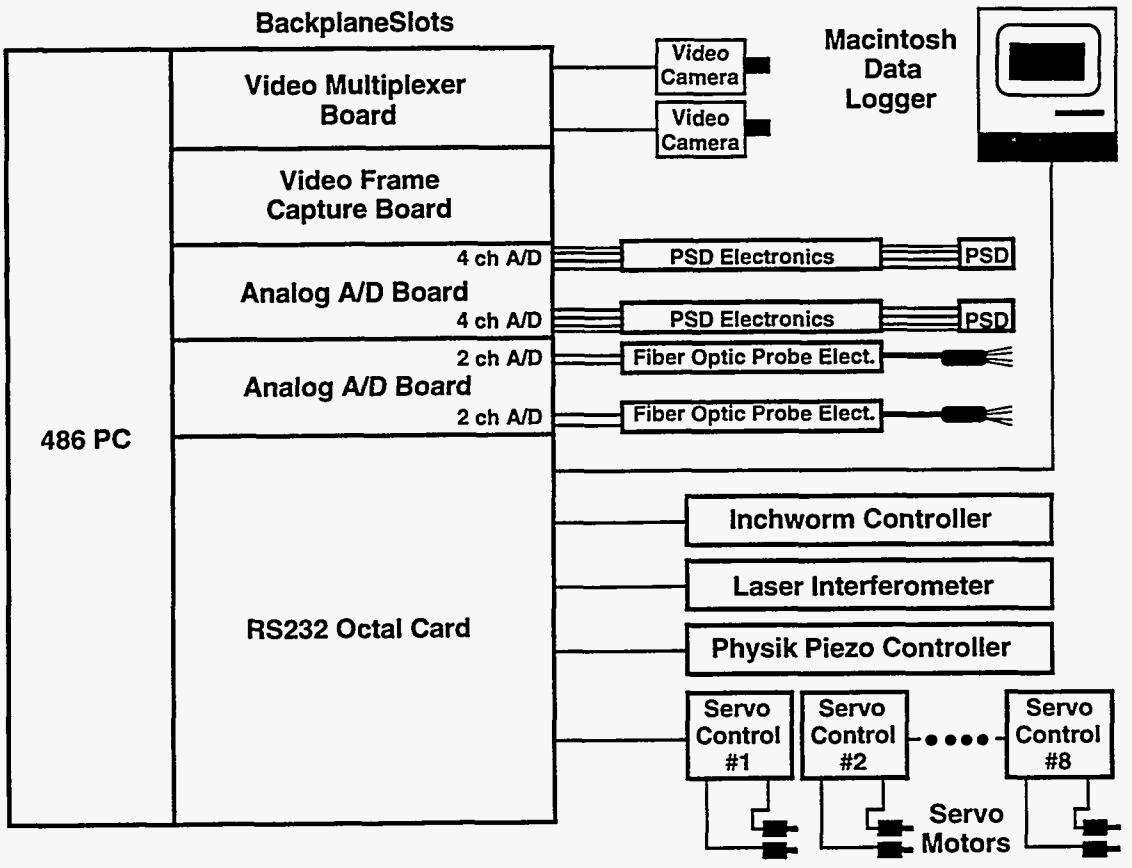

Figure 3.2.5-4 Control system block diagram.

Actuator Controllers Control for all 16 servo motors is over one RS232C interface channel. The commercial controllers are capable of interpolation of encoder data to obtain resolutions of 0.156 μm. Velocity and acceleration profiling is also possible. The discrete input/output capability of the controller is used for limit switch inputs and electronic fail-safe brake control on some of the axes.

All three axes of the short stroke piezoelectric actuators on the manipulator end effector receive motion commands, via one RS232C interface channel, from a commercial controller. Similarly, the two long stroke piezoelectric actuators for the alignment platform's axes are controlled by another commercial controller, over a single RS232C interface channel. All five piezo-driven axes are under closed-loop control.

Sensors At least two channels of video, using a commercial frame capture board located on the PC backplane, are used in the precision position feedback. A computer controlled video multiplexer is located in an adjacent slot on the PC backplane so that multiple channels of video require only one frame capture board. Sub-micron position information is extracted from the video using centroid finding algorithms. This type of position sensing is particularly useful for positioning based on distinctive features of an object, such as the corners of the silicon module, or the fiducials on the module.

Position sensitive devices (PSD) are similar to quad cells in that they develop a voltage that is proportional to the position of a laser beam impinging on its surface. The major disadvantage of the quad cell is that the beam must cover a portion of all four quadrants to produce accurate results. In contrast, the PSD has no such requirement, so the beam can be located anywhere on its surface and does not have to be close to the center of the device. The only requirement is that the beam strike the surface of the PSD.

Another advantage of the PSD is that it is capable of sub-micron resolution. Output from the PSD is amplified and processed with an electronic analog processor, and the result read by the PC controller through a 16 bit A/D converter located on the backplane of the computer.

The fiber optic probe is a new technology applied to the measurement of displacements in the sub-micron range. Output voltage of the device is proportional to the distance between the surface of an object and the tip of the probe. The voltage is read by the PC controller through a 16 bit A/D converter located on the backplane of the computer. Long term stability of the assembly system is measured with a laser interferometer capable of measuring distances with sub-micron resolution. Three channels of the interferometer are read by the PC controller over a single RS232C interface channel.

Software Software for the controller is a DOS based program written in the 'C' language with a graphical user interface. A control library for each of the devices served by the PC is written in such a manner that the actual machine control algorithm can be understood by programmers unfamiliar with the 'C' language. The controller is also capable of individual control and data logging from each device.

The data logger is connected to the PC controller through an RS232 channel, or through a dedicated PC interface line. The computer can display plots of real time data or recall previous data that has been recorded to disk. Data logger operation is independent of the PC controller.

3.2.5.4 Optical Reference System

The most important goal of our assembly procedure, and the reason we have gone to all the expense and effort to build an automated assembly system, was to be able to precisely and repetively place large numbers of silicon ladders onto the cooling rings with the high precision required for the triggering capability of the SDC detector. The philosophy of the general procedure is described in detail in Sections 3.2.5-1 and 3.2.5-2.. Briefly, the method is to center two cooling rings on the axis of rotation of two goniometers, establish a reference line between the goniometer centers, and then precisely position two microscopes to view the fixed reference points with which the fiducials on the ladder assemblies are aligned as the ladders are bonded to the cooling rings. An imaginary line between the ladder fiducials must be precisely parallel to an imaginary line between the goniometer centers. We call the concept and technique to establish a stable reference line between the goniometers centers and place the microscopes in the proper places to view the ladder fiducials the optical reference system.

Making a straight and stable reference line is not trivial, because even with the best commercial alignment telescopes, racking the telescope focus to mark a line of sight causes the line to wander more than the tolerances allowed for in assembly. As such, we propose a new concept for the alignment system. The layout to be used is shown in Figure 3.2.5-5. The first step is to center and attach the cooling rings to backing plates that are used later to hold the cooling rings onto the goniometers. Because the cooling rings cannot be manufactured with great precision, it is not possible to define their exact center. It turns out that this is not important. It is important, however, to define a reasonable center and to be able to precisely find that center again at a later time. We intend to find a reasonable center by mechanical and optical techniques and attach an arm to the back up plate that places a tooling ball at the center we define. The center of the tooling ball can be easily relocated with a lens and an autocollimator setup to approximately 0.5 μm at any later time. Next, we attach the cooling ring to the small goniometer, and locate the cooling ring tooling ball on the goniometer axis of rotation. We used this technique earlier to measured the small goniometer radial runout, which is less than ±3 μm. Next, we will remove the ball from the axis of rotation and position the

end of a 50 μm diameter optical fiber there. In the first pass, none of these steps needs to be done with great precision, but it is possible to do so and higher precision will be required in subsequent passes in later assembly steps. The fiber end on the axis of rotation of the small goniometer defines one point on the optical reference line.

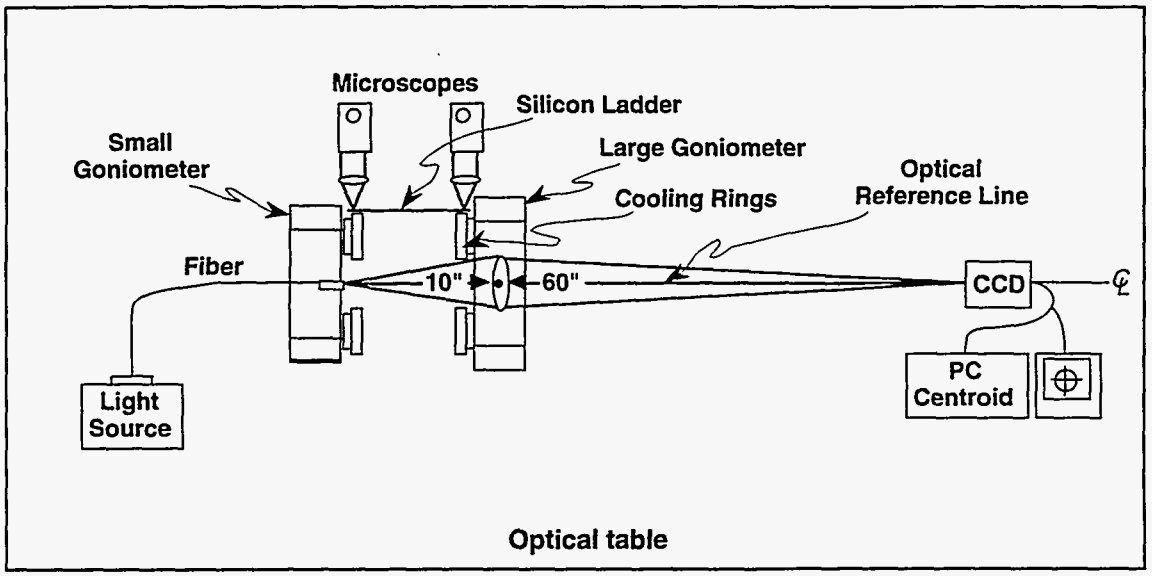

Figure 3.2.5-5 The layout of the present optical reference concept, used to align and place the detector modules precisely on the silicon shells.

The second point for the optical reference axis is established in a similar way. We first define a center for the second cooling ring, using the same method as before, but this time we will center a lens of the proper focal length on the defined cooling ring center. This can be done with the precision air bearing rotary stage we have in our laboratory. The cooling ring, with centered lens attached, is then placed onto the large goniometer and positioned to give the minimum radial runout using the 3 point system of the fiber, lens, CCD camera. The light source is of course, light from the fiber in the small goniometer. A CCD camera detector is placed at the image point of the fiber end formed by the lens in the large goniometer. When the lens is positioned for minimum runout the cooling ring is centered on the large goniometer mean rotation axis (*i.e.*, the axis has a runout of about ± 10 μm). The CCD camera in the image plane is centered on the fiber image and the pixel position is recorded. Now the fiber end, the lens, and the recorded position on the CCD camera all lie on a line, which we call the optical reference line. If either the fiber source or the lens moves the CCD camera senses the position change.

There are several advantages to this approach: 1) since the lens in the large goniometer magmifies the positioning error by about a factor of 6, the large goniometer runout is removed with high precision; and 2) of the small goniometer runout, which already is only ± 3 μm, about 90% is removed without having to correct for it; because, when the source moves due to the small goniometer runout, the large goniometer will be recentered to compensate. The new line of sight will be slightly displaced, but nearly parallel to the original line of sight. The important parameter, the direction of the line of sight, is maintained with high precision. We estimate that the sensitivity of the arrangement is better than 1 μm. We can sense a 0.1 pixel error on the CCD with a good centroid program, which corresponds to about 2 μm of image displacement, Since the optical set up has a magnification of 6, the corresponding lens displacement is 0.3 μm.

The next task is to place the telescopes in the proper position. A fiber and lens will be used to form an image point a specified distance from the line of sight, at the

mechanical position where one of the ladder fiducials is to be located when they are bonded into position. The first microscope is positioned on this image point. The cart with the fiber and lens is then moved along the line of sight to the second fiducial position to position the second microscope. When positioning the second microscope, the cart holding the fiber and lens must be placed precisely on the optical line of sight and tilted in exactly the same orientation as it was when the first microscope was positioned. This is a bit tricky, but it can be done with high precision using two afocal optical systems attached to the cart. The optical systems are shown in Figure 3.2.5-6. One system is sensitive to tilt and the other to displacement from the line of sight. The cart to position the fiber and lens on the line of sight carries a 5 axis PZT controlled platform to precisely position the fiber lens system used for microscope placement. We expect positioning errors can be sensed and corrected with micron precision.

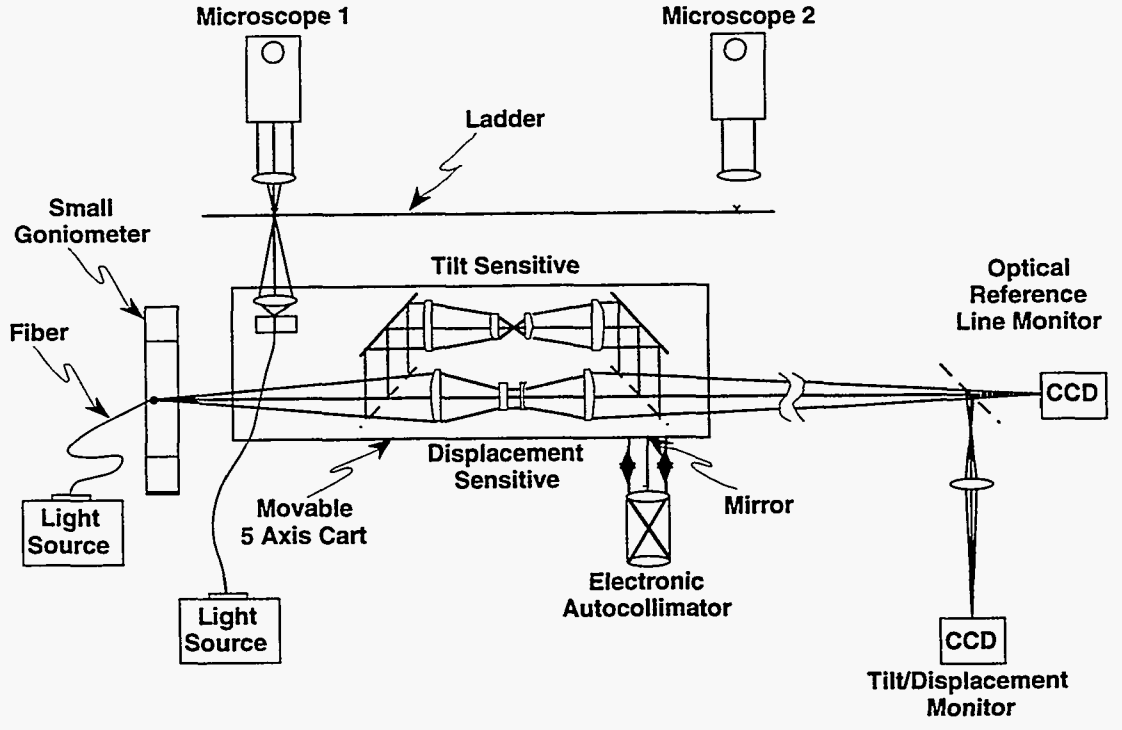

Figure 3.2.5-6 The two afocal optical systems to be used in establishing the location of the second microscope.

The bulk of the work in this area remains to be done as the above discussion deals largely with concepts that we have developed, but remain to be proven. Our intent is to prove those concepts in the remainder of FY 94 using SSC close-out funding. In addition, there are many other real alignment/assembly problems, such as, how to build a continuous monitoring system for the reference telescopes, how to move the microscopes to place ladders on the outside layer after they are set up for placement of the inside layer, and how to assemble several subsystems together with high precision.

3.3 Stability Verification

3.3.1 TV Holography Measurement System

Early in the silicon tracker design process we realized the shape stability of structures would be an important detector issue. After a search for a sensitive stability measurement technique, we decided on TV holography (TVH), which proved to be a useful tool to verify the mechanical stability and dynamic characteristics of many prototype structures. TVH is a noncontact, full field-of-view interferometric method, for measuring mechanical part shape changes caused by a variety of effects including thermal heating and mechanical stress. Interesting dynamic characteristics of mechanical systems, such as mode shapes and mode frequencies, are also determined by TVH. Often, a stated goal of stability testing is to compare predictions from finite element models (FEM) used for design, with the properties of mechanical prototypes. Because TVH provides full field-of-view, "real time" (TV frame rate) measurements with sub-micron sensitivity, it often shows features that were not predicted by the FEM. The differences between models and test results lead to better understanding, ideas for improved designs, and better modeling techniques.

Research in TVH systems has been conducted since the 1970's, but faster, smaller computers and a phase shifting technique for directly evaluating speckle intensity patterns, make TVH in the 1990's, a very useful measurement tool for many applications. The present trend in TVH system development is to build smaller systems for use outside controlled laboratory environments, and to develop more robust algorithms to quickly calculate and display surface shape changes. The newest systems use fiber optics and laser diodes. They measure 3D shape changes, in-plane or out-of-plane shape change components, as well as, absolute shape, stress profiles and dynamic characteristics. The system used at Los Alamos for SSC testing was adequate to answer many questions about silicon tracker design and stability, but it had only a modest capability compared to the systems now being developed. Since future detectors for high energy physics experiments will likely have to meet difficult stability requirements, improved TVH systems could play a useful role in determining if the stability requirements are indeed met, and in helping to identify satisfactory detector designs.

3.3.1.1 Basic Principles

A typical TVH system layout is shown in Figure 3.3.1-1. We use a 25 mW He/Ne laser that is split into 2 beams. One beam, called the reference beam, is reflected from a mirror mounted on a piezoelectric pusher and then expanded and directed toward the CCD camera. The other beam is expanded and directed toward the object, which scatters light into the CCD camera. The zoom lens on the CCD camera images the object. A measurement typically involves collecting and processing eight frames of camera data. Four frames are gathered from the object in an initial or "start" state. The other four frames are collected after the object is deformed. In each state, four frames are gathered sequentially. Between each frame in the four frame set, the piezoelectric pusher in the reference beam is moved to change the path length by a quarter wavelength of light. This is called phase stepping. Processed information is sent to the TV monitor, which displays fringes representing the shape change caused by the load. The fringe pattern is superimposed over the image of the object. Modern image processors can process and display the data at the TV frame rate. Shape changes that are slow compared to TV frame rates are observed in "real time".

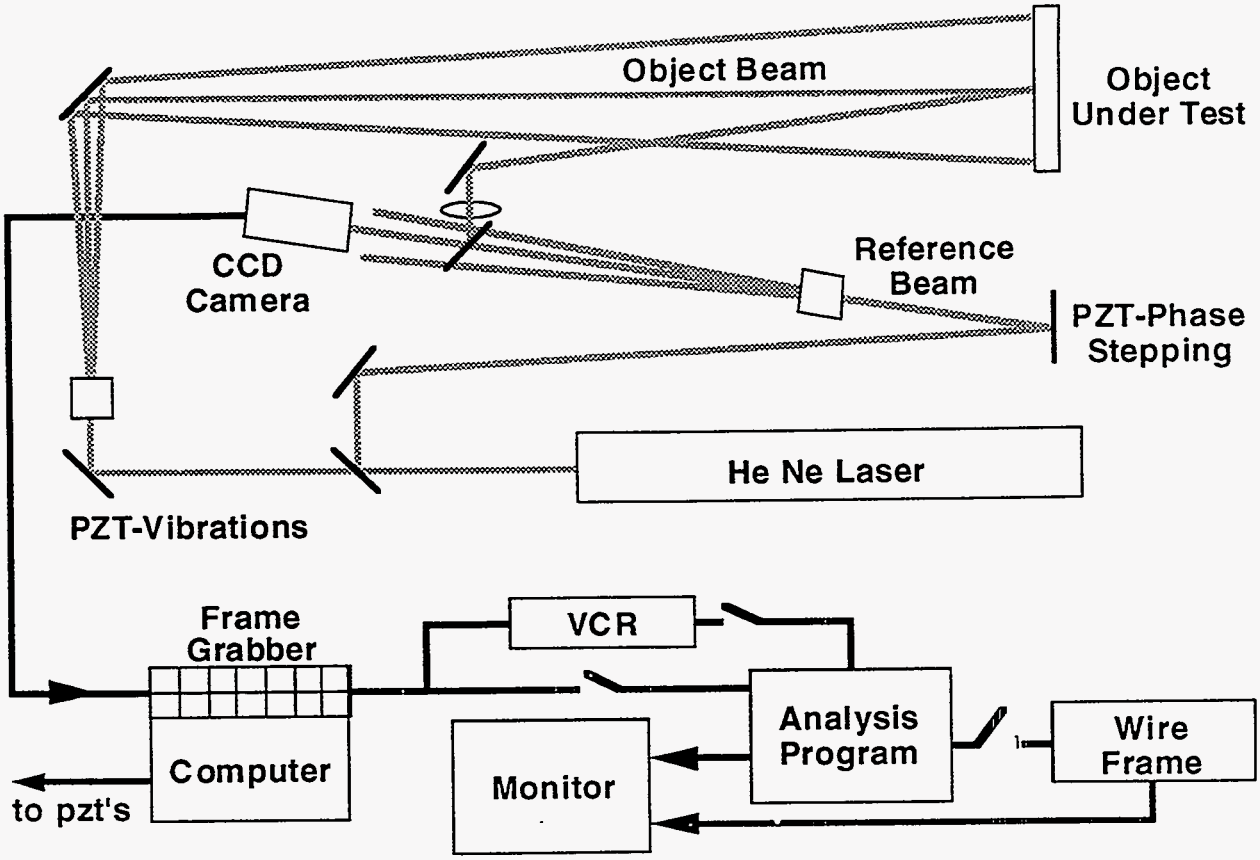

Figure 3.3.1-1 A typical TVH system layout.

For the object "start" state, the i^{th} frame intensity at each CCD camera pixel locations is described by the equation for two beam interference:

$$I_i(x_p,y_p) = I_o + I_r + 2\sqrt{I_o I_r}\cos[\phi_o - \phi_r].$$

The o and r subscripts refer to the object and reference beams, the pair (x_p,y_p) refers to the location of pixel p. The optical phases ϕ_o and ϕ_r are proportional to the path lengths of the object and reference beams from the first beam splitter to the CCD camera. After the part deforms, the pixel intensity for the j^{th} frame is given by:

$$I_j'(x_p,y_p) = I_o + I_r + 2\sqrt{I_o I_r}\cos[(\phi_o + \Omega) - \phi_r].$$

The phase shift Ω is related to the optical path length change caused by part deformation; Ω contains the shape change information. The phase Ω is separated from the three other unknowns, I_o, I_r, and $[\phi_o - \phi_r]$, by phase stepping the piezoelectric pusher in the reference beam between each frame, with phase steps of 0, $\pi/2$, π, and $3\pi/2$. The four frame intensities for the "start" state are given by,

$$I_1(x_p,y_p) = I_o + I_r + 2\sqrt{I_o I_r}\cos[\phi_o - \phi_r].$$
$$I_2(x_p,y_p) = I_o + I_r + 2\sqrt{I_o I_r}\cos[\phi_o - \phi_r - \pi/2]$$
$$I_3(x_p,y_p) = I_o + I_r + 2\sqrt{I_o I_r}\cos[\phi_o - \phi_r - \pi]$$
$$I_4(x_p,y_p) = I_o + I_r + 2\sqrt{I_o I_r}\cos[\phi_o - \phi_r - 3\pi/2]$$

After the object moves, the four frame intensities are:

$$I_1'(x_p,y_p) = I_o + I_r + 2\sqrt{I_o I_r}\cos[\phi_o - \phi_r + \Omega]$$

$$I_2'(x_p,y_p) = I_o + I_r + 2\sqrt{I_o I_r}\cos[\phi_o - \phi_r + \Omega - \pi/2]$$

$$I_3'(x_p,y_p) = I_o + I_r + 2\sqrt{I_o I_r}\cos[\phi_o - \phi_r + \Omega - \pi]$$

$$I_4'(x_p,y_p) = I_o + I_r + 2\sqrt{I_o I_r}\cos[\phi_o - \phi_r + \Omega - 3\pi/2]$$

If $D_1 = (I_1 - I_3) + (I_1' - I_3')$ and $D_2 = (I_2 - I_4) + (I_2' - I_4')$,
then the monitor display:

$$D_1^2 + D_2^2 = 32 I_o I_r (1 + \cos[\Omega]),$$

shows fringes draped over the object. More frame grabber arithmetic leads to an expression for Ω. The arithmetic is easy. Let

$$N_1 = (I_1 - I_3) + (I_2' - I_4') \qquad D_1 = (I_1 - I_3) + (I_1' - I_3')$$
$$N_2 = (I_2 - I_4) - (I_1' - I_3') \qquad D_2 = (I_2 - I_4) + (I_2' - I_4')$$
$$N_3 = (I_1 - I_3) - (I_2' - I_4') \qquad D_3 = (I_1 - I_3) - (I_1' - I_3')$$
$$N_4 = (I_2 - I_4) + (I_1' - I_3') \qquad D_4 = (I_2 - I_4) - (I_2' - I_4')$$

and let

$$N = (N_1^2 + N_2^2) - (N_3^2 + N_4^2) = 64\, I_o I_r \sin[\Omega]$$

$$D = (D_1^2 + D_2^2) - (D_3^2 + D_4^2) = 64\, I_o I_r \cos[\Omega]$$

then,

$$\Omega = \mathrm{atan}[N/D]$$

Once Ω is known, the shape change between the deformed and the reference state of the object is calculated. The arctangent calculation of Ω provides information modulo 2π, which is called phase wrapped data. Finding and taking out the 2π phase jumps is called phase unwrapping. Unwrapping would be simple if the data were clean, but scattered laser light has speckle noise, which makes unwrapping difficult; however, recently developed unwrapping algorithms have quite good noise immunity.

3.3.1.2 Static Measurements

Figure 3.3.1-2 shows the mechanical fixture used to test prototype silicon ladder assemblies. The ladders were made from four pieces of engineering grade silicon 34 mm wide. The four 60-mm long silicon pieces are butt bonded together to make a ladder 240 mm long by 34 mm wide and 300 μm thick. Down the length of each long side of the ladder, 4 mm wide and 200 μm thick graphite epoxy strips are bonded to the silicon to stiffen the part. For one of our tests, a ladder is bonded to the top and bottom sides of two graphite blocks, and this assembly is mounted to precision rotation and translation stages. With this mechanical arrangement the ladder assembly can be twisted, buckled, or hand heated. The results are shown in Figure 3.3.1-3. Each fringe spacing corresponds to approximately $\lambda/2 = 0.32$ μm of shape change. We say approximately, because there are small angle cosine effects that we did not consider. An important aspect of the technique is that large shape changes can be measured by bootstrapping; that is, the shape shown is saved, fringes are cleared and the old deformed state is made the new "start" state, then the part is further deformed until a similar number of new fringes again appear. At the end of any number of these bootstrapping steps, the total displacement is determined by adding the fringes from all the different deformation steps. In principle, the number of new "start" states can be arbitrarily large, corresponding to arbitrarily large shape changes.

One conclusion of our measurements is that in static and dynamic tests, ladders behave as one continuous piece of silicon, even though they are constructed of smaller silicon pieces bonded together with adhesive. We have not seen any fringe discontinuity at the bond joints in any of our testing.

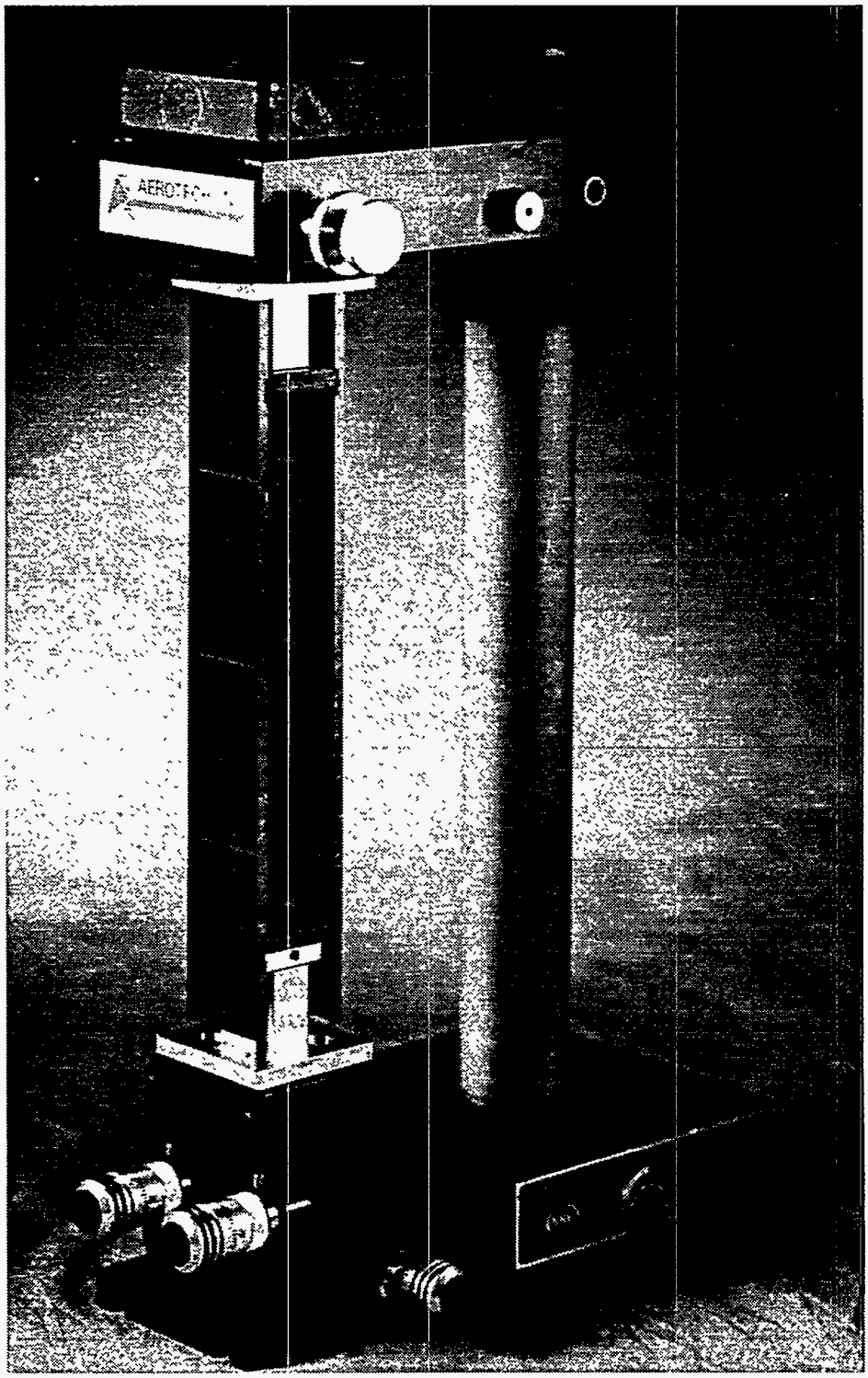

Figure 3.3.1-2 Mechanical fixture used to test prototype silicon ladder assemblies.

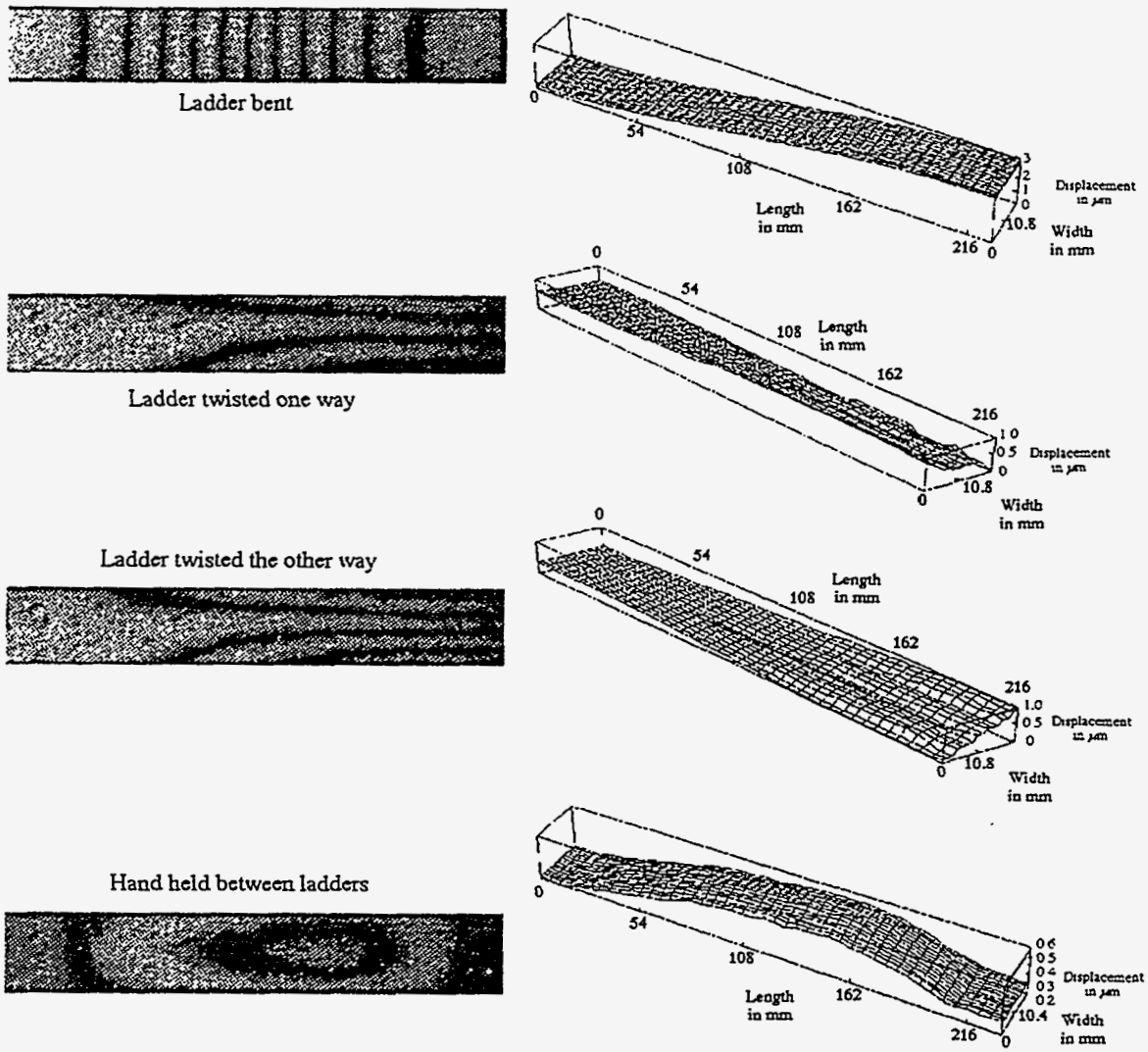

Figure 3.3.1-3 Results showing the effects of twisting, buckling, and hand heating a silicon ladder assembly.

We use a simple row-column technique and a custom *Mathematica* program to unwrap the fringe data and plot wire frames showing actual distortions. Streaks in the wire frames often occur with the simple algorithm used, which is well known to be sensitive to noise. We are working on better algorithms to unwrap fringe data. We expect that the image processing toolbox in *MathLab* will be a better platform than *Mathematica* for programming and experimenting with unwrapping algorithms. At least in the *PC Windows* version of *Mathematica* we had trouble processing large arrays of data. This may change when the *MathLink* option, which is now undergoing beta-testing, becomes available. Real time processing and fast unwrapping algorithms are also possible using a Datacube image processing system. The Datacube system was not available to us when we built our first TVH system, but this is the direction we intend to pursue with SSC close-out funds.

3.3.1.4 Dynamic Measurements

A technique called time average holography is used to display mode shapes of vibrating parts. Four phase shifted frames of data are needed to display mode shapes on the TV monitor. In time average holography, the phase Ω, which contains the mode shape information, is a function of time and position. For example, for a cantilever beam vibrating at a frequency ω,

$\Omega[x,t] = 2kD[x]cos[\omega t]$,

where $D[x]$ is the maximum displacement amplitude at position x, from the cantilever base. At each CCD pixel the intensity is given by:

$I[x,t] = I_o + I_r + 2\sqrt{I_o I_r}cos[\phi_o - \phi_r + 2kD[x]cos[\omega t]]$

If the camera frame time is much longer than the cantilever oscillation period, a camera frame records a time average of the intensity which is given by:

$\langle I[x,t] \rangle = I_o + I_r + 2\sqrt{I_o I_r}cos[\phi_o - \phi_r] J_o^2[2kD[x]] \equiv I_j$

where J_0 is the 0-order Bessel function. Four phase shifted frames (I_j) are collected and processed according to:

$(I_1 - I_3)^2 + (I_2 - I_4)^2 = 16 I_o I_r J_o^2[2kD[x]]]$

When the processed information is displayed on the TV monitor, the fringes shown are a contour map of the mode shape for the vibrating part. Fringe pattern mode shapes for a vibrating silicon ladder, supported near both ends are shown in Figure 3.3.1-4.

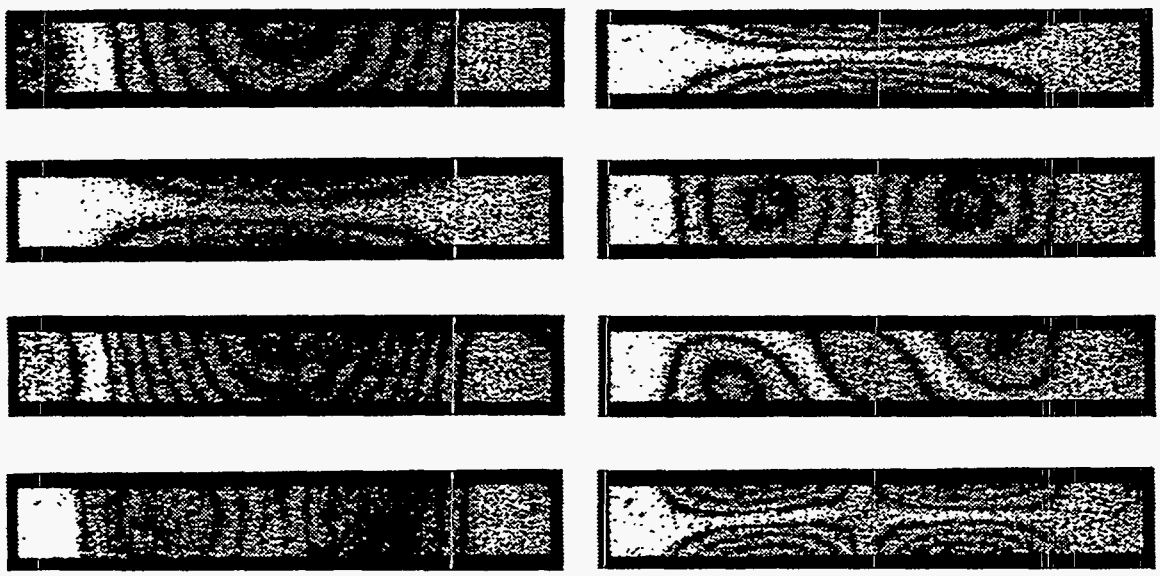

Figure 3.3.1-4 Fringe patterns mode shapes for a vibrating silicon ladder.

It is interesting to see the effect of stiffening strips on the sides of silicon wafers. In the time average holograms, absence of fringes indicate a node in the mode pattern. Figure 3.3.1-5 shows mode shapes of silicon ladders with and without graphite stiffening strips along the side. The node along the sides of the ladder with the stiffening rib clearly shows how ribs improve the rigidity of the part.

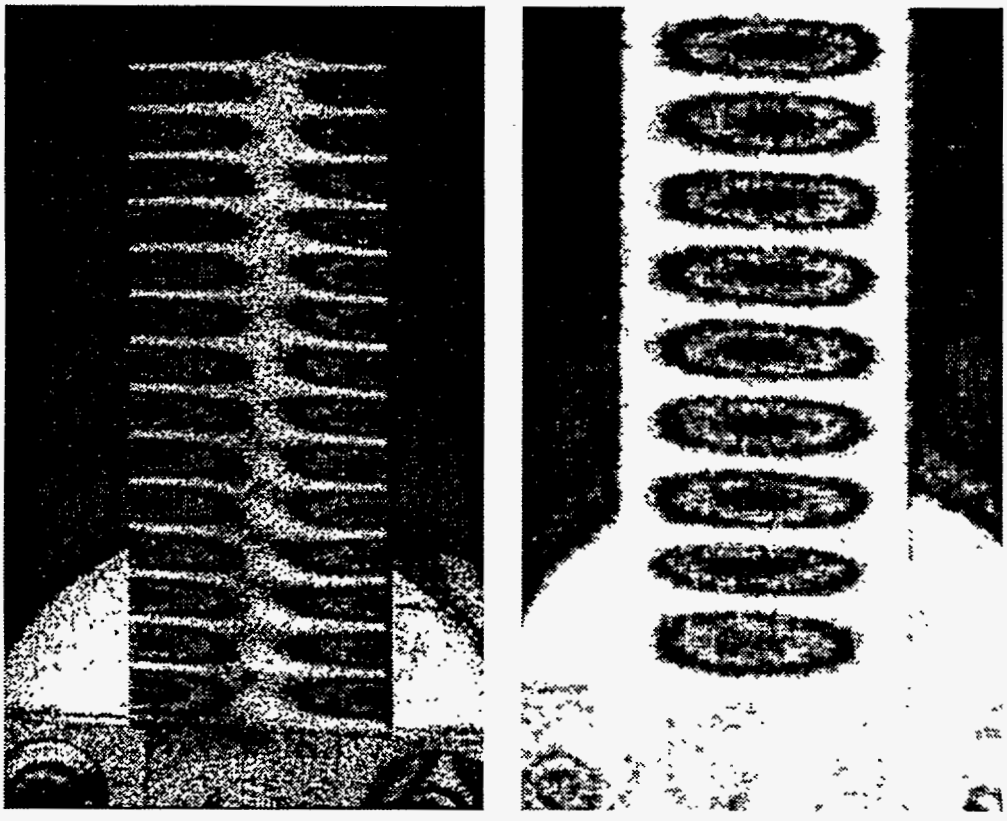

Figure 3.3.1-5 Mode shapes of silicon ladders with and without graphite stiffening strips along the side.

3.3.1.5 Test Results for Prototype Shell Assemblies

We have a large set of test results for silicon ladders, 120° arc segments of silicon shells during water cooling tests, and full 360° silicon shells during liquid butane cooling tests. The 360° shell, fully instrumented to conduct the evaporative system cooling test, is shown in Figure 3.3.1-6. The silicon wafers were painted white for the purpose of the TV holography measurements. The 360° silicon shell tests show the shape stability of a full shell with simulated electronic heat load and butane cooling. A sampling of results is shown in Figure 3.3.1-7. The full shell was kinematically supported with tooling balls and grooves as shown in Figure 3.3.1-7A. In the first test we placed a 51 gram steel ruler on the top ladder. Figure 3.3.1-7B shows the resulting distortion of the shell. The ruler was removed and replaced multiple times. The fringe pattern was always reproduced to a fraction of a fringe, indicating that the test results are repeatable within a fraction of a wave length of light. As we would expect, the shell takes an asymmetric barrel shape, with more bending at the end with a single support. The shape change with this load is small, roughly 2 μm.

It is interesting that the shape change are continuous across the boundaries of the individual ladders. This seems to be the case even when the load is increased, which indicates it is primarily the support rings that are changing shape rather than the individual ladders. The next two interferogram in Figure 3.3.1-7 show the total shape changes resulting after an additional 20 gram weight is placed first on the single support shell end and then on the double support shell end. The significance of these results follows: first, they show that an ideally supported silicon shell with external loads less than 100 grams change shape less than 5 μm; and second, and we think most important, is

that these small shape changes can be measured reproducibly using TVH. Detailed comparisons between FEM and TVH tests of shape changes would greatly improve our confidence that FEM codes reliably predict the shape changes as subsystems are coupled together to build the complicated detector structure. Unless shape changes are reliably predicted, it makes little sense to go to extreme care to make precision subassemblies, and then support them in the final detector assembly in a way that changes the subassembly shape in an unpredictable way. TVH is a useful tool for understanding shape changes that take place in a variety of situations, and finally allows one to quantify a number of the stability issues that designers worry about, but have not been able to measure.

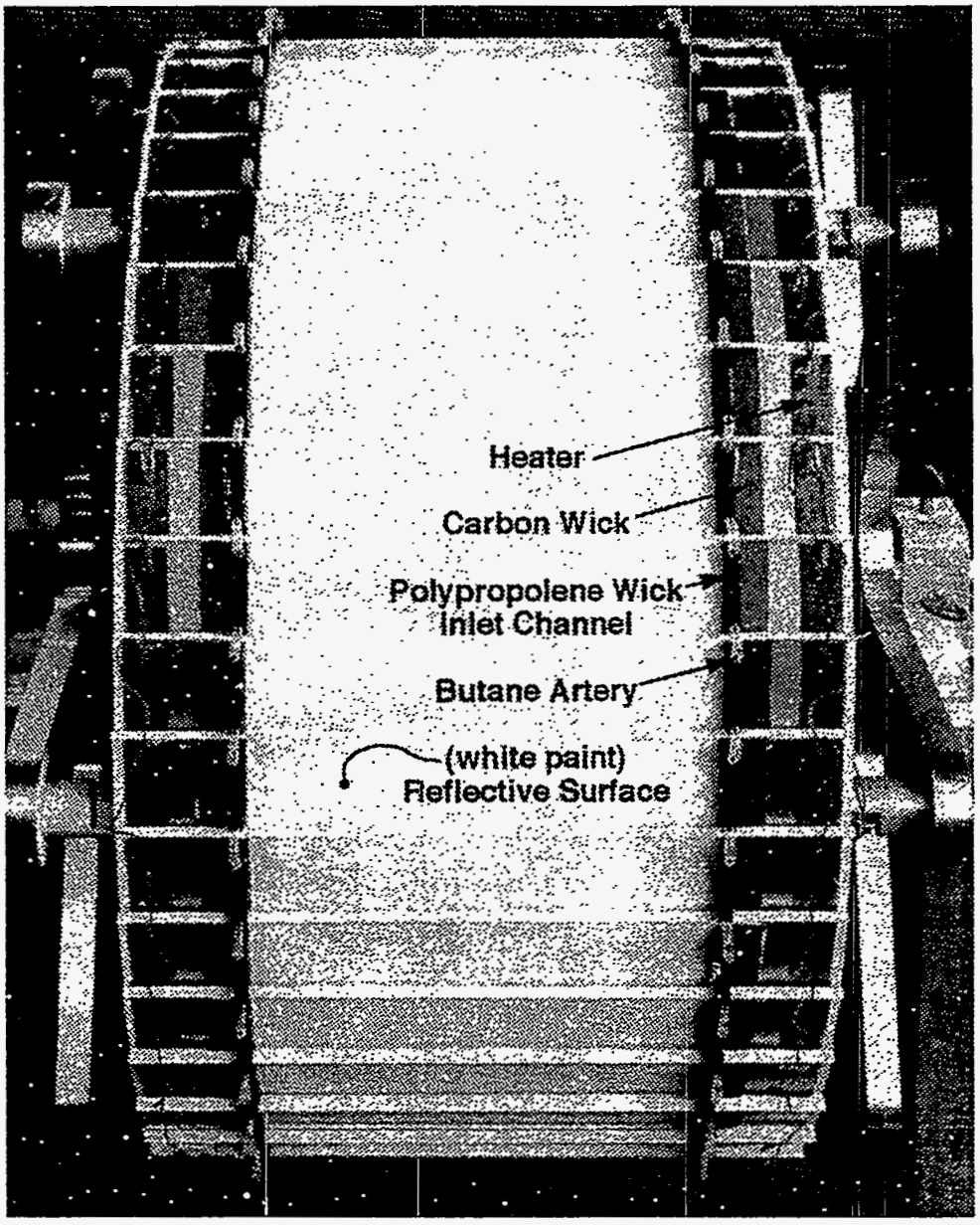

Figure 3.3.1-6 The 360° shell, fully instrumented to conduct the evaporative system cooling test.

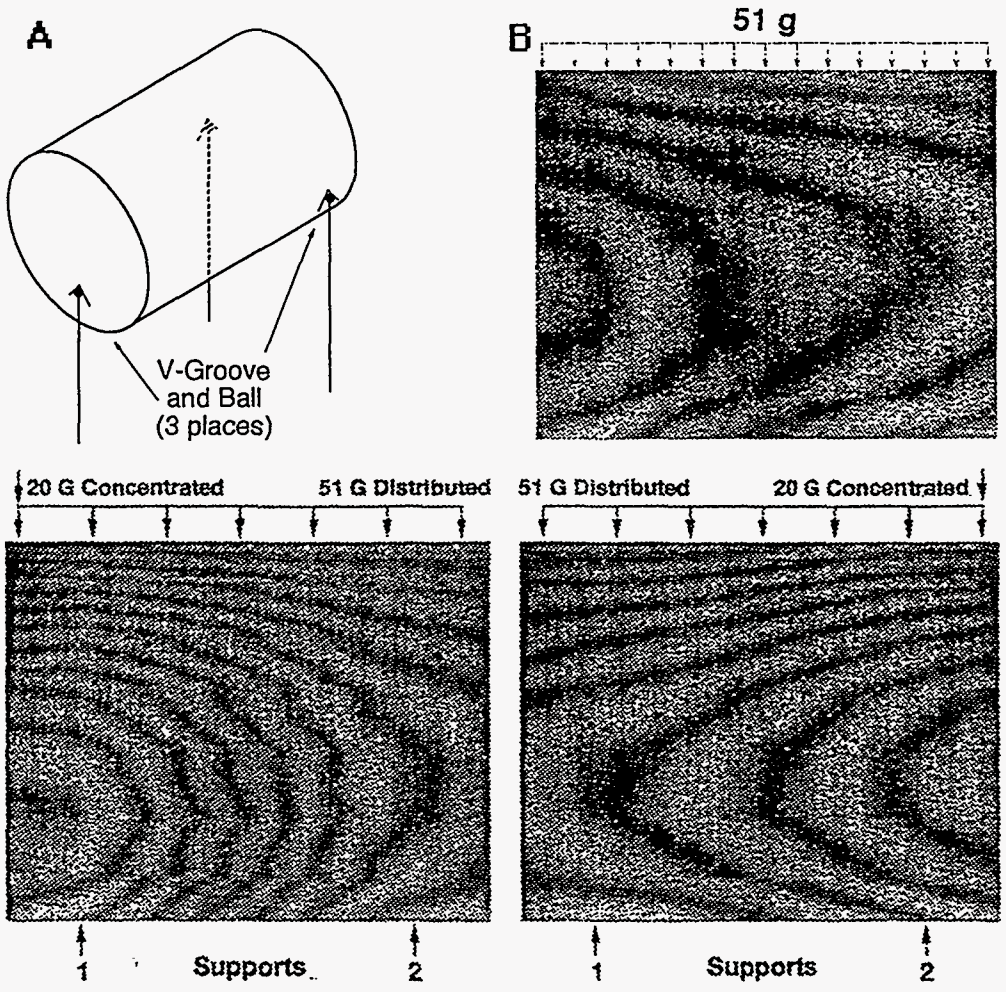

Figure 3.3.1-7 A sampling of mechanical test results for a 360° silicon shell.

A sampling of cooling test results are shown in Figure 3.3.1-8. A description of the butane cooling test is given in Section 3.4. During the tests the shell was again kinematically supported on three points in the same configuration used for the static tests. During cool-down from room temperature to 0°C the cylindrical shell takes on a barrel shape. For each 0.3°C change in temperature the radial shape change is roughly 1.8 μm. We believe that this shape change is due to the difference in the temperature coefficient of expansion of silicon and the steel topped table that supports the shell. The supports move closer together more than the silicon shrinks when the temperature changes. Eventually the structure comes to equilibrium with a new shape. In the future a zero-CTE invar topped support table will be used to eliminate this effect.

Once the structure reached equilibrium at 0°C, heaters were turned on to simulate electronic heat loads, and the evaporative butane cooling system was turned on to remove the heat load. We were interested in structure shape stability during these tests, because shape changes are indicative of cooling system performance. The results are for a 10 minute period when the whole system is seen to be in equilibrium. During this period, we can conclude that the shell did not change shape because there are no fringes on the part. The quality of the interferograms is low because of butane vapor motion and density gradients inside the tank. Nevertheless, these results are encouraging because they show, for the first time, a stable structure with the simulated full electronic heat load being removed using the evaporative butane cooling system.

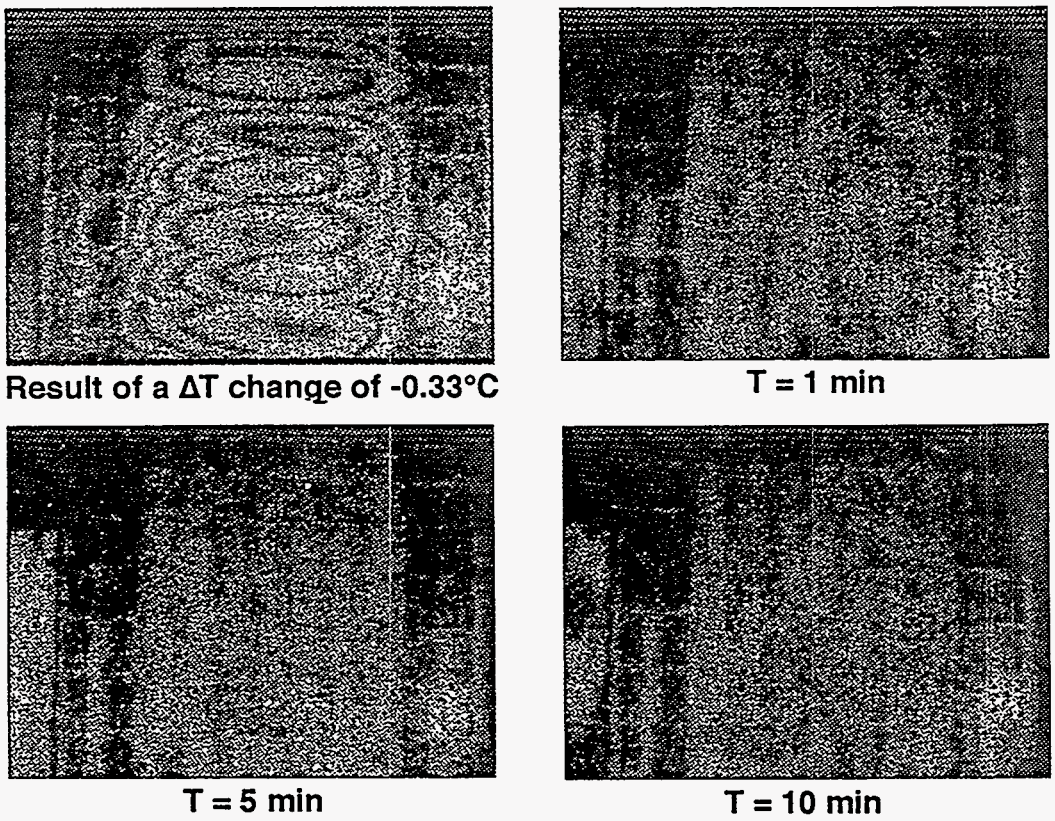

Figure 3.3.1-8 A sampling of the results for the 360° silicon shell tests showing the shape stability of a full shell with simulated electronic heat load and butane cooling.

Tests, such as those above, with large temperature changes during the cool-down phase, require compensation for rigid body motion of the tank and platform that supports the test part, otherwise rigid body induced fringes completely mask tests results. We detected and compensated for rigid body motion by mounting an invar rod as close as possible to the silicon shell. As the test tank and support table move during cool down, the invar rod also moves in a rigid way, and shows fringes. When the TVH object beam is repointed to remove the fringes on the invar rod, the remaining fringes on the test part are due only to test part shape changes.

We had just started to test the structure stability of water cooled silicon sections when the SSC project was terminated, but we do have a few results. The results for a 120° arc segment of ladders mounted on a partial support ring are shown in Figure 3.4.1-9. The support ring on one side was gripped by a clamp at just one location, so the structure was free to expand in all directions. The bottom of the second support ring rested freely on a support post. Again, heaters simulated electronic heat loads, but this time water flowed at a low rate, 250 cc/min, through the cooling channels bonded to the ladders to remove the heat. When the ladders are heated or cooled the fringe patterns immediately show non-uniformity, probably caused by uneven bond joints between the ladders and the support rings, or a strained support system coupled with the lower mechanical rigidity of an arc segment compared to that of a full shell. A full shell test with ideal kinematic support is needed to better indicate structure performance. The test was successful as no pump or flow induced vibrations were seen.

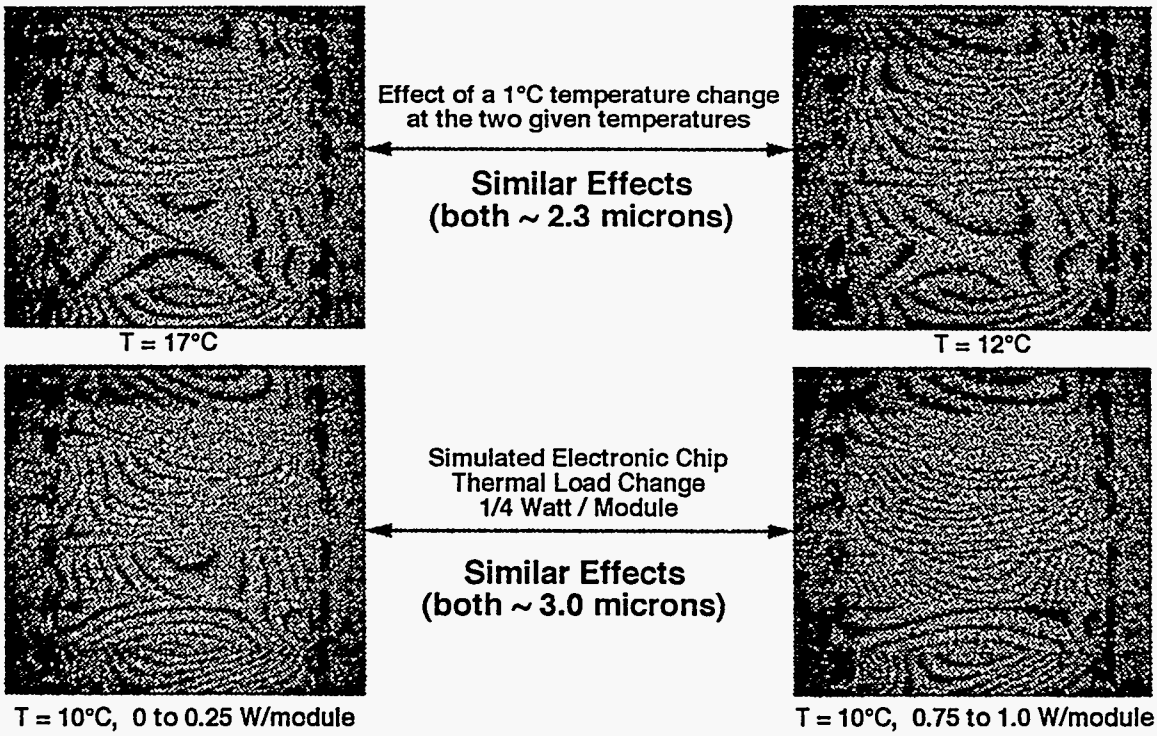

Figure 3.3.1-9 Preliminary water test on a 120° silicon shell segment.

3.3.1.5 Conclusion

TVH is a sensitive, full field of view testing method that provides essential information about the shape stability of precision assemblies in realistic test configurations. TVH is capable of providing answers to stability questions that have never been experimentally answered and cannot be answered by FEM modeling alone. TVH results are also important for developing assembly techniques that preserve the high precision built into individual parts. Because future detectors for high energy physics experiments will have to meet difficult stability requirements, TVH systems should play an important role in future detector development.

3.3.2 Detector Assembly and Alignment

The assembly and alignment of the full silicon detector subsystem to the very high precision required is an extremely difficult process. The assembly tolerance goals for the SDC silicon tracking system (STS) have been discussed in earlier reports, but they are listed here, in Table 3.3.2-1, as a reminder of the extremely tight tolerances that must be met during assembly.

Table 3.3.2-1 The assembly tolerance goals for the SDC silicon tracking system.

Radial	80 μm
Circumferential	25 μm
Along beam axis	250 μm

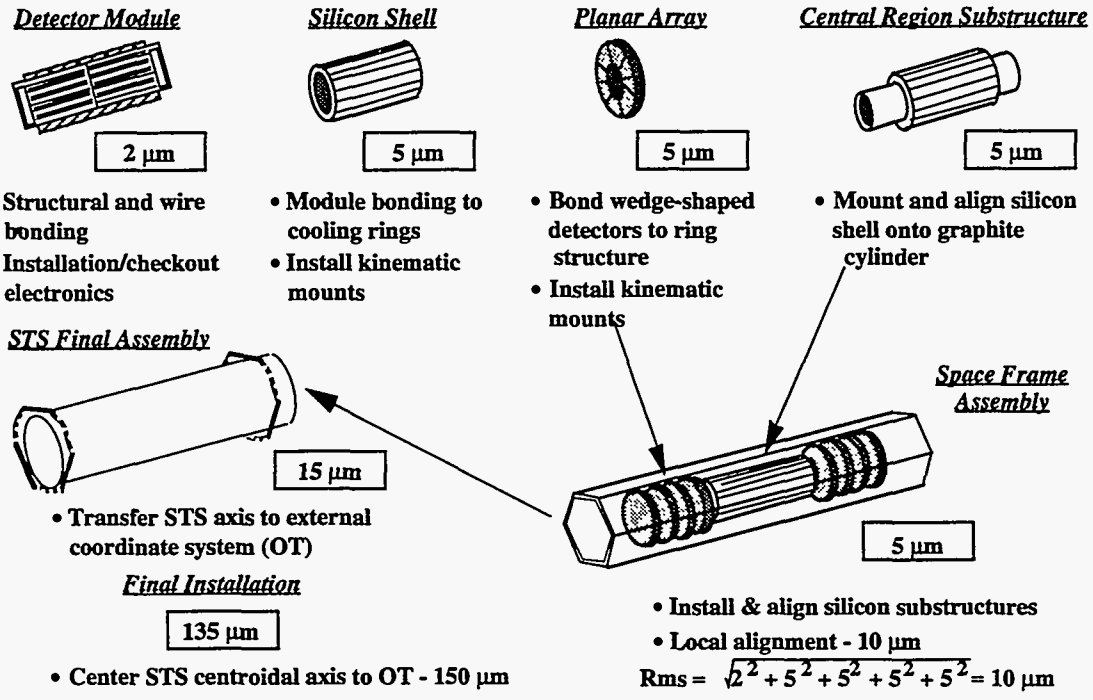

Figure 3.3.2-1 The proposed substructures and the alignment tolerances needed in the individual assembly steps in order to meet the required placement goal of 25 μm.

If one is to have any chance of achieving those tolerances, the alignment process must be an integral part of the conceptual design process of the entire silicon system from its inception, and the alignment tolerances of all the individual steps must be carefully considered. In Figure 3.3.2-1 the steps that go into assembling and placing the silicon system into the overall SDC tracking system are shown, and the tolerances associated with each step are given. Throughout the assembly process our philosophy is to deal with rigid substructures which contain multiple subunits that are all precisely aligned to each other in the preceding step. By using that approach, we need only maintain local alignment for relatively short periods of time during the construction phase of a given subassembly. We do not choose to build an extremely large structure (say the barrel region) all at once. That would easily take many months, during which time the full alignment precision over the entire barrel region would have to be continuously maintained. Instead we choose to build relatively small silicon shell structures, each containing only two layers of silicon, and each no more than 24 cm in length. With the automated pick-and-place, one of those shell structures can easily be fully assembled in ta couple of days. That short time period is how long precise alignment must be maintained. The resulting substructure is designed to be a very rigid and stable body, which can be fully inspected and its assembly precision verified if desired. The substructure can be stored until needed during later stages of assembly. The location of all the strips on the subassembly are then known once one relocates the central axis of the shell in 3-space, and locates the position of any one given strip. With that information, one can again relatively quickly and with high precision assemble a barrel superlayer substructure. The combined redetermination/relocation of the central axis also allows one to correct for any systematic tilt that may have been introduced during the shell's initial assembly.

Through a series of such high precision, relatively short duration steps, the full silicon system would be constructed. In each new stage, one has the opportunity to correct for some of the systematic errors introduced during the preceding stage. The

stages and corresponding substructures foreseen in the construction of the overall silicon tracker are:

1) Detector module construction
2a) Silicon shell assembly (barrel region)
2b) Planar array assembly (forward region)
3) Silicon shells mounted on composite shells
4) Two composite shells combined, one with detectors on its inside, and one with detectors on its outside.
5a) Composite shell pairs kinematically attached to central region space frame subassembly
5b) Planar arrays kinematically attached to forward space frame subassemblies
6) Central and forward pace frame subassemblies assembled into a single unit
7) Space frame kinematically mounted inside enclosure vessel
8) Enclosure vessel kinematically supported from outer tracker space frame

3.3.3 Full Silicon Subsystem Alignment Hardware

In preceding sections we discussed the development of a precision machine to assemble barrel and planar arrays to meet our assembly goals. As a prelude to the final full assembly activity we defined and demonstrated key alignment and assembly techniques which we needed for assembling high precision STS prototypes. During our work, it became clear that assembling the detector to the required precision would not be possible without temperature control of assembly equipment and the associated optical alignment equipment. Thus, we built and tested an inexpensive prototype temperature controlled work space for assembly operations. After this demonstration, we constructed two large temperature controlled work spaces, and equipped each room with a large optical tables (6 by 12 feet) for conducting experiments and assembling the semi-automated work station. The design and construction method employed in the temperature controlled room is discussed below. The optical tables are capable of being joined together to provide a work table for final assembly of the full 5 meter long tracker.

As discussed in the preceding sections, the key issues in implementing our alignment approach are: 1) creating and maintaining a straight and stable reference line; 2) defining the technique for the precision placement and long term optical mechanical stability of the reference microscope assemblies; and 3) sensing the module fiducials and with closed loop feedback control moving the modules, with precision, onto the microscope reference system.

Alignment System Demonstration We demonstrated the capability of our alignment concept by positioning modules in a simulated alignment demonstration to better than 1 μm. The demonstration, shown in Figure 3.3.3-1, used a bar to simulate a ladder and a 20 μm pinhole to simulate a module fiducial. The pinhole position was sensed with a microscope and camera, and we used a computer to calculate centroid position for a feedback control system. This configuration demonstrated all the concepts for our assembly alignment system, even some aspects of closed loop control. To verify the stability of the reference system, we attached a tooling ball to the center of the bar and monitored the ball position with an electronic autocollimator, which we converted into a long working distance microscope, with a lens. The lens, which attaches to the end of the electronic autocollimator barrel, together with the tooling ball on the bar, change the angle measuring autocollimator into a stable position measuring instrument with a 40 nanometer sensitivity. With that equipment we performed several tests. We randomly moved the simulated module away from the reference position, and then, using the closed

loop feedback system with a centroid program to find the pinhole center, we repositioned the pinhole center back onto the reference position, which is the center of a crosshair in the microscope. This procedure demonstrated our ability to find the centroid of a small spot, and to use the information to reposition the spot onto a reference in a few seconds. With the electronic autocollimator we monitored the replacement accuracy for this alignment approach, and we verified that the modules were always repositioned to better than 1 μm. We now have confidence that we can precisely position modules to glue them onto cooling rings. With the same technique, we also measured the long term stability of the reference alignment hardware in an ordinary laboratory space where the room temperature changed by several degrees. Typically, we observed unacceptable mechanical drifts, of about 5 μm, during several hours of measurements. We attributed the drift to thermal expansion and believe a temperature controlled room is absolutely essential, and in fact, the key element for precision assembly.

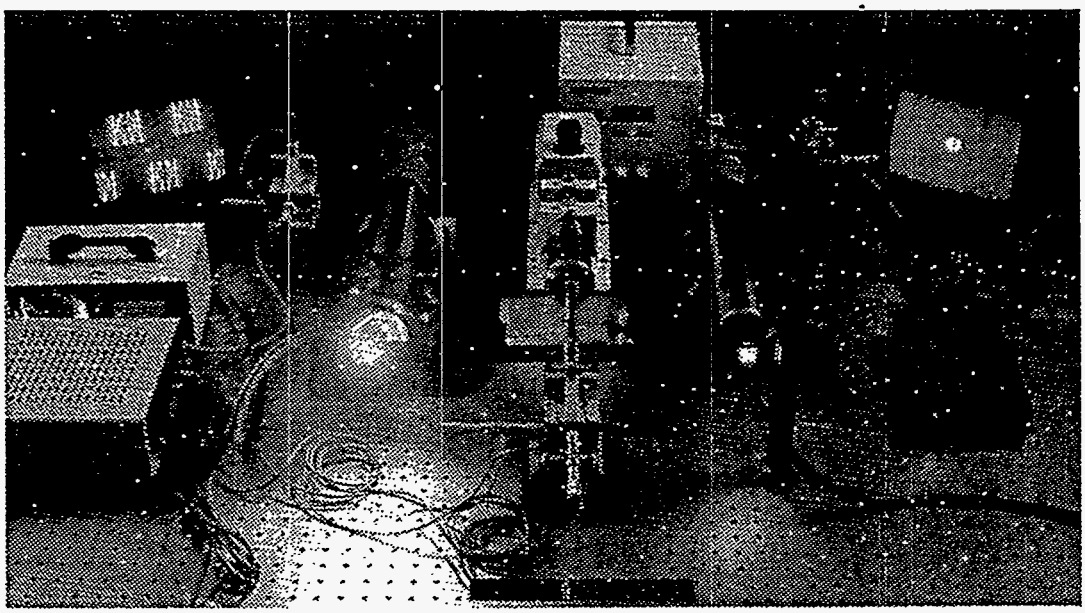

Figure 3.3.3-1 The demonstration set-up, which used a bar to simulate a module and a 20 μm pinhole to simulate a module fiducial.

Temperature Controlled Rooms Large commercial temperature controlled spaces are very expensive, so we built a prototype controlled temperature space using plastic walls, a plenum and a feedback system that regulated the brightness of a bank of light bulbs to control the temperature of the air flowing past them into the plenum. A sketch of the design, which has been used at Livermore Laboratories to control the temperature around precision diamond point turning machines, is shown in Figure 3.3.3-2. In our room, the fans pushed about two work space air exchanges per minute past the light bulbs, through the plenum and into the work space. The controller maintained the working area temperature to better than 0.1°F, with air temperature outside room changing by roughly 5°F and with people walking in and out of the working area. Based on this prototype, we decided to build similar temperature controlled work spaces over all our assembly areas. Inside a temperature controlled work space area, we rebuilt the alignment reference equipment described in a previous paragraph, and we again measured the mechanical stability of the reference alignment equipment in the improved tempera-ture environment. The results are shown in Figure 3.3.3-3. Inside the temperature controlled room, the reference alignment system was stable to better than 0.5 μm over a 3-day test period. This was very encouraging. The experiment demonstrated the long-term stability needed for the reference alignment system during assembly operations. We have continued to

have continued to use this space to check and perfect the stability of our reference systems and incoming hardware as we prepared to build precision silicon subassemblies.

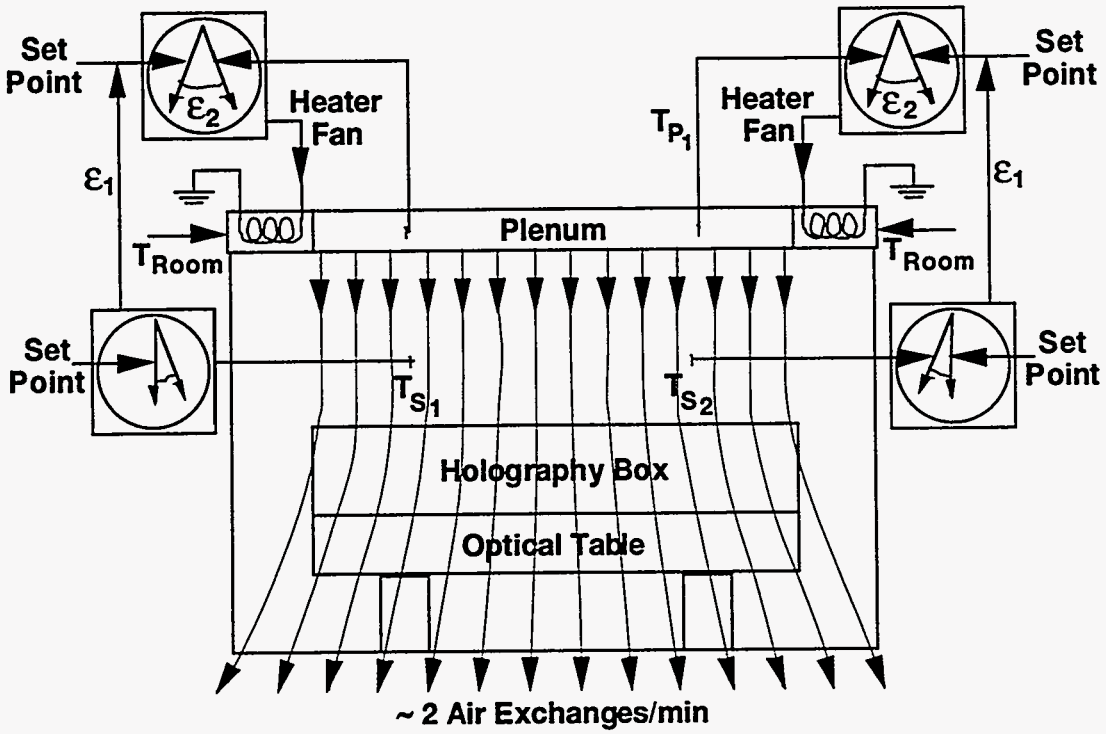

Figure 3.3.3-2 A sketch of the design, which has been used at Livermore Laboratories to control the temperature around precision diamond point turning machines, and which we have adopted and modified for our purposes.

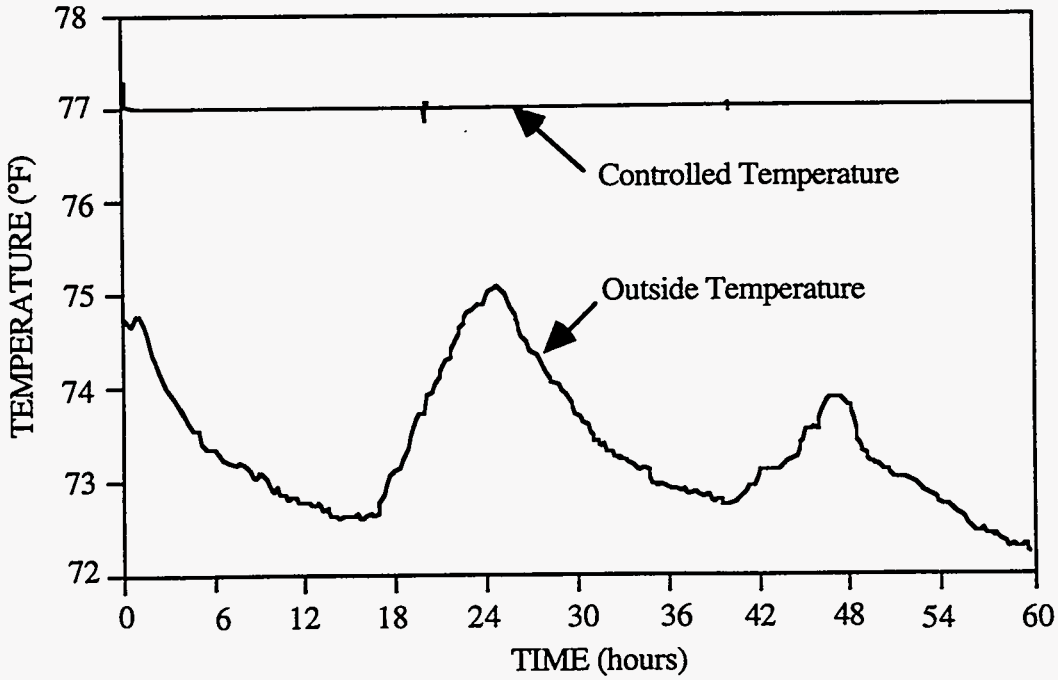

Figure 3.3.3-3 The improved mechanical stability of the reference alignment equipment resulting from installation in the improved temperature environment.

3.3.4 *In situ* Alignment Monitoring

The SDC Silicon Tracker design incorporated an *in situ* optical fiber alignment monitoring system. Its purpose was to monitor the alignment of the internal silicon substructures, one respect to another, during transport from the surface facility throughout final installation in the outer straw tracker, as well as monitoring the internal alignment during the particle tracking experiment. To accomplish this objective development of a fiber optic sensor system was initiated. Each fiber optic sensor is composed of a seven fiber bundle, with six of the seven fibers circumferentially placed around the remaining center fiber. Laser light emanating from the central fiber, which is reflected off a target point judiciously placed on a silicon substructure, is collected by the six co-axial fibers and returned to a light intensity sensing element. By measuring variations in light intensity, linear motions of the silicon surface can be discerned to the order of one micron. The fiber optic sensor would be physically mounted on one silicon substructure, and in turn would view the surface of the adjacent silicon structure. Relative motions between the two structures could thus be established. Placing these fiber optic sensors throughout the detector space provided a convenient, low-mass, nearly maintenance-free detection system.

At the conclusion of FY93 a fiber optic sensor had been built and tested by Worchester Polytechnic Institute (WPI) for our program. The extreme sensitivity of the sensor had been verified. At the point of program shut-down WPI was in the process of working on miniaturization of the sensor element for packaging in the detector tracking space.

3.4 Evaporative Cooling System

Early in the engineering development of the SDC silicon tracker, an evaporative cooling system was proposed to remove heat loads, which were thought to potentially be as large as 40 kW, and to meet the stringent temperature control requirements. The temperature control requirements were imposed primarily so that very tight stability tolerances could be met. The initial design goal was a $\pm 0.1°C$ maximum variance in local temperature with time and a $\pm 0.25°C$ maximum deviation from the design temperature of 0°C anywhere in the system at any point in time. It also was essential to keep the cooling system contribution to the radiation length to a minimum, requiring minimum mass and careful selection of materials.

The proposed solution was a type of heat pipe. A heat pipe is a hermetically enclosed vessel containing a working fluid and (usually) no other gases or vapors. Liquid is supplied from the colder (condenser) end to a hotter (evaporator) end by gravitational or capillary forces, or both. Heat input results in evaporation from the wicked evaporator surface, creating a slight pressure gradient between the hot and cold ends of the fluid loop. This pressure gradient drives the vapor to colder regions where it condenses, closing the fluid loop.

This basic concept, when applied to the SDC silicon system, was a set of individual evaporators within the hermetic enclosure coupled to a shell-and-tube condenser 25 meters distant. Liquid is supplied from the condenser to a wick structure via an arterial distribution network. The wetted wicks remove the heat load by free-surface evaporation in near liquid-vapor equilibrium. This is a very effective heat removal scheme, resulting in minimum fluid transfer requirements and minimum temperature differentials. Butane was chosen as the working fluid because its normal boiling point (-0.5°C) most closely matched the design operating temperature and because of its compatibility with other system components and materials, especially in the high radiation environment of the central tracker.

3.4.1 System Description

The Wick Structure It was recognized from the beginning that choosing a workable wick material was critical to the success of the concept. The intent was to conform the wick to the inside of the support structure for the silicon wafers. This structure, which became known as the cooling ring, was a circular ring with the outside and inside radii following a sawtooth pattern intended to support each silicon wafer at the proper angle with respect to the beam line. This complex geometry was particularly challenging, but if a workable wick could be developed, it would be possible to cool a large subset of the total number of silicon wafers with only 1 or 2 plumbing connections.

Initial wick development efforts were directed at a spray-on wick structure. The spray was a mixture of graphite particles, epoxy, and an organic "carrier." The graphite would form the wick, the epoxy would hold the graphite in place, and the organic would form a sprayable mix and insure, after evaporating out of the matrix, a suitably porous structure. It was anticipated that a reasonably high thermal conductivity wick would result.

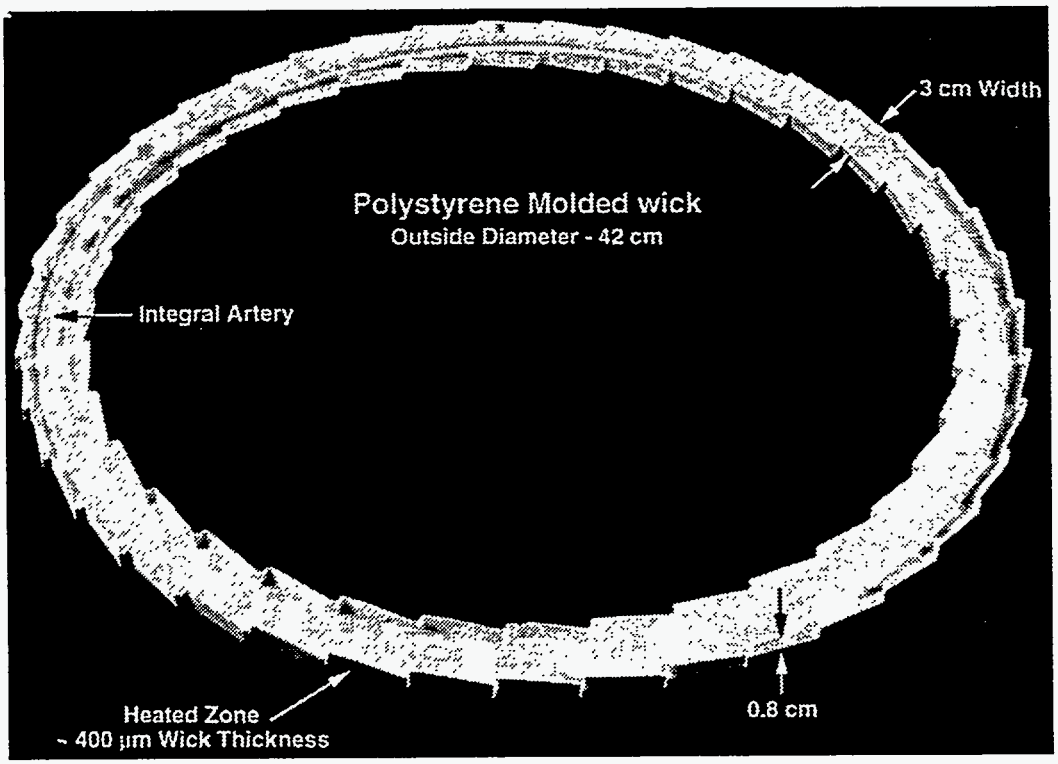

Figure 3.4.1-1 A molded 42 cm diameter polystyrene wick.

These efforts failed to produce a suitable wick. It was difficult to include enough epoxy to consolidate the particles yet maintain an open porous structure. It was also difficult to control the spray process to achieve a uniform coating on the complex cooling ring geometry.

Other wick material options were explored, such as compliant porous materials that could be formed to the required complex shape. Carbon felts and woven fabrics were good candidates, but none of these had a suitable pore structure. In general, the pores were too large to contain the working fluid or to develop enough capillary pumping to satisfy design requirements.

Ultimately, a molded polystyrene foam wick was chosen. The molding process would be costly, but the advantage of forming the wick to the cooling ring shape was deemed worth the cost. Figure 3.4.1-1 shows such a large single piece wick, which includes an integrated artery. Also, there was ample evidence that the wicking requirements could be met with this foam.

There is one consequence of choosing the polystyrene foam wick that impacts the fundamental operating characteristic of this cooling system that was not recognized at the onset. The polystyrene/working fluid matrix has a very low effective thermal conductivity. The polystyrene foam wick is comprised of large cells interconnected by smaller voids, the solid material making up a thin wall boundary of the large cells. This structure has a solid fraction of only about 9% by volume. This implies that the matrix conductivity is essentially the conductivity of the butane: 0.11 W/m-°K. With an effective matrix conductivity this low, boiling of the butane in the wick structure was inevitable and led to unforeseen problems.

Boiling occurs when the pressure of the fluid at the heat input surface, which increases with temperature, exceeds the surrounding saturation pressure by more than the amount that can be sustained by capillary forces (Figure 3.4.1-2). The additional heat needed to overcome the effects of the capillary pressure is referred to as the nucleate boiling superheat. A high thermal conductivity wick/fluid matrix results in heat conduction through the matrix and evaporation from the free surface because the nucleate boiling superheat is never reached inside the wick due to the extra pressure from the capillary forces. In contrast, a low thermal conductivity matrix results in evaporation at the heat input surface. The resulting vapor must then move through the matrix, reducing the effective liquid flow area or wick permeability. Also, continued heat transfer requires a rewetting of the solid surface so that the evaporation process can continue. However, the only forces available for driving liquid back into the dry region are capillary forces which, clearly, have already been overcome by the local pressure in the vapor bubble at the nucleation site. This can potentially lead to a very complicated and unpredictable behavior.

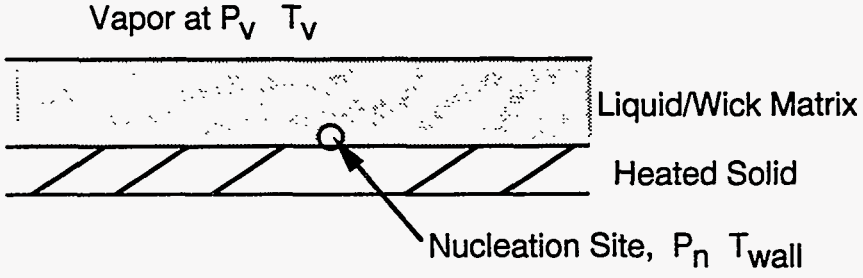

Figure 3.4.1-2 Boiling occurs when the pressure P_n, governed by the temperature T_{wall}, exceeds P_v by the maximum capillary pressure, which is inversely proportional to the pore or surface defect size.

The superheat required to boil depends upon the nucleation site size and the fluid. For the small pore wick structures under consideration, the wick pore sizes are on the same order as or smaller than the size of typical surface defects, so the pore radius can be used as the nucleation site size. Superheat required to boil can be estimated from the following semi-empirical equation:

$$\Delta T_H = \frac{3.06\sigma_l T_s}{\rho_v h_{fg} r_p} \qquad (r_p \text{ in meters})$$

where σ_l is the liquid surface tension, T_s is the saturation temperature, ρ_v is the vapor density, h_{fg} is the latent heat of vaporization, and r_p is the radius of the nucleation site. For butane at 0°C,

$$\Delta T_H = 1.16 \times 10^{-5} / r_p$$

or about 2.32°C for a 5 μm pore radius. In contrast, for a polystyrene wick, the conduction ΔT is about 9°C per 100 μm of wick thickness for a heat load of 1 W/cm^2. Clearly, with a wick thickness of 500 μm, the minimum that we could reasonably hope to achieve, boiling in the wick was inevitable. As a consequence, the system would not operate at the normal free surface boiling temperature, but rather at a temperature ΔT_H or more greater. The boiling inside the wick prevents the ΔT from reaching values as high as would occur with pure conduction, but boiling will also introduce the fluid flow problems discussed above. Nonetheless, it was believed[7,8] that we could make a wick that was sufficiently permeable to overcome the reduction in permeability from internal boiling, and that the elevation in boiling temperature would not be sufficiently large as to cause serious problems. We also had the option of choosing another working fluid with a lower normal boiling point [*e.g.*, isobutane (-11.7°C)] so that in spite of the ΔT_H, the detectors would operate at a low enough temperature. Furthermore, the advantages of the molded wick were a sufficient incentive to proceed with a polystyrene wick development program.

Priming the Artery Preliminary testing of the polystyrene wick revealed a problem with the fundamental performance of the liquid capillary pumped loop concept. The system was initially intended to operate with negative liquid gage pressure everywhere within the artery, so that no liquid-vapor interface would "bleed," or leak liquid, inside the silicon tracker. This required that the artery be "primed." This means that the artery had to be filled with liquid butane, free of all vapor and gases, and the column of liquid in the artery maintained its position against gravity via surface tension forces for the duration of the experiment.

A primed artery was not readily achieved. In a conventional heat pipe, the artery extends the full length of the pipe, back to the condenser, where the liquid and vapor pressures are always equal. In that case, the heat pipe artery can be primed by leaving a relatively large hole at the condenser end as a vent hole that will ultimately be covered by excess liquid. Furthermore, in conventional heat pipes it is normally possible to prime an artery by complete immersion in a pool of the liquid phase.

The artery network in the current system could not be primed by conventional means. The intent was to prime the artery by raising the liquid pressure high enough to expel all vapors from the artery before lowing the pressure to its operation level. Unfortunately, additional problems were found to exist in abundance. The large negative gravitational pressure and resulting small pore size made priming particularly difficult. Also, the required cryogenic, or below ambient temperature, nature of the liquid supply made the surrounding environment a heat source to the butane. Therefore, it was difficult to avoid boiling and vapor formation inside the artery itself, either during the priming or subsequent operational stage.

As a result it was decided that a system that required primed arteries and operated with static negative liquid gage pressure inside the arteries was not practical for this system, and that furthermore such a system would be subject to complete failure by a very sensitive mechanism.

A Positive Pressure System An alternative scheme was adopted wherein a small amount of bleeding would be permitted for the sake of reliability. The amount of bleeding would be minimized by reducing the wick permeability, wick thickness, and possibly the liquid pressure. Hydrodynamic tests were performed that indicated that very

low bleed rates for the small pore polystyrene foam wicks could easily be achieved. However, heat transfer tests revealed that problems with very large ΔT's and a large scatter in the ΔT's with position on a test piece remained.

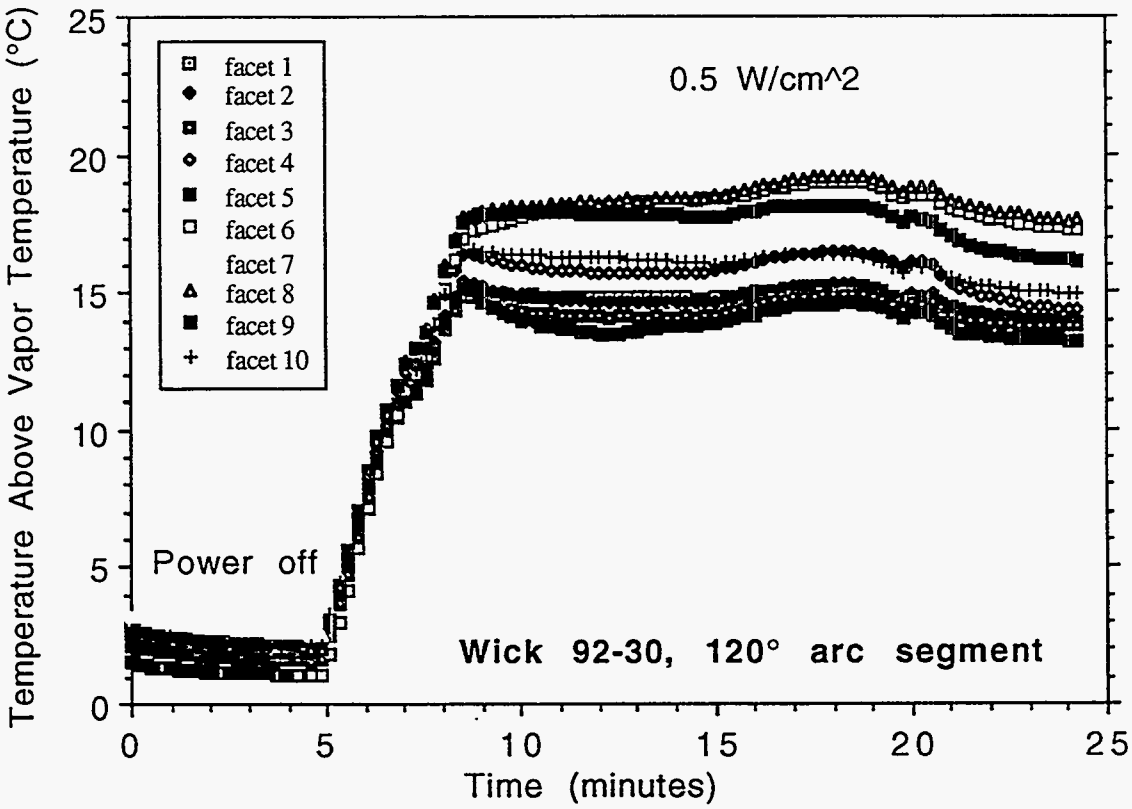

Figure 3.4.1-3 Test data from a 1.1 μm pore radius molded polystyrene foam wick. The different sets of points correspond to the ten different instrumented facets on the arc segment.

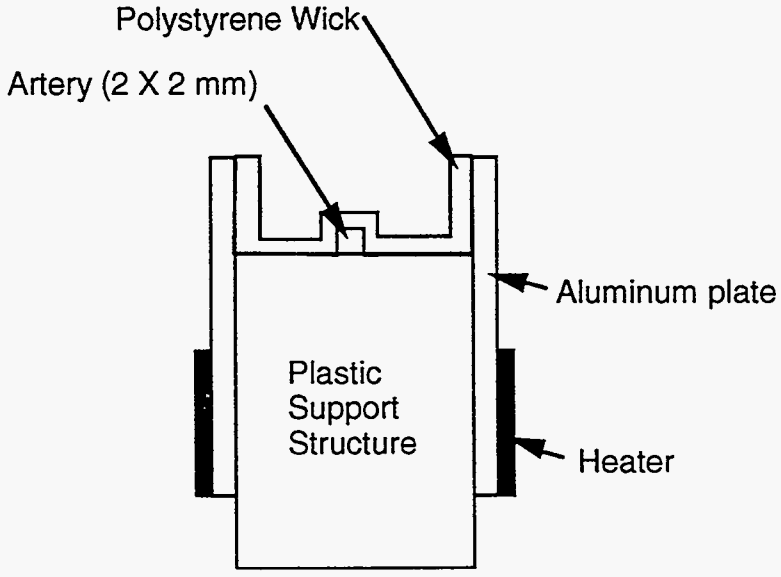

Figure 3.4.1-4 Polystyrene wick test piece. Each test piece has two heated facets.

Figure 3.4.1-3 shows the result of a 120° arc segment test (section of a 42 cm outer diameter ring). Ten heated facets at various locations on the inside and outside curvature were instrumented with thermocouples. Electrical heaters were attached to aluminum plates that were then attached to the cooling ring, much as the Be ground plane will be attached. The thermocouples were embedded inside the aluminum in the vicinity of the cooling ring. The wick, which is inside the cooling ring, is a polystyrene foam wick with an effective pore radius of 1.1 μm.

An investigation followed to determine whether or not an acceptable solution existed: Was there a polystyrene wick with a pore size which gave an acceptable ΔT and ΔT scatter, as well as acceptably low bleed rates? To this end, a series of tests using polystyrene foam wicks of various pore sizes was performed. The test pieces for this investigation were made from machined, not molded, polystyrene foam. Figure 3.4.1-4 shows a typical test piece geometry.

As a function of heat flux, ΔT was measured for each pore size. A typical test result, in this case a 6 μm pore radius wick, is shown in Figure 3.4.1-5. The result shown is typical to that of all the wick tests in that there is a significant difference between the two heated facets and the ΔT increases essentially linearly with heat flux.

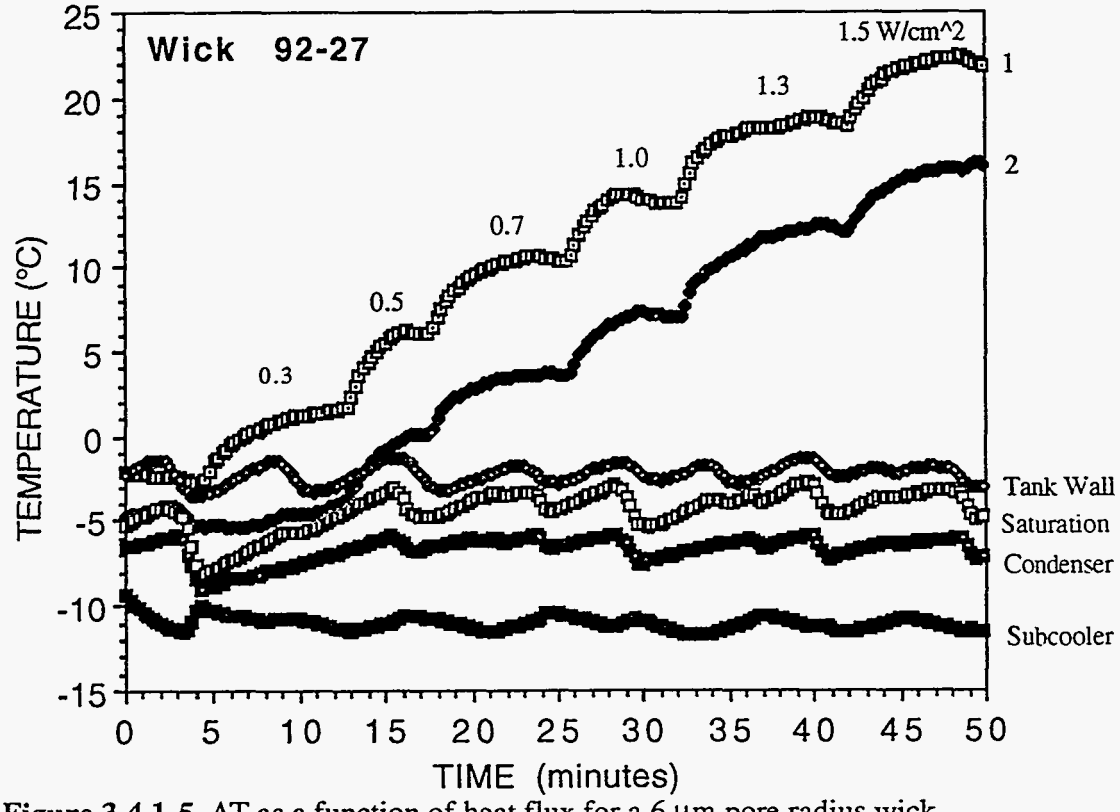

Figure 3.4.1-5 ΔT as a function of heat flux for a 6 μm pore radius wick.

The essential result of this test sequence is shown in Figure 3.4.1-6. Although corresponding bleed rates were not quantified, it was clear that there was not an acceptable solution for a polystyrene wick on this curve. Even with relaxed temperature stability requirements, a sufficiently low ΔT was not possible without unacceptable bleeding.

This test sequence did include some alternative wick materials. The point at 23 μm in Figure 3.4.1-5 is from a machined porous graphite piece and the low temperature point at 6 μm is from a machined porous beryllium piece.

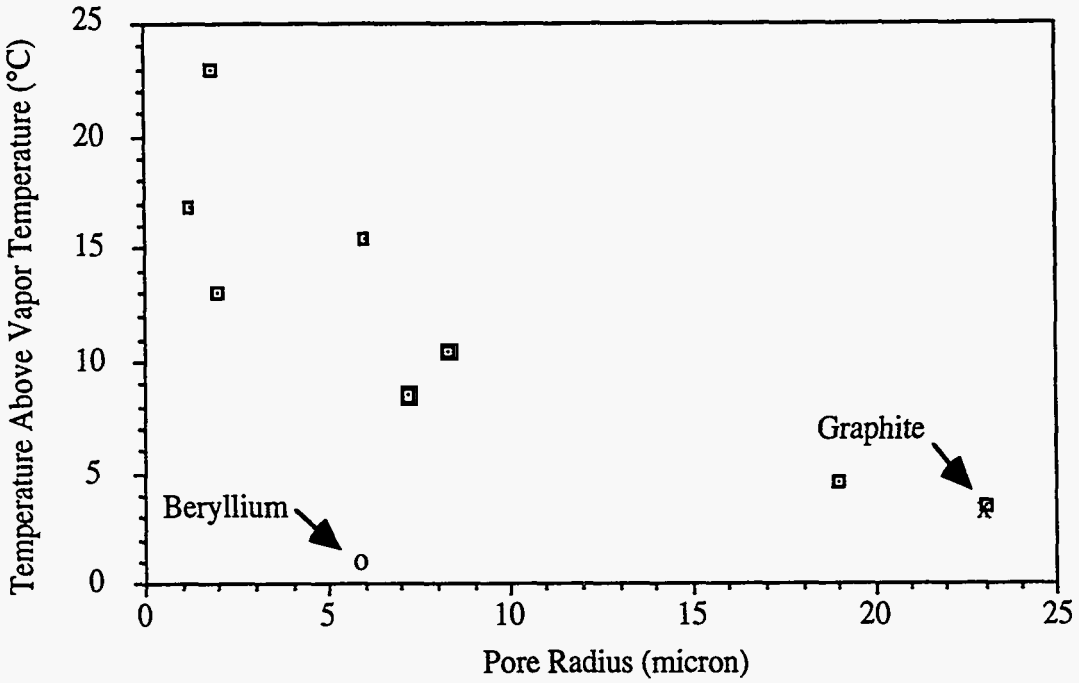

Figure 3.4.1-6 ΔT as a function of pore radius at 1.0 W/cm^2.

High Velocity, Negative Pressure System The desired low ΔT was not possible without liberal dripping from the wick surfaces. This would result in a significant excess flow of butane into the silicon tracker, flowing through the tracker in a poorly defined way. This fluid would need to be drained off to a sump and pumped back to the condenser. Furthermore, the excess liquid would tend to flood over the lowest points in the system, further lowering the local ΔT and increasing the scatter of the ΔT throughout the system.

As an alternative, it was proposed that the bleed rate be controlled by a high velocity flow through the artery. Such a scheme makes use of the venturi effect, where the local static pressure is reduced by the dynamic pressure, $\rho V^2/2$, where ρ is the liquid density and V is the velocity of the fluid. For a simplified system model where a constant diameter tube drains an elevated, static reservoir with the bottom end of the tube open to the same atmospheric condition as the top of the reservoir, the flow velocity in the tube can be calculated from

$$V = \sqrt{2.0 g \Delta h / (1 + fL/D)}$$

where g is the gravitational constant, Δh is the height difference from the top of the reservoir to the exit point at the bottom, f is a friction factor, and L/D is the length-to-diameter ratio. The gage pressure at any point along the artery can be calculated by

$$P = \rho[-g\Delta h + 0.5 f(L/D)V^2]$$

where here $-g\Delta h$ is a negative indicating the height differential from the tube exit up to the point of interest. A computer code was written to calculate pressure as a function of position along a cooling ring. This code accounted for mass loss due to evaporation, pressure losses due to bends in the artery, and possible variations in artery diameter along its path. The computer analysis revealed that the desired negative pressure throughout the artery was possible. Indeed, the problem was keeping the pressure from getting too negative. In order for the capillary to pump liquid out of the artery at a required rate, the

capillary pumping pressure must exceed the sum of the magnitude of the negative pressure in the artery plus the pressure drop in the wick itself.

This liquid feed approach concedes the necessity of a pumped liquid return. Each artery must drain to a common sump, from which a mechanical pump would be used to complete the fluid loop.

Nonetheless, the solution was judged worthy of investigation, and a series of experiments were conducted. The data from a test using the largest pore radius (19 μm) polystyrene foam wick is shown in Figure 3.4.1-7. The anomaly at 12.5 minutes was caused by a flow interruption while the test piece was rotated. The result of this test series is that bleeding and, in most cases, test piece orientation sensitivity, were eliminated. Data scatter or variations from one facet to the next was still evident, but the very large deviations due to flooding in the lower regions were eliminated. The ΔT's were essentially the same as with the positive pressure feed system. The typical flow velocity for this and other tests was calculated to be about 1.0 m/s for a 2 mm artery diameter.

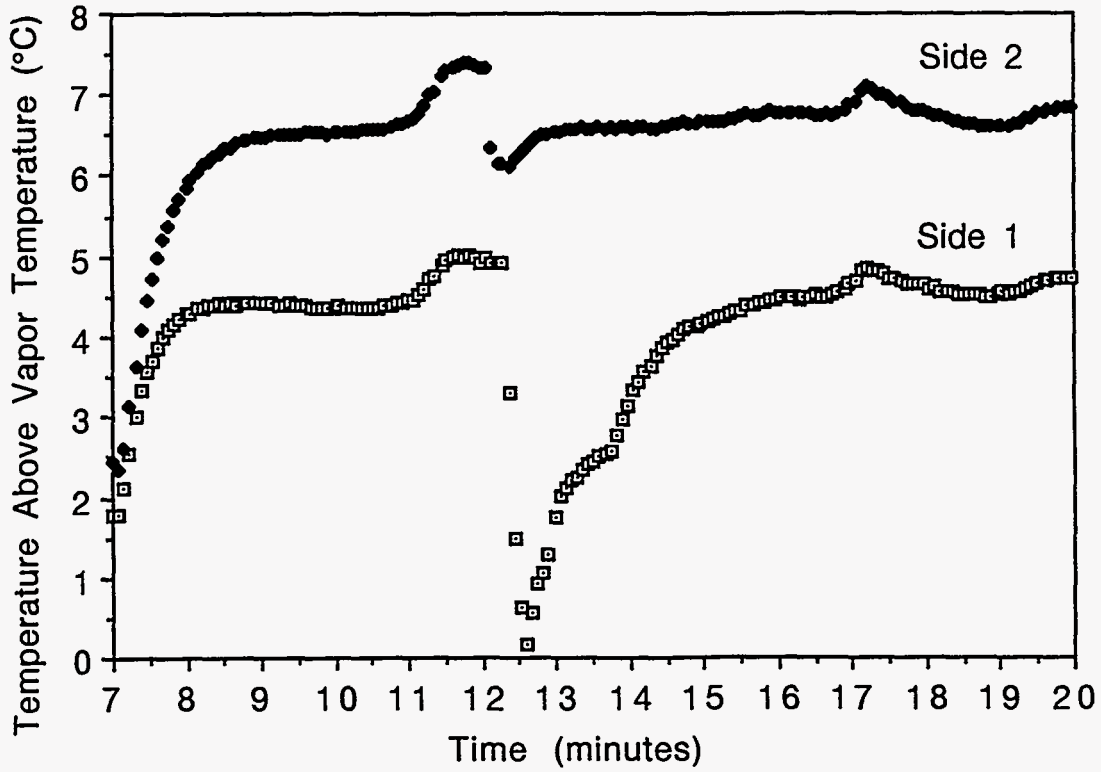

Figure 3.4.1-7 The ΔT at 1.0 W/cm^2 for a polystyrene wick with a 19 μm pore radius. The glitch at 12.5 min. is due to a flow interruption during an orientation change. Before that time, side 1 was up; after that, side 2 was up.

3.4.2 Polystyrene Molded Wick Development

The high velocity liquid flow solution is far from ideal, but it does allow for the use of the large pore foam wick, minimizing ΔT and bleeding. The wick molds were redesigned and refabricated to give the possibility of larger artery diameter and wick thicknesses than those of the earlier tests. The first new molded wicks had an artery diameter and a wick thickness of 2.0 mm.

Unfortunately, serious problems were encountered with the new molded wicks. The large pore size wicks used in the wick characterization tests had all been machined

out of blocks of foam and therefore the wick surface was always open. Evidence from pressure tests and then from micrographs of the new molded large pore wicks made it apparent that the wick surface was partially closed. The polystyrene foam was apparently wetting the delron mold material, causing the cells to close at the surface. In addition, the pore size distribution within the bulk material was highly non-uniform. It is speculated that this was due to the flow characteristics of the foam in the thin cross-section mold. The larger bubbles that ultimately create the larger pores flowed less readily than smaller bubbles, so there was a tendency to separate large and small bubbles based on flow resistance through the mold. Other problems were also evident, but the first set alone was sufficient to cast serious doubts on the feasibility of molding a satisfactory wick.

3.4.3 Porous Metal and Carbon Wick Development

Concerns about the performance of the foam wicks had already prompted a preliminary investigation into alternative wicks. The most promising candidates were a porous carbon material from Union Carbide and a porous beryllium material from Brush-Wellman. These materials were supplied in solid blocks that had to be machined to the desired shape. As such, they were not readily conformable to the cooling ring geometry. Therefore an alternative configuration with individual wick elements, one for each electronics package, mounted to the beryllium ground plane, was tried. The wick elements were interconnected by an arterial liquid feed system. The simplicity of cooling a full ring with a single tubing connection was lost, but some advantage was gained by moving the heat removal surface closer to the heat source and eliminating the need for a cooling ring with walls that have high transverse thermal conductivity.

The heat transfer for these candidate wicks is far superior to that of the polystyrene foam, both in the magnitude of the ΔT and in the ΔT variations from facet to facet, due to the relatively high wick/matrix thermal conductivities. We conducted a series of tests to determine the effect of wick thermal conductivity, and other factors on the performance of the evaporative system. Those tests are described in the following subsections.

3.4.3.1 Carbon/Graphite Experiments

Experimental evidence indicated that several parameters were affecting the isothermality of the cooling rings. These parameters included the degree of liquid butane sub-cooling, the position in the series chain of wick wafers, the position in the gravity field, the bond line thicknesses, the variations in individual wick pieces due to variations in processing *(e.g.*, clogging by epoxy or loose particles, microfractures, and thickness variations), the liquid pressure, and the thermal conductivity of the wick material. A test sequence was performed to examine in detail the relative influence of what were believed to be three of the more important parameters: the wick thermal conductivity; the position in the series chain; and the position in the gravity field.

These experiments were performed on a 120° arc segment of a nominally 42 cm diameter cooling ring, simulated by a Lexan strongback. Four electronics heating loads were simulated on this test piece, two on each end of the strongback along its outer edge. Consistent with earlier experiments, the individual wick wafers were $1.0 \times 15 \times 30$ mm with a 5 mm wide rectangular Lexan artery. The wick wafers were mounted on a $3.2 \times 30 \times 45$ mm aluminum plate, which was then attached to the strongback. A cross-section of the assembly is shown in Figure 3.4.3-1.

To isolate the wick thermal conductivity as a parameter, four carbon wicks were used that were identical in every respect except that two were cut from graphitized stock and two from ungraphitized stock. The ungraphitized carbon wicks had a thermal conductivity of 1.7 W/m-°K, while the graphite ones had a thermal conductivity of 87 W/m-°K. Both wicks had a 3.8 μm pore radius and a permeability of 0.6×10^{-13} m^2..

The wick material used was chosen from what was readily available and what was probably within a factor of two or three in terms of pore size and permeability of that which one might ultimately choose. As such, it was clearly not optimized for higher heat loads in order to provide an adequate system safety margin, but it did provide a good overview of potential problems.

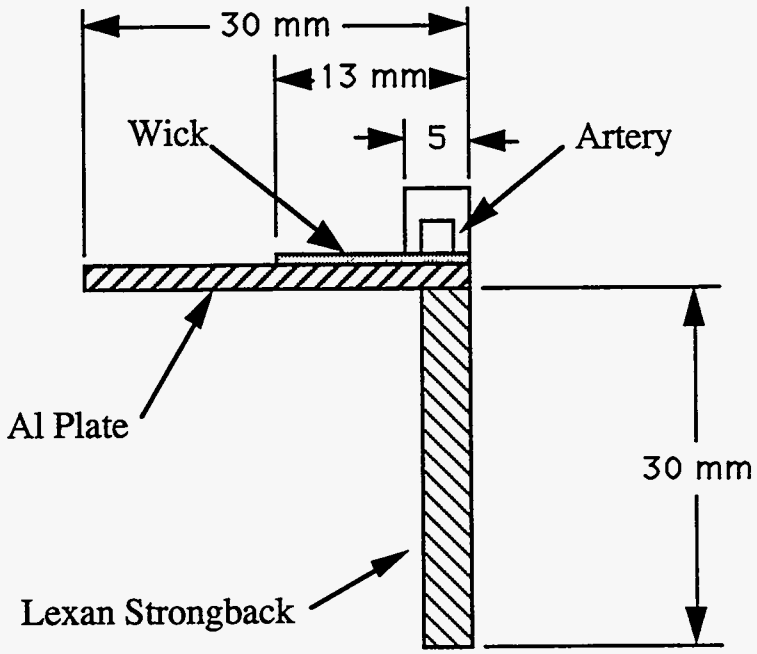

Figure 3.4.3-1 Cross-sectional view of test piece.

The wicks were arranged on the simulated 120° arc segment as shown in Figure 3.4.3-2. This arrangement allowed for the direct comparison of the two wick types against each other and a comparison of the performance of each wick against an identical wick elsewhere in the gravity field and in the series chain. The first test was operated in the orientation shown in Figure 3.4.3-2, with the carbon wick designated C1 at the lowest point in the gravity field and the first element in the liquid flow direction. Power was increased stepwise in 4 equal increments. Temperature was measured inside the aluminum plate at a point near the center of the artery. The test result is shown in Figure 3.4.3-3.

Several conclusions can be drawn from this data. Consider first the data between 20 and 30 minutes, for which the total power to the four heaters is 7.6 W, corresponding to a power level of 1.5 mW/channel. (That was the value to which the electronics design power consumption was converging to, based on chip analysis and testing.) The temperature of the two graphite wicks are essentially the same, as are the temperatures of the two carbon wicks. However, the temperature of the graphite wicks is significantly lower than that of the two carbon wicks. Several different thermal impedances give rise to the total temperature drop and together account for the ΔT between the carbon and the graphite wicks. Neglecting any temperature drop in the aluminum plate, the first thermal impedance to heat flow down the thermal gradient is the adhesive layer between the aluminum and the wick. The manufacturer's specification of the adhesive thermal conductivity is 1.15 W/m-°K. The effective adhesive layer thickness ("effective" because of the additional unknown associated with penetration of adhesive into the wick) is unknown. Next is the thermal impedance across the wick. This can be a result of one of two possible mechanisms: conduction through the wick/liquid butane matrix, or boiling of liquid butane in or near the plane of contact between the wick and the adhesive.

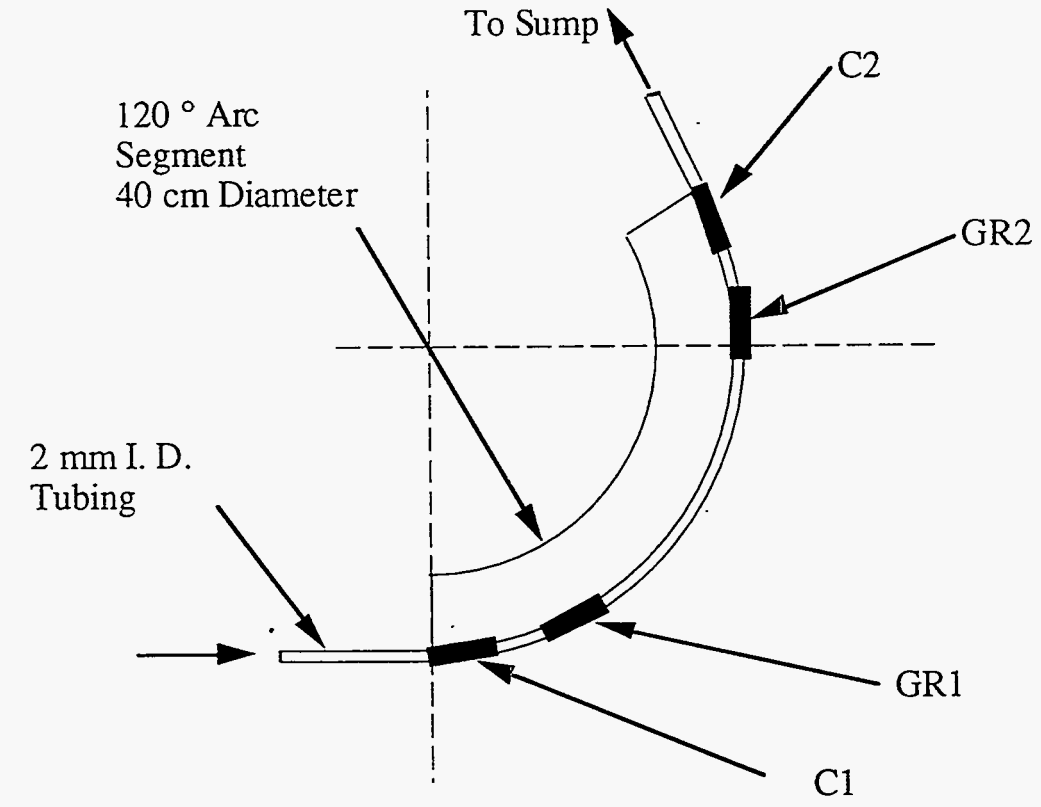

Figure 3.4.3-2 Plan view of test piece, showing relative position of the four wicks.

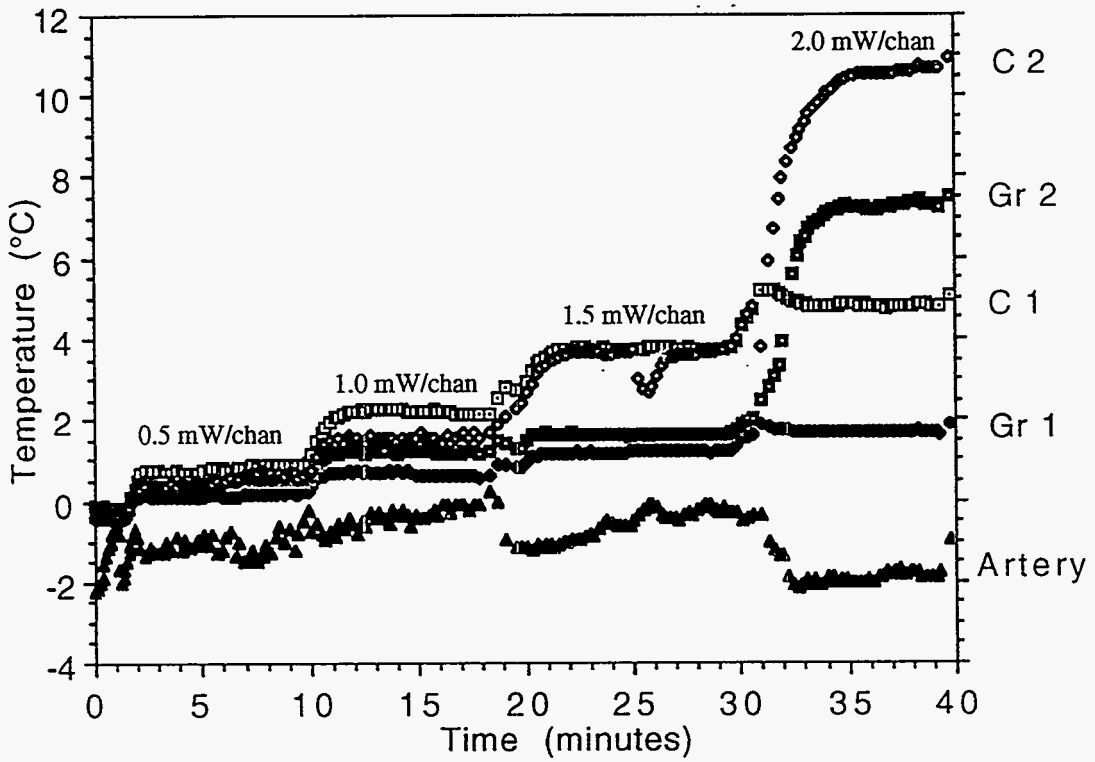

Figure 3.4.3-3 Temperature history at 4 power levels for the test piece operated in the orientation shown in Figure 3.4.3-2. Notice the linear increase in ΔT with heat flux.

First let us assume that internal boiling is not occurring. In that case, there is the conduction ΔT through the wick thickness and a free-surface evaporation of liquid at the liquid-vapor interface. Heat transfer by free-surface evaporation due to small departures from equilibrium is very efficient. For butane under these conditions, the heat transfer coefficient at the free-surface is 4.7×10^6 W/m^2-°K. Therefore, all of the observed ΔT must be in the adhesive and the wick/fluid matrix. The effective thermal conductivity of a multiple material random matrix, such as our wick, can be absolutely lower and upper bounded by series and parallel models, respectively. With a solid volume fraction of 0.5 in these wicks, the carbon/butane wick conductivity k is $0.2 < k_c < 0.6$ W/m-°K, and the graphite/butane wick conductivity is $0.2 < k_{gr} < 40$ W/m-°K. The ΔT that would be observed under the conditions of interest as a function of k is shown in Figure 3.4.3-4.

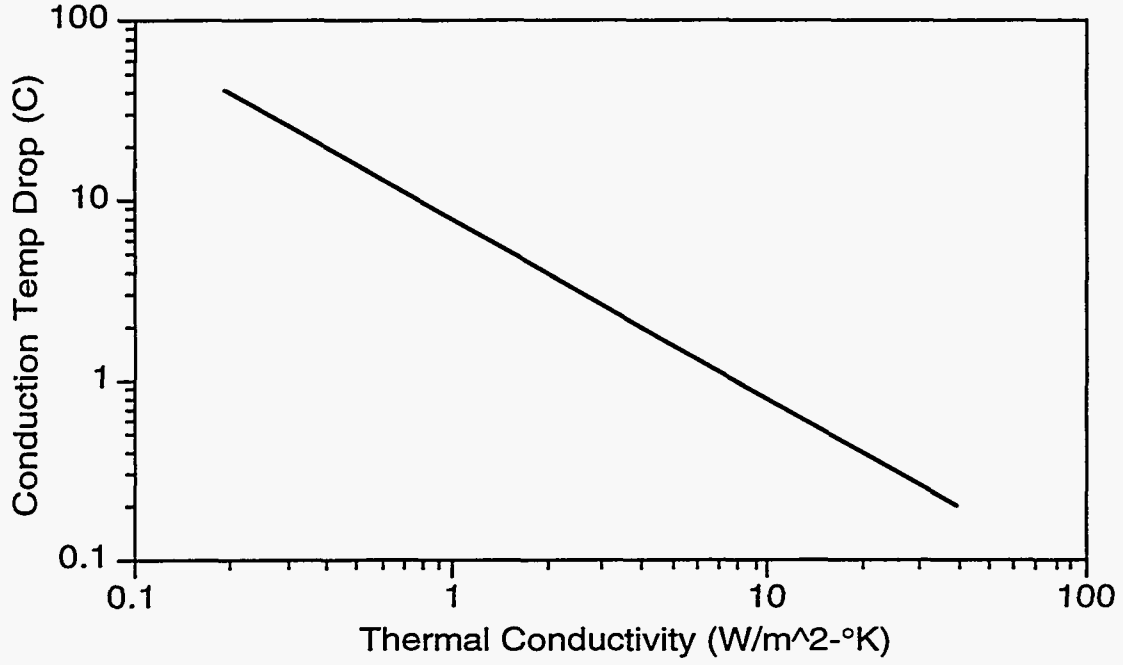

Figure 3.4.3-4 Temperature drop as a function of thermal conductivity for pure conduction assuming a 1 mm thick wick and a heat load of 0.8 W/cm^2.

This ΔT must be compared with the ΔT required to boil. Once the ΔT reaches that required to boil, heat conduction through the wick/fluid matrix becomes a secondary consideration. If boiling is occurring inside the wick, the only benefit of a higher conductivity wick is a fin effect that distributes the heat over a larger area. (This may not be insignificant, since the tendency to trap vapor in the wick and drive up ΔT's can be significantly reduced by this effect.) The ΔT required to boil the butane inside the wick for our conditions was calculated to be about 2°C and therefore it can be concluded that boiling is not occurring in the graphite wicks at the 1.5 mW/channel power level. The effective thermal conductivity of the wick/fluid matrix is at least 6.5 W/m-°K. This conclusion is consistent with a 20 μm adhesive layer thickness (with an average total ΔT of 1.25°C, a ΔT of 0.4°C in the adhesive and 0.85°C in the wick/fluid matrix). In contrast, for the plain carbon wicks, it can be concluded that boiling is occurring internally since the ΔT is greater than 2°C.

Boiling in the wick has the effect of significantly reducing the ΔT below that which would be observed by conduction alone, as witnessed by the fact that the ΔT is significantly less than the 45°C value expected for pure conduction through the carbon-butane series model wick. The ΔT expected in thin-film nucleate boiling inside the wick,

is difficult to predict, but, using a correlation by Rohsenow, a ΔT of between 4°C and 15°C can be expected (for the power density under examination), depending upon the value of a purely empirical correction factor that is a function of the fluid and the surface materials. This calculation does not include all effects due to the presence of the wick material, such as the fin effect, which should act to reduce ΔT, or the reduction of effective heat transfer area (dry-out), which would raise ΔT.

The following conclusions can be drawn from the data at 7.6 W and the analysis summarized above. The ΔT decreases as wick thermal conductivity increases, but the presence of a low conductivity fluid in the wick significantly reduces the benefit of higher conductivity. For the pore sizes used, nucleate boiling occurs when the ΔT reaches about 2°C. Once boiling starts, the ΔT required to maintain boiling increases significantly, but the magnitude of the increase is difficult to predict.

Examination of the data beyond 32 minutes supports the expectation of a change in the heat transfer mechanism when ΔT exceeds 2°C. The data also shows, with Gr2 at a higher temperature than C1, that there is an effect due to either the liquid pressure or temperature. Surface dryout was evident on the uppermost two wicks, indicating a loss of effective heat transfer area at this power level.

The evidence sited above does not fully explain the data. For example, the ΔT of C1 increases nearly linearly with power; there is no non-linearity at or near 2°C. This may be in part due to some flooding due to the higher local liquid pressure.

A second test was conducted with this test piece, wherein the test piece was rotated ~120° counter-clockwise so that C1 and C2 are at the same level in the gravity field, as are Gr1 and Gr2, with the graphite wicks only slightly above the carbon wicks. The temperature data, recorded at two power levels, is shown in Figure 3.4.3-5.

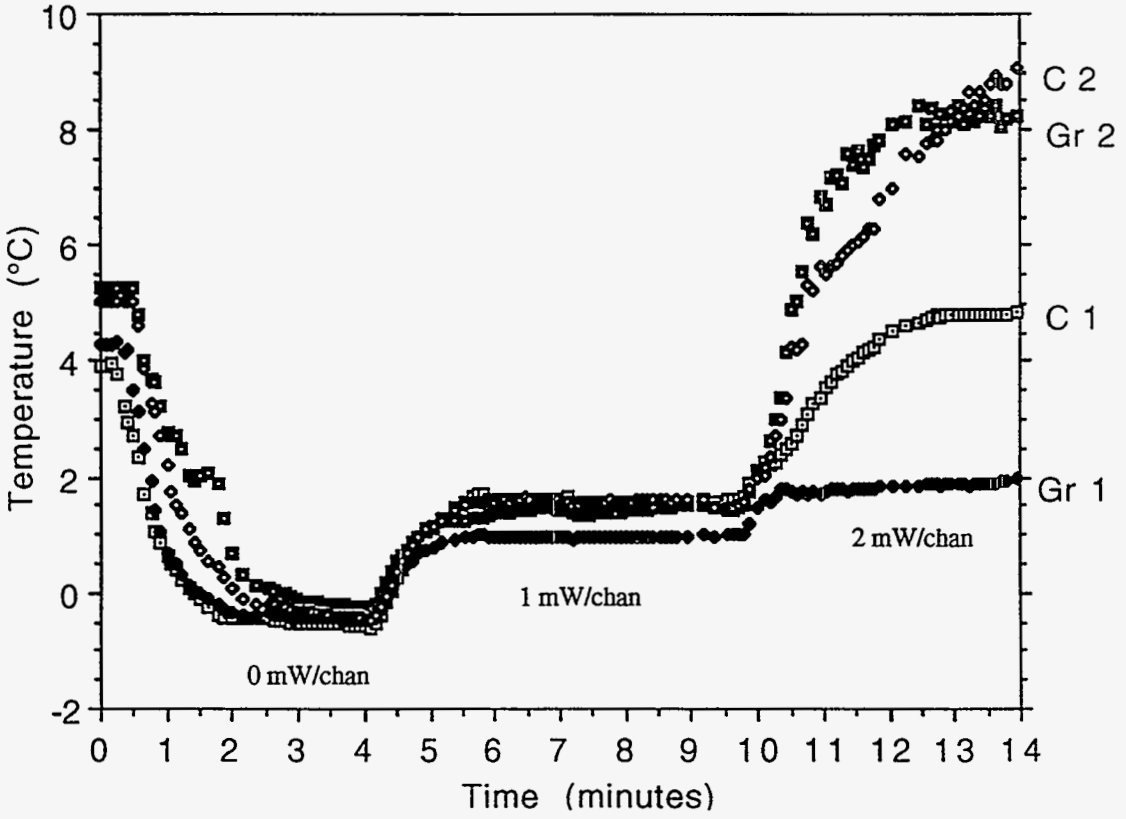

Figure 3.4.3-5 Temperature history at different power density levels with the test piece oriented with C1 and C2 in the same horizontal plane. Power levels corresponding to electronic heat loads of 0, 1, and 2 mW/channel for a double-sided detector.

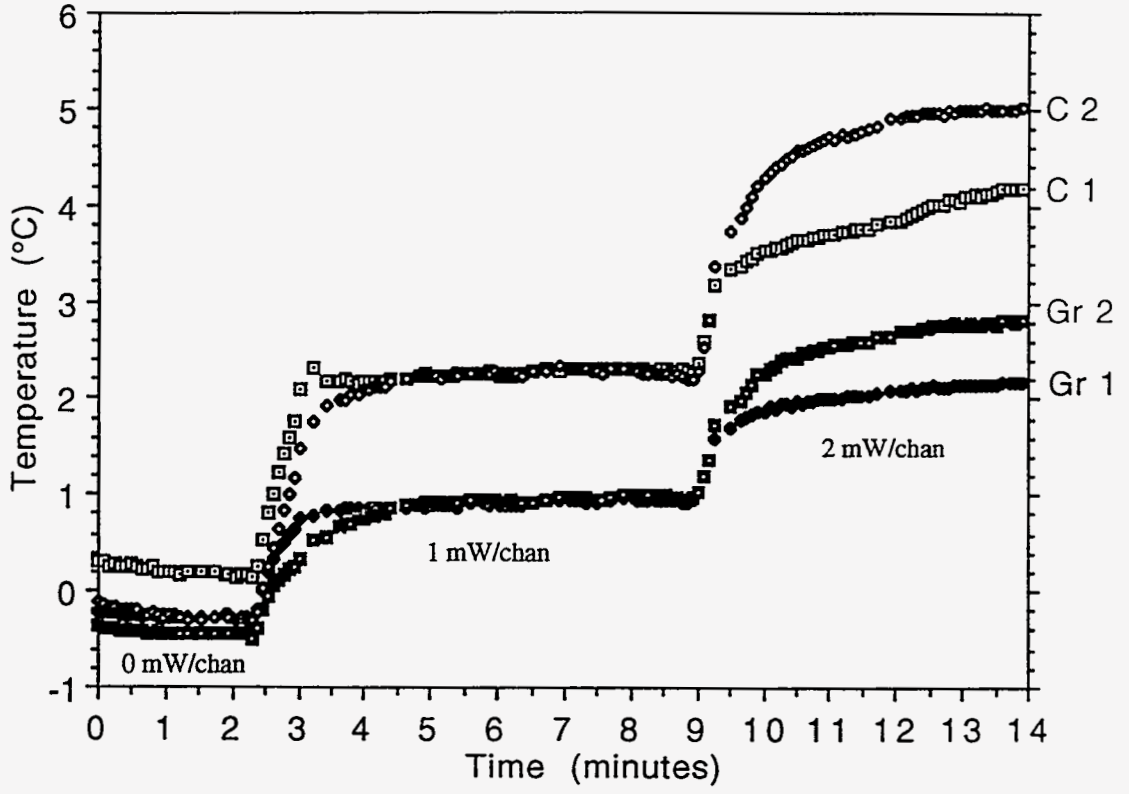

Figure 3.4.3-6 Experimental data with test piece oriented with C2 at the lowest point and first in the series.

At 1 mW/channel, the wicks are more isothermal than in the previous orientation. Equalizing the pressure has had a modest but observable effect. Compared with the results shown in Figure 3.4.3-3, at 2 mW/channel, Gr1 and C1 are essentially unchanged, whereas the temperature of Gr2 has increased 1°C, and C2, although not quite at steady-state, has decreased in temperature by about 2°C.

It can be concluded that the local liquid pressure has an observable effect, but this effect is not a major contributor to the dynamics of the heat transfer and fluid flow within the wick structure. That is, the result is not significantly different from the previous orientation. The effect could become somewhat more significant as the pressure difference becomes larger (*i.e.*, for a 1 m diameter ring). Although the pressure difference was changed, the fluid temperature difference in the artery along the flow path was unchanged. This may be a more significant parameter, influencing the propensity to boil and the amount of the wick filled with vapor.

A third experiment was conducted, identical to the first test but with the vertical orientation reversed so that C2 was the lowest point and the first wick in the series, and C1 was at the highest point. The data are shown in Figure 3.4.3-6.

This test clearly separates the two wick materials based on thermal conductivity. The test also clearly indicates that position in the series chain is an observable effect, but other factors must also have an impact. The expected effect of this orientation change was, generally speaking, a reversal of positions between Gr1 and Gr2, as well as C1 and C2 in the graphs. Although the trend was in that direction, confirming that orientation is an influential parameter, there are clearly more important considerations. Higher heat transfer coefficients are observed at Gr1 and C1 regardless of liquid pressure or temperature. This suggests that quality control, or test piece uniformity, may be the major contributor to performance variations.

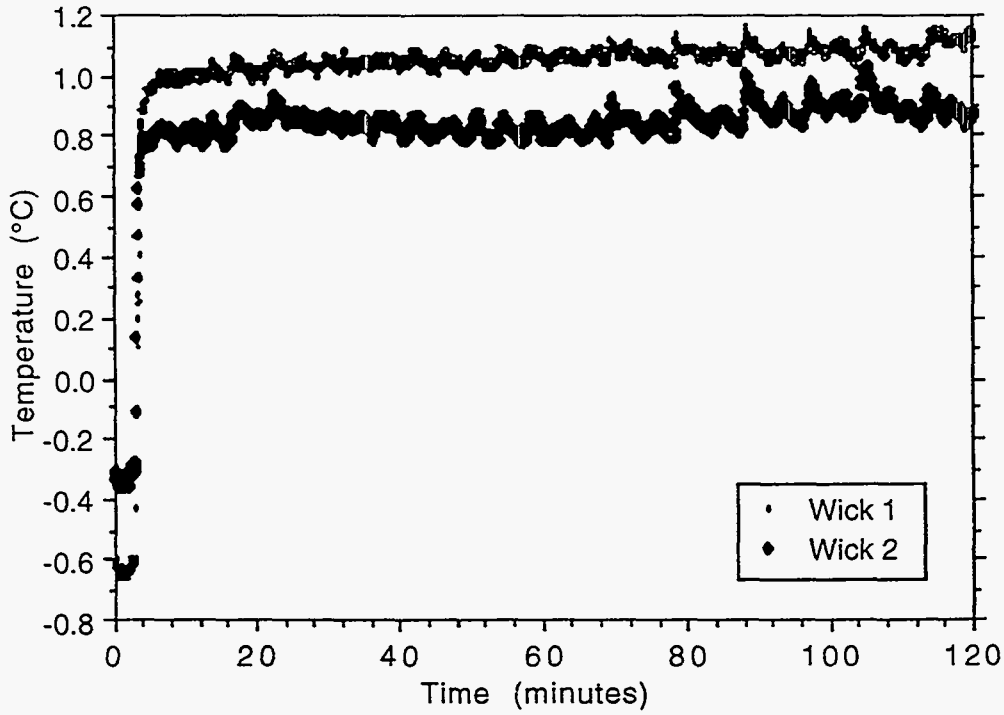

Figure 3.4.3-7 ΔT measured for 2 beryllium wick segments on a 120° arc segment at the design heat load.

3.4.3.2 Porous Beryllium Wick Test

Figure 3.4.3-7 shows the results from a 120° arc segment test with two beryllium wicks connected in series along the outer curvature of the ring. The spacing of the facets was the maximum possible on the segment. The beryllium wick was 1.0 mm thick. The pore radius was 6.8 μm. With this pore size it was reasonable to return to a positive pressure liquid feed system and to control bleeding by wick permeability and wick thickness. The permeability of this wick was 1.4×10^{-14} m^2, and the void fraction was 33%.

The results of a similar test with a graphite wick is shown in Figure 3.4.3-8. This test piece had 4 wick segments on a 120° arc segment, 2 near the upper extreme of the test piece and 2 near the bottom. This result is also very good, although not as good as for the beryllium. However, the cost of the graphite wicks is significantly lower than that of the beryllium; the beryllium cost (material plus machining) being about 100 times that of the graphite. Therefore, the graphite was pursued as the primary wick material. Further characterization of the beryllium was to be performed on a smaller scale so that a viable alternative to the graphite existed.

3.4.3.3 Wick Test Summary

From the preceding tests, it was obvious that the higher thermal conductivity wicks have a distinct advantage. The graphite wicks were found to operate stably at what was believed to be the final heat load of the system (1.5 mW/channel). However, there clearly was not a very large safety margin, but several ways to significantly improve that margin were readily apparent. First, we had not done any work on optimizing the pore sizes in the graphite material, or its solid fraction. We also showed that there was a large improvement available by going to the beryllium wick material. Finally, we could simply have increased the surface area of the wick to reduce the heat flux.

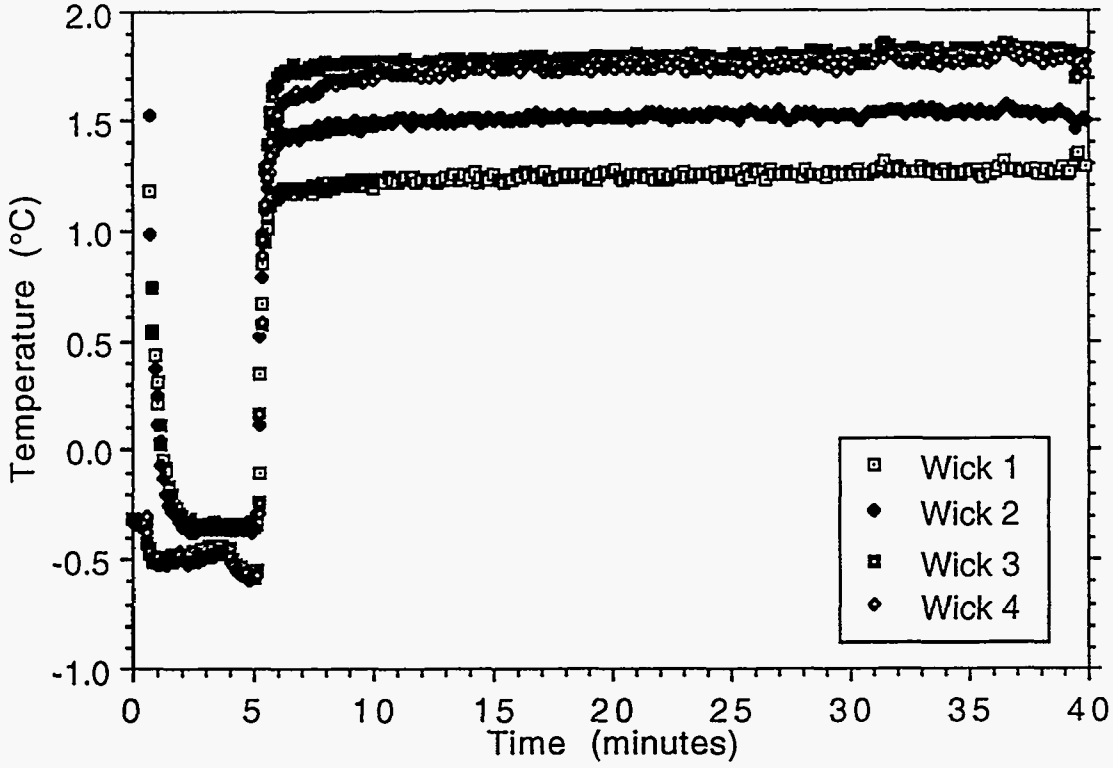

Figure 3.4.3-8 ΔT measured on 4 graphite wick wafers on a 120° arc segment at the design heat load.

3.4.4 Full Silicon Shell Cooling Tests

Testing of the butane cooling system with a fully populated 360° ring, 42 cm in diameter, was conducted. Due to time and cost constraints, and given the reasonable degree of success we had achieved with the 3.8 μm pore radius graphite wick material, wick, we chose to use it in this test. Because of assembly problems, only the heaters and wicks on the outer circumference at each end of the shell were active during these tests. That is, the silicon ladders on the outer circumference of the ring were operational, but the set of ladders on the inner circumference had no cooling, and they were not heated. The fully instrumented shell located inside a large butane vapor containment vessel and illuminated by the TV holography laser is shown in Figure 3.4.4-1.

Liquid supply to the ring began with a single feed line from the supply tank that was located about 3 m away. This feed line branched in a "Y" into two lines at the bottom of the barrel, one branch to the ring at each end of the barrel structure. Both of these branches were again split, to form a total of four lines, each serving 180° of arc, with butane flowing from the bottom and upward through the ring. The fluid exit was along a tube terminating above the level of the top of the ringand the supply tank, and far from the ring itself so that any overflow would not fall onto the ring. Furthermore, any vapor formation in the arteries would not lead to vapor lock, but rather exit naturally out of the open end of the artery. Ideally, a constant level of liquid could be maintained in these lines, above the top of the ring but below the tube exit.

In the first experiment, the piece was operated at power levels of 0.0, 0.25, 0.5, 0.75, and 1.0 times the design heat load of 1.0 W per simulated electronics package, or 2.0 W per wick, as there were heaters on both the upper and lower surfaces of the silicon (see Figure 3.4.4-2). Each wick has 2.4 cm^2 of exposed surface, for a power density of 0.83 W/cm^2.

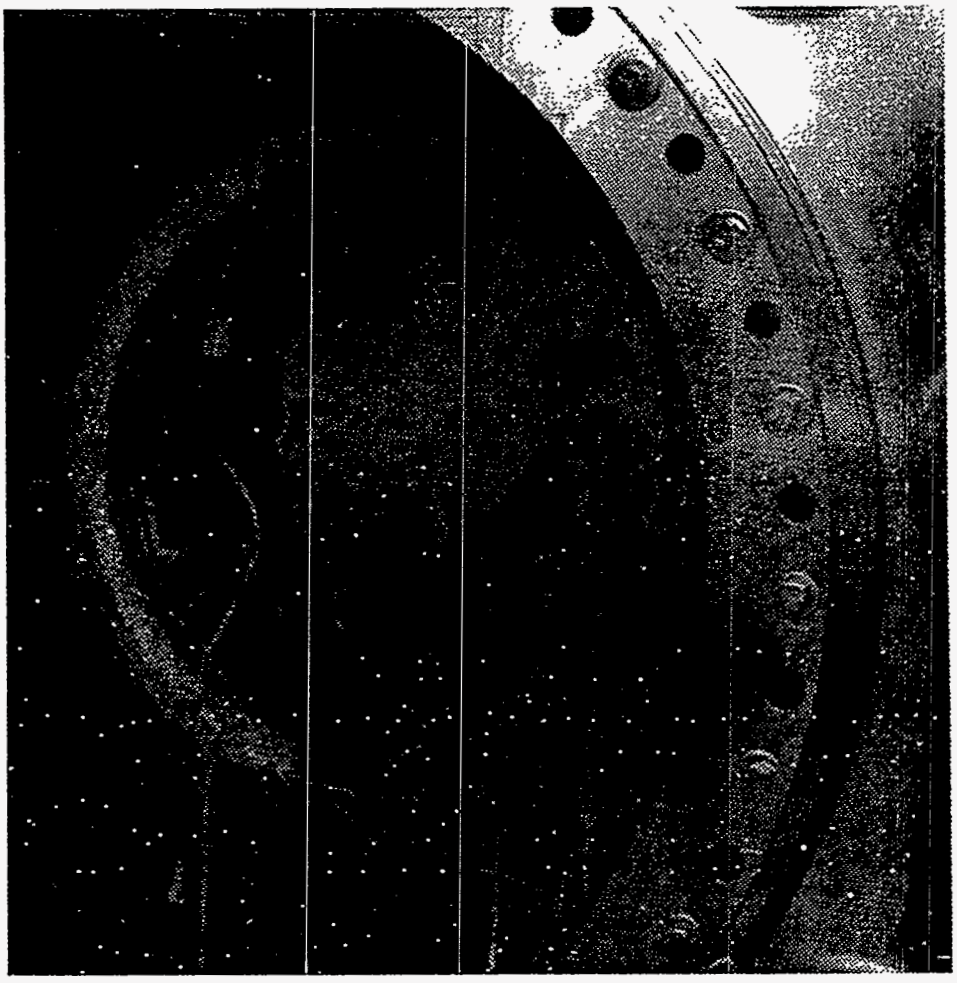

Figure 3.4.4-1 The fully instrumented silicon shell located inside a large butane vapor containment tank, and illuminated by the TV holography laser system.

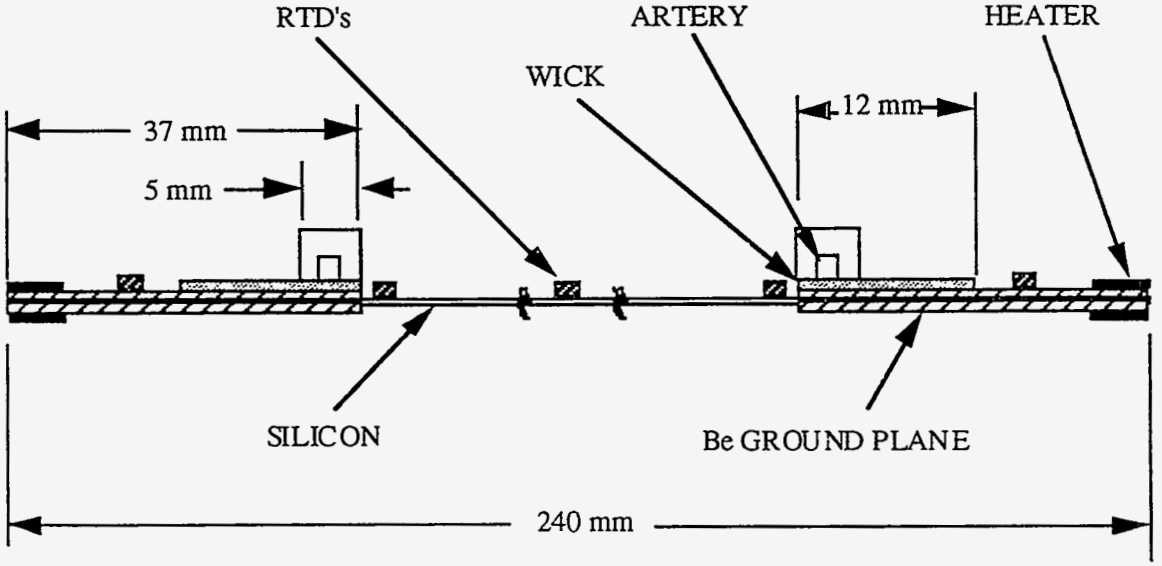

Figure 3.4.4-2 Cross-sectional view of a typical silicon ladder assembly.

One silicon ladder, at a near-vertical orientation (90° from the lowest point), was instrumented with five temperature sensors; one at the center, two on the silicon near the Be ground planes on each end, and one on each of the Be ground planes, between the cooling wafer and the heater, as shown in Figure 3.4.4-2. In addition, a temperature scan was made across this same silicon ladder with a remotely positioned IR temperature sensor.

The ΔT was observed to increase nearly linearly with power, with a ΔT of 3.5 to 4°C at full power, relative to the saturation temperature, which was calculated from the system pressure. Power was then increased to 1.1 W/cm^2. At this power density, cooling was interrupted by an apparent dry-out of the wick and temperatures increased exponentially until the heat load was reduced.

The temperatures measured by the IR probe did not agree quantitatively with those measured with the RTD's. This problem was not completely resolved, but the evidence indicated that the discrepancy was due to a combination of surface emissivity/reflectivity effects and possible IR absorption by the butane vapor, or some other effect of butane on the instrument. It was concluded that the IR data was qualitatively correct and just had to be renormalized. That was done by using the data from the RTD's. At the 0.83 W/cm^2 power level, the scans indicate that the silicon was isothermal to within less than 0.5°C. The reading over the wick surface was 2°C cooler than the reading over the silicon, and the temperature increased toward the outer edges of the Be ground plane where the heaters were located. The peak temperature at the edge of the ground plane was 2.8°C higher than the silicon wafer temperature.

Dripping from the test piece was not quantified, but it was observed to be acceptably low with this low permeability wick. We observed that the flow in the arteries became two-phase at some point along the path. This resulted in a two-phase release of liquid and vapor from the top of the artery due to the vapor expansion, even though the artery exit was above the static liquid supply level. It was believed that this could be eliminated by improved sub-cooling of the incoming liquid.

Subsequent testing was performed to examine system stability and deformation as a result of temperature changes due to tank cooling, introduction of butane vapor, and introduction of butane liquid. These results are shown in Figure 3.3.1-8.

Some butane system leaks were repaired and a final test was run with more complete instrumentation and at the nominal power level of 2 W per wick. In addition to the five thermistors on the one ladder reported above, five thermistors were added at the center point on five additional ladders around the circumference of the ring. The locations of the RTD's around the circumference are shown in Figure 3.4.4-3. Also, the IR probe was set up to scan the ring circumferentially at the midpoint of the ladders. As the view of the IR camera was blocked at the locations of several ladders, the numbering of the ladders in Figures 3.4.4-3 and 3.4.4-4 is not straight forward. The data collected from the fully instrumented shell in this test was comparable to the data reported above. The circumferential temperature log is shown in Figure 3.4.4-4. The square point indicators in the plot are the RTD outputs. The IR qualitative data was shifted to give the best quantitative match to the thermistor data. Shell wafer number 27 is the wafer that was discussed in detail above.

The trend is a slightly increasing temperature with elevation, highlighted by a marked increase in temperature with elevation on one side of the apex (wafer 17 is the highest point on one of the two arc halves). It is believed that the heat transfer here is degraded by the inability of the wick to remain wet under these power, liquid pressure, and liquid temperature conditions. However, the fact that this increase is not mirrored on the other semi-cylinder suggests that other factors are contributing, such as fabrication asymmetries, including asymmetric leaking and glue layer thickness variations.

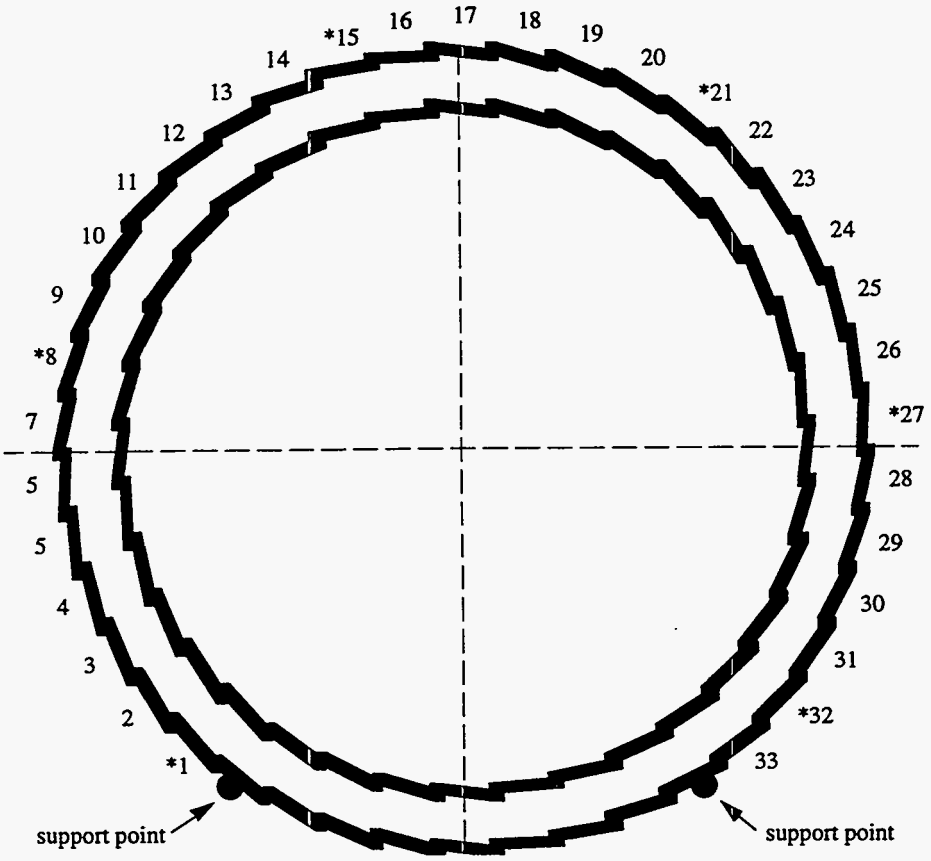

Figure 3.4.4-3 The locations of the RTD's around the circumference of the ring and the wafer numbering scheme used in Figure 3.4.4-4.

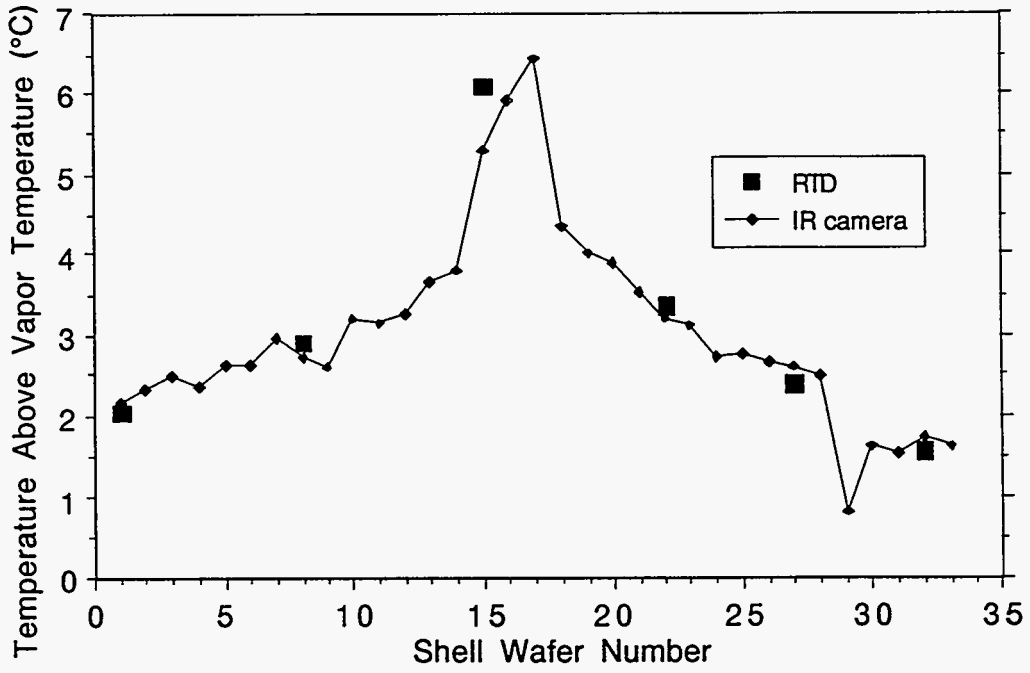

Figure 3.4.4-4 Temperature around the shell at full power. RTD data is as measured, while the IR data has been shifted vertically for best-fit to the RTD data.

3.4.5 Evaporative Cooling System Concluding Remarks

As we attempted to implement a heat pipe based cooling system, a number of modifications to the original design concept were found to be required. The first design modification came as a result of the observation that a passive, negative pressure, bleed-free system was not achievable. Also, early in the experimental program, a polystyrene foam wick was chosen to achieve a wick that would match the complex ring shape and have a minimal number of interconnections. The consequence of this choice was a system characterized by boiling within the wick structure as opposed to a free-surface evaporation.

The fluid delivery system was then modified to provide positive pressure liquid feed to the artery. The resulting bleeding had to be minimized by decreasing the permeability, or decreasing the pore size, of the wick structure. However, the smaller pore wicks resulted in higher ΔT's and larger temperature variations on a given test piece. An acceptable solution was not found.

A negative pressure system was possible with a high liquid velocity in the artery. Although this approach required that excess liquid be pumped back to the condenser from a sump, all the excess fluid was confined to the artery system, not dripping at random throughout the tracker. With this system, we could in principle use the largest pore polystyrene foam wick with the resultant lowest possible ΔT's.

Problems were encountered in the effort to mold these wicks. Ultimately, it was decided that the prospect of producing desirable polystyrene wicks by this molding process was too unlikely to continue the effort.

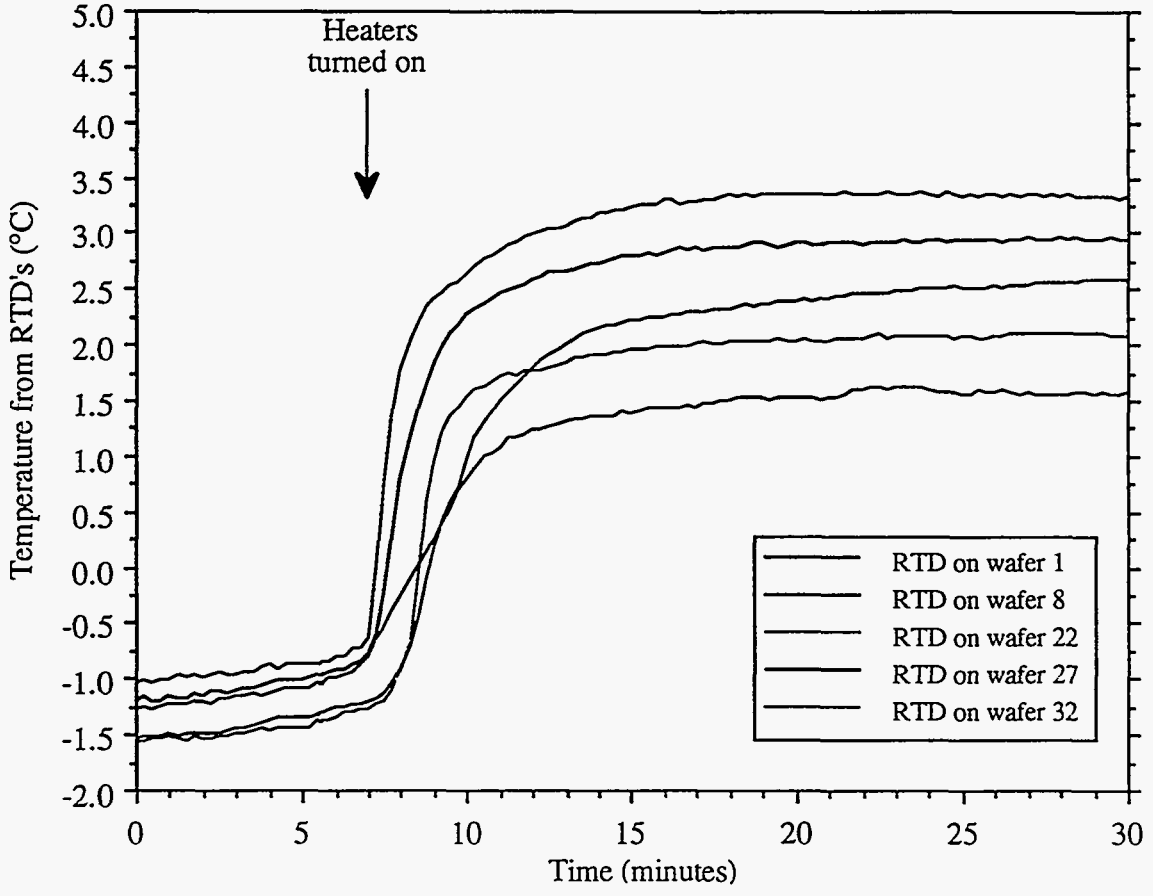

Figure 3.4.5-1 The long term temperature stability achieved during the test of the full ring prototype at a heat load of equivalent to 2 mW/channel.

Porous graphite and porous beryllium wicks replaced the molded polystyrene foam wicks. These new wicks were machined from rigid bulk material into thin wafers with the intention of mounting these wafers directly onto the beryllium ground planes. This design change sacrificed the simplicity of cooling a large number of silicon wafers using a minimum number of tubing connections, but it also moved the heat removal surface closer to the heat source. The test results from both of these wick materials were very good, especially considering that no optimization of the wick parameters was done, and we used off-the-shelf materials. Of these materials, the porous graphite is the primary wick material candidate on the basis of cost.

The tests performed indicate that an optimization of the evaporative cooling system would result in a workable cooling system. A ΔT of about $3.5 \pm 0.5°C$ could be realized. This ΔT could be lowered by increasing the wick area or by other parameter changes such as the wick solid fraction, its pore size or its permeability, or through the use of porous beryllium wicks.

We finally constructed a full shell prototype and achieved very stable temperature operation over a long time period, as shown in Figure 3.4.5-1, at a heat load comparable to electronics heating of 1.5 mW per channel.

3.5 Water-Based Cooling

On the basis of the expected performance of an optimized evaporative cooling system, the merit of such a system must be reevaluated in the context of simplicity, reliability, and safety. The use of a flammable working fluid and the requirement for a hermetically sealed containment impose constraints and design problems unique to this system that would not be encountered in single-phase cooling with water/anti-freeze solutions. Therefore, as an alternative, we began to explore such a single-phase system.

We performed scoping calculations to determine the feasibility of removing the estimated 13 kW of waste heat generated by the electronics by conduction to a water-alcohol solution. Subdividing the tracker cooling flow into three roughly equal circuits, one for each of the two forward regions, and the third for the barrel region, we determined that the cooling could in theory be done with mass flow rates of between 0.2 and 1.2 kg/sec for each of the 3 flow circuits. Those mass flow rates correspond to 6°C to 1°C bulk fluid temperature rises, respectively. With those flow rates, we found that it was possible to keep the flows laminar, and at the same time construct a negative pressure system, without being forced to unreasonably large tube diameters.

Some preliminary tests were done to investigate whether or not either laminar or turbulent flow operation of a system could be maintained without introducing vibrations, and without introducing unwanted distortions due to temperature rises in the cooling fluid as it flowed past a string of heat loads. A 120° arc segment with silicon modules was constructed with water cooling channels, and the mechanical stability of the segment was monitored both with and without a heat load being applied through resistive heaters which simulated the expected electronic heat load. The arc segment was operated at room temperature and was monitored with the TV holography system. The results are given in Section 3.3.1.5 and were promising but at the same time incomplete as the prototype tested was rather crude, and also was not a full shell which is required to give a barrel shell its full structural strength. Those tests were discontinued shortly after they began due to the termination of the SSC program.

With the SSC close-out funds that we have subsequently received, we are planning to construct a full shell with a more carefully built water cooling system. The shell will be equipped with resistive heat loads, operated at both room temperature and near 0°C, and its performance monitored with an IR thermometer and the TV holography system. We will issue a detailed report at the end of that work, which in addition to the test

results, will also include the results of more complete calculations of the flow parameters needed for a 13 kW system.

In closing, it should be noted that a water/alcohol based solution is not without its own set of potential problems. The coolant is incompatible with the electronics, and a leak could have devastating consequences. Even if the system is operated as a negative pressure "leakless" system, in which leaks would suck gas into the artery system, rather than let water seep out, problems could still arise during maintenance periods when the negative pressure would have to be removed. Finally, the water based system does not have naturally have a gas flow (as the evaporative system has),which may be required to deal with leakage current induced heating of the detectors. Such a gas flow system may well have to be added to the water based system further complicating its design. All these potential problems remain to be explored and dealt with.

4.0 CONCLUSIONS AND RECOMMENDATIONS

The SDC Silicon Tracking Subsystem R&D mechanical engineering activities encompassed many of the key issues found in very large silicon-based elementary particle tracking detectors. Although, the essential ingredient of this fairly broad based study was proof-of-principle for key design concepts embodied in the tracker construction approach, we chose not to overlook an opportunity to advance our overall conceptual tracker design concept, and assembly and alignment plans. We felt that this broadly based program would ensure that our prototyping demonstrations were well focused on design concepts that in the end would be buildable, and serviceable. In connection with these efforts we established preliminary solutions for overall assembly and alignment, and cable routing for services (*i.e.*, power and data transmission). This report largely represents a summary of the key prototype tests that were essential to demonstrating the basic concepts, and tends to gloss over many technical accomplishments of an apparent less critical nature. Nevertheless, it was the many smaller and seemingly minor developments that allowed the production of the successful prototypes that demonstrated the feasibility of our design concepts. Time constraints demanded that we summarize largely the key program elements in order the results not be lost to the high energy physics community at large.

We demonstrated that our construction concept for building a cylindrical array of concentric silicon detectors was stable to the order of 1 micron, using an evaporative cooling system. To this end a 42 cm diameter silicon shell was constructed, and the capability to remove silicon detector modules from this basic structure was proven viable. With achievement of this objective, we largely satisfied the chief concerns expressed regarding the overall design approach. Our technical accomplishments in this area, coupled with advances made in constructing composite structures, added confidence to our design approach for the large planar arrays used in the forward tracking regions.

Considerable development progress was made on the evaporative cooling system. The final arrangement was composed of individual porous graphite wicks mounted on the detector modules. The close proximity of the wick to the electronic heat load worked well in minimizing the overall silicon detector temperature. With the graphite porous wick, the mean silicon temperature was held to roughly 3 °C. Given additional time, the graphite wick material would have been replaced with a porous beryllium wick. This material would have reduced the mean silicon temperature to the order of 0.3 °C. However, much effort remained on the evaporative system as we approached the end of the fiscal year, and the additional work was not confined solely to a wick material choice. Issues that had to be addressed were operational in nature, and long term system performance. The considerable amount of work remaining provided impetus for investigating alternative cooling means.

On the basis of on our experimental cooling studies leading up to the stability tests, we felt it would be viable to construct a forced convective water-based cooling system to replace the evaporative concept. We appreciated that implementation of the water-based system would introduce the prospect of greater fluid inventory within the tracker volume, and potential damage to the silicon detectors and electronics from leaks. Our efforts were being focused on these issues when the SSC program was canceled. We did, however, perform exploratory tests that suggested the approach being taken would not lead to tracker stability problems from fluid induced vibrations. This issue has been expressed by other investigators as a potential draw-back of the forced convective system.

Numerous advances were made in the areas of optical alignment concepts, TV Holographic metrology measuring systems, and the semi-automated precision assembly unit for constructing the overall tracker system. These areas were discussed in detail in

this report. The concepts being developed in these areas are adaptable to any precision detector system.

It is recommended that in the process of closing out the SSC Program that the critical technologies established during this program be completed in sufficiency to allow preservation of the knowledge and expertise gained to date. The results of the work discussed in this report have direct applicability to large scale silicon based detectors, as well as other precision elementary particle detectors. The areas that should be specifically addressed in further close-out work are:

- Complete construction and demonstration of the semi-automated work station, including associated optical alignment components, to achieve repetitive placement of detector modules to 5 microns,
- Complete the construction of the TV Holographic metrology measuring equipment. Equipment is capable of resolving motions to less than a micron over very large viewing areas in real time,
- Complete the water-based cooling experiment and provide comparative stability data to that achieved with the evaporative system.

The Department of Energy's investment to date on this mechanical engineering program has been on the order of $6-7 million dollars. For a fraction of this expense it would be possible to preserve this technology for future high energy physics experiments.

APPENDICIES

A - Composite Materials Selection and Testing

A.1 Materials Considerations

A fundamental decision was made during the SDC Tracker conceptual design phase to use composite materials to achieve the ultralightweight, stable structure objectives. Aspects of the design associated with this design decision are contained in the body of this report. In spite of the considerable progress made in composite materials by industry, there were gaping holes in our understanding of how best to achieve our stringent objectives, particulary from a fabrication process. In addition, there was a lack of information on specific engineering property data for composite materials of interest, their stability characteristics, and their behavior in our unique tracker environment. Consequently, we found it necessary to conduct material property investigations. Initially our prototype designs proceeded on the basis of available published data and standard processing methods. From this vantage, we launched our experimental endeavors realizing that time and financial resources were quite limited, and that the scope of these investigations would be constrained. Since the baseline tracker design drew upon composites composed of continuous and discontinuous graphite fibers in a polymeric resin system, our study spanned largely those topics.

Material properties for continuous fiber and discontinuous fiber matrices are quite different. One may recall we chose a discontinuous fiber matrix for molded parts and the continuous fiber matrix for flat and shell sandwich construction techniques. These topics were addressed in the body of the report. The following sections summarize the material evaluations made for these two different types of matrices. Our studies evaluated general mechanical physical properties before and after exposure to combined radiation and a hydrocarbon (butane).

A.2 Resin and Laminate Materials Testing

The materials testing program pursued mechanical performance information on the advanced-composite-materials systems of interest. Very little information was found in the literature for these materials. The determination of the mechanical properties of these material systems was required to ensure that these materials did indeed possess the characteristics required for tracker stability. The need to define and quantify higher order stability effects, such as hygrothermal, would have been obviated if the mechanical constraints of the STS design had not been so severe. Parallel mechanical test programs were performed at LANL and Ketema/Programmed Composites, Inc. (PCI) of Brea, California. Sandia National Laboratories (SNL) of Albuquerque, New Mexico also evaluated the elastic moduli of a number of samples. This parallel testing program was designed to promote confidence and enhance quality assurance. All specimens were fabricated by PCI who subsequently tested 10 of each type and forwarded 5 specimens to LANL. Table A.2-1 demonstrates the scope of the mechanical testing program.

A.2.1 Specimen Fabrication

PCI fabricated a full complement of neat resin, longitudinal-, transverse-, and quasi-isotropic- (QI) continuous fiber specimens for mechanical testing. Fiberite, Inc. 954-3 cyanate ester (neat) resin was used for all specimens, while Amoco P-75S high-modulus graphite fiber was used in the fiber-bearing specimens. Properties of P-75S are presented in Table A.2.1-1.

Table A.2-1 Mechanical Properties Test Matrix

Test	Neat Resin	Uniaxial	QI
0° Tensile Strength, Modulus, and Poisson Ratio	x	x	x
0° Compressive Strength and Modulus	x	x	x
In-Plane Shear Modulus and Strength	x	x	—
Interlaminar Shear Modulus and Strength	—	x	—
90° Tensile Modulus and Poisson Ratio	x	x	x
90° Compressive Modulus and Strength	x	x	x

Table A.2.1-1 Properties of Amoco P-75S Graphite Fiber[a)]

Tensile Strength	1.9 GPa
Tensile Modulus	520 Gpa
Density	2.0 Mg/m^3
Filament Diameter	10 μm
Elongation at Break	0.4%
Elastic Recovery	100%
Carbon Assay	99+ %
Surface Area	0.35 m^2/g
Longitudinal Thermal Conductivity	185 W/m°K
Electrical Resistivity	7 mΩ-m
Longitudinal CTE at 21°C	-1.35 ppm/°K

a) Amoco Performance Products, Inc., Product Sheet F-5817, Rev. 4., "THORNEL Carbon Fiber P-75S 2K", 1320 Willow Pass Road, Ste. 401, Concord, California 94520

The characteristics of interest for the 954-3 resin system are high mechanical properties, very low micro-cracking, and low moisture absorption. Those characteristics make the cyanate ester resins ideal for use in low mass, dimensionally stable structures. The resin processing is similar to that needed for epoxy systems used in structural composites, including a 177°C autoclave cure cycle. However, in contrast to epoxies, the pure cyanate resins exhibit low tack and also have a low minimum viscosity (below 100 centipoise) during cure. The low viscosity reached during the cure makes a laminate more susceptible to variation in fiber volume because resin bleed is more difficult to control accurately and consistently. Another factor requiring control is the resins' hydroscopic behavior in the uncured state. Neat resins and prepregs with cyanate ester must be prevented from extended exposure to high humidity to prevent voids in a

laminate or neat resin casting caused by water vapor formed during the curing process; the source of the vapor being water in the resin which was acquired while the resin was in its uncured state. The resin or prepreg must be sealed in airtight bags at all times when not in use. Standard methods for packaging as used for epoxy/fiber prepregs are adequate if adhered to closely.

Even though the resin cure cycle is very much like that of an epoxy resin, considerable effort was needed to develop a cure cycle and bleeding scheme that produced consistent, acceptable fiber volume results. Target fiber volume was 60% to 65%. The cure cycle stipulates when pressure is to be applied to the laminate and at what viscosity or state of gelation. Definition of the bleeding scheme involves specification of the type and number of plys used to absorb resin from the laminate to control resin volume. The bleeder plys used were glass fabrics (styles 112, 120, 181, and 220 in various combinations) which have a greater degree of consistency than non-woven bleeder materials.

A total of four autoclave cures were made to determine a cure cycle and bleeding scheme that produced acceptable fiber volumes. The first test was aimed at verifying Fiberite's recommended cure cycle, C-9, and used a bleeding scheme that would be appropriate for most resins such as epoxies. The cure requires a temperature hold at 121°C for one hour, with the pressure being applied 15 minutes into the hold. After the hour at 121°C is completed, the temperature is increased to 177°C for a two-hour hold. This cure cycle produced fiber volumes up to 69% which may cause a significant degradation in interfacial properties of the laminate. A matrix of laminates was then fabricated on subsequent autoclave runs using various bleed layers and damming techniques for controlling resin flow. PCI's Signature Process Control was used during several of these runs which characterized the capacitance response of the resin during cure. Based on the information collected, the C-9 cure cycle was modified to delay pressurizing the autoclave until after full staging at 121°C and the temperature had reached 149°C in the subsequent step. The Signature Process Control monitoring also demonstrated that cross-linking of the polymer was generally complete after one hour at 177°C, the additional hour not contributing significantly to the cross-linking of the resin matrix but serving to ensure complete cross-linking throughout the laminate.

After perfecting cure cycles appropriate for each type of specimen, detailed laminate production began. The following bleeding and molding schemes were used. The modified cure cycle with controlled resin bleeding was used for the fabrication of the required test specimens. The 8-ply unidirectional and QI specimens were bled with one ply of 112 style and 120 style glass fabric, respectively. The 20-ply laminates were bled with one ply of 181 style glass fabric. All laminates used cork dams. The 160-ply laminate for transverse shear testing was layed-up in a 15.2 cm x 15.2 cm aluminum mold, covered with bleeder plys and a caul plate, then autoclave cured. The QI laminates used the following repeated ply sequence [0/45/90/135].

The 954-3 neat resin material was cast between glass plates separated by a silicone rubber gasket. A total of three molds 30.5 cm x 30.5 cm were prepared. The resin was melted and degassed in a vacuum oven preheated to 225°F After the resin exhibited a foam "break" during degassing, the resin was poured slowly onto the molds. The filled molds were then cured for three hours at 177°C. The cast resin samples were machined to thickness to remove surface voids.

Percent fiber volume and void content were measured on all laminates using the acid digestion method per ASTM-D-3171. For the neat resin castings only the void content was measured. The results of these tests are shown in Table A.2.1-2.

Sources of error which account for negative calculated void content are due to the use of theoretical fiber densities and loss of fiber during filtering of the fibers. High-modulus fibers are particularly sensitive to fiber loss during the filtering process. Void content measurements that are negative should be assumed to be zero within the accuracy of the test procedure.

Table A.2.1-2 Percent Fiber Volume and Void Content of Materials Tested

Laminate	Average Fiber Volume (%)	AverageVoid Volume (%)
8-Ply QI	62.2	+0.02
8-Ply Uni	60.3	-0.95
20-Ply QI	58.5	-0.37
20-Ply Uni	58.7	-0.77
160-Ply Uni	55.6	+0.77
Neat Resin	—	+1.68

The tensile coupons used for the composite specimens were per ASTM-D-3039 standards, and cut 12.7 mm wide by 228.6 mm long with 31.8 mm long G-10 tabs with tapers. The neat resin test specimens were dog bones per ASTM-D-638 standards and cut 114.3 mm long by 12.7 mm wide. The 20-ply compression test specimens for the Wyoming Modified Celanese method were 114.3 mm long by 12.7 mm wide. G-10 tabs 31.8 mm long with no tapers were used.

Table A.2.2-1 American Society of Testing and Materials Standards

Test	ASTM Designation
Acid digestion composition determination	ASTM-D-3171
Tensile test	ASTM-D-3039-76
Celanese compression test	ASTM-D-3410
Iosipescu shear test	approval pending
Compressive properties of unidirectional or crossply fiber-resin composites	ASTM-D-3410-87

A.2.2 Testing Systems and Fixtures

LANL used a Materials Testing Systems, Inc. 880 hydraulic device while PCI used a SATEC 50 UD hydraulic loading machine. All test specimen fabrication and testing was performed using applicable ASTM standards listed in Table A.2.2-1. The specimen grips used for the tensile loading were manufactured by MTS, #649, and are of a side-loading and mechanical wedge design. The individual test fixtures used for the program included the Celanese compression test fixture which was first introduced by the Celanese Corporation in 1971 and was later accepted by ASTM as ASTM-D-3410 in 1975. The two halves of each cone-shaped wedge grip, which are provided with alignment pins both between themselves and with the other wedge grip, are bolted together after the specimen is inserted between them, using the spacer bar provided to establish the distance between grips. Overall alignment of the fixture halves is also aided by a close-fitting sleeve that slides over the assembly after the specimen is installed and the spacer bar removed. The Celanese fixture is very compact, weighing only about 10 lb., making it easy to handle in use. However, it is frequently criticized because of its cone-in-cone arrangement of the wedge grips. In order to maintain full surface contact

between each pair of split half-cones and the mating conical cavities in the end blocks, the tabbed ends of the specimen must be fabricated to a precise thickness. Otherwise, the split-cones will not be circular when assembled.

The Wyoming Modified Celanese fixture was used for all compressive loading tests and is designed (grips flush with the body blocks) for a nominal specimen thickness in the tab regions of 4.2 mm. With the grips protruding up to 6.4 mm (a readily acceptable amount), a tabbed specimen up to 6.4 mm thick can be accommodated.

The standard gage length (*i.e.*, the distance between tabs), for all compression test fixture configurations following the general guidelines of ASTM D-3410 standard is 12.7 mm. Thus, the tab length for standard specimens used with the Wyoming Modified Celanese Compression Test Fixture is 50.8 mm. All parts other than the cone-shaped wedge grips, alignment pins, and fasteners are made of 1018 cold rolled steel, black oxide treated to reduce rusting and corrosion when kept lightly oiled. The serrated wedge grips are A6 tool steel, heat treated to R_C55, to provide durable gripping surfaces.

The Iosipescu shear test fixture was actively developed for use with composite materials during the early 1980s. An ASTM standard has just been written and is pending approval. The standard test specimen is 76.2 mm long, 19 mm wide, and of any thickness up to 12.7 mm. Typically, a specimen approximately 2.5 mm thick is used. A 90° notch is machined into each edge of the specimen, and a strain gage can be mounted to monitor shear strain.

A.2.3 Test Results and Conclusions

The test methods used by LANL and PCI were similar, conventional load frame- and load-cell-based. SNL, however, used non-destructive methods, scanning electron microscopy (SAM), to determine the elastic properties of specimens. The data generated by all institutions and methods were comparable and contributed to confidence in the findings.

The neat resin test results were the most uniform among the testing institutions as demonstrated by Table A.2.3-1. This is reasonable because few processing steps are required and fibers are not introduced, resulting in less variation between samples. Theoretically, there is no difference in the fixturing or execution of the tests for neat resin versus fiber-bearing samples, even though the lowest level of loading is sustained by neat resin. The elastic tensile, compressive, and shear moduli for the neat resin are smaller than the highly cross-linked epoxy resins such as 3501-6 and 934. The cyanate ester chosen has comparable elastic performance and much superior moisture absorption and micro-cracking characteristics however. This situation is acceptable because the structural components will primarily derive their stiffness from the high elastic modulus reinforcing P-75S fiber. Also, the moisture-induced dimensional instability, which is dominated by the resin, will be diminished by the choice of this materials system.

The post butane and 10 Mrad irradiation exposure test results for the neat resin are very encouraging. The minimal, perhaps even statistically insignificant, decrease in the elastic mechanical performance indicates that little fabrication stress release is occurring in the resin due to those conditions. The absence of dense cross-linking is responsible for this effect in the cyanate ester resin.

The comparison of LANL's test program results with that of other published data can be seen in Table A.2.3-2. As previously mentioned, the scarcity of data on cyanate ester resin systems led to the choice of the seminal C.C. Chamis data[9] for highly cross-linked polymeric neat resins as a means for comparison. Also, the recently published data for 954-3 cyanate neat and fiber-bearing resin by its manufacturer, Fiberite, Inc., are used for comparison. As demonstrated by the Table, 954-3 is comparable to an intermediate modulus, high strength (IMHS) hygroscopic resin according to Chamis. The differential in shear and tensile strength seen is more exaggerated as well as confusing.

The 954-3 results demonstrate a 44% lower shear strength than the IMHS while 954-3 possesses a 35% higher tensile strength. The manufacturer's estimate of the resins' tensile strength differs by only 6% from that of the LANL test program. This discrepancy in conjunction with the absence of the manufacturers' data for ultimate shear strength renders the LANL shear strength data questionable. It is note worthy that only one institution performed elastic property tests for the program, hence their results have not been corroborated. Of greatest importance, however, is the fact that the elastic properties of the 954-3 resin are well defined and in agreement with the manufacturer's published data where available and that the values found are highly desirable and well matched to our needs.

Table A.2.3-1 Mechanical Properties Test Results for P-75S/954-3 Laminates Normalized to 60% Fiber Volume Fraction

Mechanical Property	Test Institution	Neat Resin Only	Specimen Description 0°	90°	QI
Elastic Tensile Modulus (GPa)	LANL	3.7	323	6.9	100
	LANL*	3.4	321	6.6	110
	CONV	3.8	324	6.4	96.5
	NDE	3.7	280	8.1	97.5
Elastic Comp. Modulus (GPa)	LANL	3.7	300	6.7	81.3
	LANL*	3.5	283	6.8	81.3
	CONV	3.4	270	6.2	77.2
Elastic Shear Modulus (GPa)	LANL	1.2	4.5	1.7	—
	LANL*	1.1	4.8	1.7	—
	CONV	1.2	4.0	1.6	—
Poisson's Ratio	LANL	0.38	0.25	0.0043	0.28
	LANL*	0.37	0.25	0.0031	0.31
	CONV	0.40	0.32	0.0063	0.33
	NDE	0.40	0.32	0.0060	0.33
Ultimate Tensile Strength (MPa)	CONV	60	1000	23.4	294
Ultimate Comp. Strength (MPa)	CONV	—	337	41.7	131

* Denotes results for specimens environmentally conditioned by 10 Mrad ^{60}Co and butane.

The fiber-bearing specimen data is generally consistent. The non-destructive testing methods demonstrate the largest departure from other findings. Again, the butane and 10 Mrad radiation exposure have a statistically insignificant effect on the mechanical performance of the laminates. The largest performance reduction is seen in the elastic shear modulus, differing by 15% after environmental conditioning. Closer inspection of this data reveals that the spread of the data from the three testing institutions is a maximum for this case. As noted, the non-destructive method differs from the average of the destructive method by 21% whereas the conditioned sample differs from the destructive test average by only 3%. This places the accuracy of the non-destructive data in serious question for this attribute.

The lone laminate data previously available for 954-3 is for a unidirectional lay-up normalized to a 60% fiber volume fraction published in November, 1992 by Fiberite, Inc. The agreement of the LANL test program data with this is impressive for both the elastic and inelastic mechanical properties of the laminates, save the shear strength previously described.

Table A.2.3-2 Published Data on Mechanical Properties for Laminates Normalized to 60% Fiber Volume Fraction

	LANL Averag		Chamis Data[a]	Fiberite Data[b]	
Test	Neat Resin	Laminate 0° Uni.	IHMS Neat Resin	Neat Resin	Laminate 0° Uni.
Elastic Tensile Modulus (GPa)	3.7	309	3.4	2.76	296
Elastic Compressive Modulus (GPa)	3.6	285	___	___	241
Elastic Shear Modulus (GPa)	1.3	4.3	___	___	___
Poisson Ratio	0.39	0.3	0.41	___	___
Ultimate Tensile Strength (MPa)	60	1000	48.2	56.5	1000
Ultimate Compressive Strength (MPa)	___	337	145	___	359
Ultimate Shear Strength (MPa)	27.1	39.2	48.2	___	58.6

[a] C. C. Chamis, "Simplified Composite Micromechanics Equations for Hygral, Thermal, and Mechanical Properties," *SAMPE Quarterly*, April 1984, p. 17.

[b] ICI Fiberite, "ICI Fiberite Materials Handbook," 2055 East Technology Circle, Tempe, Arizona 85284, November 1, 1992, Rev. C.

The overall conclusion of the mechanical properties test program is that the P-75S/954-3 materials system is now mechanically fully described and qualified. All elastic moduli and the Poisson ratio of the system were evaluated by independent institutions using both destructive and non-destructive means to obtain comparable results. Inelastic parameters, though of lesser importance, were also defined, compared to published data and found to be acceptable. The system's sensitivity to a combination of liquid butane and 10 Mrad of irradiation was investigated and found to be negligible. A comparison to published data for an intermediate modulus, high strength densely cross-linked resin and to the manufacturer's data for the neat and fiber-bearing resin proved to corroborate the results from their test program. This important agreement provided confidence in the materials system's ability to meet the STS's performance objectives. Previously, the elastic properties of the materials system, as stated by the manufacturer in private communications and inferred from other technical sources, had provided the only basis for STS performance calculations. In summation, mechanical properties testing program has demonstrated the acceptability of the P-75S/954-3 materials system's mechanical performance for achieving STS baseline performance objectives.

A.3 Discontinuous Fiber Composite Material Development

A.3.1 Thermal Conductivity Enhancement

Chopped fiber/resin compression molded products are theoretically quasi-isotropic. However, long fibers (*e.g.*, fiber length greater than product wall thickness) when compression molded into ultra thin shapes will be forced to be parallel to the mold wall. Both the resin and the transverse fiber thermal conductivity are low; hence, thermal conductivity through the wall cross section is quite low, <1 W/m-°K. In the SDC cooling ring application, it was important to minimize the thermal gradient from the readout chips to the cooling system's evaporative wick structure; this required a minimum gradient through the ring wall. If the gradient were not minimized, the silicon strip detectors would operate considerably above the desired 0°C. This topic was presented in detail in Section 3.2.3.2. To this end, we have investigated means of enhancing the transverse thermal conductivity of the composite cooling ring, including the loading of the adhesives with high thermal conductivity particles.

The thermal gradient through the cooling ring was predicted using properties for the composite thermal conductivity (both transverse and in-plane), and the evaporative wick film coefficient. Finite element (FE) solutions were obtained as a function of transverse thermal conductivity (k_t) for a constant heat flux. The solution accounted for the thermal fin effect of the cooling ring side wall. For a low k_t (*e.g.*, 0.8 W/m-°K) characteristic of the MX4952 carbon/phenolic system, heat flows down the ring side wall, as well as through the top surface of the ring, as shown in Figure A.3.1-1. The temperature gradient for the 1.8 W/cm^2 design electronic chip heat flux is ameliorated by the higher in-plane composite wall thermal conductivity; however, not sufficiently to satisfy our design goals. The results of this study clearly identified the benefit of achieving a k_t of 4 W/m-°K.

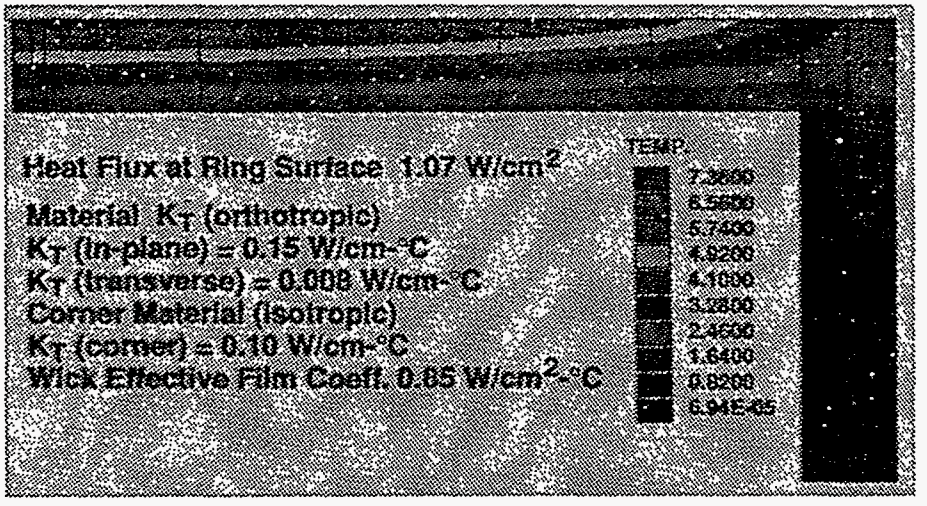

Figure A.3.1-1 Heat flow in ring: (k_t = 0.8 W/m-°K).

Our first inclination in enhancing the transverse composite ring thermal conductivity was to fill the resin system with particles. Clearly, at the onset, we did not appreciate to what extent introduction of particles would enhance the k_t in a composite ring, or interfere with the ring's moldability. We knew that the complex ring geometry necessitated compression molding with fiber lengths much shorter than standard chopped prepreg material. The structural aspects of the ring design also dictated a high fiber volume fraction; consequently, the volume fraction of additional particulates in the

resulting matrix would be quite limited. From this vantage point we initiated a cursory investigation. We experimented with three different techniques: resin loaded with an additive; resin filled with a combination of discontinuous graphite fibers; and particulates, and finally, random orientation of discontinuous fibers. Following the brief experimentation period, we concentrated on comparing our results with other related work to form a basis for moving forward in the ring molding development effort, reference Section 3.2.3.4. Our filler additive study was confined to aluminum nitride and diamond particles.

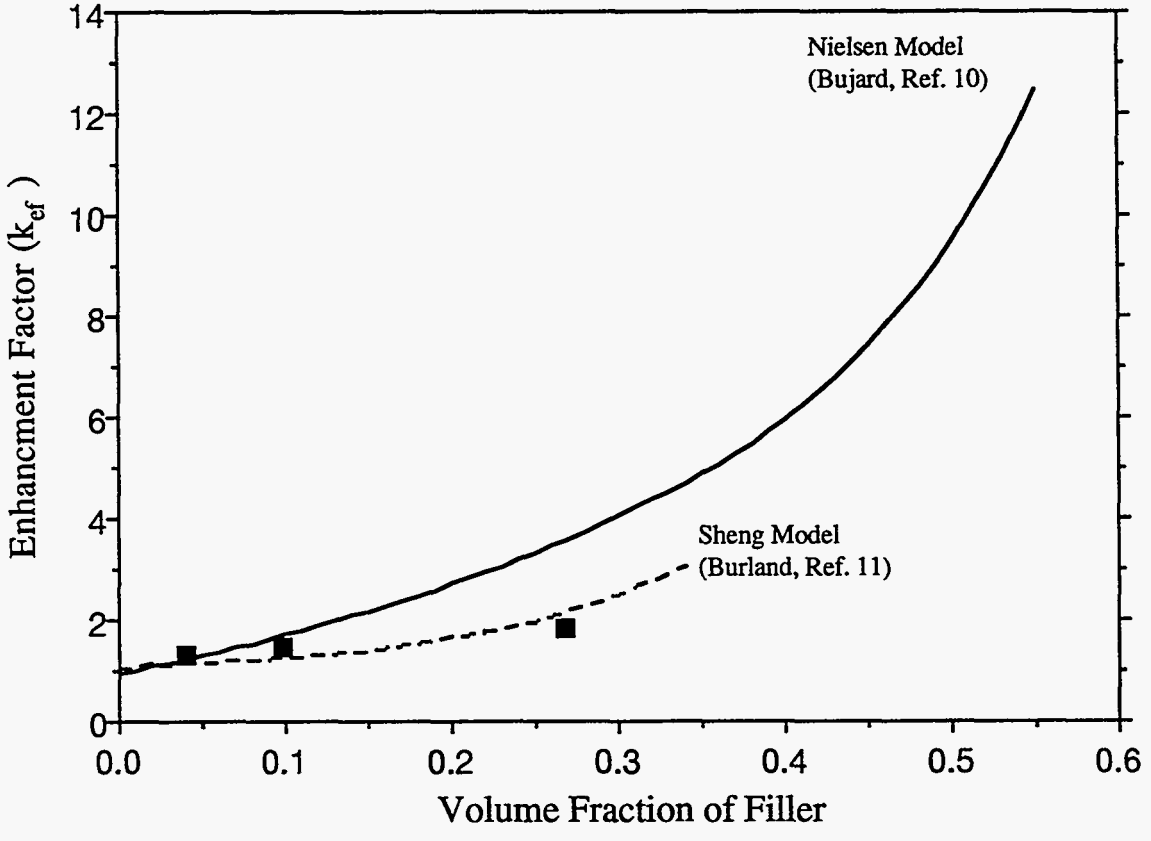

Figure A.3.1-2 Thermal conductivity enhancement factor, k_{ef}, of cyanate ester resin filled with aluminum nitride particles.

The thermal enhancement of aluminum nitride spherical particles in a cyanate ester resin system is shown in Figure A.3.1-2. The thermal conductivity was evaluated for discrete volume fractions up to a maximum of 27% . Specimens were cut from 3.1 mm thick compression molded disks (3.45 MPa), and tested by a standard laser flash diffusivity technique to obtain the thermal conductivity. These results were compared with experimental data previously published by Bujard[10].

Bujard developed the curve in Figure A.3.1-2 using the Lewis-Nielsen model to fit his measured thermal conductivity data. The Nielsen model can be characterized in terms of an enhancement factor k_{ef}, where:

$$k_{ef} = \frac{k_s}{km} = \frac{1 + ABV_f}{B\psi V_f} \text{ and}$$

k_s = sample thermal conductivity

k_m = neat resin thermal conductivity
k_f = filler thermal conductivity
B = $(k_f/k_m - 1)/(k_f/k_m + A)$
ψ = $1 + ((1 - \phi_m)/\phi_m^2)V_f$
A = factor depending on particle geometry (1.5 for spherical particles)
V_f = filler volume fraction
ϕ_m = maximum volume ratio obtained from sedimentation experiments

Bujard obtained a best fit to his data using a shape factor A of 8 with a particulate thermal conductivity of 6 W/m-°K, which he indicates is representative of "particle clusters". The 6 W/m-°K contrasts with the intrinsic thermal conductivity of aluminum nitride which is 280 W/m-°K. He also obtained a maximum packing fraction parameter (ϕ_m) of 0.62. Bujard concluded that the high shape factor of 8 versus a value of 1.5 for spherical particles was a consequence of the formation of thermally conductive clusters and could be explained through bond percolation theory.

A predicted curve extracted from a reference[11] is also depicted in Figure A.3.1-2. This model originates with Sheng[12]. Sheng's predicted curve is for randomly oriented ellipsoidal particles with filler to resin thermal conductivity ratio of 100. Reference 11 also shows that when this ratio exceeds 50, very little further increase in thermal conductivity enhancement is obtained. This observation is also true of the Nielsen model, where, as the parameter B approaches 1, the magnitude of the particulate material thermal conductivity plays a minor role. Since in our case the intrinsic aluminum nitride to C-E resin thermal conductivity ratio is well above this criteria, we were able to use the prediction by Sheng directly. It should be noted that this curve agrees reasonably well with our data. A good correlation with our data is obtained with the Lewis-Nielsen model by reducing the geometry factor A from 8 to 1.5, representative of spherical particles as cited by Bujard and others. At the low volume fraction tested, the effect of bond percolation was not evident.

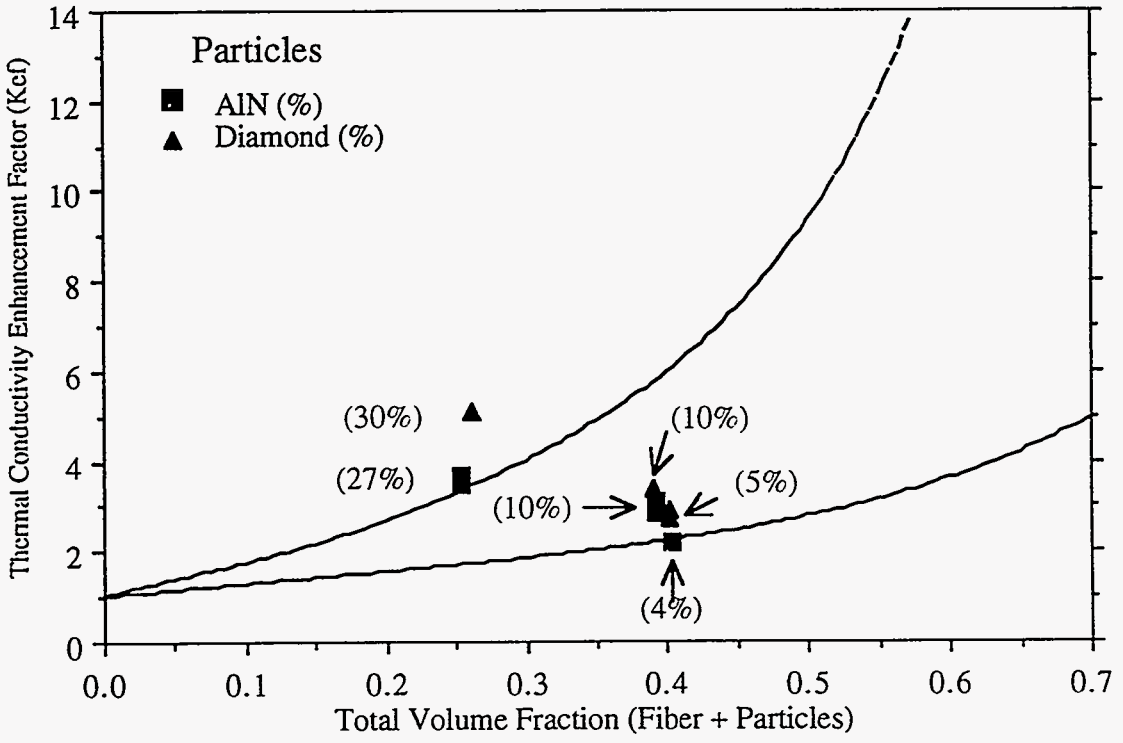

Figure A.3.1-3 Thermal conductivity enhancement factor, k_{ef}, for a filled cyanate ester resin, as a function of total volume fraction of particles and P-75 fiber.

A second sampling of material specimens was produced with the addition of 100 μm-long P-75S fibers to the matrix. The actual fiber length distribution was rather asymmetric, ranging from 90 to 600 μm, with 100 being representative of the peak. Specimens with various volume fractions of particulates and fibers were produced. In general, the volume fraction of solids ranged from 45 to 56%. A thermal conductivity enhancement ratio was formed by normalizing the composite properties to that of the neat resin. We plotted this enhancement ratio as a function of the volume fraction of P-75 fibers, the most dominate solid matrix fraction. Figure A.3.1-3 shows this enhancement ratio with the various volume fractions of particulates denoted as a secondary parameter.

Other references[9,13] contain several theoretical models for the transverse thermal conductivity of continuous graphite fiber/resin systems. The simplified model by Chamis[9] contains the following expression:

$$k_{f22} = (1 - \sqrt{V_f})\, k_m + \frac{k_m \sqrt{V_f}}{1 - \sqrt{V_f}(1 - k_m / k_{f22})} \quad \text{and}$$

k_m = neat resin thermal conductivity
k_{f22} = fiber transverse thermal conductivity
V_f = fiber volume fraction

The above expression accounts for the fiber transverse thermal conductivity k_{f22} that is typically an order of magnitude lower than the fiber longitudinal k_{f11} As before in the particle filler case, it can be shown that once the thermal conductivity reaches a value of 50, little further benefit is gained by introducing fibers that possess a higher k_{f22}.

Springer's[12] expression for the transverse thermal conductivity agrees remarkably well with the Chamis expression. Springer's model does, however, tend to predict more of an increase in the transverse thermal conductivity k_t above a volume fraction of 0.6 than the Chamis model, as one might expect. Referring to Figure A.3.1-3, the experimental data is distinctly above the predicted Chamis fiber-only curve. One data point for the very large volume fraction of spherical diamond particles (30%) is noticeably higher. For comparative purposes, Bujard's curve for the aluminum nitride has been added to Figure A.3.1-3. We notice that for high volume fraction particulates and lower volume fraction fibers, some correlation with the particulate-only curve exists. Thermal clusters of particulate matter, which span the material thickness, seem to exist under this situation.

Several cooling ring arc segments were produced with aluminum nitride/graphite fibers (11% AlN, 39% fiber). The transverse thermal conductivity agreed with the compression molded disc data, although the ring section was much reduced in thickness, 0.5 mm versus 3.2 mm. We observed that molded rings with combined solid volume fractions over 50% tended to be brittle. This limited tests series tended to rule out molding a composite ring from two solid constituents.

At this juncture, we realized that the aspect ratio of the particles was extremely important to attaining high thermal conductivity enhancement ratios. Two options appeared to be open. First, the investigation could be repeated using hexagonal boron nitride particles which evidently produced very effective thermal clusters[14], or secondly, we could redirect the study efforts toward achieving a random distribution of fibers. The 100-μm-long fibers are similar to particles with an aspect ratio of 10. We chose to continue our investigation solely with fibers, and expand the study to include 400-μm-long fibers, yielding a nominal aspect ratio of 40. The 400-μm fiber length was chosen as a means to span the ring wall thickness and utilize the high fiber thermal conductivity property to enhance the k_t.

Compression molded ring segments were produced with balled-milled fibers where the nominal fiber length was 400 μm. As before, the distribution of fiber length was skewed about this mean, ranging from roughly 90 μm to 800 μm in length. Some attempt

was made to achieve a random orientation of fibers, although our ability to accomplish this desired condition was quite limited. The volume fraction of fibers to C-E resin was 60/40% in all cases. Figure A.3.1-4 illustrates the measured transverse thermal conductivity for these rings. Thermal conductivities very near our design goal of 4 W/m-°K were obtained. We observed that the k_t data for composite ring specimens produced with 100 μm-long fibers were decidedly lower. As a further comparison, thermal conductivity data obtained with the early MX4925 carbon/phenolic molded ring with relatively long fibers is included. This data tends to agree with the Chamis prediction for long fiber composites.

The Sheng model prediction for a randomly oriented prolate ellipsoid particle with an aspect ratio of 10 is also depicted in Figure A.3.1-4. This aspect ratio conforms to our 100 μm-long fiber. Reference 11 also has similar predictions for the long axis of ellipsoidal particles oriented normal to the direction of heat flow. For this case, the thermal conductivity would be similar in magnitude to the Chamis model at volume fractions less than 40%. For higher volume fractions, the Sheng model predicts considerable enhancement in spite of the adverse particle orientation. For random fiber orientation the Sheng model predicts even higher enhancement than evident from our data. This situation may be explained by the fact that our fiber orientation was far from being random.

We have observed a factor of 7 improvement in the transverse thermal conductivity over our first ring molding attempts. The design goal of 4 W/m-°K transverse thermal conductivity was attained. As mentioned earlier, further investigations concentrated on perfecting a means of reliably obtaining random fiber orientation, such as spraying the prepreg material into the mold to achieve random fiber orientation. There is still much to be learned regarding the reproducibility of composite mechanical properties and the ability to predict the material thermal conductivity *a priori*.

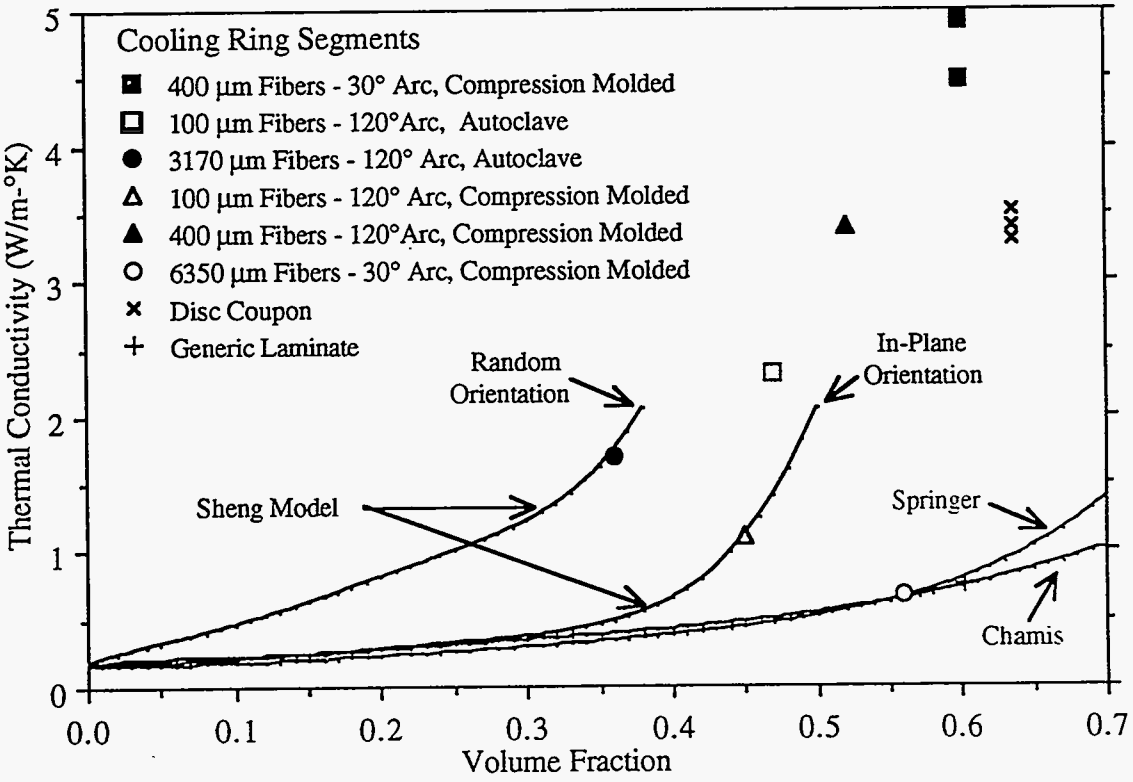

Figure A.3.1-4 Transverse thermal conductivity of 450-micron thick cooling ring segments from compression-molded cyanate-ester/P75 discontinuous fibers (100. 400μm)

A.3.2 Fiber Length and Resin Volume Fraction Considerations

As in the case of the cooling ring thermal conductivity enhancement investigation, the Lewis and Nielsen model can be used to characterize the mechanical properties of composites. In particular, the elastic modulus is given as a function of fiber aspect ratio and volume fraction. The general expression for the modulus ratio (*i.e.*, the composite modulus to the unfilled resin modulus (M_m))) is of the same form:

$$\frac{M}{M_m} = \frac{1 + ABV_f}{1 - B\psi V_f}$$

In the foregoing expression, M can be any modulus (*i.e.*, shear, tensile, or compressive). The constant A is a simple multiple of the fiber aspect ratio for uniaxial orientation of the fibers. For a longitudinal elastic modulus case, E_l, A becomes:

$$A = 2L / D = 2A_R$$

where L and D are fiber length and diameter respectively, and A_R is the fiber aspect ratio.

The expression for B is of the same form as before, except it now contains the ratio of the fiber modulus to resin modulus in place of the material thermal conductivities. Again, B is expressed as:

$$B = \frac{E_f / E_m - 1}{E_f / E_m + A}$$

where E_f and E_m are the fiber and resin Young's moduli respectively.

Factor ψ takes into account the volume fraction of the fibers. The expression, as before, is:

$$\psi = 1 + \frac{1 - \phi_m}{\phi_m^2} V_f$$

Here the value of ϕ_m is the maximum packing factor for the fibers. The value of ϕ_m varies with particle shape and state of agglomeration. It is difficult to predict ϕ_m from theory. It is generally experimentally determined from sedimentation measurements or from the maximum packing of dry particles, or fibers, under vibratory motion. For fibers, Another reference[15] gives the following values for cubic packing, 0.785; and for hexagonal packing, 0.907. In general, random close packing will lie between these limits. For our study we chose 0.82 as an initial value in correlating the composite test data.

It is possible to generate a figure depicting Young's modulus (tensile) for the composite as a function of fiber aspect ratio and volume fraction for longitudinal fiber orientation. The result is shown in Figure A.3.2-1 in a non-dimensional form for fiber and resin properties corresponding to P-75S/Cyanate Ester. At a fiber aspect ratio of 1000, the modulus ratio for 60% volume fraction is 82.11, which is approaching a continuous unidirectional fiber matrix. Extrapolating out to A_R = 10,000, the modulus ratio increases only slightly more, becoming 83.6. For the cyanate ester resin, we established a tensile modulus of 3.7 GPa; consequently, the predicted composite modulus for the long fiber (0.1 meter) would be 309.3 GPa (Nielsen Model). The value closely agrees with our measured value of 321.3 GPa. Figure A.3.2-1 shows the strong dependence of modulus on fiber aspect ratio. The aspect ratio must be greater than 100 to realize the stiffness comparable to that of a unidirectional composite.

Figure A.3.2-1 also demonstrates the importance of obtaining a high fiber volume fraction. For an aspect ratio of 100, 60% versus 40% fiber fraction produces a factor of 1.7 greater stiffness. The improvement in stiffness also is apparent at lower fiber aspect ratios. Achieving high fiber volume fractions has been our goal from the onset. The Nielson model affords an opportunity to qualitatively assess this factor.

In our molded composite cooling ring, we are using fiber aspect ratios on the order of 10 to 40, and with the fibers being randomly oriented to some unkown extent. The above figure cannot be used to predict the stiffness behavior for such a complex matrix. However, Reference 15 recommends a method for adjusting the predicted curves for the individual situations of two and three dimensional randomly oriented fibers. The expressions for these two cases are:

$$E_{2d}/Em = (^3/_8\, E_L/E_m + {}^5/_8\, E_T/E_m) \text{ 2-dimensional}$$

$$E_{3d}/E_m = (^1/_5\, E_L/Em + {}^4/_5\, E_T/Em) \text{ 3-dimensional}$$

E_L/Em is the longitudinal modulus ratio previously calculated. To evaluate the transverse modulus ratio (E_T/E_m) required by these expressions, the same procedure is used as before, except the value of A becomes a constant 0.5. The predicted results derived from these expressions are shown in Figure A.3.2-2. We chose not to use a non-dimensional format in order to provide a direct comparison with our composite cooling ring structural test investigation.

Measured values of elastic modulus for specimens extracted from the compression molded cooling ring (P-75/cyanate ester resin) are shown in Figure A.3.2-2. The data is plotted at nominal aspect ratios of 10 and 320, corresponding to a fiber length of 100 μm and 0.32 cm. Acid digestion tests placed the fiber volume fractions at nominally 45%, for the lower aspect ratio and 36% for the higher aspect ratio, considerably below our goal of 60%. The higher aspect ratio specimens were produced using the hard rubber ring molding process described in section 3.2.3.4. It is difficult to estimate to what extent the composite specimens approached 3-dimensional matrix. A review of the ultrasonic Non Destructive Evaluation (NDE) measurement we conducted suggests that the composite tends to be somewhere in between a 2- and 3-dimensional (*i.e.*, more fibers are oriented in the plane of the cooling ring wall) matrix. We also observed from these measurements that the average length of the fibers in the final part was less than that of the fibers prior to molding. It is likely that the molding process causes a random fracturing of the fibers inhibiting our ability to achieve higher aspect ratio molded parts.

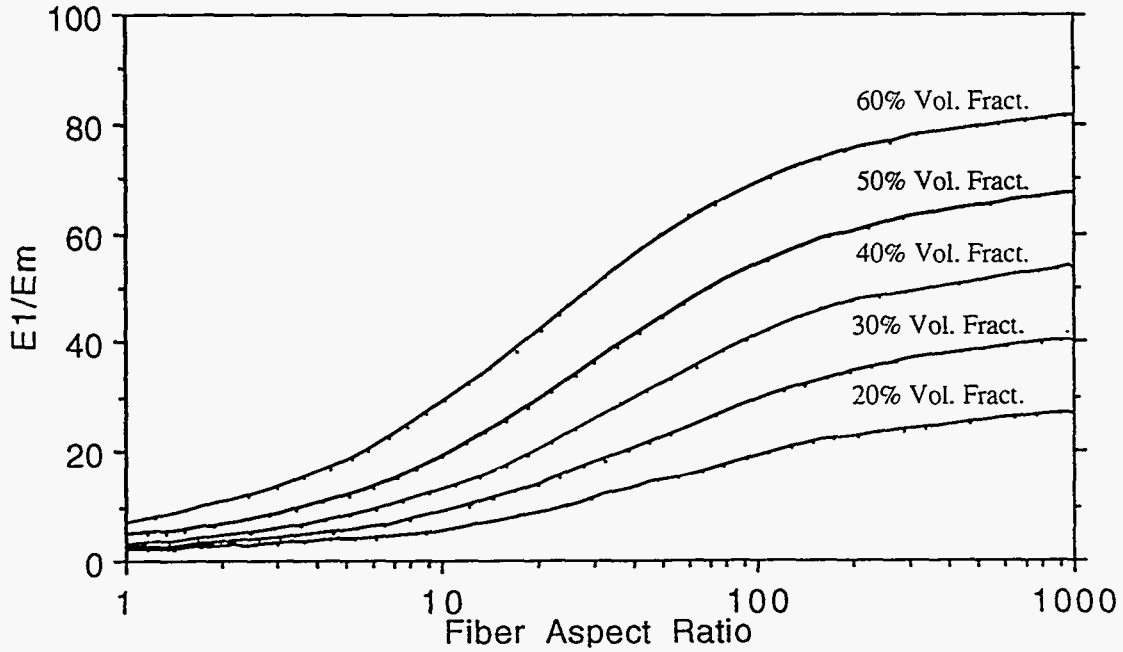

Figure A.3.2-1 Ratio of longitudinal composite modulus of elasticity (E_1) for P-75S/954-3 to matrix modulus (E_m).

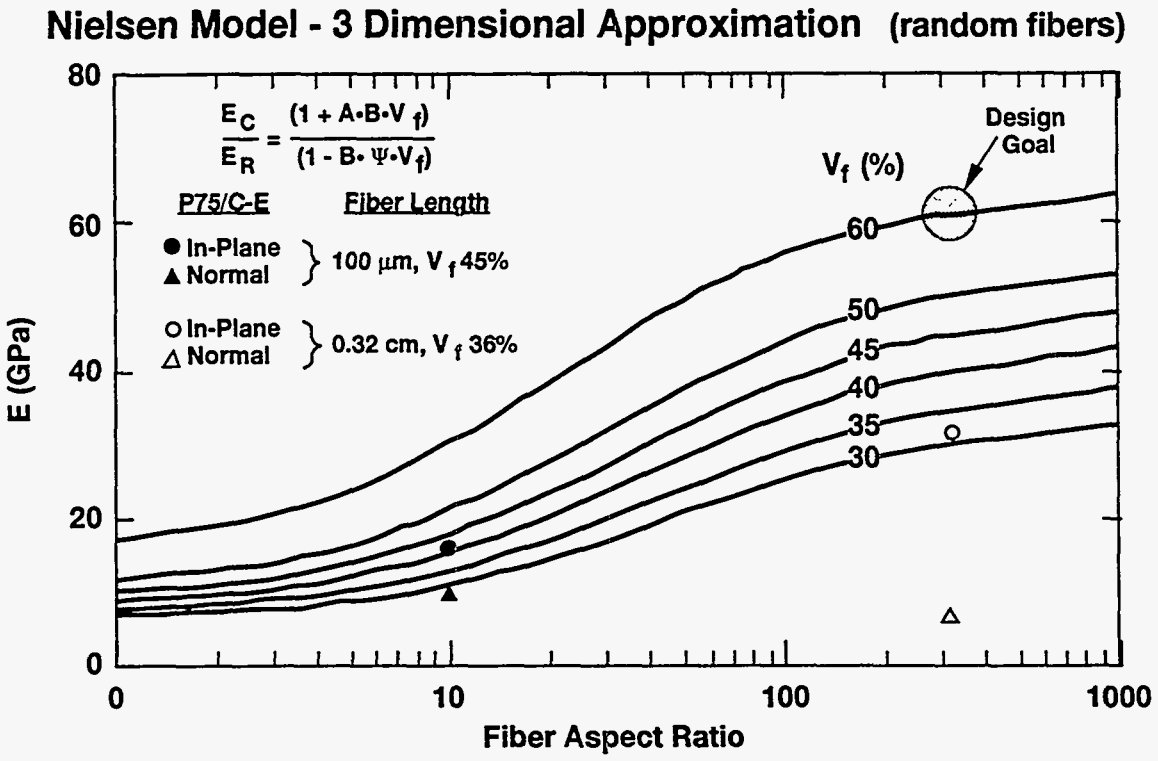

Figure A.3.2-2 Composite Modulus (E) versus fiber aspect ratio, for both 2D and 3D randomly oriented fibers for 60% and 40% fiber volume fractions.

Continued process development using the hard rubber molding produced higher fiber volume fraction ring specimens. Unfortunately, this lead to some brittleness in the part. We discontinued the development at this stage, without determining whether the elastic modulus of the part had been improved. The need to produce full scale rings for the first silicon shell prototype was the prime driving factor in curtaining the development tests.

In the above expressions for elastic modulus, one will find that the 2-dimensional modulus calculation for an $A_r = 10000$ yields a predicted value of 118 GPa for a quasi-isotropic composite. This value is close to the 98 GPa value we measured on quasi-isotopic continuous fiber coupons. Although our study is far from complete, it would appear that the Nielsen model for elastic modulus can provide a reasonable approximation for a domain ranging from discontinuous to continuous fibers.

A.4 Material Study Summary

The overall conclusions of the mechanical properties test program for the polymeric resin and laminate material is that the P75S/Cyanate Ester material is now fully described and qualified. All elastic moduli and Poisson's ratio of the system were evaluated by independent institutions using both destructive and non-destructive means to obtain comparable results. The P75S/Cyanate Ester sensitivity to combined radiation (10MRad) and butane exposures were investigated and found to be negligible.

Elastic material properties established for the discontinuous composite matrix were disappointingly low. This was not expected at the onset. We learned that the resultant elastic modulus of a discontinuous fiber polymeric system is far more sensitive to fiber aspect ratio than envisoned by some industry experts, as well as being a strong function

of fiber volume fraction. At the onset, we had an appreciation that the elastic modulus was favorably enhanced by high volume fraction fiber content, nonetheless, we were unable to achieve the desired elastic modulus for molded components. However, we were able to enhance the transverse thermal conductivity of the discontinuous fiber composite signficantly, achieving a factor of 7 enhancement, which was needed for this application.

References:

1 Los Alamos National Laboratory Report, LA-12029.

2 E. Barberis et al., "Temperature Effects on Radiation Damage to Silicon Detectors", Nucl. Instr. and Meth., **A362** (1993) 373.

3 H. Ziock et al., "Temperature Dependence of the Radiation Induced Change of Depletion Voltage in Silicon PIN Detectors", Nucl. Instr. and Meth., **A342** (1994) 96.

4 Special Issue on Acoustic Microscopy, IEEE Trans. Sonics and Ultrasonics, SU-32, no. 2 (1985).

5 J. H. Gieske and R. E. Allred, "Elastic Constants of B-Al Composites by Ultrasonic Velocity Measurements," Experimental Mechanics, 1974, no. 3:158-165.

6 T.-T Wu and Z.-H. Ho, "Anisotropic Wave Propagation and Its Applications to NDE of Composite Materials," Experimental Mechanics, 1990, no. 12, p313-318.

7 E. Ishibashi, Z.H. Liu, "Saturated Pool Boiling Heat Transfer Characteristics of Porous Polyurethane Covered Heaters Under Atmospheric and Reduced Pressure Conditions", Heat Transfer-Japanese Research", Vol 17, #6, (Nov-Dec 1988).

8 S.V. Conev, J. Mitrovic, "An Explanation for the Augmentation of Heat Transfer During Boiling in Capillary Structures", International Journal of Heat and Mass Transfer, Vol. 29, no. 1, 1986, p91-94.

9 C. C. Chamis, "Simplified Composite Micromechanics Equations for Hygral, Thermal, and Mechanical Properties," SAMPE Quarterly, April, 1984.

10 P. Bujard and J. P. Ansermet, Thermally Conductive Aluminum Nitride-Filled Epoxy Resin, Ciba-Geigy Limited, Research Center, 1701 Friborg, Switzerland.

11 D. Burland, D. Shattuck, and J. Perrin, "The Thermal Conductivity of Elastomer Composites for Electrophotography," *Journal of Imaging Technology* 15:257-263 (1989).

12 P. Sheng, "Theory for the Dielectric Function of Granular Composite Media", *Phys. Rev. Lett* 45:60-63 (1980); "Microstructure and Dielectric Properties of Granular Composite Films," *Opt. Laser Tech.* 13:253-260 (1981).

13 G. S. Springer and S. W. Tsai, "Thermal Conductivities of Unidirectional Materials," Chap. 2, Environmental Effects on Composite Materials, Edited by G. Springer, ISBN 087762-300-7.

14 P. Bujard, "Thermal Conductivity of Boron Nitride Filled Epoxy Resins: Temperature Dependence and Influence of Sample Preparation," Ciba-Geigy Limited, Research Center, 1701 Friborg, Switzerland.

15 S. Seehra, et al., "Effects of Space Environmental Conditions of Graphite Epoxy Composites," SAMPE Journal, March/April, 1985.